



Pilkington Library

Author/Filing Title HOLLAND

Vol. No. Class Mark T

**Please note that fines are charged on ALL
overdue items.**

FOR REFERENCE ONLY

0402694368





Numerical Modelling of the Riverine Thermal Bar


Paul R. Holland

A DOCTORAL THESIS.

SUBMITTED IN PARTIAL FULFILMENT OF THE REQUIREMENTS
FOR THE AWARD OF
DOCTOR OF PHILOSOPHY OF LOUGHBOROUGH UNIVERSITY
OCTOBER 2001.

Supervisor: A. Kay, Ph.D. Loughborough University

© P.R. HOLLAND 2001

 Longborough University Library
Date Feb 02
Class
Acc No. 040269436

Never does nature say one thing and wisdom another

Juvenal: *Satires XIV*

Acknowledgements

I would firstly like to extend sincere thanks to my supervisor, Tony Kay, for much useful guidance and a necessary, constructive and sometimes welcome pedantry in his criticism of my written work. This thesis would be unrecognisable were it not for the continued assistance and input of Vincenzo Botte, whose dedication to achieving me a Ph.D. and subsequent career has far surpassed the bounds of a rational human's empathy. I'm still waiting for the catch.

The production of this thesis was a task requiring a constant stream of personal support and encouragement, and to this end I must sincerely thank Jo, whose illuminating company brightened the darkest of Loughborough winters and allowed me the freedom to dedicate myself to this work. Also, I consider my parents' commitment to my education and wellbeing flawless, and I cannot begin to thank them for their unquestioning support and guidance throughout the more turbulent phases of my life.

I have benefited considerably from useful discussions with Ruslan Gnatovsky, Nickolay Granin, Ian Fisher, and many other dedicated scientists from all parts of our shrinking world. I am also indebted to Keith Watling for juggling the heavily stressed Sun network which carried this work, and for laughing loudly at technical problems which would make lesser men weep.

Finally I would like to thank Kerrie, Ben, the rest of my family, the Stevensons and all of my friends from Loughborough, Norwich, and Warwick for making my time as a research student an enjoyable and instructive period. I can only hope that my time as a sentimental Ph.D. holder will be as much fun.

Loughborough, October 2001.

In fond memory of Jim Stevenson, 1942-2001.

Abstract

A Finite-Volume discretisation of the Navier-Stokes equations is used to study various aspects of the physics and ecology of the riverine thermal bar. The classical thermal bar is a downwelling plume which is formed twice a year in temperate lakes when the shallows warm or cool through the temperature of maximum density (T_{md}). The riverine thermal bar is a similar sinking plume arising at the confluence of river and lake waters which are on either side of the T_{md} . The dynamics of this poorly understood riverine case may be considerably more complex due to the additional effects of river salinity and velocity on the downwelling plume.

A series of deep-lake simulations forms the initial study of the riverine thermal bar in the Selenga River delta in Lake Baikal, Siberia. While the decrease in the T_{md} with depth (pressure) prevents the classical thermal bar from sinking far, this study shows that a saline riverine thermal bar may be able to sink to greater depths and thus take part in Baikal's vigorous deep-water renewal.

Attention then focusses on a model of the smaller Kamloops Lake in British Columbia, which is used to reproduce the only field observations of a riverine thermal bar and test the effects of coriolis forces, bathymetry, and surface heating on the resulting flow field. Plankton ecosystem models are then coupled to these validated dynamics, and results are presented which extend and test the findings of a previous modelling study on the effects of the classical thermal bar on plankton populations.

Contents

Abstract	iv
Contents	v
1 Introduction	1
1.1 The Thermal Bar	2
1.2 Riverine Effects	6
1.3 Previous Studies of Thermal Bar Dynamics	8
1.4 Lake Baikal	12
1.5 Kamloops Lake	16
1.6 Thermal Bar Interaction with Plankton Ecosystems	19
1.7 Overview and Objectives	22
2 Model Formulation	24
2.1 Governing Equations	24
2.2 Boundary Conditions	28
2.3 Lake Baikal Dynamical Model	32
2.4 Kamloops Lake Dynamical Model	39
2.5 Ecosystem Modelling	43
3 Numerical Solution	52
3.1 Discretisation Procedure	52
3.2 Solution Procedure	58
3.3 Numerical Techniques for Linear Systems	62
3.4 Balance of Convection and Diffusion	65

4	Modelling of Turbulence	70
4.1	The Eddy-Viscosity	71
4.2	The Horizontal Eddy Viscosity	73
4.3	Parameterisation of Vertical Mixing in Lakes	76
4.4	Models of Vertical Eddy Viscosity	79
4.5	Numerical Testing of Models	81
5	Preliminary Results	89
5.1	Simulation <i>C</i>	89
5.2	Simulations <i>S1</i> and <i>S2</i>	91
6	Results - Simulation of The Thermal Bar	93
6.1	Flow Dynamics	94
6.2	Transport of River-Borne Materials	103
6.3	Effects of Inflow Velocity u_R	110
6.4	Effects of Thermobaricity	112
7	Results - Effects of Salinity	115
7.1	Simulation <i>T9</i>	116
7.2	Simulation <i>T11</i>	126
7.3	Simulation <i>T7</i>	128
8	Results - Small Lake Dynamics	131
8.1	Background Flow-Field	132
8.2	Effects of Model Improvements	139
8.3	Effects of Thermobaricity	146
8.4	Effects of Salinity	147
8.5	Transport of Riverine Substances	149
8.6	Consequences for Deep-Lake study	153
9	Results - Plankton Modelling	157
9.1	Temporal Evolution of Plankton Population	158
9.2	Closer Examination of Plankton Growth	162
9.3	Variation of Riverine Boundary Conditions	171
9.4	Discussion and Comparison with BK	176

Chapter 1

Introduction

The constant decrease in the cost of computer power has transformed many areas of science and generated several new fields of study which are disciplines in their own right. One of the sciences which has been directly affected is the classical study of fluid mechanics, which is rich in problems involving the partial differential equations and nonlinearity which prove so challenging to traditional mathematical analysis. The inception of Computational Fluid Dynamics (CFD) as a mainstream research tool has radically broadened the scope of the modern study of fluid phenomena.

The versatility of CFD means that, unlike classical fluid mechanics which tends to address simplified general problems, it may be successfully applied to complex individual engineering applications such as turbomachinery, missile and aircraft design. Large-scale environmental flows may also be addressed, allowing the development of many sizeable operational atmosphere and ocean models which are dedicated solely to predicting the general circulations and climatological conditions of the Earth.

While these General Circulation Models are still under active development due to the need for ever-improving predictions and fears over our changing climate, progressively more powerful computers have precipitated an important increase in the modelling of the relatively small-scale phenomena which produce and interact with these large motions. This includes a vast increase in the use of desktop machines rather than supercomputers to perform CFD modelling of environmental flows in smaller domains, such as lakes, rivers, urban air spaces, etc.

A relatively small and important mechanism which is extremely well suited to CFD modelling is the thermal bar. The essential nonlinearity in the equation of state makes mathematical analysis of the thermal bar problematic, particularly when haline effects are involved, while laboratory experiments cannot achieve the high-Reynolds-number regime present in nature and flows are generally too slow and widespread to be measured accurately in the field. The classical thermal bar has been the subject of sophisticated CFD treatment by many authors (see section 1.3), but to my knowledge the riverine thermal bar has never previously been modelled in any way. In this thesis, the limited computational resources available to this study are applied to a numerical model of the riverine thermal bar.

1.1 The Thermal Bar

Fresh water is unusual in that it has a nonlinear dependence of density on temperature over the full limnological range of temperature, pressure, and salinity. Figure 1.1 shows the nonlinear form of the equation of state given by Chen & Millero (1986) (displayed at atmospheric pressure), and the increase in density due to salinity. This nonlinearity leads to the cabbeling instability, which in turn causes the thermal bar phenomenon, as described below.

At atmospheric pressure and zero salinity, thermal increases after ice melt (in the range $0^\circ - 3.98^\circ\text{C}$) result in increased molecular agitation which causes the hydrogen bonding of H_2O to rupture, filling the voids in the ice lattice structure (Wetzel 1983). This causes an increase in density with temperature. As the temperature progresses above 3.98°C the amplitude of the inter-molecular vibrations increases, and so do the inter-atomic distances, increasing the volume of the water and thus decreasing the density (Wetzel 1983). It is the interaction of these processes which causes the nonlinear form of the equation of state. The temperature at which these two effects combine to give the minimum specific volume for water (and therefore the maximum density) is called the *temperature of maximum density* (T_{md}).

These processes are affected by salinity and pressure, so that the T_{md} varies spatially within lakes. Figure 1.2 shows the effect of salinity and pressure on the T_{md} ; note that

the pressures found in deep lakes have a particularly drastic effect. This influence of pressure on the thermal expansion of water, termed *thermobaricity*, results in a decrease in the T_{md} of roughly 1°C per 500 m depth (Eklund 1963).

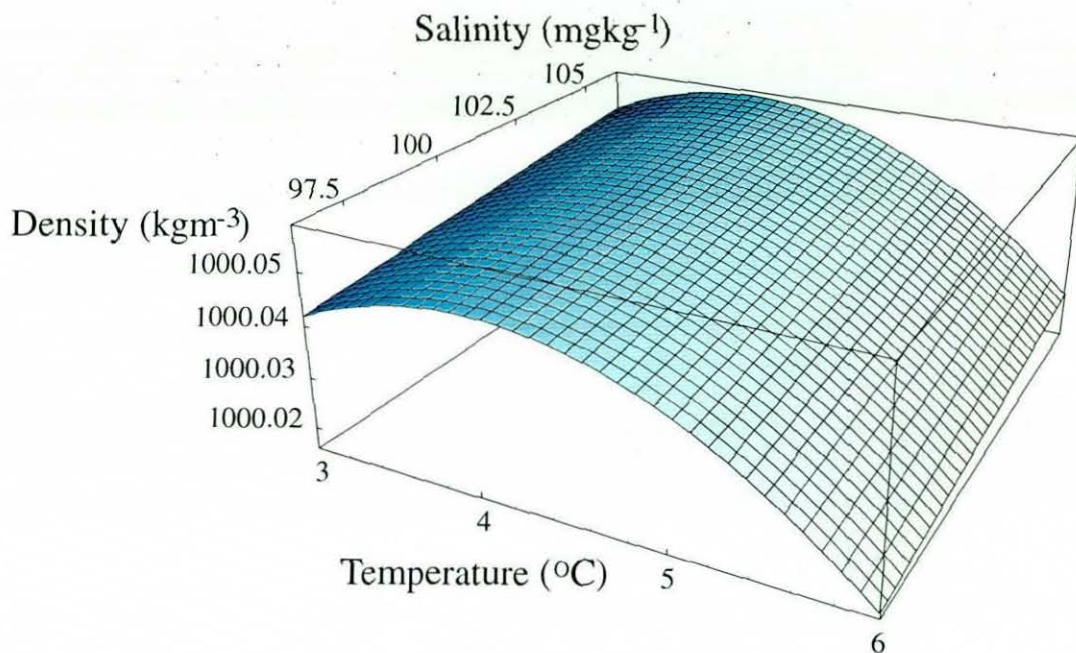


Figure 1.1: The equation of state at atmospheric pressure over the range of temperature and salinity considered in this work.

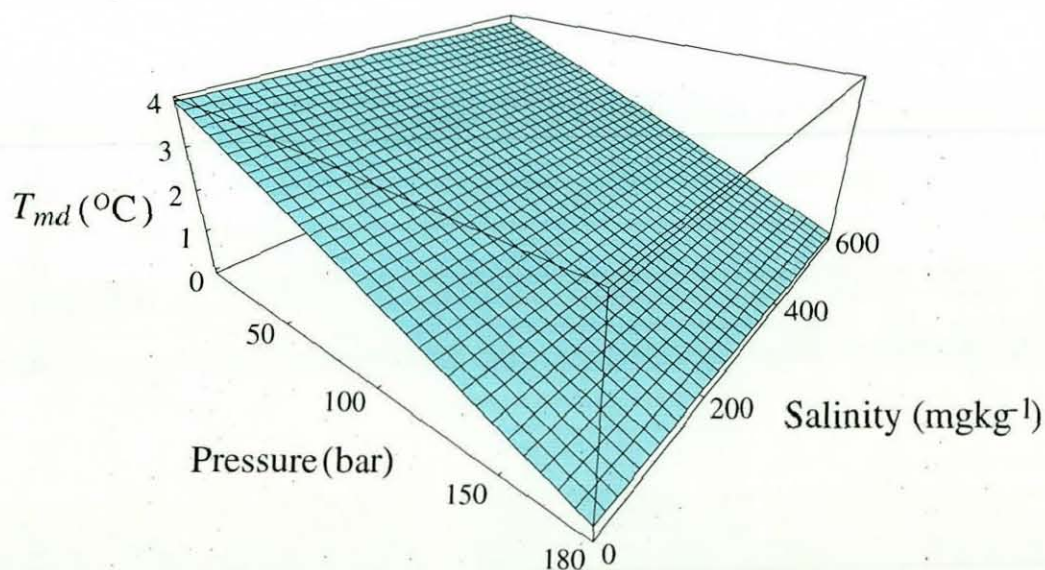


Figure 1.2: Variation of the T_{md} over all pressures and salinities for which the Chen & Millero (1986) equation of state is valid.

When water masses with temperatures on either side of the T_{md} meet, the mixed water at the interface will be closer to the T_{md} , and thus denser, than either of the component bodies. Density increase upon isobaric mixing of two dissimilar water types is generally referred to as *cabbeling* (Witte 1902, Foster 1972). In lakes, this area of maximally dense, cabbeling water forms a descending plume which draws in surrounding waters, causing a sharp thermal front about the surface signature of the $T = T_{md}$ contour. Such a front was first observed by Forel (1880) in Lake Geneva, who called it the *barre thermique* (*thermal bar*) as it forms a barrier between waters warmer and cooler than the T_{md} . The first measurements showing the existence of a thermal bar were made in Lake Ladoga by Tikhomirov (1963).

Previous analytical and numerical studies of the thermal bar have mainly been limited to the 'classical' case where a surface heat flux causes differential warming of the lake water due to bottom topography, e.g. Shimaraev et al. (1993), Malm (1995), and Farrow (1995*b*). For example, moderately-sloping shallow regions near the shores of a lake will warm faster than the deeper centre in spring due to their smaller volume and additional radiation absorption by the lake bed (St. John et al. 1976). If the initial temperature of the lake was cooler than the local T_{md} then eventually the shallow region will be warmer than the T_{md} and the deep region cooler. A thermal bar will then form between these waters as the mixture is at the local T_{md} and thus denser than either of the two component bodies (see figure 1.3).

As the whole lake gradually warms, the thermal bar propagates out into the lake until the surface temperature is above the T_{md} everywhere. The lake then becomes stably stratified as warmer water overlies cooler dense water (Zilitinkevich et al. 1992). As the air cools in the autumn the reverse of this process occurs, with the shallow areas cooling through the T_{md} more quickly than the deep waters. In this way all temperate lakes have a twice-yearly ventilation of lower waters from these downwelling episodes. However, the autumnal thermal bar is less well-defined due to the generally stronger wind-mixing and weaker temperature gradients present at that time of year (Ullman et al. 1998).

Under a geostrophic balance, the converging pressure gradients on either side of

the surface T_{md} will generate ‘thermal wind’ flows in the alongshore direction, parallel to the thermal front. These flows consist of a strong cyclonic circulation inshore of the thermal bar (as a result of the relatively steep temperature gradients there) and a weaker anticyclonic circulation offshore. The thermal bar therefore acts as a barrier between parallel horizontal flows in exactly opposing directions. As an illustration of this circulation, if the section of figure 1.3 were in the northern hemisphere then horizontal flows would be directed ‘out of the page’ inshore of the thermal bar and ‘into the page’ offshore, with a surface stagnation point in between.

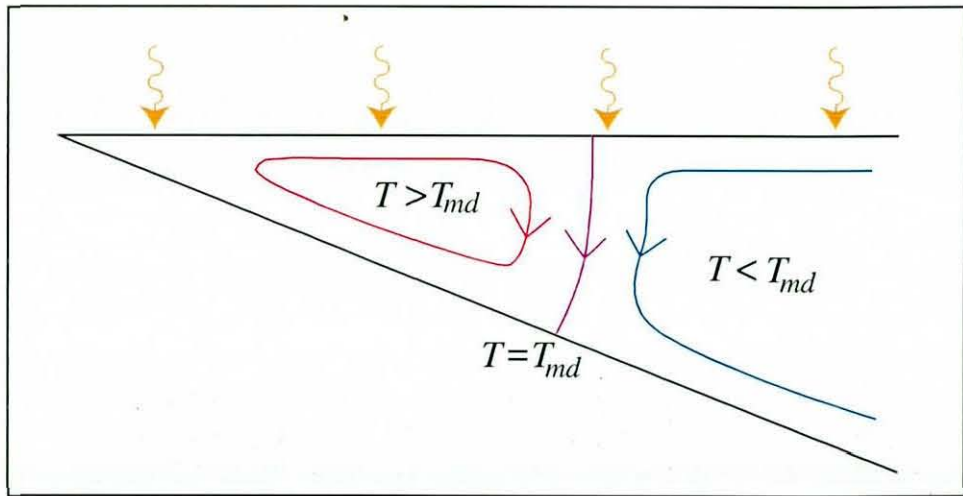


Figure 1.3: Schematic of the ‘classical’ spring thermal bar driven by a surface heat input. The internal arrowed lines are streamlines.

Water within the thermal bar plume sinks until it reaches a depth where it is no longer denser than the surrounding fluid. This may happen for several reasons, such as entrainment of lower density water into the plume or varying thermal characteristics of the surrounding water. Importantly, the decrease of the T_{md} with depth (pressure) may also suppress the downwelling motion of the thermal bar (Carmack & Weiss 1991). If the subsurface temperature profile decreases slowly with depth, as is usually the case in deep temperate lakes, then any water sinking at the surface T_{md} will no longer be densest at great depths, where slightly colder (and thus denser) water will form a barrier to free convection (figure 1.4). This provides a theoretical maximum penetration depth for the thermal bar phenomenon, so that the plume will only reach the bottom of the lake if it is shallow enough for the decrease in T_{md} to be negligible. It is therefore believed that

some external mechanism is required to trigger convection to the bed of the deepest lakes (Farmer & Carmack 1981).

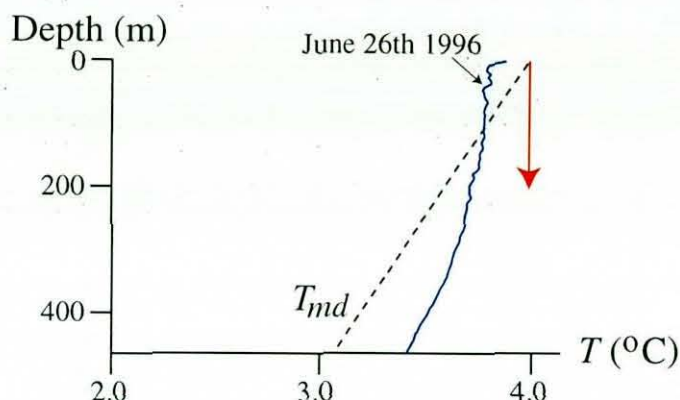


Figure 1.4: A typical temperature profile from the South Basin of Lake Baikal. Water sinking at the surface T_{md} is less dense than the waters below and will therefore be unable to descend past a certain depth.

1.2 Riverine Effects

The riverine thermal bar is formed at the mouth of a river where the temperatures of the river and lake are on opposite sides of the T_{md} (Carmack 1979). In theory this produces a downwelling plume of a similar form to the classical thermal bar, but the river's characteristics other than temperature will complicate the buoyancy forces governing the thermal bar circulation (Holland et al. 2001*a*).

As a river-lake system is warmed in spring, the river will heat up faster than the lake because the heat influx acts upon a shallower, well-mixed volume and extra radiant energy is absorbed by the river bed (St. John et al. 1976). In temperate regions both river and lake are cooler than the T_{md} over the winter, so the warmed river is densest and therefore enters the lake as a sinking gravity current which flows towards the lake bed (Carmack et al. 1979). As the warming continues the river's temperature passes through the T_{md} before the lake, and a thermal bar plume will form (figure 1.5). In a similar manner to the classical case, this plume moves away from the inflow as warmer

and warmer water is fed into the lake by the river. Eventually the whole lake is warmed to above the T_{md} and the buoyant river enters as a surface overflow on the denser, stratified lake water (Carmack et al. 1979).

In autumn the analogous case happens with a surface cooling, as the river generally responds to external forcing more quickly than the lake. In this way the twice-yearly mixing of temperate lakes can be dominated by riverine effects rather than differential heating of the shallow and deep areas, so that even a steep-sided lake can be ventilated by thermal bars (Carmack 1979).

The main difference between the classical and riverine thermal bars is caused by the influx of salinity from the river. Throughout this study the term 'salinity' is taken to mean total milligrams of dissolved solids per kilogram of saline water. The introduction of saline effects on density provides a contrast between the unusual buoyancy forcing of the pure thermal bar and the straightforward sinking associated with salinity gradients, revealing the differing influences of near-linear and nonlinear components of the equation of state. Also the effects of a river inflow velocity on the propagation of the thermal bar may be apparent as a high velocity will increase advection of heat into the lake and potentially cause a warming rate which is not possible in the classical scenario.

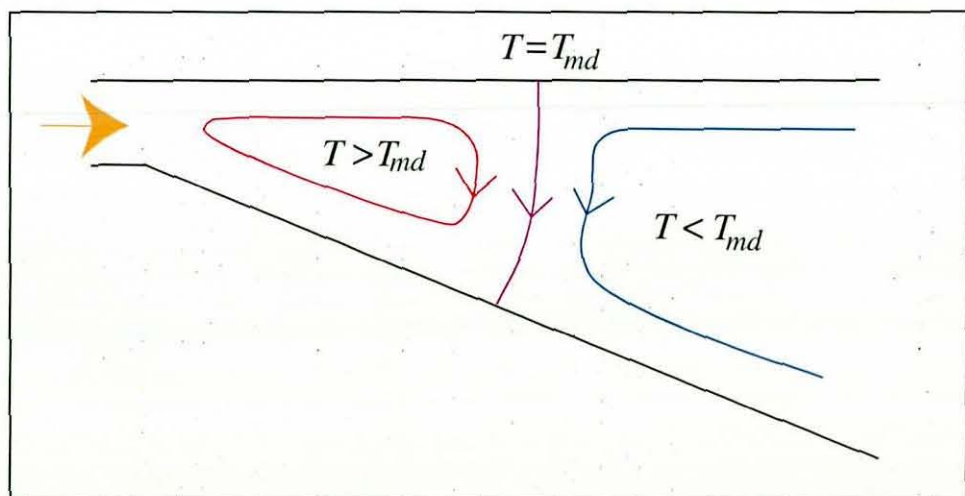


Figure 1.5: Schematic of the spring riverine thermal bar.

Elucidating the differences between the classical and riverine thermal bars is the aim

of this study. Of particular interest is the question of whether a saline riverine thermal bar may overcome the 'thermobaric barrier' to sinking and therefore penetrate deep waters despite the significant decrease in the T_{md} which is found in very large lakes.

1.3 Previous Studies of Thermal Bar Dynamics

Observations of the classical thermal bar have been made in most temperate Great Lakes and several smaller lakes since the first studies of Lake Ladoga by Tikhomirov (1963) and the Laurentian Great Lakes by Rodgers (1965). For example, Lakes Baikal (Shimaraev et al. 1993, Parfenova et al. 2000), Superior (Hubbard & Spain 1973), Huron (Moll et al. 1980), Michigan (Huang 1972, Bolgrien & Brooks 1992, Moll et al. 1993), Ontario (Csanady 1971, Gbah & Murthy 1998), and Ladoga and Onega (Naumenko 1994, Avinsky et al. 1999) have all been the subject of detailed studies. Also, laboratory-scale models of the laminar thermal bar in a non-rotating frame have been studied (Elliott & Elliott 1969, Elliott & Elliott 1970, Kreiman 1989), and small-scale idealised tank experiments have increased our understanding of the basic processes involved in the cabbeling instability (Marmoush et al. 1984, Inaba & Fukuda 1986, Lankford & Bejan 1986, Ivey & Hamblin 1989).

A review of the work referenced above highlights the strong sensitivity of the thermal bar circulation to the particular bathymetry, wind stress, and surface heat flux of the lake under consideration. The thermal bar is generally a large, long-lived density front which emerges at some point in May or June and persists for one to two months. The frontal propagation rate fluctuates in addition to decreasing with time, and may even become negative under certain conditions (Hubbard & Spain 1973, Gbah & Murthy 1998). This fluctuation is due to the effects of wind, which may totally outweigh the buoyancy-driven circulation in the short term. However, the thermal bar is usually significant in the presence of a wind-driven circulation due to the persistence of the buoyancy forcing (Csanady 1971, Scavia & Bennett 1980).

The thermal front is at least 1 km wide and all references show that the cabbeling water within it sinks at a rate of $1 - 30 \times 10^{-4} \text{ ms}^{-1}$. Flows converging at the thermal bar suppress most cross-frontal exchange so that it forms a barrier to horizontal mixing

despite the lateral shear in longshore flows (Gbah & Murthy 1998). Flows perpendicular to the shoreline are of order 10^{-2} ms^{-1} , yielding mid-latitude Rossby numbers of $O(10^{-1})$ based upon a minimum length scale of 1 km. The strongest motion in the thermal bar circulation is therefore the thermal wind which runs parallel to the thermal front (Huang 1971, Huang 1972). Many observers agree that these flows are $O(10^{-1}) \text{ ms}^{-1}$, while cross-frontal flows are $O(10^{-2}) \text{ ms}^{-1}$ and the (relatively strong) descending flows are $O(10^{-4}) \text{ ms}^{-1}$.

While there are many thermal bar studies in which an inflowing river plays some part in the spring warming of the shallows (e.g. Hubbard & Spain (1973), Moll & Brahce (1986), Bolgrien et al. (1995)), detailed observations of predominantly-riverine thermal bars are only available for a few Canadian lakes, of which those of Kamloops Lake are by far the most comprehensive (St. John et al. 1976, Carmack 1979, Carmack et al. 1979, Wiegand & Carmack 1981, Carmack et al. 1986). This limited geographical and bathymetric coverage makes it impossible to draw rigid conclusions about the differences in character between riverine and classical thermal bars, but some general observations may be made.

It seems obvious that, on any fixed bathymetry, the riverine thermal bar will propagate more quickly because the lake water experiences a riverine heat flux in addition to the surface heat flux. However, it is possible for riverine thermal bars to propagate more slowly than their classical counterparts as they are able to exist as a well-defined phenomenon in lakes with much steeper bathymetries. This allows increased advection of heat downwards, reducing the horizontal spread of warmer water which is responsible for moving the $T = T_{md}$ isotherm and thus slowing the propagation of the thermal bar.

Due to a higher spring warming rate, the warm waters inshore of the riverine thermal bar are more likely to have the character of a surface gravity-current than in the classical case. The wedge-like regions of warm water inshore of the classical thermal bar are mixed a little more thoroughly as a result of its slower warming and propagation rates. The riverine thermal bar may therefore exist as a mixing plume at the nose of a warm surface intrusion, rather than acting on the boundary of a completely-warmed stable shallow region. This allows a more significant return current to upwell inshore of the

T_{md} , producing the 'arrested thermocline' visible in Carmack (1979) and notably absent from the details of Hubbard & Spain (1973), Naumenko (1994), and Gbah & Murthy (1998).

All theoretical and numerical studies of the thermal bar to date have been limited to the classical case. Killworth & Carmack (1979) constructed a one-dimensional 'filling-box' model of Kamloops Lake with a river inflow at a seasonally varying temperature, producing a good agreement with the observed annual variation of the lake's (river-dominated) thermal structure. However, there have not been any previous attempts at modelling the effects of a range of riverine salinity and temperature distributions on the thermal bar phenomenon or its resulting circulation.

Huang (1969) was the first to attempt a mathematical description of the thermal bar, balancing coriolis and buoyancy forces in steady-state to yield the relevant temperature and flow fields. Csanady (1971) later achieved similar results with a two-dimensional numerical model. Transient features were then resolved by assuming a balance between vertical shear and horizontal pressure gradients, using a two-dimensional model driven by a one-dimensional temperature equation in the absence of horizontal convection (Elliott 1970, Elliott & Elliott 1970, Elliott 1971). This yielded the thermal bar position as a function of time (agreeing well with field observations (Elliott & Elliott 1969, Elliott & Elliott 1970)) and revealed that the cabbelling plume may be inclined to the vertical.

Rotational effects were introduced into two-dimensional numerical models by Bennett (1971), Huang (1971), and Huang (1972) who employed a third, longshore coordinate in which no gradients were permitted. These studies showed that the thermal wind is the dominant flow of the thermal bar in large lakes, a result which is in agreement with the asymptotics of Brooks & Lick (1972), who studied a rotating annulus under a horizontally-varying surface heat flux.

The first model to incorporate a surface wind stress was that of Scavia & Bennett (1980), who concluded that the thermal bar is highly susceptible to this forcing. Zilitinkevich et al. (1992) then refined the horizontal propagation rate estimates of Elliott & Elliott (1970) by elucidating the effects of horizontal heat advection. The numerical

and asymptotic results of Farrow (1995*a*) and Farrow (1995*b*) on the non-rotating case then showed that the downwelling plume may become separated from the thermal front due to inertial effects, a feature not yet noticed in the field.

In a departure from heat-balance or general circulation models, Kay et al. (1995) obtained plume velocity and temperature gradient predictions as a function of the Prandtl number by analysing the thermal bar as a free-convection boundary layer. Malm (1995) then carried out a comprehensive numerical study of thermal bars under a range of wind and bathymetric conditions, finding that the wind sensitivity is highly dependent upon slope bathymetry, which strongly affects flow speeds even in the absence of a wind forcing.

Gbah et al. (1998) are the only authors to adopt a higher-order turbulence closure in the study of the thermal bar, obtaining turbulent diffusivities as part of the solution procedure and producing reasonable estimates of the bar formation and migration timescales under a range of wind forcings. Tsvetova (1995) and Tsvetova (1999) made significant advances with the first thermobaricity-resolving (and fully compressible) model of the thermal bar applied to Lake Baikal but unfortunately failed to fully explore the details of thermobaric control of the sinking plume. More recently, Botte & Kay (2000) (hereafter referred to as BK) briefly studied thermobaricity as part of their plankton population study in the vicinity of a spring thermal bar in Lake Baikal, and have also examined the balance of wind, coriolis, and buoyancy forcings of this phenomenon (Botte & Kay 2001).

All of these works fail to scrutinise two significant aspects of the riverine thermal bar circulation, which will therefore be the primary objects of this study. The first is thermobaricity, which is crucial to the circulation of Lake Baikal and will be fully examined in a deep domain representing the Selenga River delta (Holland et al. 2001*a*). The second is the effect of a riverine salinity influx, which will redistribute the buoyancy forces and could provoke some very interesting dynamics, including the possibility that saline plumes will overcome thermobaric effects (Holland et al. 2000, Holland et al. 2001*a*). Other subjects addressed in this thesis include the influence of inflow velocity and the effects of surface heating, coriolis forces, and bathymetry. The latter three are

tested on a shallower domain which is a nominal fit to the bathymetry of Kamloops Lake (Holland et al. 2001*b*).

1.4 Lake Baikal

Lake Baikal in Siberia is the deepest lake in the world with a maximum depth of 1636 m and has a volume of approximately $23,015 \text{ km}^3$, comprising roughly 20% of the world's fresh surface water (Shimaraev et al. 1993). It is situated between $51:29 - 55:46^\circ\text{N}$ and $103:40 - 109:55^\circ\text{E}$, 456 m above sea level in the Baikal Rift Zone which completely surrounds the lake. Figure 1.6 shows the bathymetry of Lake Baikal, which consists of three major basins divided by the Selenga Delta and Academician Ridge, which is situated near the Barguzin River inflow. The Central basin is the deepest, followed by the South and North basins (figure 1.6).

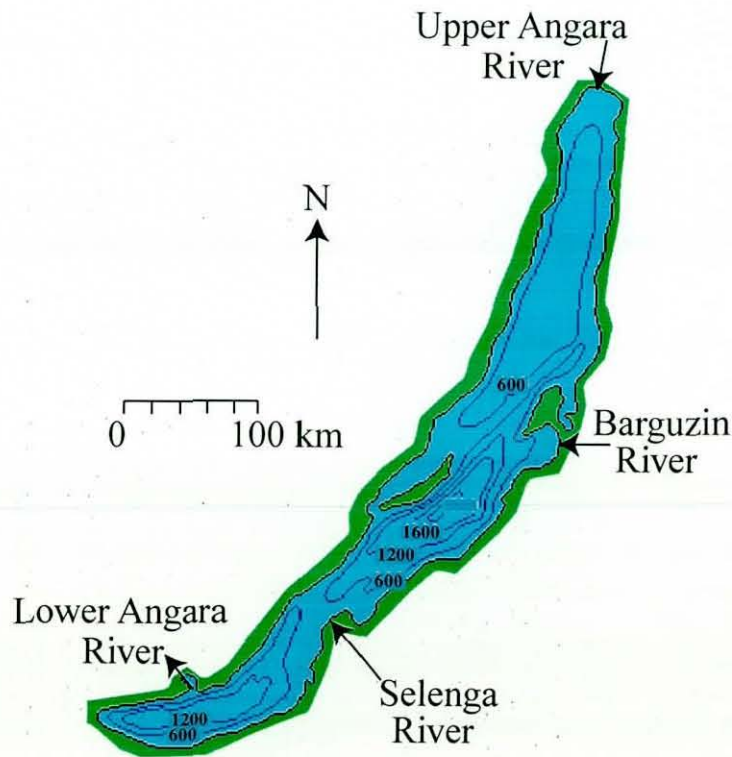


Figure 1.6: Lake Baikal bathymetry. Isobaths are given in metres.

Baikal is of scientific interest for many reasons, mainly due to its great depth and age. The lake has accumulated sediments over 30 million years (Callender & Granina

1997), which hold a unique continuous record of ancient climatic and biological conditions. Improved research on the processes governing the spatial deposition of sediments will bring a better understanding of both prehistoric climatic conditions in the area and recent changes to the Baikal ecosystem (Edlund et al. 1995, MacKay et al. 1998, Karabanov et al. 2000). Lake Baikal has many aquatic plants and animals found nowhere else in the world, comprising some 87% of the lake's species, as a result of the unusual penetration of oxygen to lacustrine depths at which pressures are extremely high and light is scarce. The relative purity of Baikal waters, which is maintained by several species of filtering copepod, make it a primary source of drinking water for the area and thus also important in the local economy.

Construction of pulp mills next to the lake and on the Selenga River has provoked strong protest from the local public and scientists, as the waste effluent discharges directly into the lake and Selenga respectively. Waste water from nearby industry also discharges into the Selenga and the total amount of industrial effluent in the area exceeds 300,000 m³ per day (ILEC n.d.). In total Votintsev (1993) calculates that over 800,000 tons of mineral salts from wastewater have been discharged into Baikal in the 15 years since the first mill opened. Although Votintsev (1993) found that the effect on the overall water quality was small, the localised effects of this pollution could be much greater near sources of pollutants to the lake. One such source is the Selenga inflow, whose delta is a major zone of heavy-metal retention (Grachev 1991). This is crucial to the ecosystem because, among many other species, the delta harbours the largest concentrations of *Acipenser baerii baicalensis*, Baikal's unique subspecies of the Siberian Sturgeon (Ruban 1997).

As shown in table 1.1, which is taken from Gronskaia & Littova (1991), the water budget of Lake Baikal is absolutely dominated by riverine throughput, with Votintsev (1993) calculating that 82.7% of the annual influx is contributed by rivers. After the construction of Irkutsk hydro-power station in 1960 the outflow of the lake came under control of the dam and the water budget changed, with Gronskaia & Littova (1991) calculating a resulting imbalance of 0.46 km³yr⁻¹.

Lake Baikal is fed by some 300 inflowing tributaries and has just one outlet, the Lower

Angara River (figure 1.6). The largest inflow is the Selenga River, which contributes approximately 49% of the total annual riverine inflow (Votintsev et al. 1965) from its 447,000 km² watershed (Shimaraev et al. 1993). The climate of the Baikal area is severely continental with long, cold and dry winters and very short cool summers. This partly explains the dominance of riverine throughput to the lake, as evaporation and precipitation totals are similar and budget contributions almost cancel each other out when averaged over the year. The dominant riverine influx shows a marked annual variability, with 70–80% of it occurring May–September due to increased precipitation and the spring thaw.

Input	km ³ yr ⁻¹
Riverine inflow	61.1
Precipitation	12.36
Total	73.46
Output	km ³ yr ⁻¹
Outflow (Irkutsk HPS)	59.16
Evaporation	13.84
Total	73.0

Table 1.1: Water budget of Lake Baikal, 1962–1988, after damming of the Lower Angara River (from Gronskaia and Littova (1991)).

Studies of various tracers in Lake Baikal have shown that it has an extremely active circulation rate for its great depth, with deep waters ranging from 8 - 16 years of age (time elapsed since last surface contact) depending upon location in the lake, and all waters exceeding 80% of relative oxygen saturation (Weiss et al. 1991, Killworth et al. 1996). A particularly fascinating observation is that bottom waters are commonly younger than mid-depth waters (Weiss et al. 1991), which has led to great scientific effort in determining the relative importance of the various large-scale convective mechanisms in the lake. Although recent studies have shown that vertical diffusion in the depths of Baikal is much larger than previously thought (Ravens et al. 2000, Kipfer et al. 2000), diffusion cannot be totally responsible for Baikal's vigorous and localised vertical transfer.

An accepted source of deep-water renewal in Baikal is riverine inflow, particularly the Selenga, as its plume can sink to the bottom of the Southern and Central basins in April or May and October (Hohmann et al. 1997). The *thermobaric instability* has also been cited as a probable cause of oxygen penetration to great depths (Weiss et al. 1991). Free convection is caused by this instability when a reversely-stratified body of water is made conditionally unstable as the interface at the base of the mixed layer is lowered to a depth where its temperature matches that of maximum density (Farmer & Carmack 1981, Carmack & Weiss 1991, Walker & Watts 1995).

This instability mechanism is particularly relevant to this study because it has been observed that the thermal bar can cause the vertical displacement of a water mass which is necessary to trigger a deep mixing event via thermobaric effects (Shimaraev et al. 1993). Also Walker & Watts (1995) found that the thermobaric instability is a lot more effective at renewing deep waters when active adjacent to a boundary (or river delta perhaps) rather than in an open lake. Work is still in progress to determine whether the thermal bar alone is capable of ventilating the lower waters with assistance from wind stress (Botte & Kay 2001), or salinity gradients (this study).

Unsurprisingly the geochemistry of Lake Baikal is dominated by riverine fluxes, mainly due to the large proportion of the total water exchange contributed by rivers. The small input into the lake from groundwater sources has not been chemically characterised, but there is no evidence to suggest it plays a major role in the chemical balance of the lake (Falkner et al. 1997). Contributions to the chemical fluxes in and out of Baikal due to evaporation and condensation have also been shown to be generally insignificant (Callender & Granina 1997). Hydrothermal vents in the north-eastern region of Baikal appear to have negligible effect on the ionic balance of the lake when compared to the 330-year time scale of riverine residence (volume/discharge).

Well-mixed conditions within the lake mean that the major ions do not generally display a large spatial variability away from the shoreline. Thus Falkner et al. (1991) have calculated a single value for weight-based salinity of $96.3 \pm 0.6 \text{ mgkg}^{-1}$, which is applicable for use in the equation of state (2.8) throughout the lake.

While riverine effects dominate the salinity of Baikal, most tributaries do not have much influence on the chemistry as they are either too small or are of a similar composition to the lake water. The Selenga River is a notable exception to this rule. Its salinity is large with respect to the lake, at 126.8 mgkg^{-1} , and its influence is accentuated by its high discharge and the large distances Selenga water travels within the lake as a distinct water mass (Votintsev 1993).

1.5 Kamloops Lake

Kamloops Lake in British Columbia, Canada, is a much smaller lake located in a relict glacial valley on the Thompson Plateau, with steep embankments on all sides. In lacustrine terms Kamloops Lake is still considered to be large, with a volume of 3.7 km^3 and maximum depth of 143 m (St. John et al. 1976). It appears to be a widening of the Thompson River, as it is very long and narrow, with a length of 25 km and an average width of just 2.1 km (figure 1.7). The lake is situated between $50:26 - 50:42^\circ\text{N}$ and $120:03 - 120:32^\circ\text{W}$, downstream of Kamloops City at 336 m above sea level.

Kamloops Lake is important as a primary rearing ground for three species of Pacific Salmon; Coho, Chinook, and Sockeye (Ward 1964). It is also en route for many adult Salmon returning to upstream breeding areas, as well as smolts heading downstream to the Pacific Ocean. The lake was included in the recent 7-year Fraser River Action Plan (FRAP) as part of the Thompson River (Gray & Tuominen 1999), which is a major tributary of the deteriorating Fraser. Serious environmental concern over the Fraser watershed prompted this wide-ranging ecosystem study which encompassed effects of pollutants on the Thompson River's wildlife.

Just upstream of the lake the Weyerhaeuser pulp mill discharges a daily average of $182,000 \text{ m}^3$ of biologically treated effluent into the South Thompson River (ILEC n.d.). In addition up to $35,000 \text{ m}^3\text{day}^{-1}$ of sewage from Kamloops City is discharged into the river during October and November each year (ILEC n.d.). Improved treatment and controlled release of these nitrogen- and phosphorous-rich effluents succeeded in reducing nutrient loadings to the Thompson River, but ever-increasing mill activity has almost outweighed this saving.

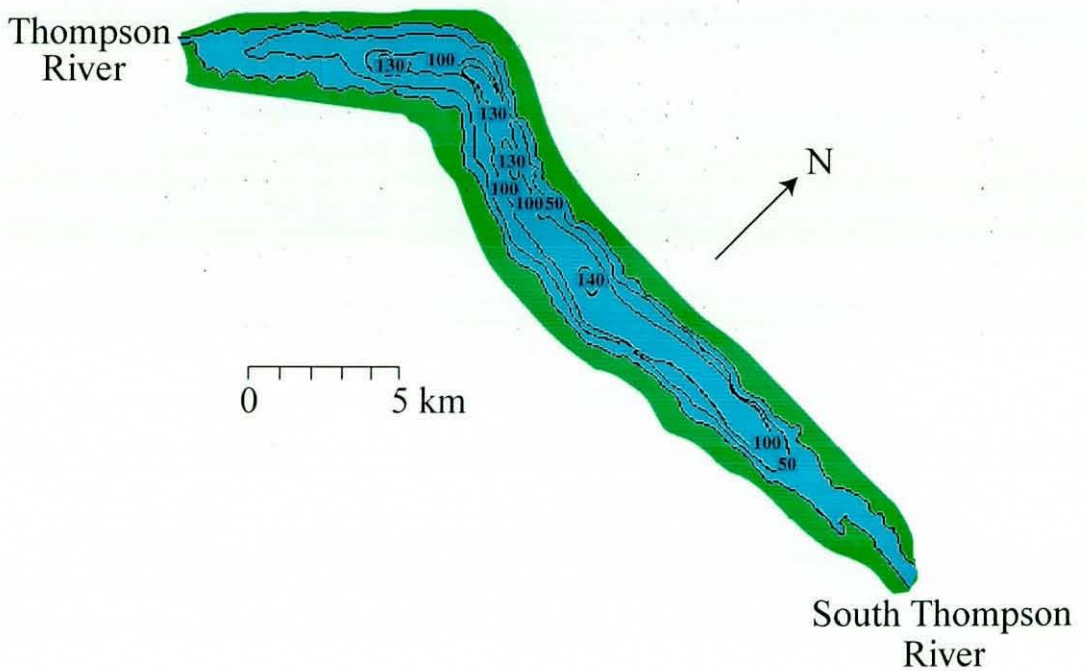


Figure 1.7: Kamloops Lake bathymetry. Isobaths are given in metres.

Surprisingly this huge nutrient loading has not resulted in eutrophication of Kamloops Lake. In many ways the circulation of the lake is responsible for this, as considerable pollution problems have been encountered downstream (Carmack et al. 1979). The high turbidity of the upper layers of the lake inhibit algal photosynthesis by blocking light, and deep mixing of the river inflow transports pollutants away from the photic zone. Also the low residence time of the lake means that any algal buildup is quickly transported downriver.

The variability of circulation patterns within Kamloops Lake (due to changes in inflow density and speed) creates more and less favourable times for the release of pollutants into the lake. The concentration of substances entering the lake can be 20 times higher in winter than in the freshet period due to these effects (Carmack et al. 1979), as explained below.

The limnology of Kamloops Lake is controlled by the Thompson River, which enters at the east end shortly after the North and South Thompson rivers converge below Kam-

loops City. Many studies have shown how the discharge and thermal characteristics of the South Thompson River govern the thermal stratification, residence time, and distribution of dissolved matter within the lake (Ward 1964, Carmack et al. 1979, Killworth & Carmack 1979). The Thompson River's discharge into the lake has a large annual fluctuation, with over 60% occurring during the freshet period in May - July. Peak discharge is in June at approximately $3,400 \text{ m}^3\text{s}^{-1}$ while flow from the Thompson is only $120 \text{ m}^3\text{s}^{-1}$ during February (St. John et al. 1976). Residence times are therefore very short in Kamloops Lake, with an average of 60 days in a range of 20 - 340 days (Carmack et al. 1979). The outflow of the lake is hydraulically controlled by the discharge cycle of the upper Thompson River, creating a significant annual variation in the lake volume. The maximum surface height variation in the year March 1972 - April 1973 was 7.67 m corresponding to an increase in lake volume of approximately 10% (St. John et al. 1976).

The annual cycle of flow patterns is well-described in Carmack et al. (1979). The spring circulation begins with the river water warming faster than the lake, so a thermal bar is created as the inflow passes through the T_{md} and propagates out into the lake as warming continues. The lake then becomes stably stratified over the summer with the lighter river water forming the initial thermocline and then flowing over the surface, providing a swift transport through the lake. As the air cools in early autumn, the summer stratification breaks down and the river cools so that it becomes denser than the lake water and sinks upon entry to the lake. The equilibrium depth of this descending flow (where its density matches that of the ambient lake water) sinks lower and lower until the river water is spreading out along the lake bed, renewing deep waters and producing the highest residence times. Another thermal bar is generated when the river temperature passes below the T_{md} in late autumn, before the whole lake cools to below the T_{md} and the colder inflow again becomes a surface overflow. As the new spring approaches, the reverse winter stratification is broken when the inflow begins to warm towards the T_{md} , sinking to the lake bed before initiating the thermal bar circulation once again.

As the outflow water from Kamloops Lake is always drawn from surface layers, the depth of inflow determines the residence time of water within the lake. The inflow in late spring has the lowest residence time of the year, flowing straight across the lake as

a surface overflow while the South Thompson attains its peak discharge. This spring runoff also has a high turbidity, which limits primary production in the lake by reducing the depth of light penetration. The maximum residence time occurs in late winter as the lowest discharge from the South Thompson combines with deep sinking of the inflow. This yearly cycle of residence times and inflow plume behaviour creates a build-up of soluble material in the lake during the winter and a flushing period in spring. This is hazardous for the Thompson downstream of Kamloops, as the lake's pollutants are flushed into it at exactly the right time for algae to thrive.

The great variability in river discharge makes the salinity of Kamloops Lake hard to characterise. St. John et al. (1976) calculated weight-based salinity from specific conductivity to be in the range of 36 - 104 mgkg⁻¹, with the lower values representing the freshet peak in late spring and the highest values in winter after the gradual buildup over the long residence time period. In summer, the South Thompson River's salinity can actually be lower than that of Kamloops Lake as a result of the high inflow discharge (St. John et al. 1976).

1.6 Thermal Bar Interaction with Plankton Ecosystems

As the thermal bar greatly affects the flow characteristics of most temperate lakes (see section 1.3), it follows that it has a considerable influence on their ecological functioning (Moll & Brahe 1986, Bolgrien et al. 1995, Bondarenko et al. 1996, Goldman et al. 1996, Budd et al. 1999). This influence is extremely important, since a proper understanding of an ecosystem's interaction with relevant fluid phenomena is required to correctly determine minimum-impact nutrient loading levels for a lake (Carmack et al. 1979, Lean et al. 1987, Ullman et al. 1998). A comprehensive view of spatial plankton behaviour could also allow the inference of useful information from sedimentation trends, especially in the ancient, 6 km-thick sediments of the Selenga delta (Kozhova & Izmet'eva 1998). A final motivation for the investigation of ecosystem effects is that the presence of biomass may inhibit light penetration, reducing the surface heat flux and potentially altering the regime of the thermal bar (Franke et al. 1999).

Many studies have emphasised the importance of stability considerations in the growth of plankton, as the restriction of vertical mixing by static stability prevents the removal of biomass from the photic zone and thus promotes continued growth (Jasper et al. 1983, Scavia & Fahnenstiel 1987, Bolgrien et al. 1995, Goldman et al. 1996, Botte & Kay 2000). The thermal structure of a lake therefore strongly influences the productivity of its ecosystem. As a boundary between warm, stable, shallow waters and cool, isothermal, deep waters, the thermal bar forms a barrier between favourable and less favourable conditions for growth. As a result, the frontal zone often marks the position of steep gradients in plankton biomass and available nutrients in addition to temperature. The passage of the thermal bar therefore heralds the spring phytoplankton growth which accompanies the beginning of summer stratification and the autumn ecosystem slowdown which follows the end of it (Moll et al. 1993, Avinsky et al. 1999).

The thermal bar's influence on plankton population distribution is often not as a simple boundary between regions of high and low biomass. Due to the horizontal flows converging at the surface T_{md} signature, the thermal bar may accumulate plankton, other organisms and debris at the surface, forming a local population maximum (Mortimer 1974, Likhoshway et al. 1996, Avinsky et al. 1999, Parfenova et al. 2000). This localised bloom depends upon the incoming flows of the thermal bar circulation to supply nutrients and avoid feeding limitation, so it follows the progression of the T_{md} into deeper waters as the surface heat flux continues.

Vertical motions associated with the thermal bar may also be particularly important to lacustrine plankton populations. Certain types of plankton (particularly diatoms) have significant sinking rates and therefore require upwelling motions to keep them in the photic zone (Reynolds 1994, Kelley 1997), while the downwards transport of organic matter leads to increased microbial activity at depth (Parfenova et al. 2000). Also the upwelling of deep nutrient supplies may be crucial to the maintenance of surface productivity (Lean et al. 1987).

BK are currently the only authors to model the effects of the thermal bar on a plankton ecosystem, as many numerical plankton models still ignore spatial phenomena such as currents, turbulence, sinking, and light penetration in favour of simple

one-dimensional or box models (Truscott & Brindley 1994). Using a basic Nutrient-Phytoplankton-Zooplankton (*N-P-Z*) model which is conditioned for nitrogen-limited plankton in the oceans, BK produced a good fit to observations of a phytoplankton bloom following the spring thermal bar in Lake Baikal (Likhoshway et al. 1996).

Due to the effects of dissolved and suspended matter, the influence of the riverine thermal bar on ecosystem function is even more important than that of the classical case (Jasper et al. 1983, Avinsky et al. 1999). The differing properties of river and lake water mean that the spring riverine thermal bar operates as a barrier between nutrient-rich, turbid, warm and stable waters inshore of the T_{md} and relatively nutrient-poor clear, cool and isothermal conditions offshore (Ullman et al. 1998, Budd et al. 1999). Depending upon the exact balance of the river in question, this extra turbidity and nutrient influx could either increase or decrease the favoured plankton growth inshore of and at the thermal front.

Lacustrine plankton will also be affected by new populations which are carried by an inflowing river. For example, these populations could seed a new plankton bloom (Moll et al. 1993, Likhoshway et al. 1996) or increase predation (Avinsky et al. 1999), depending upon the particular species and conditions in question. However, plankton concentrations in rivers are generally lower than those in lakes, despite the difference in temperature, because rivers have higher turbidities and are mixed more thoroughly and flushed more rapidly (Soballe & Kimmel 1987, Reynolds 1994, Akopian et al. 1999, Welker & Welz 1999). This means that, although conditions inshore of the T_{md} are favourable for plankton growth, there is generally a significant influx of plankton-free water which may dilute or displace the in-situ growth (Soballe & Kimmel 1987, Avinsky et al. 1999, Welker & Welz 1999).

Our lack of understanding of the riverine thermal bar becomes critical when considering the ecology of a river-dominated temperate lake, such as Kamloops. Although there are no specific observations of plankton population distributions in the presence of a riverine thermal bar, the general discussion of St. John et al. (1976) on the spring growth in Kamloops Lake can be used in conjunction with the physical limnology study of Carmack (1979) (which was undertaken at the same time) to form the basis of a nu-

merical study of the ecology of a riverine thermal bar. To this end, this thesis presents the results of a study which couples the *N-P-Z* plankton model of Franks et al. (1986) (as used by BK) to the Kamloops Lake dynamical simulation introduced in section 1.3. This work extending the simple results of BK to the riverine case is then scrutinised further by adoption of the more sophisticated Nutrients-Phytoplankton-Zooplankton-Detritus (*N-P-Z-D*) model of Parker (1991).

1.7 Overview and Objectives

Throughout this introduction, several deficiencies in our understanding of the thermal bar have been identified, particularly in the riverine case. Employing the same numerical modelling techniques throughout, this thesis addresses three distinct questions:

1. Is it possible for the riverine thermal bar to ventilate the deep waters of Lake Baikal under the influence of salinity?
2. Is it possible to reproduce and test the flow field responsible for the riverine thermal bar observations of Carmack et al. (1979)?
3. How does this riverine thermal bar affect plankton populations, in comparison to the classical case?

The riverine thermal bar in Lake Baikal is modelled in an abstracted rectangular deep domain which is nominally representative of the Selenga delta. A series of thermal and haline scenarios are studied, elucidating the range of possible dynamics available to the riverine thermal bar in a deep lake. Particular attention is paid to the influence of thermobaricity and salinity on the vertical motions.

Computational requirements are then reduced by considering the much smaller domain which represents Kamloops Lake. This model is more realistic than the deep-lake study, and is run for a longer timespan in order to include coriolis effects and qualitatively reproduce the results of Carmack et al. (1979). A sensitivity study is then performed on the riverine thermal bar dynamics with respect to the various forcings and subtleties of this improved model.

The same physical model is then used in conjunction with various ecosystem models to test the response of plankton populations to the riverine thermal bar. Particularly riverine phenomena are identified by comparison of the *N-P-Z* model results with BK, before the two models chosen for this thesis are compared to assess the value and applicability of greater model sophistication.

The study begins with a discussion of the model formulation and numerical solution in chapters 2 and 3, before a full discussion of the chosen turbulence parameterisation is presented in chapter 4. Chapter 5 details the results of some preliminary simulations in the deep lake section and full results of the deep-lake riverine thermal bar are then presented in chapters 6 (non-saline) and 7 (saline). Attention then turns to the smaller Kamloops Lake section, with all dynamical results contained in chapter 8 and results of the two plankton models in chapters 9 (*N-P-Z*) and 10 (*N-P-Z-D*).

Chapter 2

Model Formulation

In this chapter the characteristics of the mathematical model which is used to study the riverine thermal bar are summarised. The underlying assumptions and governing equations are outlined here, while a brief discussion of the Navier-Stokes equations is given in chapter 4 as part of the explanation of the eddy-viscosity parameterisation. The choices of lake bathymetry and boundary conditions are described separately for the Lake Baikal and Kamloops Lake cases, and then the ecosystem models used for the plankton population studies are explained.

2.1 Governing Equations

While the thermal bar is clearly a phenomenon which generates significant flows in three dimensions, it is simply impossible to run a complete three-dimensional model with the limited computational resources available to this study. Following the approach of many previous authors, a two-dimensional section is adopted on the basis that gradients normal to the shore are much larger than those parallel to it, which are neglected accordingly (Huang 1969, Malm 1995, Tsvetova 1999).

The model is based on a quasi-incompressible form of the Reynolds-averaged Navier-Stokes equations which are derived in chapter 4. The x -coordinate is taken to be perpendicular to the shoreline and the z -coordinate represents depth, taken as positive upward from the model bottom (see figures 2.4 and 2.8). For the purpose of calculating coriolis forces, the y -coordinate is defined in the Kamloops Lake model in the alongshore direction (figure 2.2), or ‘into the page’ in figure 2.8.

As mentioned above, variations in the alongshore direction are taken to be zero (i.e. $\frac{\partial}{\partial y} = 0$) such that all dynamics are driven by the cross-frontal gradients. However, the momentum equation of v , the flow component in the y direction, is included in the model so that coriolis forces may be calculated in the other momentum equations when necessary in the Kamloops Lake study.

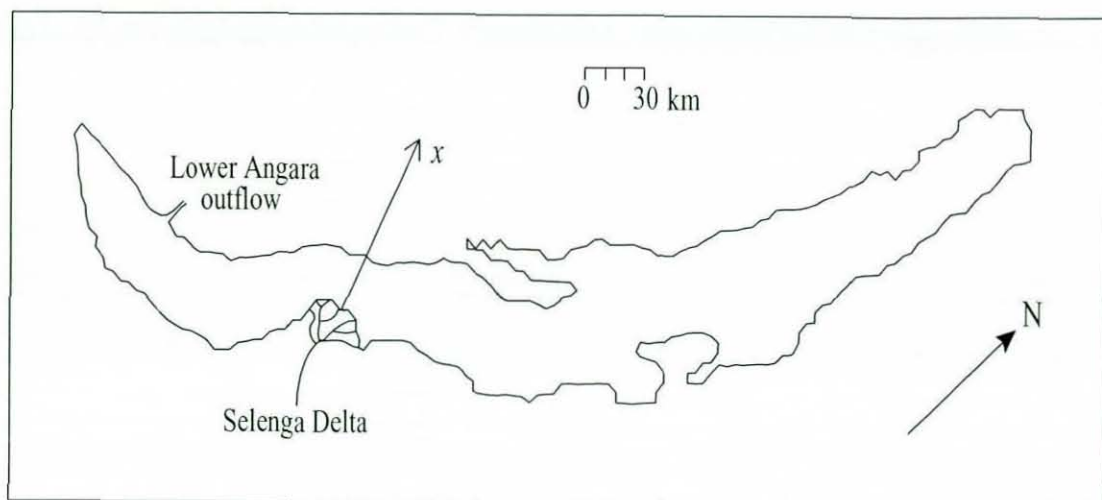


Figure 2.1: Approximate position of Baikal section and orientation of axes.

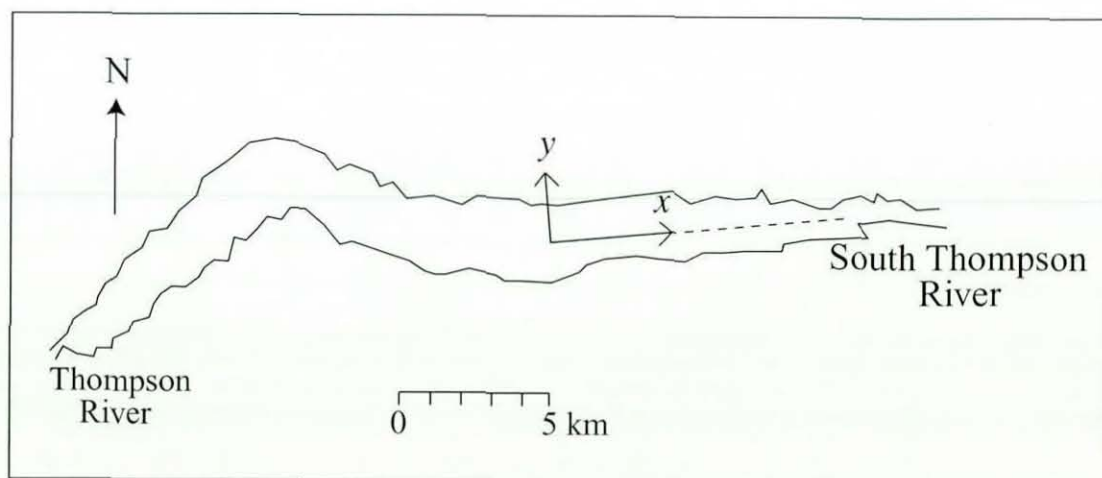


Figure 2.2: Approximate position of Kamloops section and orientation of axes.

Under these assumptions the continuity equation is written as:

$$\frac{\partial u}{\partial x} + \frac{\partial w}{\partial z} = 0 \quad (2.1)$$

where u and w are the velocity components in the x and z directions respectively.

In the quasi-incompressible momentum formulation applied here the Boussinesq approximation is adopted, whereby the density is supposed constant, $\rho = \rho_c$, everywhere except in the buoyancy term of the equation for w , the vertical velocity component (Boussinesq 1903). ρ_c is taken to be the maximum density of water at surface pressure and zero salinity, assumed to be $\rho_c = 999.975 \text{ kgm}^{-3}$ when $p = S = 0$ and $T = T_{md}$. As described in chapter 4, the Boussinesq (1877) eddy-viscosity concept is adopted whereby the Reynolds stress terms are incorporated in the momentum equations via eddy-viscosity coefficients, which are assumed to be different in the vertical and horizontal directions.

Adopting these hypotheses the three components of the momentum equation can be explicitly written as:

$$\frac{\partial u}{\partial t} + u \frac{\partial u}{\partial x} + w \frac{\partial u}{\partial z} = \frac{\partial}{\partial x} \left(A_h \frac{\partial u}{\partial x} \right) + \frac{\partial}{\partial z} \left(A_v \frac{\partial u}{\partial z} \right) - \frac{1}{\rho_c} \frac{\partial p}{\partial x} + 2\Omega_z v - 2\Omega_y w \quad (2.2)$$

$$\frac{\partial v}{\partial t} + u \frac{\partial v}{\partial x} + w \frac{\partial v}{\partial z} = \frac{\partial}{\partial x} \left(A_h \frac{\partial v}{\partial x} \right) + \frac{\partial}{\partial z} \left(A_v \frac{\partial v}{\partial z} \right) + 2\Omega_x w - 2\Omega_z u \quad (2.3)$$

$$\frac{\partial w}{\partial t} + u \frac{\partial w}{\partial x} + w \frac{\partial w}{\partial z} = \frac{\partial}{\partial x} \left(A_h \frac{\partial w}{\partial x} \right) + \frac{\partial}{\partial z} \left(A_v \frac{\partial w}{\partial z} \right) - \frac{1}{\rho_c} \frac{\partial p}{\partial z} - \frac{\rho}{\rho_c} g + 2\Omega_y u - 2\Omega_x v \quad (2.4)$$

where A_h and A_v are eddy-viscosity coefficients in the horizontal and vertical directions respectively, Ω_x , Ω_y , and Ω_z are the components of the Earth's angular velocity vector, Ω , and g is the acceleration due to gravity. It is emphasised here that equation (2.3) and the coriolis forcing terms of equations (2.2) and (2.4) are not used in the deep domain model of Lake Baikal.

The vector Ω has magnitude:

$$|\Omega| = \frac{2\pi}{86,400} \text{ s}^{-1} \quad (2.5)$$

and in cartesian coordinates its components are:

$$\begin{aligned}\Omega_x &= |\Omega| \cos \phi \sin \delta \\ \Omega_y &= |\Omega| \cos \phi \cos \delta \\ \Omega_z &= |\Omega| \sin \phi\end{aligned}\tag{2.6}$$

where ϕ is the latitude of the section and δ represents the orientation of the section relative to north. When coriolis is included in the model, a Kamloops latitude of $\phi = 52^\circ$ is adopted, along with a nominal section angle of $\delta = 85^\circ$ which is chosen to represent the centreline of Kamloops Lake near the South Thompson inflow.

Examination of the momentum equation for the transverse velocity (2.3) gives rise to the concern that coriolis forces may produce spurious inertial oscillations as a result of the neglect of the pressure terms, which would otherwise balance these accelerations. However, closer examination of the terms in this equation shows that the coriolis forcings are generally significantly smaller than the transport terms (at $O(10^{-7}) \text{ ms}^{-2}$ to $O(10^{-4}) \text{ ms}^{-2}$ respectively), and the transverse velocity is therefore controlled by forcings within the two-dimensional section. This analysis is consistent with the observation that inertial oscillations are absent from all of the results.

The transport of the scalar quantities of temperature, T , and salinity, S , which create the density variations of interest, is represented here by a simple advection-diffusion balance. The components of each plankton model are also governed by this equation and, since density dependance on both temperature and salinity is included in the equation of state (2.8), a scalar ‘tracer’, φ , is introduced which effectively tracks the river inflow to the lake for unbiased visualisation purposes. This tracer can be used to follow substances carried by the fluid which do not affect the flow, such as neutrally-buoyant pollutants, and is used here to assess the general characteristics of transport by each thermal bar. The transport equation for a general scalar quantity, Φ , is written as:

$$\frac{\partial \Phi}{\partial t} + u \frac{\partial \Phi}{\partial x} + w \frac{\partial \Phi}{\partial z} = \frac{\partial}{\partial x} \left(K_h \frac{\partial \Phi}{\partial x} \right) + \frac{\partial}{\partial z} \left(K_v \frac{\partial \Phi}{\partial z} \right)\tag{2.7}$$

where $\Phi = T, S, \varphi$, and plankton components as discussed later. In these equations K_h and K_v are eddy diffusion coefficients for scalar properties, which are assumed to be

equal to A_h and A_v for all Φ as they primarily quantify transport of information due to convective motions on a subgrid scale rather than any particular rate of molecular diffusion.

The density calculations employ the equation of state given by Chen & Millero (1986), who claim an accuracy exceeding $2 \times 10^{-6} \text{ gcm}^{-3}$ over the range of $0 - 600 \text{ mgkg}^{-1}$ salinity, $0^\circ - 30^\circ\text{C}$, and $0 - 180 \text{ bar}$. These values are more than sufficient for the ranges encountered in Lakes Baikal and Kamloops, so the following formulation is adopted:

$$\rho(p, S, T) = \rho_0 \left(1 - \frac{p}{H(p, S, T)} \right)^{-1} \quad (2.8)$$

where

$$\begin{aligned} \rho_0 = & 0.9998395 + 6.7914 \times 10^{-5}T - 9.0894 \times 10^{-6}T^2 + 1.0171 \times 10^{-7}T^3 \\ & - 1.2846 \times 10^{-9}T^4 + 1.1592 \times 10^{-11}T^5 - 5.0125 \times 10^{-14}T^6 \\ & + (8.181 \times 10^{-4} - 3.85 \times 10^{-6}T + 4.96 \times 10^{-8}T^2)S \end{aligned}$$

and

$$\begin{aligned} H(p, S, T) = & 19,652.17 + 148.113T - 2.293T^2 + 1.256 \times 10^{-2}T^3 - 4.18 \times 10^{-5}T^4 \\ & + (3.2726 - 2.147 \times 10^{-4}T + 1.128 \times 10^{-4}T^2)p \\ & + (53.238 - 0.313T + 5.728 \times 10^{-3}p)S. \end{aligned}$$

Here ρ and ρ_0 are in kgm^{-3} , T is in $^\circ\text{C}$, S is in gkg^{-1} , and p and H are in bars. Note that the entire formulation of (2.8) must be used as pressures ranging up to $\approx 140 \text{ bar}$ may be reached in a lake of Baikal's great depth.

2.2 Boundary Conditions

The chosen models of the riverine thermal bar include a mass flux from the inflowing river into the domain. In order to preserve continuity there must be an accompanying outflow, so boundary conditions must be set on a 2-dimensional lake cavity with a free surface and inflow and outflow regions in the side boundaries. Diagrams of each model domain are given in figures 2.4 and 2.8.

The rigid lid approximation is used in this model, whereby all vertical displacements of the free surface ($z = F$) are neglected, which is reasonable given the vertical resolution of each grid. Apart from the surface heat flux applied to Kamloops Lake (described in section 2.4.2), all mechanical forcings and scalar fluxes at the surface are ignored so that the fundamental dynamics are buoyancy-driven by riverine sources. This gives the conditions on the free surface as:

$$\left. \frac{\partial u}{\partial z} \right|_F = \left. \frac{\partial v}{\partial z} \right|_F = \left. \frac{\partial \Phi}{\partial z} \right|_F = w \Big|_F = 0 \quad (2.9)$$

where $\Phi = T, S, \varphi$ and all plankton model components.

On all solid boundaries the velocity components and fluxes of scalar quantities across the boundary are set to zero. Thus the conditions on a solid boundary B are:

$$\left. \frac{\partial \Phi}{\partial n_o} \right|_B = u \Big|_B = v \Big|_B = w \Big|_B = 0 \quad (2.10)$$

where n_o is the co-ordinate direction normal to the boundary.

The influx of a scalar variable Φ is modelled by assuming the value of Φ_R to act on the cells in the first column of the domain which are adjacent to the open boundary representing the river mouth. Thus on the open inflow boundary, B_{oI} , the scalar conditions are:

$$\Phi \Big|_{B_{oI}} = \Phi_R. \quad (2.11)$$

Neumann boundary conditions are set for the scalar quantities over the outflow boundary, B_{oO} , so that

$$\left. \frac{\partial \Phi}{\partial x} \right|_{B_{oO}} = 0. \quad (2.12)$$

In every simulation the scalar tracer is initially assigned values of $\varphi_R = 1$ in the inflow and $\varphi_L = 0$ in the domain such that the concentration of river water everywhere in the lake can be viewed as a mixing ratio on a scale of 0 (pure lake water) to 1 (pure river water). Explicit values of the initial and inflow values of salinity and temperature are given for each case in sections 2.3.2 and 2.4.2.

Similar conditions are set for velocity at the open parts of the side boundaries, B_o , representing the river inflow and outflow. The horizontal velocity in the plane of the section, u , is fixed to the rate of river flow on both sides, while perpendicular and vertical velocities v and w are not constrained by shear effects, giving:

$$u \Big|_{B_o} = u_R \quad (2.13)$$

and

$$\frac{\partial w}{\partial x} \Big|_{B_o} = \frac{\partial v}{\partial x} \Big|_{B_o} = 0. \quad (2.14)$$

An horizontal riverine velocity is ascribed to the inflow because it seems more physically reasonable to have a mass flux into the domain than a purely diffusive river flow. All simulations start from a flow-field consisting of u_R attributed to the top rows of cells in the domain which are between the inflow and outflow and zero velocity everywhere else (e.g. figure 2.3). This initial velocity distribution represents an idealised situation in which a river of equal density to the lake passes directly across the surface due to a lack of any buoyancy forcing.

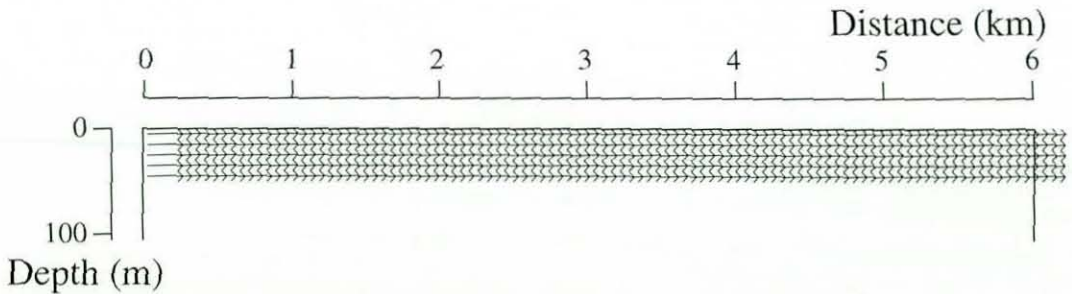


Figure 2.3: Initial velocity field for all Lake Baikal simulations shown at half of the actual grid resolution

Under the conditions of these initial velocity fields (particularly $w = 0$ everywhere), and zero coriolis force, the vertical momentum equation (2.4) yields the hydrostatic equation:

$$\frac{\partial p}{\partial z} = -\rho g. \quad (2.15)$$

Under the condition of $p|_F = 0$, this is used to iteratively calculate the initial fields of pressure and density from thermal and haline information, a procedure which is required due to the explicit dependance of density on pressure which is an important feature of this work.

Examination of results from thermal bar simulations show that the approach of simply fixing velocities on the open boundaries causes inaccuracies in the predicted flows once the thermal bar has traversed the lake and approaches the arbitrary outflow condition. In reality, neither the far boundary (opposite the inflow) nor the fixed velocity on the open outflow region exist. Therefore, in order to preserve the applicability of model findings, the results are disregarded as soon as the influence of the arbitrarily-fixed outflow rate on the far boundary becomes apparent in the predicted dynamics. The stage at which this happens is decided by running test simulations on a wider domain and determining the point at which the two sets of results disagree significantly, as described in sections 2.3.4 and 2.4.3.

The obvious solution to these problems seems to be a change in outflow velocity conditions. Unfortunately, in order to simulate a mass flux through the domain there are only two possible choices of condition on the horizontal velocity component at this surface outflow, a fixed-velocity Dirichlet condition as chosen here, or a Neumann condition:

$$\frac{\partial u}{\partial x} \Big|_{B_{oO}} = 0, \quad (2.16)$$

such that for each row of cells the horizontal velocity over the outflow region is simply assumed identical to the horizontal velocity at the adjacent column of cells in the interior of the lake. Unfortunately, however, the rigid-lid condition at the surface implies that a Neumann condition, via the assumption of incompressibility, will forbid any vertical flow at all in the outflow cells of the column immediately adjacent to the right-hand boundary.

This consideration has a severely detrimental effect on the flow-field after relatively short periods of time, so there is no choice but to proceed with the fixed value of outflow velocity u_R . Since this condition has little effect on the flow-field until the thermal bar is relatively close to the outflow (as shown below), results are considered to be valid before

this point and disregarded afterwards. Lessening the effects of the outflow by dividing u_R over the entire far boundary is not considered to be a solution to these problems because this method may draw inflowing waters downwards and thus ruin the delicate quantification of vertical transport which a primary achievement of this study.

As this study focuses on density effects, u_R should be kept low so that the river enters the lake as a buoyancy-dominated plume rather than a jet. However, a purely diffusive inflow (i.e. with $u_R = 0$) seems somewhat unrealistic in rivers with spring discharge values of the magnitude of the Selenga and South Thompson. Also the case of zero inflow velocity is a rather similar scenario to the ‘classical’ thermal bar generated by warming of shallow regions from a surface heat flux, which has been studied in detail by many authors (as summarised in chapter 1). In each simulation a reasonable value of u_R is chosen so that the horizontal momentum flux has an effect but does not dominate the propagation of the riverine thermal bar.

2.3 Lake Baikal Dynamical Model

2.3.1 Domain and General Remarks

To enable a fundamental study of the processes governing the riverine thermal bar in a deep temperate lake, the domain onto which these equations are applied is chosen to be a simple rectangular box of depth $F = 1$ km and width $L = 6$ km, as shown in figure 2.4. To properly resolve the subtle gradients responsible for the thermal bar and thermobaric effects, a grid cell in the deep-lake study has the dimensions of $h_x = 20$ m \times $h_z = 5$ m, producing a system of 60,000 grid nodes. Since the timestep is limited to a maximum of $\Delta t = 30$ s to ensure convergence of the numerical procedure (and less in some of the higher-salinity simulations), the system cannot be solved over long periods of model time with the computational resources available to this study.

Coriolis forces are neglected in this deep-lake study due to the brevity of each simulation. Numerical testing has shown that during the first few days of simulation the coriolis forces engage in a period of ‘spin-up’ whereby they act in the opposite direction to their long-term influence in an effort to initiate the v -velocity (see section 8.2.2). In the Baikal simulations, this means that the coriolis force would have a misleading

influence throughout the whole period of thermal bar development. In any case, it is a worthwhile study to elucidate the buoyancy forcings governing the riverine thermal bar in a deep lake in the absence of rotation, which can then be included in future work.

Boundary conditions (2.11) - (2.14) are fixed on open inflow and outflow regions which are taken to be 50 m deep in this case. A discussion of the initial and boundary conditions for temperature and salinity is given in sections 2.3.2 and 2.3.3, while the rest of this section is concerned with presenting a reasoned basis for the domain choices outlined above.

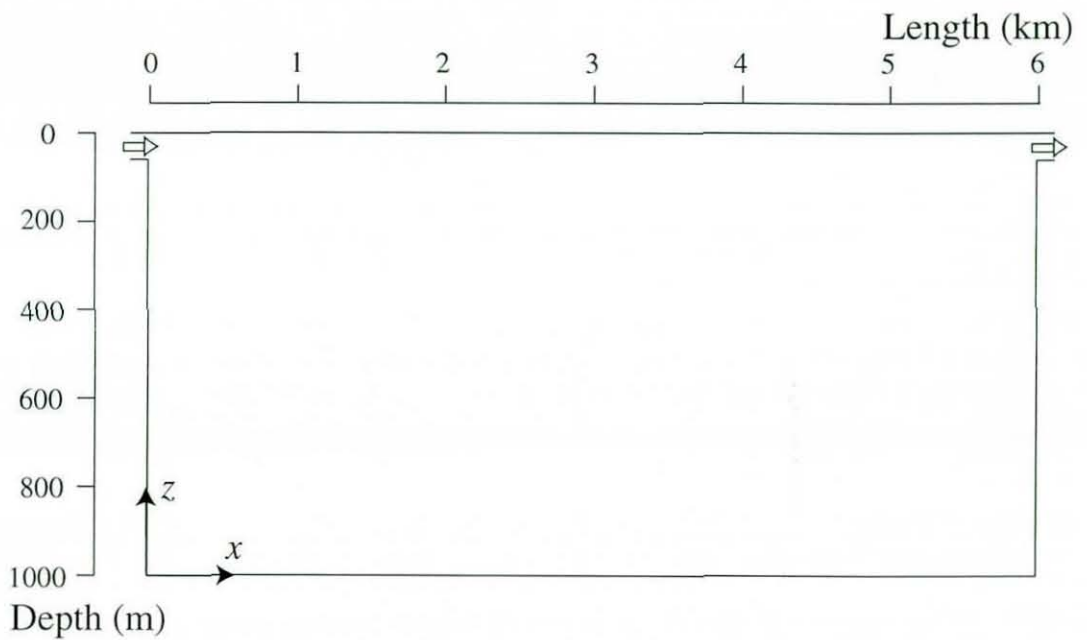


Figure 2.4: Chosen Baikal section with positioning of axes and river sources.

Initially the shape of this domain may seem to be an oversimplification of the problem but this choice ensures that the underlying buoyancy-driven dynamics, which are the object of this study, are not obscured by effects relating to the topography of any particular Baikal section. Most importantly, this choice of domain ensures that the results presented in this work could be regarded as generally applicable to any deep temperate lake with a riverine forcing.

A triangular river-delta section in the style of Malm (1995), or exact Selenga Delta bathymetry, seem to be better choices in that they are more realistic than a rectangular

box and yet are still fairly generalised sections. In a domain of this type, however, it is extremely difficult to assign reasonable boundary conditions on the open-lake boundary opposite the shallow near-shore region. This is solely due to the river inflow, since a symmetry condition similar to that of Malm (1995) implies a lake with an inflow at both sides whenever salinity is introduced. Alternatively, a shallow near-surface outflow condition similar to that of the chosen section would give an unrealistic 'wedge' geometry, while a completely open bound is not desirable as the necessity of setting a nominal velocity condition on the bound would adversely affect the predictions of vertical convection, potentially causing water to sink due to mechanical rather than buoyancy forcings.

2.3.2 Boundary and Initial Conditions

Setting riverine boundary conditions for the deep-lake study is particularly troublesome due to a lack of detailed temperature and flow rate data from either the Selenga River or any other river flowing into Baikal. Thermal data are virtually nonexistent in the literature, and personal enquiries at the Limnological Institute in Irkutsk revealed only monthly data from the 1970s, which were taken at a station in the shallow Selenga River upstream of the river delta. In these data the Selenga River switches from $T_R \approx 3^\circ\text{C}$ in early May to $T_R \approx 19^\circ\text{C}$ in late June with no intermediate readings (R. Gnatovskii, personal communication).

While the ideal model of the riverine thermal bar would involve a coupled river and lake which are initially cooler than the T_{md} and then subjected to a surface heat flux, the data and long runs required by this approach makes it unfeasible for the purposes of the deep-lake study. Warming of the river and lake is therefore simulated by two separate one-dimensional 'preconditioning' models under a surface heat flux, as described in section 2.3.3 below. The results of these models are then used after various simulation times to provide boundary and initial conditions for the main two-dimensional mixing studies. By altering the river salinity in certain scenarios it is then possible to complete a dynamical study of a range of conditions present during the generation of a riverine thermal bar in a deep lake.

Salinity is initially assumed to have a homogeneous distribution in the river and lake,

at the average Baikal value of $S_L = 96.3 \text{ mgkg}^{-1}$ (Falkner et al. 1991). The salinity of the Selenga River is given at 126.8 mgkg^{-1} by Votintsev (1993) but unfortunately this accurate value is again inappropriate for this study because considerable dilution must take place in the shallow delta region between the river mouth (where the reading was taken) and the 50 m-deep inflow of our model. Salinity increases of just 1, 2, 5, and 10 mgkg^{-1} are therefore applied to the river (in each thermal case) while S_L is kept constant.

A nominal river velocity of $u_R = 0.005 \text{ ms}^{-1}$ is adopted throughout the deep-lake work, a value which is quite difficult to justify in this somewhat idealised model. Monthly discharge rates seem to be the only flow data available for the Selenga river (Shimaraev et al. 1994), and without any information of the shape or depth of the river delta this is of little use when considering a 50 m deep inflow to a two dimensional section. However, these data do show that there is a significant annual variability in Selenga discharge into Baikal, and an increase from $7.9 \text{ m}^3\text{s}^{-1}$ to $166.9 \text{ m}^3\text{s}^{-1}$ occurs over the warming period of March to July (calculated from Shimaraev et al. (1994)), which allows some freedom in our choice of an exact value.

To examine the effect of u_R , results are presented in section 6.3 from a comparison of predicted velocity vectors from three *T9* simulations, with $u_R = 0, 0.005$, and 0.01 ms^{-1} . The thermal characteristics of the basic *T9* simulation and an explanation of the simulation-naming convention are described in the next section and appendix A.

2.3.3 One-dimensional Models and Thermal Scenarios

These studies of cabbelling in a deep lake are intended to reveal the particular forcing mechanisms behind the dynamics of the riverine thermal bar at several stages of the spring warming process. For this reason the initial conditions for the lake and the boundary conditions for the river need to be as realistic as possible given the spring warming regime in and around Baikal, and one-dimensional preconditioning models are adopted. This is the most realistic alternative to employing simulations in which the river and lake gradually warm through the T_{md} , which is not possible with the computational resources available to this study.

The preconditioning models are based on the unsteady diffusion equation

$$\frac{\partial T}{\partial t} = \frac{\partial}{\partial z} \left(K_v \frac{\partial T}{\partial z} \right) \quad (2.17)$$

where formulation (4.15) is adopted for K_v . Radiative heating is simulated through a thermal boundary condition at the surface, which is written in terms of the surface heat flux Q_s as

$$\rho_c c_p K_v \frac{\partial T}{\partial z} = Q_s \quad (2.18)$$

where c_p is the specific heat at constant pressure and Q_s is measured in Wm^{-2} and is considered positive when entering the domain, i.e. directed towards negative z . A value of $Q_s = 250 \text{ Wm}^{-2}$ is used throughout the model, which corresponds to the June value given by Shimaraev et al. (1994). A percentage of the solar radiation is supposed to pass through the surface to deeper regions of the lake, and the resulting heat source is assumed to have an exponential decay in intensity with depth. The vertical attenuation coefficient of this decay is taken to be 0.3 m^{-1} , the value used by BK.

The river and lake are both assumed to have an initial temperature of 3.4°C , which is a realistic value for the given regions of Lake Baikal immediately prior to the onset of cabbeling, as shown in figure 2.5. The riverine thermal bar is then studied in three different forms by utilising results of the one-dimensional models after 7, 9, and 11 days of simulation, when the river is warmer than the T_{md} but the lake is still cooler (see figure 2.6). This gives an insight into the range of thermal bar circulations which may be achieved with different riverine forcings, and the metamorphosis of the riverine thermal bar during the spring warming.

In reality it is impossible to tell whether the one-dimensional river model gives a reasonable representation of the river warming in spring. These preconditioning models are used primarily to give a qualitative indication of the river and lake temperatures relative to the T_{md} at various stages of the spring warming, and are thought to be slightly more reasonable than simply guessing temperatures for the river and lake. Due to the lack of data the river temperature is fixed during the actual mixing studies, which is the most sensible choice since any warming rate cannot be physically justified.

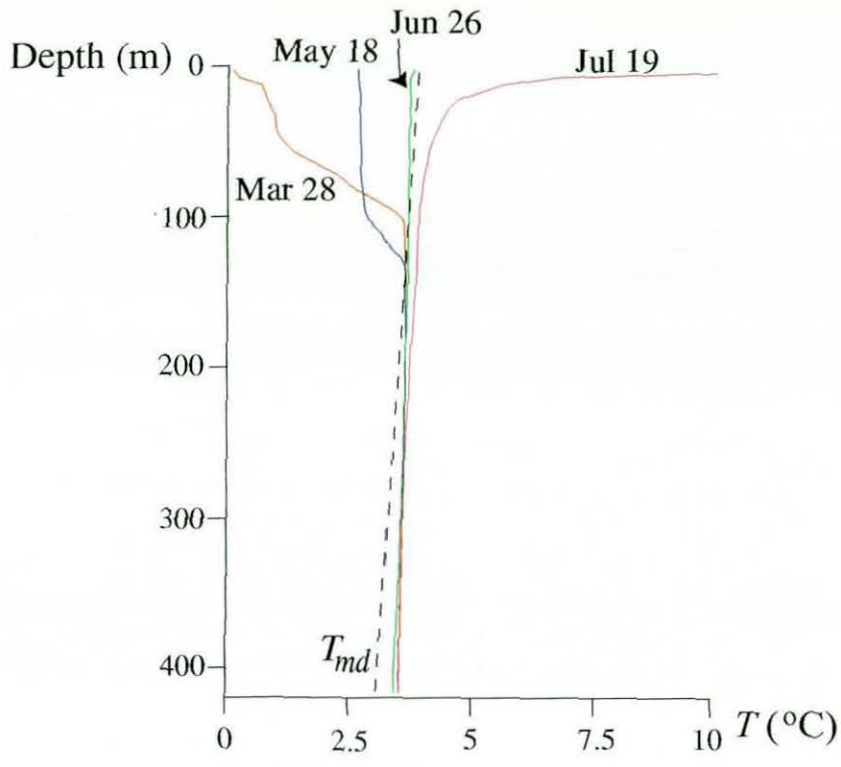


Figure 2.5: Vertical temperature profiles measured in 1996 at the centre of the South Basin.

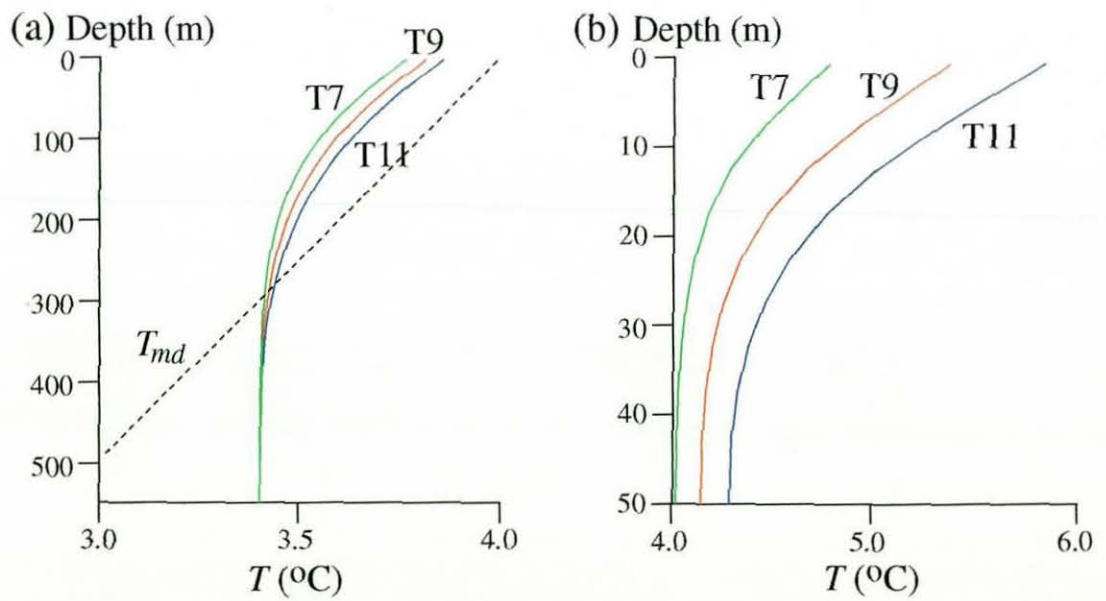


Figure 2.6: Results of the one-dimensional preconditioning models: (a) initial lake temperatures, (b) river temperatures throughout the simulation.

In order to simplify the discussion, the following nomenclature is adopted to identify each of the 12 different thermal bar simulations in this deep-lake study. A simulation is referred to as $T\tau S\sigma$, where τ is the number of days of simulation of the one-dimensional river and lake models before mixing and σ is the amount of salinity added to the river in mgkg^{-1} . For example, $T9S2$ is the case mixed after 9 days with a salinity increase of 2 mgkg^{-1} , producing an absolute riverine salinity of 98.3 mgkg^{-1} .

2.3.4 Validity Timespan of results

The timespan over which the Lake Baikal simulations are considered reasonable is limited by many factors, most of which are the assumptions which are necessary to cover a lack of data or computational resources. For example, the effects of the Earth's rotation are neglected on the basis that a short simulation is in a state of spin-up throughout, and *in-situ* surface heating of the lake and variation of the river temperature can be neglected because on short timescales these thermal changes are negligible in comparison with the underlying temperature difference between the river and lake. Also river inflow velocity is held to be constant despite the increasing Selenga discharge noted during spring by Shimaraev et al. (1994).

Due to the lack of available data on the variation of these factors, it is impossible to comment upon their effects on the rate of degradation of the solution validity. However, one validity-limiting factor which becomes important rather quickly is the presence of a solid boundary (with a fixed-velocity river outflow) only 6 km from the source of the riverine thermal bar. The effects of this false boundary are examined with a test simulation, $T9D$, which is identical to simulation $T9$ but has a domain width of 10 km.

Figure 2.7 shows a comparison of vertical velocities with 6 and 10 km domain widths after 4 and 8 days of simulation. Figure 2.7(a) reveals that the arbitrary outflow does not affect the thermal bar after 4 days but clearly after 8 days the horizontal propagation of the thermal bar is quickened by the presence of the fixed-velocity outflow in its path (figure 2.7(b)).

While this finding discredits the applicability to Lake Baikal of results from around the 8-day period and later, flow patterns from day 8 can still be used in section 6.1.1

to illustrate the importance of the thermobaric suppression of vertical flows and to draw comparisons with the laboratory findings of Marmoush et al. (1984). Also, results after long periods of simulation are successfully employed in section 4.5 to justify the chosen parameterisations of the vertical eddy-viscosity, as it is the long-term behaviour of buoyancy forces which is of interest in that procedure rather than the accuracy of predicted flows.

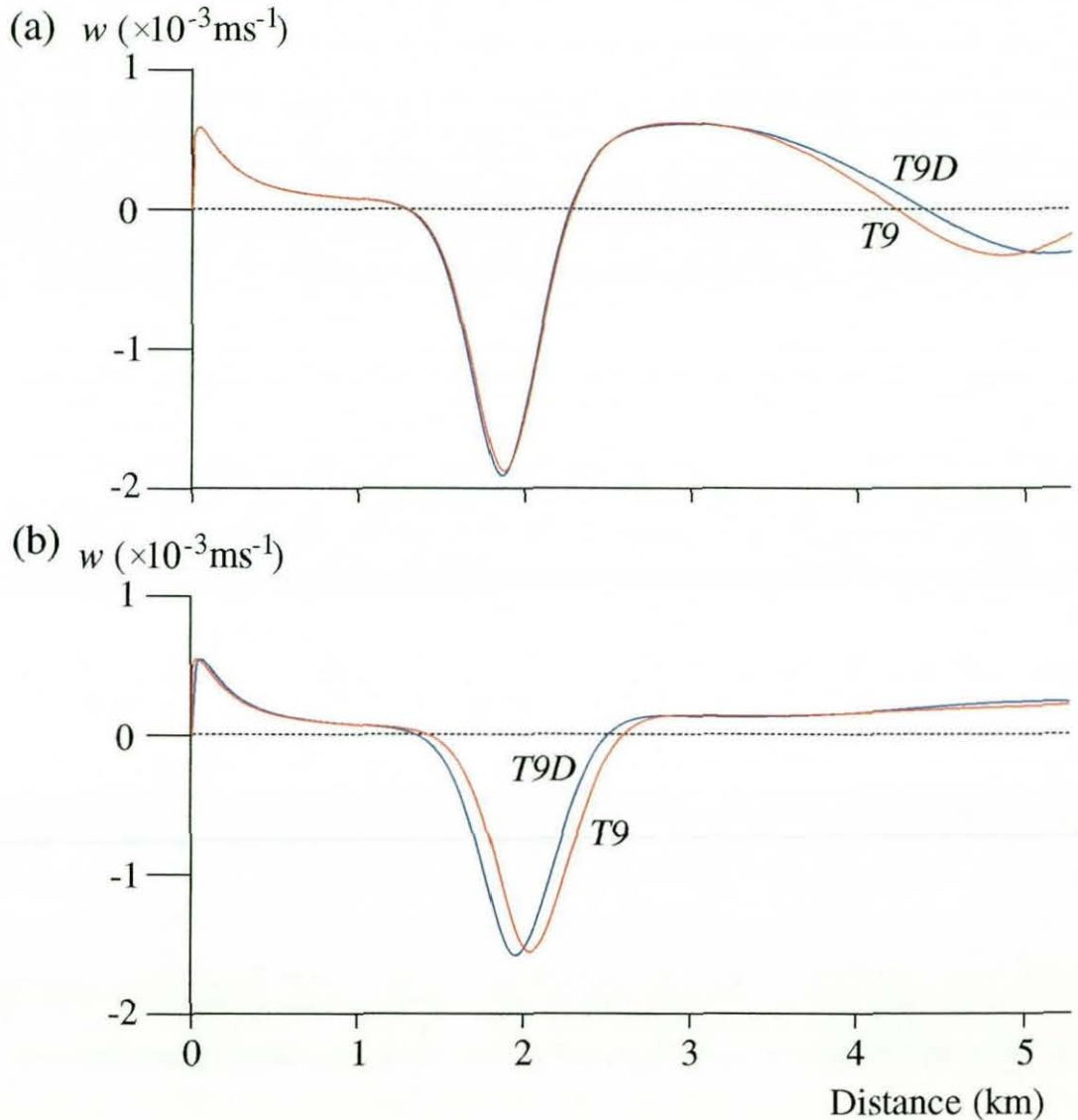


Figure 2.7: Effect of the far boundary on vertical velocity at 25 m depth in simulation $T9$: (a) after 4 days, (b) after 8 days.

2.4 Kamloops Lake Dynamical Model

2.4.1 Domain and General Remarks

The good availability of temperature data showing the riverine thermal bar of Kamloops Lake means that this model can be approached as a realistic case study of the riverine thermal bar rather than a test case designed to produce fundamental results. The 150 m maximum depth of Kamloops Lake is also crucial to this difference, as it allows a drastic reduction in the number of grid nodes even though a relatively fine resolution is maintained. This means that much longer simulations (of 30 days or more) can be produced at the same computational expense as the deep-lake work.

The ability to perform much longer simulations means that in this case it is possible to employ the desired scenario of starting with a river and lake which are cooler than the T_{md} and then heating both until the river warms through the T_{md} and the thermal bar appears. As described in the next section, this plan is implemented by applying a surface heat flux to the lake and raising the river temperature uniformly throughout the simulation.

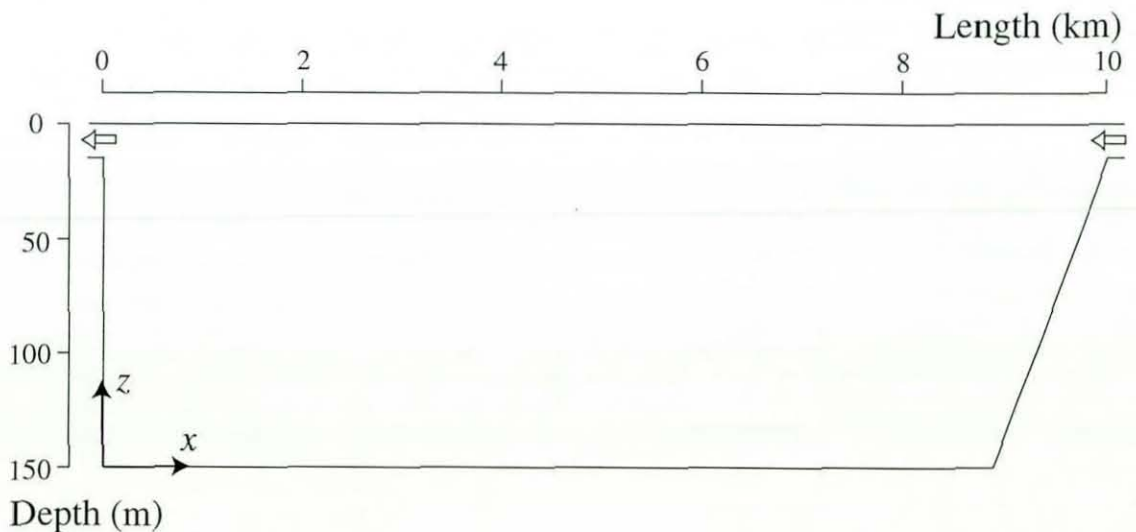


Figure 2.8: Chosen Kamloops section with positioning of axes and river sources and a sample of the grid-spacing.

In these simulations a grid cell has the dimensions $h_x = 25 \text{ m} \times h_z = 3 \text{ m}$, and the

lake section is taken to be a $10 \text{ km} \times 150 \text{ m}$ box with a river inflow on the right-hand side (figure 2.8). Since the aim of this study is to produce a faithful prediction of Kamloops Lake in spring, a sloping river delta is placed underneath the South Thompson River inflow, which is taken to be 15 m deep in this work. This produces a computational grid of only 19,010 nodes which, in conjunction with a doubled timestep of $\Delta t = 60 \text{ s}$, allows a massive increase in reasonable simulation times.

As well as permitting changes to the thermal regime, these longer simulation times contradict the basis of the neglect of coriolis forces. The simulations are lengthy enough for the predicted flows to spin up properly from rest, so coriolis forces can be accurately represented in the later stages of the Kamloops Lake model.

2.4.2 Boundary and Initial Conditions

All thermal data for the standard Kamloops Lake model (simulation *K*) are taken, calculated, or inferred from the work of Carmack (1979) and Carmack et al. (1979). The lake is initially assumed to be isothermal, with $T_L = 2.4^\circ\text{C}$, while the river initially has $T_R = 3.6^\circ\text{C}$, a scenario approximately corresponding to the status of Kamloops Lake and the South Thompson River on April 8th, 1975. The lake is then subjected to a surface heat flux using a similar condition to the one-dimensional models of section 2.3.3, but with $Q_s = 170 \text{ Wm}^{-2}$. While this heating continues the river is warmed uniformly by $0.2^\circ\text{C day}^{-1}$, so that the thermal bar appears on the third model day. The simulation is continued for 27 days after this in order to reproduce longitudinal Kamloops isotherm sections given in Carmack et al. (1979).

Salinity in Kamloops Lake is supposed to be uniform at 100 mgkg^{-1} (St. John et al. 1976) and the river's salinity is fixed to the same value for the purpose of reproducing the measured spring thermal bar. As a sensitivity study, riverine salinity is later varied in a similar manner to the deep-lake work and it is found that changes of up to 50 mgkg^{-1} are necessary to significantly affect the dynamics of this riverine thermal bar.

To ease the comparison of results from this simulation with the data of Carmack (1979) and the numerical results of BK, the river inflow is taken to enter the lake on the

right-hand boundary but the model coordinates and origin stay the same. The inflow velocity therefore takes the value of $u_R = -0.01 \text{ ms}^{-1}$, a speed which is chosen arbitrarily on the same basis as before.

2.4.3 Validity Timespan of results

These longer simulations on the shallower lake have far fewer simplifying assumptions to restrict the validity of results. All of the limiting factors listed in section 2.3.4 are resolved here apart from a variation in river discharge and the existence of a false boundary facing the river inflow. Since there is no data on the variation of the South Thompson River flow rate, it is left to the influence of far boundary effects to govern the maximum timespan of supported results.

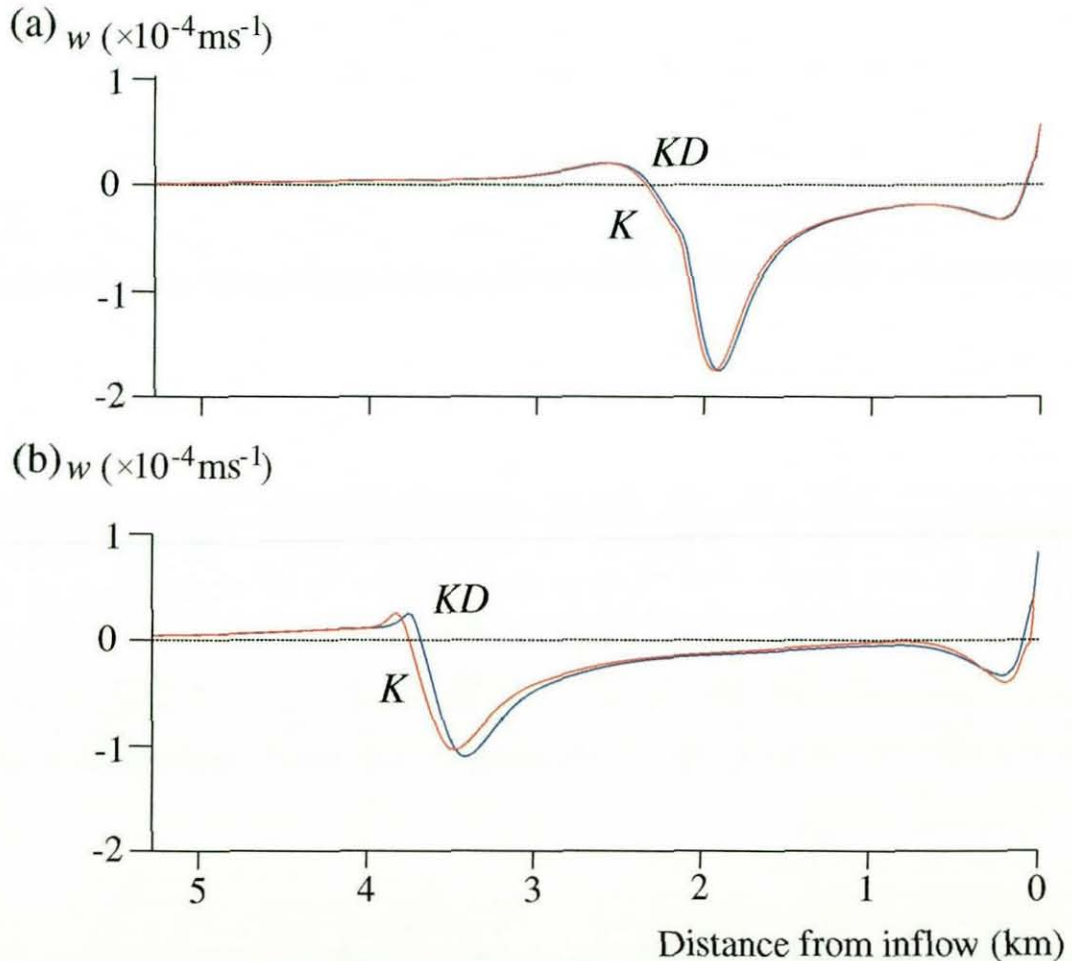


Figure 2.9: Effect of the far boundary on vertical velocity at 7.5 m depth in simulation *K*: (a) after 16 days, (b) after 24 days.

Figure 2.9 shows near-surface vertical velocity profiles from simulations K and KD , which have domain widths of 10 and 20 km respectively. The far boundary clearly grows in importance to the flow-field during the simulation, and the effects on the thermal bar's propagation are seriously adverse after 24 days (figure 2.9(b)). Although the general character of the vertical flow within each thermal bar is the same after this time, the position and strength of the main downwelling is altered by the fixed-velocity outflow, which pulls the thermal bar across the lake.

2.5 Ecosystem Modelling

Coupling a multi-component biological model to the dynamical study described in the preceding sections is a relatively straightforward process. As with the other scalar quantities, the variable representing the i th component of the model, C_i , is governed by an advection-diffusion balance:

$$\frac{\partial C_i}{\partial t} + u \frac{\partial C_i}{\partial x} + w \frac{\partial C_i}{\partial z} = \frac{\partial}{\partial x} \left(K_h \frac{\partial C_i}{\partial x} \right) + \frac{\partial}{\partial z} \left(K_v \frac{\partial C_i}{\partial z} \right) + \mathbb{S}_{C_i} \quad (2.19)$$

where \mathbb{S}_{C_i} represents the source terms which contain the interaction between plankton model components, such as photosynthesis of nutrients, zooplankton grazing, and plankton mortality. Formulating any particular plankton model therefore becomes a question of deciding the number and type of components C_i and processes governing the interactions contained in \mathbb{S}_{C_i} .

The description of the ecosystem modelling begins with a discussion of the sets of source terms comprising the two plankton models used in this thesis. A full description is then given of the difficulties involved in setting initial and boundary conditions for the plankton model components in the absence of detailed data.

2.5.1 Plankton Model of Franks et al. (1986)

The simplest plankton model adopted in this work is that of Franks et al. (1986), which has only three components: Nutrients, Phytoplankton and Zooplankton. As this model is used in BK to study plankton populations in the vicinity of the classical thermal bar, it is also adopted here in order to provide an initial model comparison and therefore reveal which parts of the ecosystem evolution are specifically riverine.

This influence over the model choice has a minor drawback: the Franks et al. (1986) model is conditioned for a Nitrogen-limited system while St. John et al. (1976) find that production in Kamloops Lake is co-limited by Nitrogen and Phosphorous during the spring warming and associated plankton growth. However, the negative impact of this particular situation is limited because this model is conditioned for the pelagic marine ecosystem and thus only a qualitative first description of the plankton distribution in the vicinity of the riverine thermal bar is sought. In a model this simple the nutrient variable could be assumed to be any combination of the nutrients limiting production at a particular time.

The full formulation of each source term is as follows:

Phytoplankton:

$$S_P = (G - m_P) P - IZ \quad (2.20)$$

Zooplankton:

$$S_Z = [(1 - \gamma)I - m_Z] Z \quad (2.21)$$

Nutrients:

$$S_N = (-G + m_P) P + (\gamma I + m_Z) Z \quad (2.22)$$

where G is the phytoplankton primary production rate:

$$G = V_m e^{-\eta d} \frac{N}{N + k_s} \quad (2.23)$$

and I is the zooplankton grazing rate:

$$I = R_m \Lambda P (1 - e^{-\Lambda P}). \quad (2.24)$$

It can be seen from equation (2.23) that in this formulation the uptake of nutrients by phytoplankton follows the Michaelis-Menten relation with a half-saturation constant of k_s . Primary production is also light-limited, with the penetration of sunlight following an exponential decay with depth. The grazing formulation (2.24) is of the Mayzaud & Poulet (1978) food-acclimatised type, which assumes that the zooplankton ingestion

rate rises as food concentrations increase, so that the grazing rate has no asymptotic limit (Parsons et al. 1967). The other interactions are all relatively simple, with constant plankton mortality rates and an ‘unassimilated fraction’ of the zooplankton grazing, γ , which is not converted into biomass and therefore returns to the nutrient pool.

Table 2.1 shows the values adopted for the various parameters in the model, all of which are chosen to match the simulation of BK for comparative purposes. These values originate from Franks et al. (1986) and Wroblewski & Richman (1987), and are all adopted here so that the ecology of the riverine thermal bar can initially be predicted using a highly simplified and well-understood model. Note that the units in which the component concentrations are expressed are all converted from $\mu\text{g-atom N } l^{-1}$ in the original model to mmol N m^{-3} here¹ and that all values listed as day^{-1} are converted into s^{-1} for use in the numerical procedure.

Parameter	Description	Value
V_m	Maximum phytoplankton growth rate	2.0 day^{-1}
η	Light extinction coefficient	0.1 m^{-1}
k_s	Nutrient uptake half-saturation constant	$0.2 \text{ mmol N m}^{-3}$
m_P	Phytoplankton death rate	0.1 day^{-1}
R_m	Maximum ingestion rate of zooplankton	0.5 day^{-1}
Λ	Ivlev constant for zooplankton grazing	$0.5 \text{ mmol N m}^{-3}$
γ	Unassimilated fraction of Z grazing	0.3
m_Z	Zooplankton death rate	0.2 day^{-1}
$N_L-P_L-Z_L$	Initial lake values of $N-P-Z$	$4-1-1 \text{ mmol N m}^{-3}$
$N_R-P_R-Z_R$	River boundary conditions for $N-P-Z$	$4-1-1 \text{ mmol N m}^{-3}$

Table 2.1: Parameters and conditions for the plankton model of Franks et al. (1986)

¹The letter N is used several times in this thesis to represent quite different quantities. N represents the nutrient component in a plankton model, while N is the Nitrogen in which all components of the plankton models are expressed. In addition, N^2 is defined as the stability (i.e. the square of the Brunt-Väisälä frequency) and $\mathbb{N}(\alpha, \beta)$ is used in equation (2.31) to indicate a normal distribution with mean α and variance β .

2.5.2 Plankton Model of Parker (1991)

In order to test the shortcomings of the Franks et al. (1986) model both in this work and that of BK, the more sophisticated ecosystem model of Parker (1991) is also coupled to the Kamloops Lake dynamical model in a separate study. This model contains a fourth component, detritus, which represents the distribution of deceased plankton cells and zooplankton fecal matter. This component therefore presents an intermediate stage between plankton and nutrients, which could slow ecosystem development by preventing the Nitrogen in these plankton byproducts from immediately becoming available nutrients for further phytoplankton growth. Other additional features of this model are temperature dependance, a total reformulation of the light-limitation of primary production, and the adoption of a constant zooplankton grazing rate.

The interactions are formulated as follows:

Phytoplankton:

$$\mathbb{S}_P = [(G - m_P - IZ) P] q \quad (2.25)$$

Zooplankton:

$$\mathbb{S}_Z = [((1 - \gamma_N - \gamma_D) IP - m_Z) Z] q \quad (2.26)$$

Nutrients:

$$\mathbb{S}_N = [-GP + \gamma_N IPZ + C_o D] q \quad (2.27)$$

Detritus:

$$\mathbb{S}_D = [m_P P + \gamma_D IPZ - C_o D + m_Z Z] q \quad (2.28)$$

In these equations, G is the phytoplankton primary production rate:

$$G = V_m \left[\left(\frac{L_d}{s_c} \right) \exp \left(1 - \frac{L_d}{s_c} \right) \right] \frac{N}{N + k_s} \quad (2.29)$$

with

$$L_d = L_s \exp \left(-\eta d - S_s \int_d^F (P + Z + D) dz \right), \quad (2.30)$$

where

$$L_s = \left(\frac{75\sqrt{2\pi}}{4} \right) \mathbb{N} \left(0.5, \frac{1}{64} \right) \quad (2.31)$$

is the surface insolation. In addition, m_P is the phytoplankton death rate:

$$m_P = M \exp \left(-(n_1 N)^2 \right), \quad (2.32)$$

and q is the thermal limitation factor:

$$q = 2.5 \left(\frac{T-15}{10} \right). \quad (2.33)$$

The source terms (2.25) - (2.28) reveal the effects on the plankton dynamics of detritus, which gains waste matter from the plankton and is converted into available nutrients (by unmodelled bacteria) at a constant rate. The unassimilated fraction of zooplankton grazing is now shared between the nutrients and detritus due to the wide range of biological phenomena which it represents. It is interesting to note the lack of zooplankton grazing on detritus, which is known to occur at times (Paffenhöfer & Knowles 1979). Depending upon the species composition of the Z component, N - P - Z - D models sometimes include this interaction (Fasham et al. 1990, Popova et al. 1997), which is neglected here for simplicity.

By far the largest difference between the two models is the formulation of photosynthesis, which governs the initial development of the ecosystem in these simulations which start from spring nutrient-pool conditions, as described in section 2.5.3. Comparing expressions (2.23) and (2.29) we can see that the formulations differ only in the representation of light penetration of the euphotic zone, which is very simple in the Franks et al. (1986) model but considerably more sophisticated in the Parker (1991) formulation.

It can be seen from equation (2.31) that the daily surface insolation L_s (in Einstein $\text{m}^2\text{day}^{-1}$) is assumed to have a Gaussian variation with time, which is modelled here by a normal distribution with mean 0.5 day and variance $1/64 \text{ day}^2$. This value is then adjusted so that the maximum light input is $150 \text{ Em}^2\text{day}^{-1}$ at noon (Parker 1986). The light reaching any particular depth L_d is calculated by equation (2.30) according to an exponential decay as before, but an additional light depletion is included to represent the biological phenomenon of self-shading, whereby plankton and detrital biomass suppresses light penetration to regions directly beneath it. Inhibition of growth according

to the available light is then simulated in equation (2.29) using the function of Steele (1965) with a saturation coefficient, s_c , which is chosen to be 40% of the noon insolation (Parker 1991).

The temperature dependence of the Parker (1991) model is fairly straightforward, and is represented by a simple factor q which multiplies all component interactions. In this way the entire ecosystem development is promoted by warmth and suppressed in cool regions, which has some particularly interesting implications in the present context of a warm river inflow to a cold lake.

Although most of the model is more sophisticated than that of Franks et al. (1986), such as the phytoplankton mortality (which now contains a nutrient dependency), the zooplankton grazing parameterisation is reduced to a constant rate in the Parker (1991) model. This feature is not modified in this work as changing one component with no physical basis could upset the model's balance, and it is important to ensure that both models are internally consistent.

The parameters employed in this model are all taken to be the original values of Parker (1991), as listed in table 2.2. Although these parameters are conditioned for a marine setting, and many of these values directly contradict the adopted values of the Franks et al. (1986) model (table 2.1), the original formulation must be adhered to due to a lack of the data required to calculate values which are more appropriate for Kamloops Lake.

Since the aim of the plankton model comparison is to assess the importance of the various improvements of the Parker (1991) model over the Franks et al. (1986) model, it is necessary to perform test simulations in which certain components of the more complex model are neglected. The methods of assessing each particular model feature are described below for simulations *PD*, *PS*, and *PT* (see appendix A), a discussion which also applies to simulation *PTSD* which has all of these modifications simultaneously.

Simulation *PD* has the detritus component removed altogether, so that C_o is set to 0 and all other source terms in equation (2.28) are redirected to \mathbb{S}_N . Neglecting

self-shading in simulation *PS* is a far simpler process, as it is accomplished by merely setting the coefficient S_s in equation (2.30) to zero. In order to examine the effects of temperature dependence in simulation *PT*, $T = 20^\circ\text{C}$ is substituted into equation (2.33) so that q becomes a constant multiplier. This particular value is chosen for comparative purposes, since BK state that this temperature is consistent with the assumptions made in the formulation of the (temperature independent) Franks et al. (1986) model.

Parameter	Description	Value
V_m	Maximum phytoplankton growth rate	2.8 day^{-1}
s_c	Light saturation coefficient	$60 \text{ Em}^2\text{day}^{-1}$
η	Light extinction coefficient	0.15 m^{-1}
S_s	Self-shading coefficient	$0.02 (\text{mmol N m}^{-3})^{-1} \text{ m}^{-1}$
k_s	Nutrient uptake half-saturation constant	$0.6 \text{ mmol N m}^{-3}$
I	Ingestion rate of zooplankton	0.2 day^{-1}
M	Maximum phytoplankton death rate	0.5 day^{-1}
n_i	Phytoplankton death rate coefficient	$1 (\text{mmol N m}^{-3})^{-1}$
γ_N	Unassimilated Z grazing to nutrients	0.4
γ_D	Unassimilated Z grazing to detritus	0.3
m_Z	Zooplankton death rate	0.1 day^{-1}
C_o	Detritus to nutrient conversion rate	0.02 day^{-1}
$N_L-P_L-Z_L-D_L$	Initial lake values of $N-P-Z-D$	4-1-1-1 mmol N m^{-3}
$N_R-P_R-Z_R-D_R$	River boundary conditions for $N-P-Z-D$	4-1-1-1 mmol N m^{-3}

Table 2.2: Parameters and conditions for the plankton model of Parker (1991).

2.5.3 Initial and Boundary Conditions

Selecting appropriate initial and boundary conditions for the ecological model is a major difficulty in the physical setting of a continuously-interacting river and lake. Since a comparison is sought both between the two models in this study and between this work and that of BK, initial conditions analogous to those of BK are adopted for both models,

as detailed in tables 2.1 and 2.2. These choices are physically justified by the spring timing of the period of interest in this study; over winter the plankton productivity is low in Kamloops Lake, while mortality remains proportional to population levels, so that the low-biomass and nutrient-rich lake adopted here is in a theoretically suitable condition for the start of spring (St. John et al. 1976).

It is important to note that the N_R - P_R - Z_R - D_R conditions of 4-1-1-1 mmol N m⁻³ adopted for the Parker (1991) model are a significant departure from the 7-0.1-0.1-0.1 mmol N m⁻³ values of the original paper. This modification is permissible, however, because the total Nitrogen in the system is similar; the ecosystem is held to be in a different period of the growth cycle but generally of the same character.

Setting the riverine boundary conditions for the model is also extremely problematic, since upstream values of each component will have a very strong influence on the near-river lake region throughout the entire simulation. The preferred modelling approach would be to couple a one-dimensional river version of the plankton model (on a vertical section) to the two-dimensional lake section and use the one-dimensional results to give the riverine plankton levels which flow into the lake model. However, testing of this approach shows that the ecosystem models adopted here, which are conditioned for deep, slowly-moving bodies of water in which light and nutrient availability are the dominant limiting factors, are seriously flawed in the context of a river plankton ecosystem.

The fundamental problem with this application of these models is that river plankton communities are often dominated by physical, rather than biotic, interactions (Reynolds et al. 1994). For example, in a well-mixed river the phytoplankton are rapidly brought into and out of contact with nutrient and light concentrations which are suitable for growth, so that the individual plankton production rate is of vital importance to bulk plankton growth (Reynolds 1994). Even if an attempt were made to apply these models to the river ecosystem, nutrient limitation practically never occurs in rivers due to the presence of rapid flushing rates (Soballe & Kimmel 1987) and river turbidities are usually so high that light-extinction coefficients would have to be greatly increased by an arbitrarily-chosen amount (Dokulil 1994).

After a coupled model solution has been ruled out, the next most reasonable approach seems to be fixing an initial state to the river ecosystem and then imposing an arbitrary transfer of Nitrogen between the river plankton model components in a crude attempt to reproduce basic river ecosystem dynamics in spring. Unfortunately data from St. John et al. (1976) are inconclusive regarding the river ecosystem variation in spring, and it is rather dangerous to apply vague river-plankton growth principles since it is likely that spring productivity in the South Thompson River is strongly influenced by local nutrient loadings and temperature and turbidity fluctuations.

After these possibilities have been ruled out, the most sensible option is to fix the values of each inflowing plankton component to a constant value throughout the simulation. These values are chosen so that riverine component levels abide by the initial lake scenario of high nutrient levels and small plankton populations. This choice is partly made on the basis of evidence that biologically-available Nitrogen and Phosphorus were relatively constant in the South Thompson River during April 1975 (St. John et al. 1976). In addition, Carmack & Gray (1982) and Jasper et al. (1983) found that throughout spring the Kootenay River supplies high-nutrient and low-plankton water to Kootenay Lake, British Columbia, which shares many physical characteristics with the Kamloops Lake - Thompson River system. Also it is well-documented that plankton grow much more slowly in rivers than lakes under similar nutrient-availability conditions, an observation which is mainly due to the higher turbulence and turbidity of shallow, rapidly-flushed rivers (Jasper et al. 1983, Soballe & Kimmel 1987, Reynolds 1994). The basic assumption is therefore that the river plankton do not grow or deplete nutrients significantly for 30 days after the ecosystem starts to develop in the lake. Although this condition is clearly not totally realistic, it seems a more sensible choice than attempting to guess the real spring variation in riverine plankton levels.

Chapter 3

Numerical Solution

A numerical solution to the governing equations described in the previous chapter is obtained by dividing the domain of interest with a grid and approximating the global solution in a piecewise manner by solving discretised equations at every grid node. A Finite Volume formulation is used to produce and solve the resulting system of equations numerically. This chapter explains the numerical procedures which are used in each of the models to generate flow predictions from the governing equations and boundary conditions.

3.1 Discretisation Procedure

The partial differential equations (2.2) - (2.7) representing the velocity components, properties of the fluid, and components of the plankton model are discretised by representing the value of the dependent variable at a node X , Φ_X , as a function of the surrounding values:

$$a_X \Phi_X = \sum_{nb=E,W,N,S} a_{nb} \Phi_{nb} + \mathbb{S}_X \quad (3.1)$$

where $nb = E, W, N, S$ represent the surrounding nodes (as shown in figure 3.1) and Φ_{nb} the corresponding node values. Writing equation (3.1) for every point in the domain gives a system of linear equations which, after rearrangement, is stored in coefficient matrix form:

$$\hat{A}\Phi = \mathbf{s} \quad (3.2)$$

where \hat{A} is the matrix of coefficients, Φ is the vector of node values and \mathbf{s} represents the right-hand side due to unsteady and source terms.

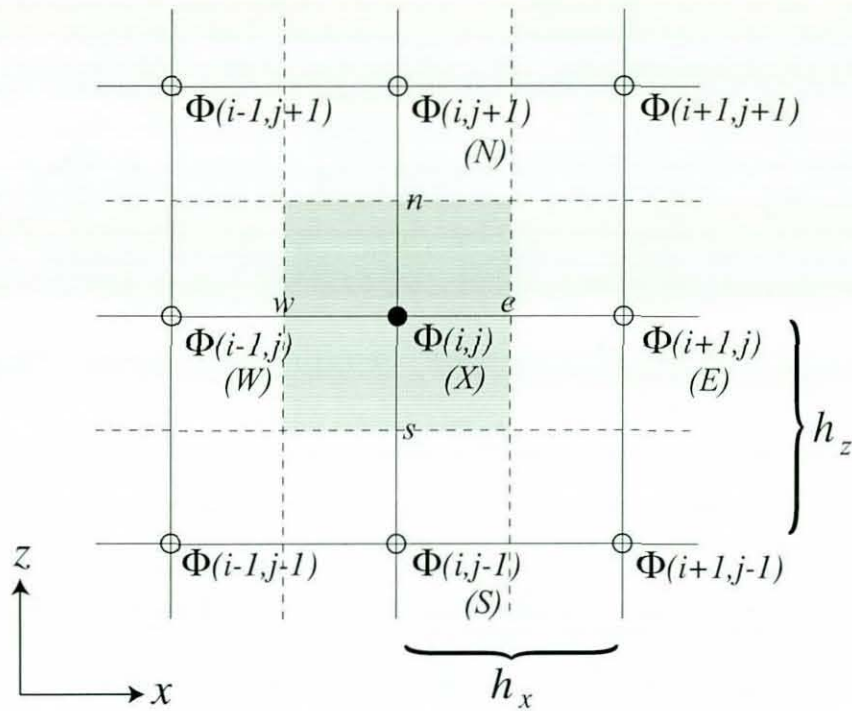


Figure 3.1: Scalar variable Φ evaluated over chosen grid. The shaded area represents a single control volume.

Note from figure 3.1 that subscripts e, w, n, s represent the faces of the cell in question. In equation (3.1), \mathbb{S}_X represents the source term at point X , which contains physical sources of Φ , \mathbb{S}_Φ , due to the surface heating and effects of interaction between the components of a plankton model. \mathbb{S}_X also contains other terms resulting from the discretisation, some of which are grouped under \mathbb{S}_X in order to improve the conditioning of the system (3.2) which is to be solved numerically.

The solution procedure is applied to a *staggered grid* over the model lake domain (figure 3.2), such that the velocity components are evaluated at the cell faces of the grid used for other variables. This avoids the following problems which can arise from evaluating the pressure and velocity components on the same grid (Patankar 1980). If velocity and pressure are calculated at the same point in space, then any attempt find a pressure gradient at that point will result in a formulation which is dependent only on the pressure at neighbouring nodes. If the pressure field is oscillatory, this may result in a misrepresentation of pressure gradient forces, since gradients are calculated from alternate pressure values, not adjacent ones. Evaluating the velocities on a cell face

between two pressure nodes is the best way to ensure that pressure gradients used in the velocity equations (2.2) and (2.4) avoid these problems.

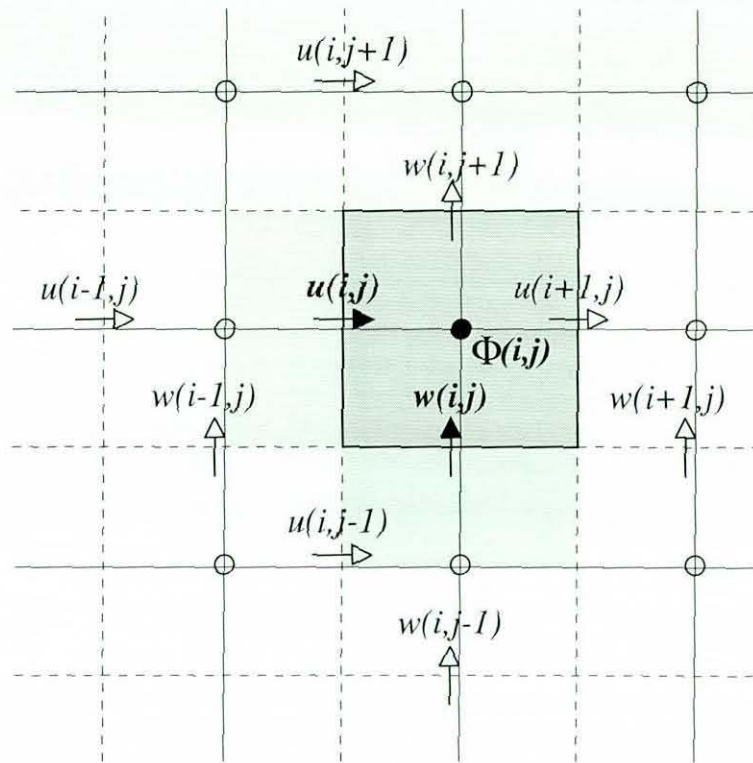


Figure 3.2: Velocity components corresponding to backward-staggered grid

The coefficients a_{nb}, a_X in (3.1) represent the weighting of the effect of Φ_{nb} values at neighbouring nodes on Φ_X , the value of Φ at the node of interest. These coefficients are calculated by integration of the original differential equations over the control volumes defined by the given mesh (figure 3.1). Applying Gauss' Theorem, volume integrals of each governing equation are expressed as surface integrals over the four faces of each cell.

A generic unsteady advection-diffusion equation for Φ under the Boussinesq (1903) approximation may be written

$$\underbrace{\frac{\partial \Phi}{\partial t}}_{\text{Unsteady}} + \underbrace{\nabla \cdot (\mathbf{u}\Phi)}_{\text{Convection}} = \underbrace{\nabla \cdot (K \nabla \Phi)}_{\text{Diffusion}} + \underbrace{\mathcal{S}_\Phi}_{\text{Source}} \quad (3.3)$$

and it is easy to observe that the governing equations (2.2) - (2.7) and (2.17) are all of this form. Since the convection term is only included in the two-dimensional modelling

here, the discretisation of this equation will be presented term by term.

Unsteady and Source terms:

Considering Φ constant over each control volume of integration, V_Φ , we integrate to find

$$\int_{V_\Phi} \frac{\partial \Phi}{\partial t} dV_\Phi = \left(\frac{\Phi^{n+1}(i, j) - \Phi^n(i, j)}{\Delta t} \right) h_x h_z \quad (3.4)$$

where Φ^n is the value of Φ at time t and Φ^{n+1} refers to Φ at time $t + \Delta t$. It is therefore chosen that the unsteady term be discretised using a first-order forward-differencing scheme. The source term is simply integrated to find that

$$\int_{V_\Phi} \mathbb{S}_\Phi dV_\Phi = \mathbb{S}_\Phi h_x h_z. \quad (3.5)$$

Diffusion terms:

The volume integral of the diffusive term in each direction is split into surface integrals over the faces of a control volume, for example the diffusion term in the x -direction becomes

$$\int_{V_\Phi} \frac{\partial}{\partial x} \left(K_h \frac{\partial \Phi}{\partial x} \right) dV_\Phi = (K_h)_e \left(\frac{\partial \Phi}{\partial x} \right)_e h_z - (K_h)_w \left(\frac{\partial \Phi}{\partial x} \right)_w h_z \quad (3.6)$$

which is

$$\begin{aligned} & \left(\frac{K_h(i+1, j) + K_h(i, j)}{2} \right) \left(\frac{\Phi^{n+1}(i+1, j) - \Phi^{n+1}(i, j)}{h_x} \right) h_z \\ & - \left(\frac{K_h(i, j) + K_h(i-1, j)}{2} \right) \left(\frac{\Phi^{n+1}(i, j) - \Phi^{n+1}(i-1, j)}{h_x} \right) h_z \end{aligned} \quad (3.7)$$

after discretisation. It is assumed here and in the convection discretisation that flux terms for Φ are evaluated at time $t + \Delta t$, yielding a fully-implicit scheme.

Convection terms:

Representation of the convective terms requires a more sophisticated approach. Using the x -direction as an example again, a standard volume integral yields

$$\int_{V_\Phi} \frac{\partial(u\Phi)}{\partial x} dV_\Phi = (u\Phi)_e h_z - (u\Phi)_w h_z. \quad (3.8)$$

The use of a staggered grid means that u_e and u_w are known quantities, so the discretisation of convective terms becomes a matter of calculating cell face values Φ_e and Φ_w .

The initial approach here is the use of the first-order *Upwind* technique, which simply approximates the convected property value on a cell face to be that of the node immediately upstream. The upstream node is selected by the sign of the convecting velocity on the cell face in question, so that

$$\Phi_w = \begin{cases} \Phi_W & u_w > 0 \\ \Phi_X & u_w < 0 \end{cases}, \quad \Phi_e = \begin{cases} \Phi_X & u_e > 0 \\ \Phi_E & u_e < 0 \end{cases}. \quad (3.9)$$

The use of Upwind differencing has the favourable effect of stabilising convergence of the iterative solvers used here, but unfortunately this is due to the introduction of 'false' numerical diffusion by this technique (Patankar 1980). The Upwind method is therefore only suitable for use unmodified when the model diffusion coefficients are significantly larger than the added numerical diffusion.

When convection is not too much stronger than diffusion, as determined by the cell Peclet number (Pe), Central Differencing of the convection terms gives a better representation than Upwind Differencing due to the removal of the numerical diffusion associated with the Upwind approach. A classical approach to the discretisation of convective terms is therefore to adopt a 'conditional' scheme (e.g Hybrid, Power-Law, etc.) whereby Upwind Differencing is employed for $Pe > 2$ (dominant convection) and Central Differencing is adopted otherwise. However, Leonard & Drummond (1995) have shown that these schemes are seldom more economical than some higher-order schemes, which have a greater accuracy. Central Differencing is therefore not considered in this study.

One such higher-order scheme is the *QUICK* (Quadratic Upstream Interpolation for Convective Kinematics) scheme of Leonard (1979). In this method, the value of the variable on a cell face is calculated using a three-point quadratic interpolation, where the two upstream and one downstream nodes used for the interpolation are chosen depending upon the direction of the convecting velocity on the cell face.

Figure 3.3 shows the generalised node notation surrounding a cell face f which will be used hereafter to describe the QUICK method. The value on the cell face (Φ_f) is calculated as a linear interpolation of the two nodes surrounding it in the direction orthogonal to the cell face (Φ_C and Φ_D), plus correction terms proportional to the

curvature of the quadratic interpolation at the immediately upstream node (Φ_C), so that in two dimensions

$$\Phi_f = \frac{1}{2}(\Phi_C + \Phi_D) - \frac{h_x^2}{8} \left(\frac{\partial^2 \Phi}{\partial x^2} \right)_C + \frac{h_z^2}{24} \left(\frac{\partial^2 \Phi}{\partial z^2} \right)_C. \quad (3.10)$$

The full derivation of this formula may be found in Leonard (1979).

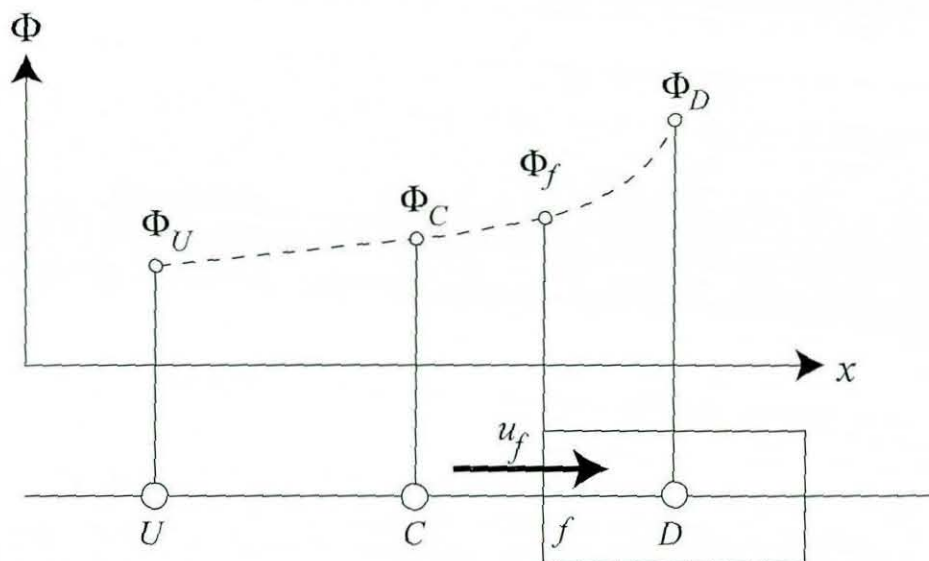


Figure 3.3: Node notation for theory of QUICK differencing.

While numerical viscosity from Upwind differencing makes the coefficient matrix better-conditioned for inversion, the coefficients which result from the use of (3.10) may become negative, with drastic consequences for the stability of the solution procedure. In order to maintain the matrix-conditioning benefits of Upwind differencing but gain the higher accuracy of QUICK, a *deferred correction* procedure is used whereby the cell-face value of Φ , used to calculate the coefficients from equation (3.8), is written in terms of the Upwind value plus a correction:

$$\Phi_f = (\Phi_f)_{Upwind} + [(\Phi_f)_{QUICK} - (\Phi_f)_{Upwind}]. \quad (3.11)$$

The correction term is then included in the source term so that the coefficient matrix is identical to that of the Upwind approach. As the converged solution is reached for each time-step, the first-order contributions cancel and the solution is consistent with the QUICK scheme everywhere.

Another problem with higher-order convection schemes is the possibility of unphysical *overshooting*, whereby a cell-face value of Φ is found to be outside the range of the two adjacent nodes, i.e. $\Phi_f \notin [\Phi_C, \Phi_D]$. This phenomenon may lead to non-linear instability, for example if a computed turbulence quantity becomes negative as a result of an oscillation in temperature or salinity fields, and a negative calculation of eddy-viscosity is the result. A convection boundedness criterion, based upon physical assumptions, is used in the model and briefly defined here. This *flux-limiter* is based upon the technique of Gaskell & Lau (1988), in the normalised-variable formulation of Leonard & Mokhtari (1990), of which a thorough description is given in Botte (1999). The logic is as follows:

- in locally monotonic regions, i.e. where $\Phi_C \in [\Phi_U, \Phi_D]$, the value on the cell face should lie between the value of adjacent nodes, i.e. $\Phi_f \in [\Phi_C, \Phi_D]$.
- if $\Phi_C \notin [\Phi_U, \Phi_D]$ then there is no information to limit the interpolated value Φ_f and the (always bounded) Upwind scheme is used.

In section 3.4, the effectiveness of Upwind and QUICK convection schemes are studied on the Lake Baikal and Kamloops Lake simulations. It is found that the QUICK scheme produces few appreciable benefits for the Kamloops Lake solution, and the Upwind scheme is used there in its most basic form. However, applying QUICK differencing to the Lake Baikal simulation produces significant improvements to the velocity solution, so the QUICK scheme is employed in the deep-lake simulations. Since more accurate methods require increased computational effort for relatively small accuracy gains, QUICK is the most sophisticated convection scheme considered here.

3.2 Solution Procedure

Two-dimensional model:

Writing equation (3.1) for every grid point in the domain gives a linear system of $n = n_x \times n_z$ equations in n unknown variables. The coefficient matrix of these systems is symmetric in shape but not in values, and it is not positive definite (BK). Each equation for a node is written in terms of no more than 4 other nodes (since the deferred QUICK correction, which involves other nodes in the second derivatives, appears in the source

term), so the coefficient matrix for the rectangular box geometry has a pentadiagonal structure with a_X coefficients in the leading diagonal (figure 3.4(a)).

The coefficient matrix for the irregular geometry of the plankton studies has a slightly more complex structure, as the cells are not in even rows and columns. The three leading diagonals are the same as before but coefficients a_E and a_W are no longer at the same distance from a_X for every cell in the domain, as this distance is dependent upon the total number of cells in the column of interest.

Figure 3.4 consists of two matrix diagrams, (a) and (b), enclosed in large parentheses. Diagram (a) shows a pentadiagonal matrix with a main diagonal of dots. Non-zero coefficients are placed at the top-left, top-right, and bottom-right corners, and at the bottom-left. Specifically, the top row contains a_{1X} , a_{1N} , and a_{1E} . The second row contains a_{2S} and a series of dots. The n_z -th row contains $a_{n_z W}$ and a series of dots. The $(n-n_z)$ -th row contains a series of dots and $a_{(n-n_z)E}$. The $(n-1)$ -th row contains a series of dots and $a_{(n-1)N}$. The bottom row contains 0 , a_{nW} , a_{nS} , and a_{nX} . Diagram (b) shows a tridiagonal matrix with a main diagonal of dots. Non-zero coefficients are placed at the top-left and bottom-right corners. The top row contains a_{1X} and a_{1N} . The second row contains a_{2S} and a series of dots. The $(n-1)$ -th row contains a series of dots and $a_{(n-1)N}$. The bottom row contains a_{nS} and a_{nX} . Large zeros are placed in the upper-right and lower-left quadrants of both matrices.

Figure 3.4: Form of the coefficient matrices to be solved, (a) pentadiagonal matrix from two-dimensional problem, (b) tridiagonal matrix from one-dimensional problem.

Given a correct pressure field, the discretised versions of the momentum equations (2.2) and (2.4) will predict a velocity field which satisfies continuity. However, the pressure field needs to be calculated from the velocities as part of the solution procedure, and therefore a method of linking pressure and velocity is required. In this study, an unsteady pressure correction procedure similar to the steady *SIMPLE* (Semi-Implicit Method for Pressure-Linked Equations) method of Patankar & Spalding (1972) is used to refine the calculated velocity field to one satisfying the continuity equation (2.1).

Briefly, the SIMPLE method is a guess-and-correct procedure which regards the correct pressure p as the sum of a guessed pressure p^* and a *pressure correction* p' :

$$p = p^* + p'. \quad (3.12)$$

Then, given p^* (which in this case corresponds to the pressure from the previous iteration), we require a routine for calculating the pressure correction p' and formulae for finding the associated velocity corrections.

To illustrate the calculation of p' let us consider u_e , the horizontal velocity evaluated on an eastern cell-face. Discretisation of the momentum equation (2.2) gives

$$a_e u_e = \sum_{nb} a_{nb} u_{nb} + S_e + (P_X - P_E) h_z \quad (3.13)$$

where S_e is the source term \mathbb{S}_e minus the pressure gradient forcing on face e , which is explicitly included above. If we consider the desired horizontal velocity u to be comprised of an imperfect velocity (calculated with the guessed pressure field, and therefore corresponding to the previous time-step in this study) plus a correction

$$u = u^* + u', \quad (3.14)$$

then we may also obtain a discretisation for u_e^* :

$$a_e u_e^* = \sum_{nb} a_{nb} u_{nb}^* + S_e + (P_X^* - P_E^*) h_z. \quad (3.15)$$

Subtracting equation (3.15) from equation (3.13), we have

$$a_e u_e' = \sum_{nb} a_{nb} u_{nb}' + (P_X' - P_E') h_z. \quad (3.16)$$

To proceed from this point to a velocity-correction formula, we must drop from this equation the term containing the summation of contributions from neighbouring nodes. This bold step is justified in that if we retained these terms we would end up with a velocity correction equation for u_e involving velocities and pressure corrections at every other point in the domain¹. A thorough discussion of the consequences is given by Patankar (1980), and omitted here.

¹This results in the name of the SIMPLE procedure; by neglecting these terms we lose the implicit influence of the pressure correction from neighbouring nodes but retain the implicit influence of the pressure correction on velocity at the node in question.

Utilising equation (3.14) we then arrive at a formula giving the required velocity correction from the pressure correction:

$$u_e = u_e^* + \frac{h_z}{a_e}(P'_X - P'_E), \quad (3.17)$$

and a similar equation may be written for the vertical direction.

An equation for the pressure correction is found by integrating the continuity equation (2.1) over a control volume as before:

$$\int_{V_\Phi} \frac{\partial u}{\partial x} + \frac{\partial w}{\partial z} dV_\Phi = (u_e - u_w)h_z + (w_n - w_s)h_x = 0. \quad (3.18)$$

After substitution of cell-face velocity relations similar to (3.17) and appropriate grouping of known quantities into coefficients and a source term $\mathbb{S}_{P'}$, this yields the pressure-correction equation:

$$a_X P'_X = \sum_{nb} a_{nb} P'_{nb} + \mathbb{S}_{P'} \quad (3.19)$$

where coefficients a_i are all known quantities.

Now that we have a pressure correction equation and associated velocity-correction formulae, a procedure for calculating u and w velocities in one time-step can be constructed as follows:

1. Set the initial pressure field p^* to p from the previous time-step.
2. Calculate T, S and ρ using velocities from the previous time-step.
3. Using p^* , calculate u^* and w^* from the discretised versions of the momentum equations (2.2) and (2.4).
4. Solve the pressure correction equation (3.19).
5. Calculate p from equation (3.12).
6. Correct velocities using equations similar to (3.17).

While the steady SIMPLE procedure iterates the above steps towards a converged solution, in this unsteady case the time step is kept small enough for the pressure p^* from

the previous time step to be close enough to the new correct pressure field p for a good solution to be obtained from just one application of steps 1-5. In this way the procedure converges over the time-steps so that the pressure correction equation becomes easier to solve as the simulation proceeds.

In the absence of any other information, the pressure is supposed correct in the bottom left-hand corner of the domain (i.e. $p' = 0$ at $i = 1, j = 1$) to fix the pressure correction routine to absolute rather than relative calculations of the pressure field. This avoids the numerical difficulties associated with the singular coefficient matrix which results from the use of Neumann boundary conditions everywhere.

One-dimensional model:

The one-dimensional models which are used to evaluate the initial and riverine conditions are much simpler to manage numerically. Since each node has at most two neighbours, the coefficient matrix has a tridiagonal structure (figure 3.4(b)), representing a system of n_z equations in n_z unknown quantities, where n_z is the depth in cells of the river or lake under consideration. Since the fluid is considered to be motionless in the one-dimensional models, complex pressure correction routines are not necessary. Instead pressure is simply evaluated from hydrostatic equilibrium (2.15) for use in the calculations of Brünt-Väisälä frequency.

3.3 Numerical Techniques for Linear Systems

General two-dimensional case:

For every variable apart from the pressure correction, a sparse systems iterative solver is used to invert the matrices of coefficients which arise from the discretisation process. Due to the characteristics of these matrices the *GMRES* (Generalised Minimum Residual) acceleration procedure of Saad & Schoults (1986) is used as the appropriate variant of the *Conjugate Gradient* (CG) method. Conjugate Gradient methods use the *residual* of a system after each iteration to decide how to maximise convergence in the next iteration. Adopting the notation of equation (3.2), if we represent the system to be solved iteratively for \mathbf{x} as:

$$\hat{A}\mathbf{x} = \mathbf{s}, \quad (3.20)$$

then the residual corresponding to an intermediate solution \mathbf{y} is given by:

$$Res(\mathbf{y}) = \hat{A}\mathbf{y} - \mathbf{s}. \quad (3.21)$$

The Conjugate Gradient method proceeds by generating vector sequences of iterates², residuals corresponding to the iterates, and search directions to optimise the updating of the iterates so as to minimise the residual corresponding to the following iterate (Oppe et al. 1988). We consider the solution converged when $Res(\mathbf{y})$ is sufficiently small to give the required error tolerance for the whole system.

GMRES is the CG variant used for nonsymmetric linear systems, and generally uses a modified Gram-Schmidt procedure to form the orthogonal vectors. The main problem with this procedure is that it requires storage of the whole sequence of vectors (unlike CG), but this difficulty can be overcome by *restarting* the iteration every so often (Barrett et al. 1994). However, the memory requirements were satisfied in this study so restarting was not used in order to preserve the speed of convergence.

Preconditioning the matrix can sometimes help to improve the speed of convergence or accuracy of the iterative process by favourably transforming its shape and thus its spectral properties. Jacobi preconditioning, incomplete Cholesky factorisation, incomplete LU factorisation, truncated Neumann and least squares polynomial expansions have all been tested and found to be uneconomical in this case, so the null preconditioner was adopted.

Pressure-correction case:

When solving the system representing the pressure correction, GMRES converges extremely slowly due to the ill-conditioning of the matrix (Botte et al. 1996). Since the accuracy of solution for the pressure correction must be very good to provide a realistic flow-field with one implementation of the SIMPLE procedure per time-step, the total solution time would be prohibitive even if GMRES ever attained the required accuracy.

The performance of several other acceleration routines was tested against GMRES but unfortunately little improvement in convergence time is possible. Testing with

²These vectors are conjugate (or orthogonal), hence the name of CG methods.

the preconditioners mentioned previously also failed to solve this problem, so a direct solver had to be employed for the pressure correction case only. This decision was taken reluctantly as the extra memory requirement of a direct solver drastically reduces the maximum number of gridpoints which can be solved in a reasonable time, and therefore decreases the maximum resolution and domain size of the model. Direct methods are generally very slow but in this case total solution times are an improvement over GMRES.

The use of a direct solver for the pressure correction solves all of the numerical problems as it gives the most accurate solution possible, at machine levels of error, and has no problem with the conditioning of the matrix in question. The amount of fill-in during factorisation is reduced by pre-processing the coefficient matrix with a re-ordering heuristic based on the *multiple degree algorithm* of Liu (1985). The symmetric pattern of the matrix is utilised by setting the solver to favour diagonal pivoting during the factorisation.

The factorisation process continues by finding a sparsity-preserving and numerically acceptable pivot order and computing the $\hat{L}\hat{U}$ factors such that $\hat{P}\hat{A}\hat{Q} = \hat{L}\hat{U}$, where \hat{P} and \hat{Q} represent the pivot order. The chosen solver uses the *multifrontal* method (Liu 1992), which factorises the matrix using a series of small dense *frontal* matrices, which are not limited to square matrices in the unsymmetric case. The system is then solved using update matrices to carry the intermediate results from the variables being eliminated to the variables which are not yet processed. Assembly of update matrices (corresponding to variables eliminated previously) to form the current frontal matrix may have to occur before the elimination of a variable. The frontal matrix is then partially factorised, and the new update matrix is formed.

One-dimensional case:

The tridiagonal coefficient matrices of the one-dimensional models are much simpler to solve. The TDMA (Tri-Diagonal Matrix Algorithm) procedure of Thomas (1949) was employed for the inversion of these coefficient matrices. The TDMA is a very simple direct method which uses a process of forward elimination to link each variable to the next, and then back-substitution to explicitly determine each node value.

We may write a general equation for the j th node value of a variable Φ in a one-dimensional system, Φ_j , as dependent only upon its two neighbours:

$$a_{jX}\Phi_j = a_{jS}\Phi_{j-1} + a_{jN}\Phi_{j+1} + s_j \quad \text{for } j = 1 \dots n_z \quad (3.22)$$

subject to the boundary conditions

$$\Phi_1 = \Phi_{bottom} \quad (3.23)$$

$$\Phi_{n_z} = \Phi_{top}. \quad (3.24)$$

When compared to equation (3.22), condition (3.23) implies that Φ_2 is only dependent upon Φ_3 (since Φ_1 is known), which is therefore only dependent upon Φ_4 , and so on. Using forward-elimination we can obtain a set of equations where the j th variable is written solely in terms of the $(j + 1)$ th:

$$\Phi_j = Q_j\Phi_{j+1} + S_j. \quad (3.25)$$

Then, since we know the n_z th variable explicitly (3.24), we can use a process of back-substitution on equation (3.25) to explicitly determine all values of Φ .

3.4 Balance of Convection and Diffusion

In this section the balance of convective and diffusive terms in the governing equations (2.2) - (2.7) is studied in each of the two models included in this work. Knowledge of the relative importance of convection and diffusion is crucial to the choice of convection scheme (section 3.1) and the sophistication of the turbulence parameterisation (chapter 4), and is therefore a subject which is correctly placed in this chapter as it is strongly associated with numerical modelling.

This section shows that convection and diffusion are of evenly-balanced importance in both the Lake Baikal and Kamloops Lake simulations. However, horizontal diffusion is more erratic inshore of the thermal bar in the Lake Baikal scenario, which allows convection to play a slightly more influential role than in Kamloops Lake.

This difference leads to the adoption of different convection schemes in the two models: QUICK for Lake Baikal and Upwind for Kamloops Lake. The influence of

each of these schemes is tested in this section by introducing two new simulations for comparative purposes. *T9* is compared to *T9UP*, which has Upwind differencing, and *K* is compared to *KQ*, which uses QUICK. Comparisons of horizontal velocity predictions with and without the QUICK scheme are shown in a typical sample of each case to justify the final model choice.

3.4.1 Lake Baikal

Figure 3.5(a) shows horizontal profiles of convective and diffusive transport of the riverine tracer in simulation *T9* at a depth of 25 m, corresponding to half of the inflow depth. A positive value of either transfer mechanism indicates that it is increasing the tracer concentration at the position in question, while a negative value reveals that the in-situ tracer concentration is being depleted. The plot also contains indicators marking the horizontal positions of both the $T = T_{md}$ contour and the horizontal stagnation point ($u = 0$) at this depth.

Convection and diffusion terms are generally of a similar magnitude here, although horizontal convection seems to considerably outweigh diffusion inshore of the horizontal stagnation point, where both mechanisms hold a positive value and are therefore increasing local tracer levels. Comparing the convective term profile to this stagnation point shows that tracer concentrations inshore of the thermal bar plume are increasing due to in-situ advection of river water from the inflow, while offshore flows deplete local concentrations by advecting tracer-free water from the open lake.

While diffusion neatly balances convection offshore of the T_{md} , providing little net concentration change in front of the advancing thermal bar, the fluctuating nature of diffusion inshore of the T_{md} leads to a dominance of convection there. The rapid local variation in diffusion is caused by a fluctuating gradient in the horizontal tracer profile in this region (figure 3.5(b)), which in turn is caused by the oscillatory nature of vertical flows at this depth, as shown in figure 6.1. These vertical flows advect tracer preferentially into certain regions, causing diffusion to act erratically as it attempts to smooth the tracer profile.

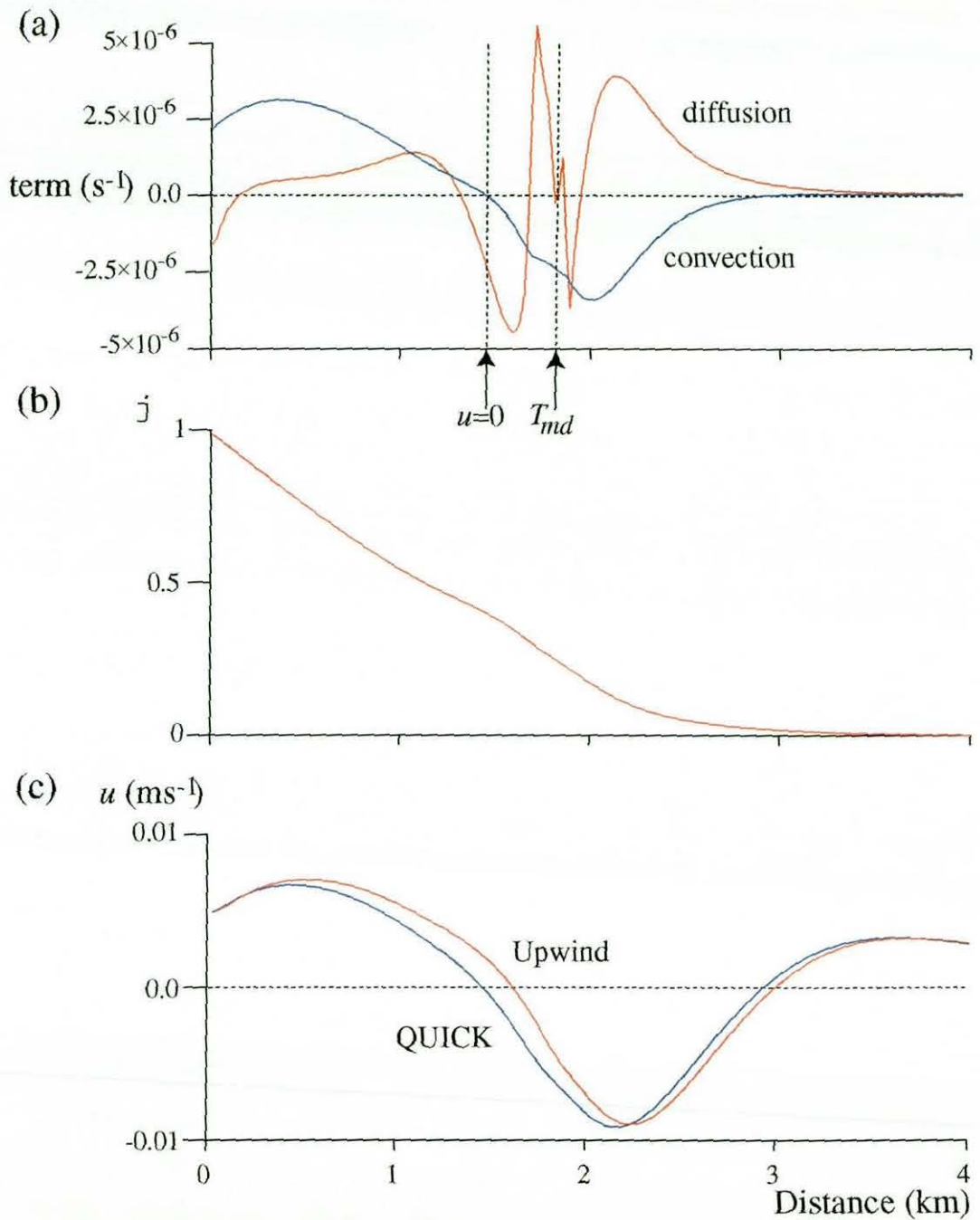


Figure 3.5: Horizontal profiles at 25 m depth after 2 days of simulation: (a) horizontal tracer convection ($-u \frac{\partial \varphi}{\partial x}$) and diffusion ($\frac{\partial}{\partial x} (K_h \frac{\partial \varphi}{\partial x})$) terms in simulation *T9*, (b) tracer concentration in simulation *T9*, (c) horizontal velocity in simulations *T9* and *T9UP*.

The fine balance of convection and diffusion in front of the thermal bar is responsible for the significant differences between simulations *T9* and *T9UP* which are noted in figure 3.5(c). Using Upwind differencing instead of QUICK increases the numerical

diffusion of heat in this region, shifting the transport balance towards positive change, which leads to increased heat transfer and therefore a quickened propagation of the thermal bar. This explains why the horizontal stagnation point in case *T9UP* is furthest from the river inflow after 2 days.

3.4.2 Kamloops Lake

Figure 3.6(a) shows that the balance between convection and diffusion is different in the Kamloops Lake simulation *KQ*, which is studied here to enable a comparison between the two different lake simulations. A different distribution of riverine tracer near the inflow gives a much smoother diffusion profile, which now acts in opposition to convection everywhere and is significantly stronger than convection offshore of the T_{md} .

The diffusion profile of simulation *KQ* is much less variable than that of *T9* because the tracer profile follows a steady transition from increasing to decreasing curvature away from the river inflow (figure 3.6(b)). In addition, diffusion opposes convection inshore of the horizontal stagnation point because the horizontal gradient of tracer grows in magnitude away from the inflow instead of shrinking as it does in simulation *T9*, a consequence of the 'flatter' tracer distribution in the near-shore region (compare figures 3.5(b) and 3.6(b)).

The weaker convection and smoother (and more dominant) diffusion of simulation *KQ* shows that the benefits to be gained from more sophisticated convection schemes are severely limited in the Kamloops Lake scenario (figure 3.6(c)). As the modelled diffusion of heat away from the river inflow is clearly responsible for the propagation of the thermal bar in simulation *KQ*, it can be seen that the QUICK scheme's removal of a small amount of numerical diffusion only slows the propagation of the thermal bar by a tiny amount. The simpler and more economical Upwind scheme is therefore adopted in the Kamloops Lake simulation.

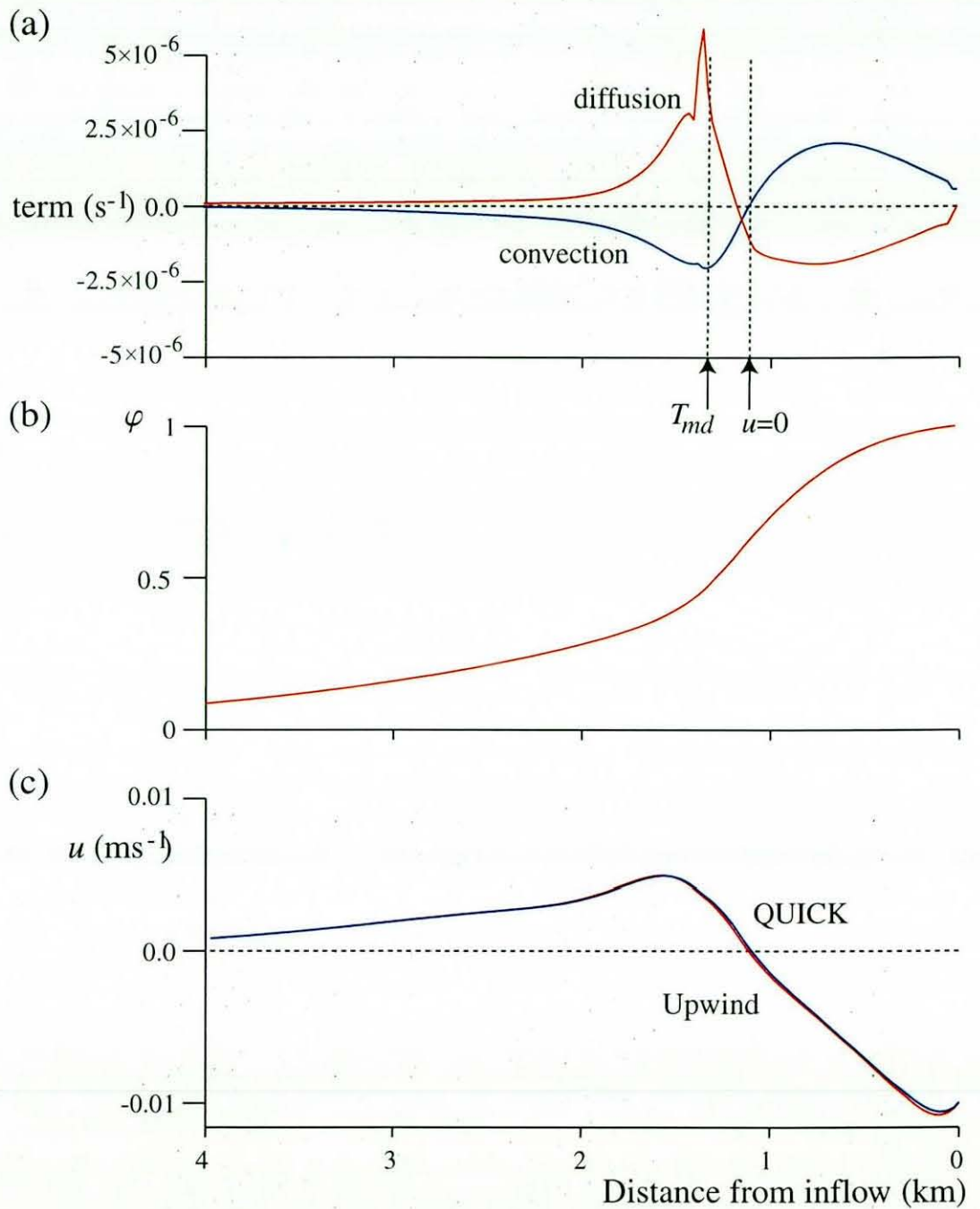


Figure 3.6: Horizontal profiles at 7.5 m depth after 12 days of simulation: (a) horizontal tracer convection ($-u \frac{\partial \varphi}{\partial x}$) and diffusion ($\frac{\partial}{\partial x} (K_h \frac{\partial \varphi}{\partial x})$) terms in simulation KQ , (b) tracer concentration in simulation KQ , (c) horizontal velocity in simulations K and KQ .

Chapter 4

Modelling of Turbulence

This chapter is intended to describe the chosen representation of subgrid turbulent flow and to provide a short introduction to some of the theoretical background underpinning turbulence modelling in limnology. Although the approach used here is not the most sophisticated available, it is shown empirically that the most appropriate formulation is adopted.

In contrast to laminar motion, turbulent flow is characterised by a swirling, tortuous fluid motion in which any chosen particle seems to take a random path. Important characteristics of turbulence are the irregular velocity fluctuations at any given point in space and the great variation in the scale of the motions involved. In a fully-developed turbulent flow motion on all scales is present, from the largest on the scale of the flow region to the smallest scale of motion allowed by dissipative processes (Landahl & Mollo-Christenson 1986). For low-viscosity fluids like water the vast majority of real environmental fluid flows are turbulent in nature.

In order to visualise a turbulent flow with a full spectrum of scales, the concept of a turbulent eddy is often introduced. A turbulent eddy is a local swirling motion whose characteristic length scale is the local turbulence scale, and these eddies overlap in space such that the smaller ones are superimposed on the larger (Wilcox 1993).

A statistical approach to turbulence modelling is adopted here whereby fluctuating quantities are averaged and the net properties of the motion examined. Of particular interest is the transport of fluid properties across the flow direction, since these fluctuations and eddies provide a very efficient means of dispersion. Indeed, it will be shown

in the rest of this chapter that when viewed over a 'large' time-scale compared to that of the eddying (here assumed to be one model time-step), the net effect of turbulence is an increase in the diffusion of fluid properties.

4.1 The Eddy-Viscosity

A time-averaging process is applied to the Navier-Stokes equations in order to obtain the laws of motion for 'mean' turbulent properties of the flow. A differential form of the equation of motion for an incompressible fluid may be obtained by integrating the momentum conservation equation over a surface and applying Gauss' theorem (Hirsch 1988):

$$\rho \frac{\partial \mathbf{u}}{\partial t} + \nabla \cdot (\rho \mathbf{u} \otimes \mathbf{u} + p \hat{\mathbf{I}} - \hat{\boldsymbol{\tau}}) = \mathbf{F} \quad (4.1)$$

where \mathbf{F} represents external forcing and $\hat{\mathbf{I}}$ is the unit tensor. $\hat{\boldsymbol{\tau}}$ is the viscous shear stress tensor, which is the product of the mean strain-rate tensor and an eddy-viscosity, μ^V , which represents the molecular diffusion rate of momentum:

$$\tau_{ij} = \mu^V \left[\left(\frac{\partial u_i}{\partial x_j} + \frac{\partial u_j}{\partial x_i} \right) - \frac{2}{3} (\nabla \cdot \mathbf{u}) \delta_{ij} \right] \quad \text{for } i = 1, 2, 3. \quad (4.2)$$

In order to derive the equivalent governing equations for mean turbulent quantities, a time-averaging process is introduced so that any scalar Φ is represented as

$$\Phi = \bar{\Phi} + \Phi' \quad (4.3)$$

where $\bar{\Phi}$ is the mean value of Φ over time Δt and Φ' represents the fluctuation from this mean. Applying this process to the equation of motion (4.1) we arrive at the Reynolds-averaged incompressible Navier-Stokes equations:

$$\rho \frac{\partial \bar{\mathbf{u}}}{\partial t} + \nabla \cdot (\rho \bar{\mathbf{u}} \otimes \bar{\mathbf{u}} + \bar{p} \hat{\mathbf{I}} - \hat{\boldsymbol{\tau}}^V - \hat{\boldsymbol{\tau}}^R) = \bar{\mathbf{F}} \quad (4.4)$$

where $\hat{\boldsymbol{\tau}}^V$ is the averaged version of the viscous shear stress tensor given in (4.2). The only new term generated by this averaging process is therefore $\hat{\boldsymbol{\tau}}^R$, the Reynolds stress tensor, which has components given by:

$$\tau_{ij}^R = -\rho \overline{u_i' u_j'} \quad (4.5)$$

Thus we can conclude that the only effect of averaging the Navier-Stokes equations over time is an extra shear stress term due to the fluctuations of the turbulent velocity. Unfortunately the problem is no longer closed as the symmetric tensor $\hat{\tau}^R$ introduces 6 new independent scalar unknowns, so that the use of these time-averaged equations requires a model for the new terms. From now on all overbars are omitted, and all quantities are regarded as averaged over the time-step Δt .

The simplest of all turbulence models are known as algebraic models, since they employ simple algebraic representations of relevant physics to calculate the components of the Reynolds stress tensor. In section 4.5 some results are presented which rule out the use of more sophisticated turbulence closure models (which introduce extra differential equations to tie up these remaining unknown quantities) for the purposes of this study. Boussinesq (1877) used an analogy between molecular mixing, governed by (4.1), and turbulent mixing, governed in averaged form by (4.4), to propose that the Reynolds stress tensor be expressed in a similar way to the viscous shear stress tensor (4.2). Thus we write $\hat{\tau}^R$ as the product of a general eddy viscosity, μ^R , and the mean strain-rate tensor. Grouping $\hat{\tau}^V$ and $\hat{\tau}^R$ into one term, the final eddy-viscosity becomes

$$\mu = \mu^V + \mu^R. \quad (4.6)$$

This implies that the sole effect of turbulence when averaged over a discrete time-step is equivalent to an increase of diffusion in the property of interest.

Some commonly-used turbulence models in computational fluid dynamics, such as the k - ϵ formulation, link eddy viscosities to gradients of velocity in each coordinate direction. However, on a grid-scale which is large compared to turbulent eddies, such as ours, a constant value or simple formulation for the eddy viscosity based on gradients of temperature or density is sufficient.

Note that in this study turbulent diffusion of momentum and scalar fluid properties are assumed to be the same, equivalent to setting $A_h = K_h$ and $A_v = K_v$, which seems to give good results in large-scale lacustrine modelling, e.g Jones & Marshall (1993), Walker & Watts (1995). This is justified as turbulent mixing is much more important than molecular diffusion ($\mu^R \gg \mu^V$) on the grid scales used here.

4.2 The Horizontal Eddy Viscosity

In practice the eddy viscosities are multipurpose in a numerical model, as they are used partly as a tool to smooth spurious noise in the model solution which is known to result from the use of coarse grids (Blackman & Tukey 1959). The choice of eddy viscosities is thus determined by a balance between modelling the turbulent diffusion as accurately as possible and providing a stable solution to the governing equations. Horizontal eddy viscosities are simply assumed to take a constant value here, which is usually the case in large-scale modelling of this nature. The precise values of $A_h = 5 \text{ m}^2\text{s}^{-1}$ and $2.5 \text{ m}^2\text{s}^{-1}$ for Lake Baikal and Kamloops Lake respectively were chosen by numerical testing, as they are the smallest values which allow a stable solution to the governing equations with a reasonable time-step. This is well within the range of expected values, as typical inferred values for A_h in lakes have been found to be of order 0.1 to $10 \text{ m}^2\text{s}^{-1}$ (Hamblin 1971, Cheng et al. 1976), although larger values have been used in similar models in the literature.

The problems associated with spurious solution noise and the effects of increasing A_h are illustrated in figure 4.1, where results are compared from simulations *T9A2.5*, *T9*, and *T9A7.5*, which are variants of the Lake Baikal simulation *T9* with $A_h = 2.5$, 5, and $7.5 \text{ m}^2\text{s}^{-1}$ respectively. Using an eddy viscosity which is too low results in an unpredictable flow-field containing many areas of spurious vertical motion (figure 4.1(a)). These plumes arise when small oscillations in the velocity solution grow through the localised buoyancy forcing which results from a small vertical transport of heat.

Increasing the eddy viscosity damps these initial motions and thus suppresses their heat transfer, preventing the growth of small errors and allowing the large-scale dynamics to dominate (figure 4.1(b)). Raising A_h farther than is strictly necessary to provide a stable solution results in a similar circulation but it can be seen that the smoothing effect weakens horizontal gradients and results in a wider and slightly weaker downwelling (figure 4.1(c)). The best choice therefore appears to be $A_h = 5 \text{ m}^2\text{s}^{-1}$, which gives a stable solution with the minimum possible damping of the flow-field.

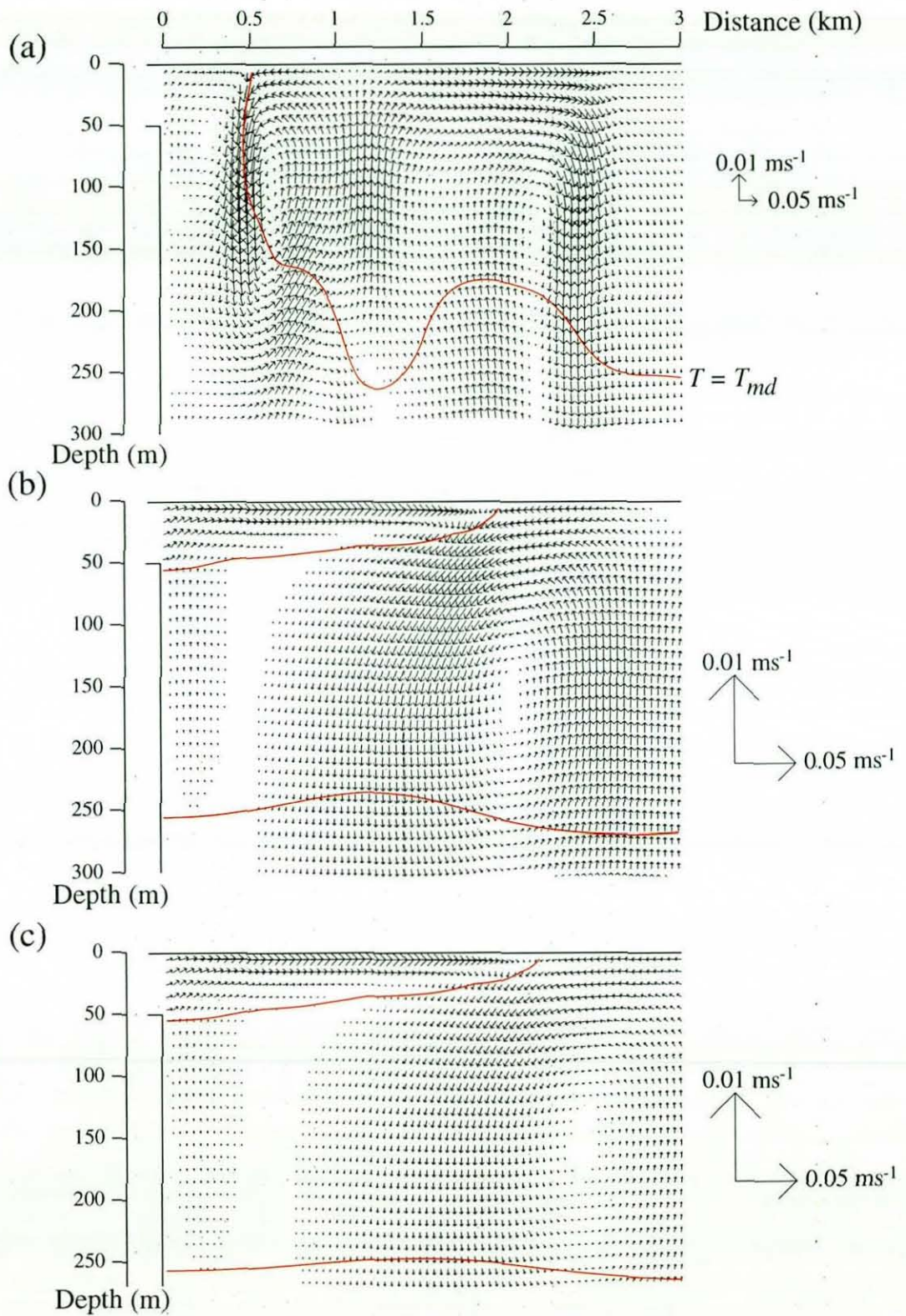


Figure 4.1: Velocity vectors and $T = T_{md}$ line for several cases of simulation $T9$ after 2 days illustrating the effect of varying A_h : (a) $T9A2.5$, (b) $T9$, (c) $T9A7.5$.

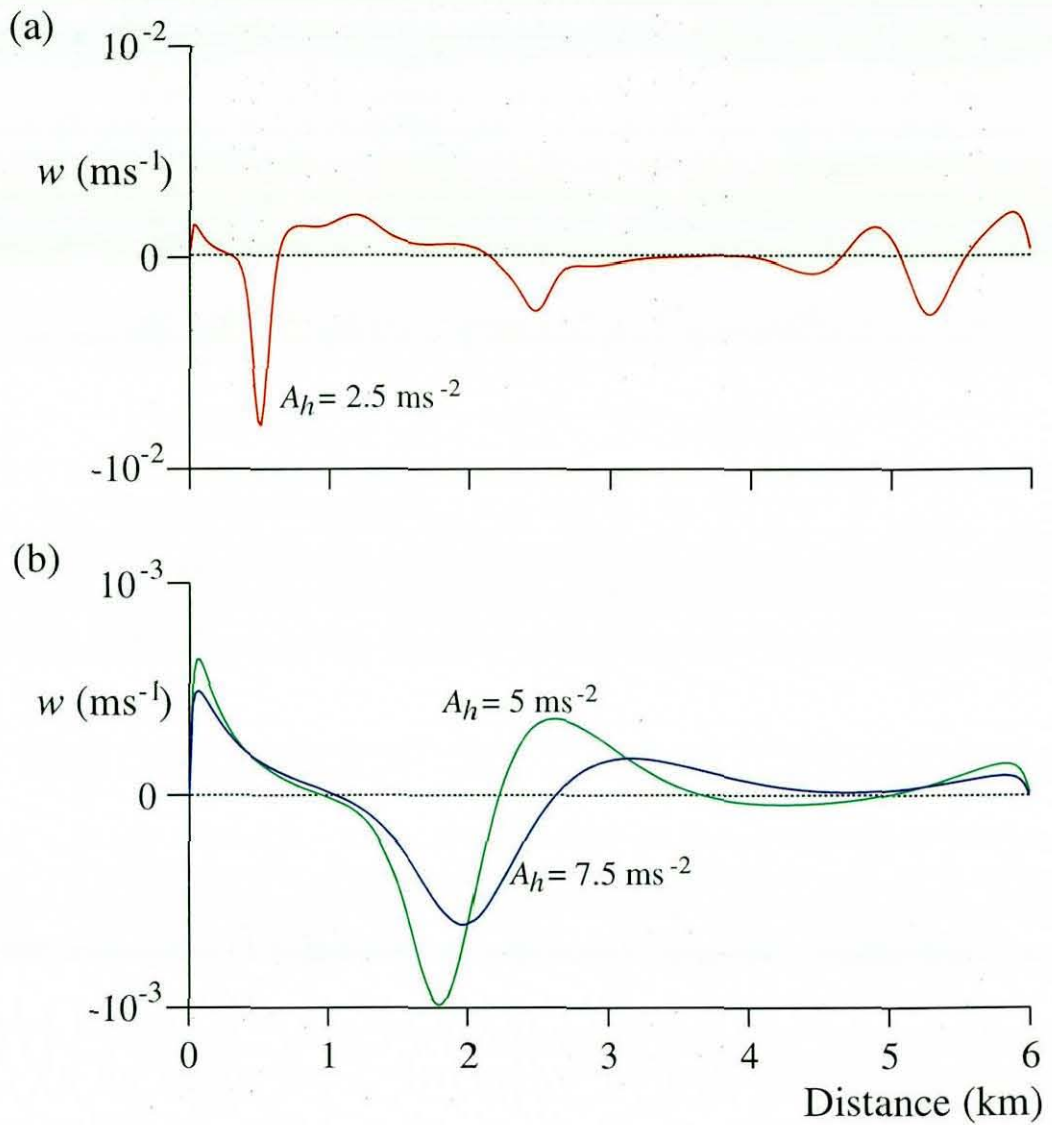


Figure 4.2: Vertical velocity at 25 m depth for several cases of simulation $T9$ after 2 days illustrating the effect of varying A_h : (a) $T9A2.5$, (b) $T9$, (c) $T9A7.5$.

A horizontal profile of vertical velocity in case $T9A2.5$ (figure 4.2(a)) clearly shows the spurious oscillations in the solution and also illustrates the sharp spatial variation in vertical velocity which results from the reduced diffusive transfer of information between adjacent grid nodes. While it is impossible to definitively state that this erratic velocity profile is incorrect, the presence of seemingly random fluctuations in the flow field certainly brings the use of this A_h value into question. In contrast, a profile from simulation $T9$ (figure 4.2(b)) show a smoothly-varying profile with few oscillations and a Gaussian velocity profile within the thermal bar plume. Increasing the horizontal eddy

viscosity in case *T9A7.5* is again seen to weaken the horizontal gradients governing the thermal bar plume, resulting in a slower descending flow spread over a wider area (figure 4.2(b)).

Vertical eddy viscosities are known to be much smaller and more variable, as they are controlled by several physical mechanisms which must be accurately modelled before realistic vertical temperature profiles can be achieved. The vertical eddy viscosity is therefore allowed to vary in space, as described in the next section.

4.3 Parameterisation of Vertical Mixing in Lakes

Due to the simplicity underlying the whole eddy-viscosity approach, only a basic formulation of the relevant processes is required to produce values of A_v such that the mixing in the model generates a reasonable thermal profile. On the scale of importance here, the first step is to quantify the reduction of vertical mixing caused by the presence of stable stratification in a lake.

If a body of fluid is stably stratified (i.e. density increases with depth) then vertical motion is suppressed, since any parcel of fluid within that system will feel a restoring buoyancy force if perturbed vertically from its initial position. The vertical eddy-viscosity should therefore be sensitive to stable stratification, as it will limit small-scale vertical motions. The *Brunt-Väisälä frequency*, N , is a very useful parameter in quantifying the existence and strength of stable stratification.

The following formulation for N^2 , the stability, is used in the model (Imboden & Wüest 1995):

$$N^2 = g \left[\alpha \left(\frac{\partial T}{\partial z} - \Gamma \right) - \beta \frac{\partial S}{\partial z} \right] \quad (4.7)$$

where α and β are the coefficients of thermal expansion and haline contraction of water, given by:

$$\alpha = -\frac{1}{\rho} \left(\frac{\partial \rho}{\partial T} \right)_{p,S} \quad (4.8)$$

$$\beta = \frac{1}{\rho} \left(\frac{\partial \rho}{\partial S} \right)_{p,T} \quad (4.9)$$

and Γ is the the adiabatic temperature gradient, defined as:

$$\Gamma = -\frac{g\alpha}{c_p}(T + 273.15). \quad (4.10)$$

Here the vertical density gradient has been formulated in terms of salinity and temperature gradients, as detailed by Gill (1982). The inclusion of saline effects on the T_{md} and density in general then avoids any misrepresentation of stability when temperature gradients are close to the adiabatic rate, a hazard which was highlighted by Chen & Millero (1977).

N is essentially the frequency of internal waves in a fluid, which is real only in stable situations and increases with stronger stratification. If $\frac{\partial \rho}{\partial z} < 0$ (stable stratification) then oscillatory behaviour is permitted whereby small vertical perturbations generate wavelike motion and vertical mixing is suppressed. If $\frac{\partial \rho}{\partial z} > 0$ (unstable stratification) then small perturbations will grow exponentially with time and vertical convection is initiated. Thus, since $N^2 \propto -\frac{\partial \rho}{\partial z}$, we obtain a stability criterion:

$$N^2 > 0 \Rightarrow \text{stable stratification}$$

$$N^2 < 0 \Rightarrow \text{unstable stratification}$$

Despite the effects of density stratification, the presence of shear flow with strong vertical gradients of horizontal velocity can induce vertical turbulent mixing even in a strongly stratified layer. Some consideration of the vertical gradient of velocity is therefore desirable when expressing the vertical eddy viscosity. Following the discussion of Wetzel (1983), formation of the Kelvin-Helmholtz instability in a two-layer stratified fluid with shear in the flow parallel to the interface is now considered, as shown in figure 4.3.

At low velocities the flow is laminar and little mixing takes place between the two layers. However as shear increases, any perturbations on the density interface will overcome buoyancy forces and grow in amplitude, eventually breaking into vortices and mixing the two layers together thoroughly as the flow becomes fully turbulent. Thus vertical mixing can be generated by this Kelvin-Helmholtz mechanism whereby there is stability up to a critical shear rate (for a given density gradient) and instability beyond it (Mortimer 1974). This effect is quantified by the *gradient Richardson number* (Smith

1975):

$$Ri = \frac{N^2}{\left(\frac{\partial u}{\partial z}\right)^2 + \left(\frac{\partial v}{\partial z}\right)^2} \quad (4.11)$$

which hereafter will simply be referred to as the Richardson number.

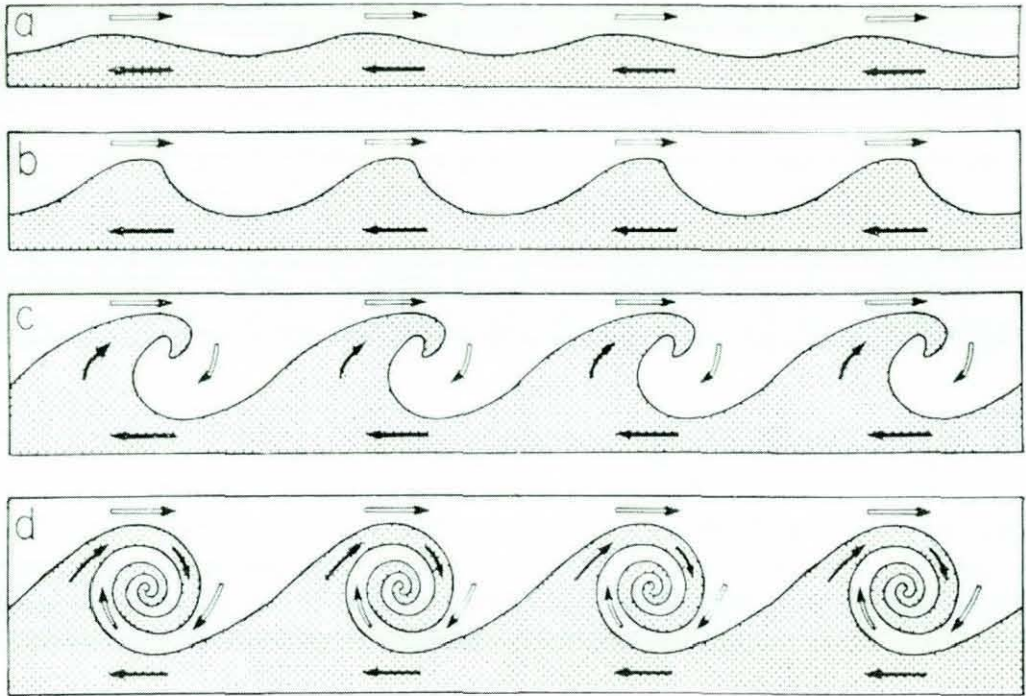


Figure 4.3: Increasing the strength of shear over a stable density interface in a 2-layer system. Eventually buoyancy forces are overcome and vertical mixing is induced with the onset of the Kelvin-Helmholtz instability. (after Mortimer (1974))

From the ratio of stability suppression to shear generation of turbulence (4.11) it is possible to deduce that the onset of turbulent vertical mixing is energetically possible once the Richardson number becomes less than 1. However in reality dynamical effects require that Ri be considerably less than unity for small perturbations to grow into turbulent vortices which persist against the density gradient in a stably-stratified shear flow. Miles (1961) and Howard (1961) both proved that the Kelvin-Helmholtz instability is not possible for $Ri > 0.25$ and the fluid is then stable as before.

4.4 Models of Vertical Eddy Viscosity

Algebraic models of these processes have been in use for some time, of which a good discussion may be found in Henderson-Sellers (1984). Generally the eddy viscosity for unstable conditions is nominated a constant value, and then a formulation for mixing in stable regions using N^2 or Ri is attached for evaluation in the relevant areas of the domain. A comparison of models with and without a representation of shear effects is outlined below, and a formulation is chosen after a discussion of results from a test simulation.

Vertical derivatives of temperature evaluated in the hypolimnion are often seen to be very small, and this is liable to give rather small values of N^2 when stable. This produces large values of eddy viscosity under most models (as usually $A_v^{-1} \propto N^2$) in a region where the effects of turbulent mixing should theoretically be smallest. The solution procedure adopted also seems to respond to these high values of viscosity by producing anomalous flows around the model bottom. These problems are avoided by choosing a 'cut-off' depth, \bar{d} , near to the lake bed and decreasing the eddy viscosity for $d > \bar{d}$ exponentially from the value at this depth, $A_v|_{\bar{d}}$, towards the reference molecular viscosity $\nu_{ref} = 10^{-6} \text{ m}^2\text{s}^{-1}$. A nominal extinction coefficient for this decay is chosen to be -0.025 m^{-1} , although numerical testing shows that the exact value makes very little difference to the final predicted distributions of scalar quantities. Note also that as long as \bar{d} is far enough below the thermocline, results are not greatly affected by its exact depth and thus it is chosen to be the deepest value which suppresses the spurious flows at the bottom of the domain.

Model 1: A commonly-used formulation for A_v in a stably-stratified fluid which includes representation of all these effects through the Richardson number is given by Pacanowsky & Philander (1981):

$$A_v = \nu_b + \frac{\nu_0}{(1 + rRi)^s} \quad (4.12)$$

where ν_b is the background viscosity for stable conditions, ν_0 is the viscosity for unstable

conditions, and r and s are constants. The model for vertical eddy-viscosity is:

$$A_v = \begin{cases} \begin{cases} \nu_0 & Ri \leq 0 \\ \nu_b + \frac{\nu_0}{(1+rRi)^s} & Ri > 0 \end{cases} & d \leq \bar{d} \\ \nu_{ref} + A_v|_{\bar{d}} \exp[-0.025(d - \bar{d})] & d > \bar{d} \end{cases} \quad (4.13)$$

Model 2 For comparative purposes an alternative formulation, adapted from the relation of Welander (1968), is tested here. As before the viscosity for unstable conditions is given as a constant, but here the vertical viscosity for stable conditions contains no expression of the shear effects as it is based solely on the Brunt-Väisälä frequency:

$$A_v = \nu_b + r(N^2)^{-s} \quad (4.14)$$

where r and s are again constants. This gives the following formulation:

$$A_v = \begin{cases} \begin{cases} \nu_0 & N^2 \leq N_{min} \\ \nu_b + r(N^2)^{-s} & N^2 > N_{min} \end{cases} & d \leq \bar{d} \\ \nu_{ref} + A_v|_{\bar{d}} \exp[-0.025(d - \bar{d})] & d > \bar{d} \end{cases} \quad (4.15)$$

where a minimum value for the stability has been introduced in order to avoid large values of A_v for weakly stable conditions. To provide a continuous transition between states N_{min} should satisfy the following formula:

$$N_{min} = \left(\frac{r}{\nu_0 - \nu_b} \right)^{\frac{1}{s}} \quad (4.16)$$

The constants r and s in this model are usually chosen so that the results of the simulation of vertical mixing can be validated against measured data of other variables. For example a series of vertical temperature profiles (BK), the velocity of resulting flows (Pacanowsky & Philander 1981), or even explicit diffusion measurements from tracer studies (Quay et al. (1980), Michalsky & Lemmin (1995)) can be utilised to indicate appropriate values. This is impossible in the case of the riverine thermal bar as even if detailed data were available then it would be erroneous to suppose that the characteristics of the real lake could quantify the amount of vertical mixing in a model

with no surface flux of heat or momentum. Instead these constants are chosen to model relative diffusion rates between stable and unstable conditions and to produce a realistic temperature profile after a long time of simulation, since the exact positioning of near-surface source terms should make little difference to the final temperature solution.

Initially a value of viscosity for unstable conditions, ν_0 , and a value of minimum viscosity for stable conditions, ν_b , are chosen with reference to similar modelling in the literature (particularly BK). Then with a given profile of Ri or N values for r and s are selected to significantly reduce vertical mixing during periods of strong stratification but ensure as closely as possible a reasonable transition between stable and unstable values. The whole process is repeated with different choices of viscosities and r and s until the resulting temperature distributions seem as realistic as possible after a nominal period of simulation.

4.5 Numerical Testing of Models

This section presents the results of an empirical study which shows that the Brunt-Väisälä frequency is the best quantity on which to base our model for the vertical eddy viscosity. Although all testing shown is carried out on the deep-lake Baikal section, the same procedure was followed in the Kamloops Lake model, which requires a different set of parameters to produce similar temperature profiles to those reported by Carmack (1979).

The Richardson number formulation initially appears to be most suitable for our purposes as it resolves both the stability and shear of the fluid in question. Testing of both parameterisations is carried out on simulation *T9* with the values shown in table 4.1 adopted in the turbulence models.

Results of these experiments in the centre of the domain after 20 days of simulation (long after the lake has become stable in the upper region and the thermal bar has disappeared) are presented in figures 4.4 to 4.7, on which the following discussion is based. Predicted temperature profiles in the centre of the lake (compare figures 4.4(a) and 4.6(a)) are similar in shape but it is clear that temperatures in the stable region

Parameter	Baikal Model 1 -	Baikal Model 2 -	Kamloops Model
	Richardson number	Brunt-Väisälä frequency	
ν_0	$2 \times 10^{-2} \text{ m}^2\text{s}^{-1}$	$2 \times 10^{-2} \text{ m}^2\text{s}^{-1}$	$2 \times 10^{-2} \text{ m}^2\text{s}^{-1}$
ν_b	$5 \times 10^{-4} \text{ m}^2\text{s}^{-1}$	$5 \times 10^{-4} \text{ m}^2\text{s}^{-1}$	$4 \times 10^{-4} \text{ m}^2\text{s}^{-1}$
r	5	6×10^{-7}	6×10^{-7}
s	2	0.5	0.5
N_{min}	—	$9.46 \times 10^{-10} \text{ s}^{-2}$	$6.51 \times 10^{-10} \text{ s}^{-2}$
\bar{d}	900 m	900 m	120 m

Table 4.1: Values of vertical turbulence parameters in testing and final models

of model 1 ($d \lesssim 430 \text{ m}$) remain closer to the T_{md} line than in model 2. This implies that in model 1 there must be a drastic decrease in the vertical diffusivity after stable stratification is attained near the surface, as the viscosity for unstable conditions is identical in the two models. Further examination of the eddy viscosity in figure 4.4(b) reveals that as soon as the fluid becomes stable (at $N^2 > 0$ here), model 1 reduces A_v directly to its background level ν_b without any intermediate region or regard for the degree of stratification or shear.

Inspection of the Richardson number in figure 4.4(d) and (e) also weakens our confidence in this model as it can be seen to fluctuate wildly over several orders of magnitude within the space of a few metres in the vertical direction. More importantly it only predicts turbulent mixing in the stable layer (i.e. $0 < Ri < 0.25$) for a very small proportion of the domain, as Ri is usually evaluated to be orders of magnitude larger than 0.25. By plotting the components of the Richardson number in figures 4.4(c) and (f) it can be noted that the cause of this behaviour is that when evaluated numerically, the shear term is generally many orders of magnitude smaller than N^2 , which results in the large values of Ri which reduce A_v sharply to the background level ν_b .

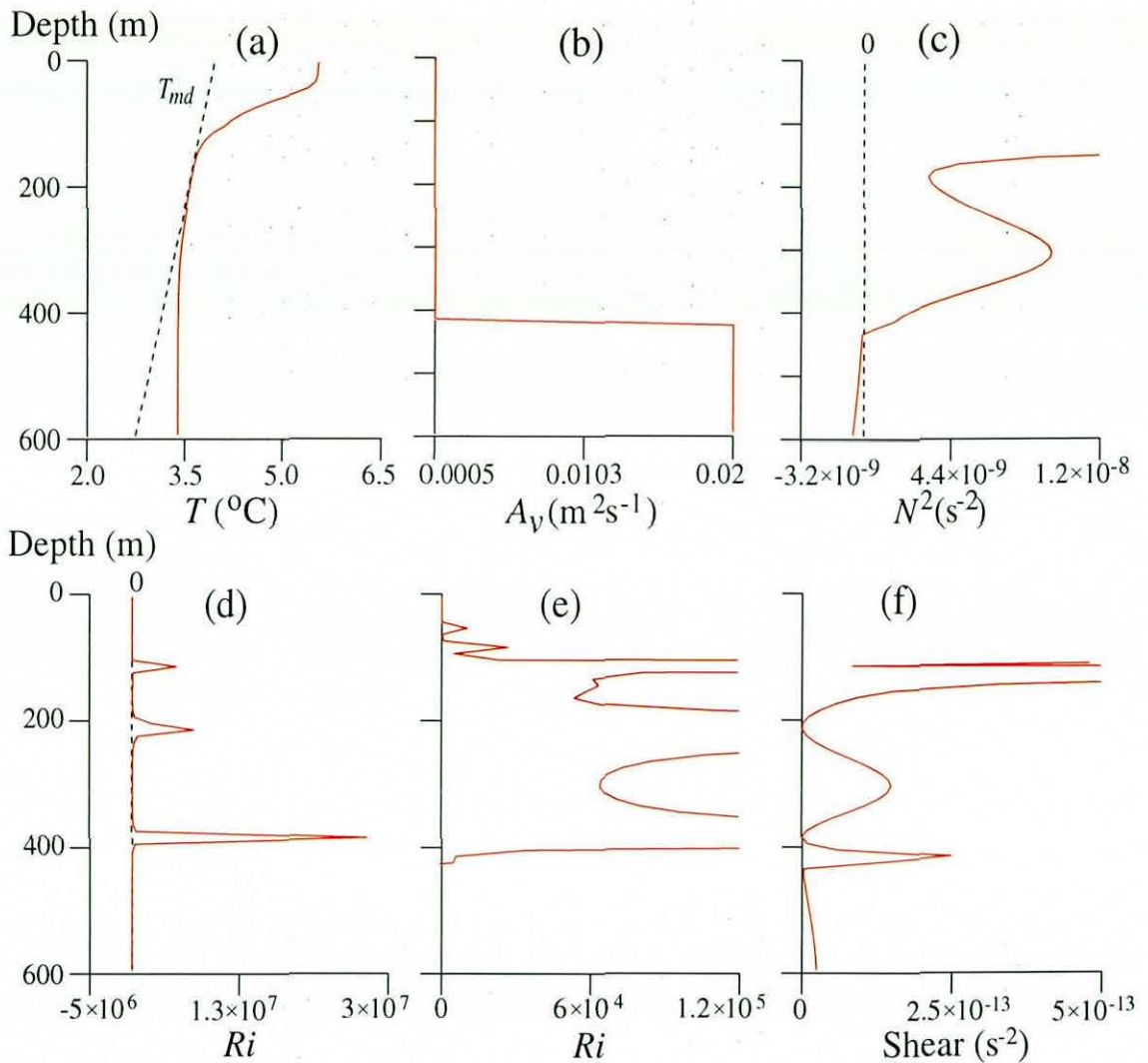


Figure 4.4: Properties of simulation *T9* with model 1 in the centre of the lake after 20 days: (a) temperature, (b) vertical eddy viscosity, (c) stability, (d) Richardson number, (e) detail of Richardson number, (f) shear term $\left(\frac{\partial u}{\partial z}\right)^2 + \left(\frac{\partial v}{\partial z}\right)^2$.

Attempts to adjust the formulation (4.12) by choosing r and s so that mixing is allowed at higher Richardson numbers have all been unsuccessful as numerical instability is initiated by the consequential magnification of the large variations in Ri . Here it is useful to define the critical value of Ri , Ri_c (physically 0.25), where stratification overcomes shear in a stable region. Several simulations were made which scaled the effect of the Richardson number until Ri_c was between 10 and 100 but all produced unsatisfactory results. The large variation of the Richardson number in a small space produces regions of rapid vertical mixing adjacent to areas of strong stratification and

suppressed vertical mixing, resulting in a step-like temperature profile as seen in figure 4.5(a). This invalidates any attempt to apply the formulation (4.12) to our turbulence model.

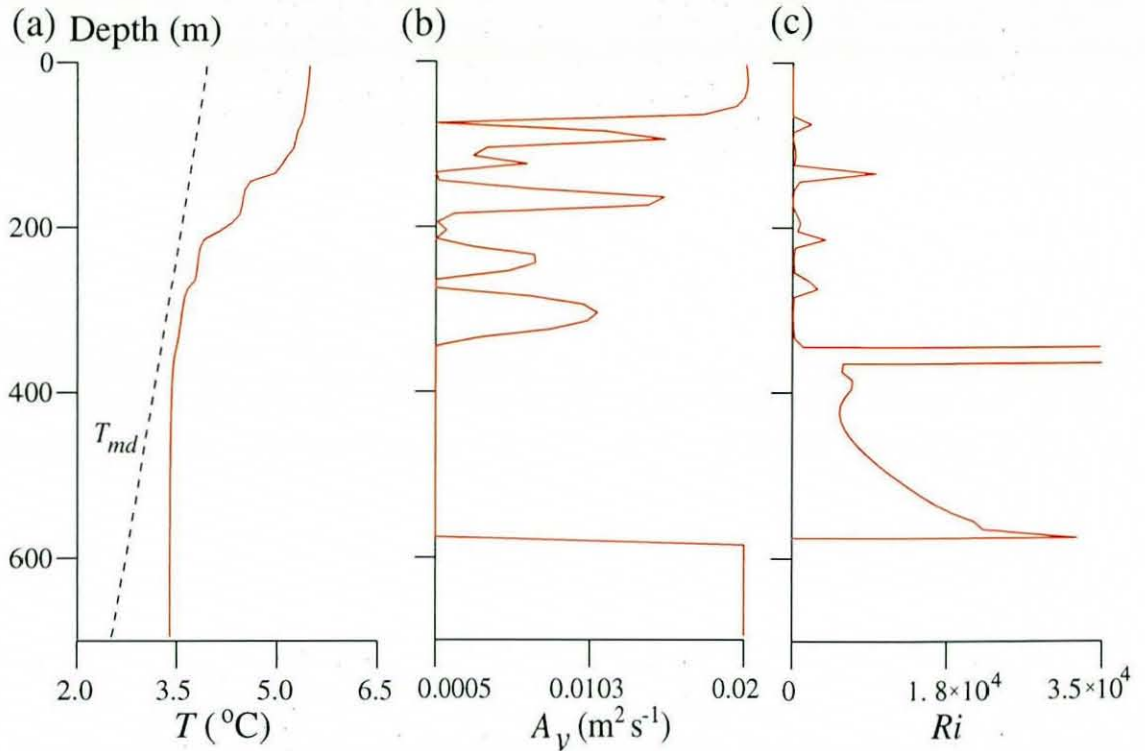


Figure 4.5: Properties of simulation $T9$ with model 1 in the centre of the lake after 20 days where r,s are chosen to scale Ri_c to match predicted Ri . Here $r = 7.18 \times 10^{-4}$ and $s = 10$. (a) temperature, (b) eddy viscosity, (c) Richardson number.

The previous observations on the Richardson number also provide good reasoning for the abandonment of turbulence closure models, which are superior to the algebraic models presented here because they avoid use of the Boussinesq eddy-viscosity approximation by directly estimating the components of the Reynolds stress tensor (4.5). Unfortunately, the closure models which are usually adopted in oceanography, such as the models first introduced into mainstream oceanographical literature by Mellor (1973), tend to predict a mixing coefficient which is a function of the local Richardson number (Mellor & Durbin 1975) and rarely allow any mixing at all for Ri greater than approximately 0.25 (Archer 1995).

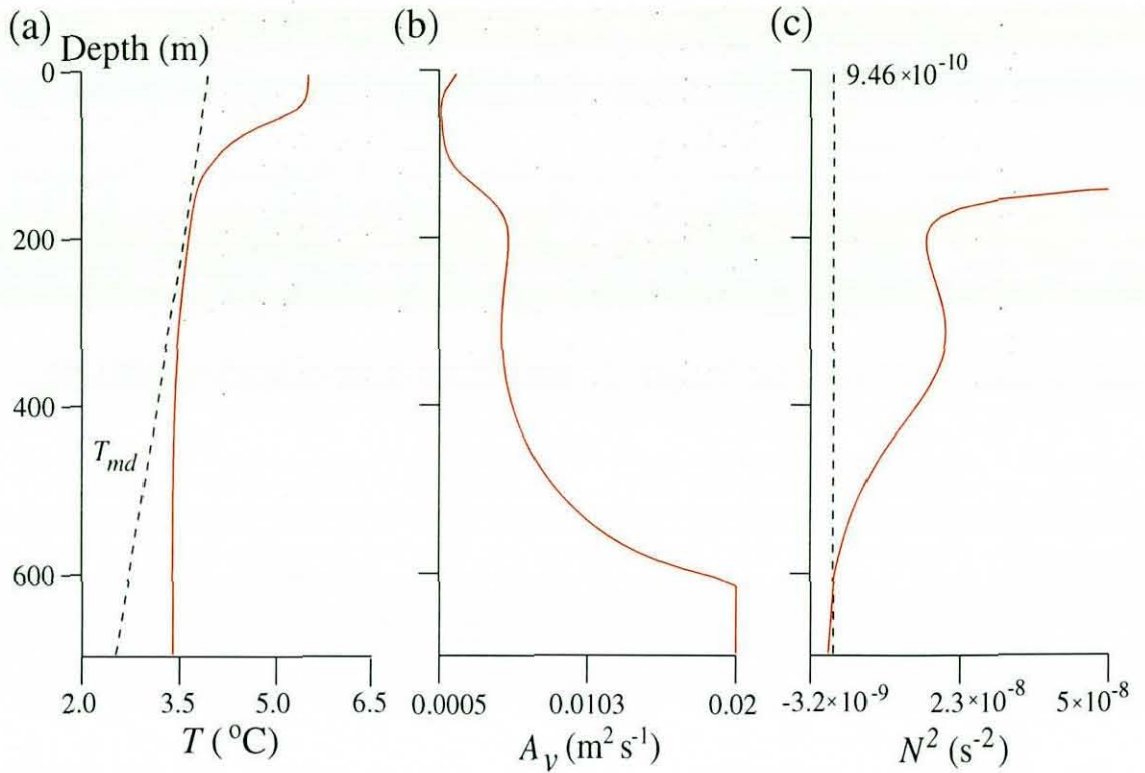


Figure 4.6: Properties of simulation *T9* with model 2 in the centre of the lake after 20 days: (a) temperature profile, (b) vertical eddy viscosity, (c) stability.

Results of model 2 are considerably better, and the temperature profile after 20 days seems more reasonable as it is further from the line of T_{md} , implying that a vertical diffusion of heat which is reduced but still present is operating after the upper lake has become stable. Plotting the eddy viscosity in figure 4.6(b) illustrates the improvement over model 1; the transition from unstable viscosity to stability-reduced levels is much less abrupt and the background value ν_b is only approached in the region of relatively strong stable stratification. Comparison of the eddy viscosity and Brunt-Väisälä frequency (figures 4.6(b) and (c)) reveals the amount of physical information reaching A_v from N^2 which was lost in model 1.

The discussion so far has centred on the 20th day of simulation when the model is settling down to a stable situation, while the period of most interest to this study is when the thermal bar is traversing the lake in the very early stages of each model run. Contours from simulation *T9* after 2 days presented in figure 4.7 reveal that the

differences between the models are significant even at this early stage. Isolines of Ri (figure 4.7(a)) show that already it has taken large values, and only a tiny proportion of the stable region has $0 < Ri < 0.25$. The fluctuating behaviour and sudden growth of Ri is not as pronounced as later in the simulation because here the stable region is where the horizontal surface flows feed the thermal bar, so the shear terms in this region are evaluated to be of the same order of magnitude as the Brunt-Väisälä frequency. This plot shows that model 1 cannot be used to predict vertical mixing as the Richardson Number is so large everywhere while model 2 may be used as the the Brunt-Väisälä frequency quantifies the water-column stability in a smoothly-varying manner.

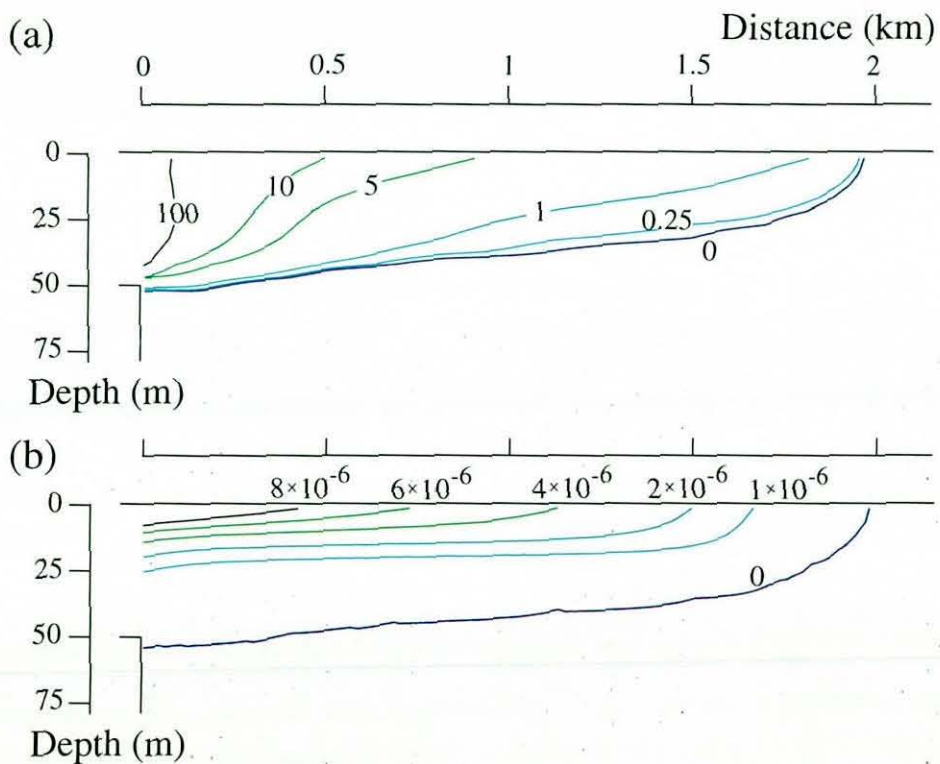


Figure 4.7: Results of simulation $T9$ with each model after 2 days: (a) Ri for model 1, (b) N^2 for model 2 (s^{-2}).

The above justification of model parameter choices is based upon the formulation of the eddy viscosity producing a realistic stable thermal profile after most of the motion has ceased. However in the case discussed the stability is purely a function of vertical gradients of temperature which is not the case throughout this work. Addition of salinity to a thermally-buoyant inflow will always tend to increase vertical diffusion by reducing

the overall stability as it causes a density increase near the surface as the river intrusion spreads across the lake.

For these reasons, simulation of a thermal bar with saline input has a quite different stable state to which it tends. Addition of salinity near the surface (in the absence of temperature variations) will tend to produce mixing until the whole column is marginally stably stratified, i.e. of almost uniform salinity. Thus when temperature and salinity are introduced simultaneously near the surface the stable state will be a combination of the two, where a stable profile of one constituent balances an unstable profile of the other so that overall the fluid is stable apart from double-diffusive instabilities.

The results presented in figure 4.8 are from simulation *T11S1*, which has a rather warm inflow and 1 mgkg^{-1} added to river salinity (see appendix A). It is clear that the stable temperature profile is balancing the unstable distribution of salinity so that the water as a whole is stable. Comparing the temperature profiles in figures 4.6 and 4.8 shows that much more diffusion has taken place in the upper half of the lake than previously as a result of destabilisation due to the surface saline input. The lake is also stable to a greater depth after the same simulation time due to the extra vertical diffusion of temperature and salinity. It can therefore be seen that the Brunt-Väisälä formulation behaves in a physically justifiable manner when under the influence of salinity gradients.

It must be concluded from this overall discussion that a model based on the Richardson number is unsuitable for the purposes of this study. Due to the way in which Ri is predicted on this grid, any attempt to link A_v to the shear of the flow-field simply results in the removal of any stability information from the vertical viscosity, which produces an excessively damped vertical transport. For this reason model 2 is adopted throughout this work and the eddy viscosity is assumed solely a function of the stability of the water column. This can have adverse effects on the accuracy of the predicted flow in stable regions with large velocity gradients but the general absence of strong kinematic forcing in these areas makes this model acceptable for the purposes of this study. It has been shown in BK that this particular model replicates very well the measured thermal profiles of a spring warming episode (which is mainly controlled by stability considerations) in the southern basin of Lake Baikal.

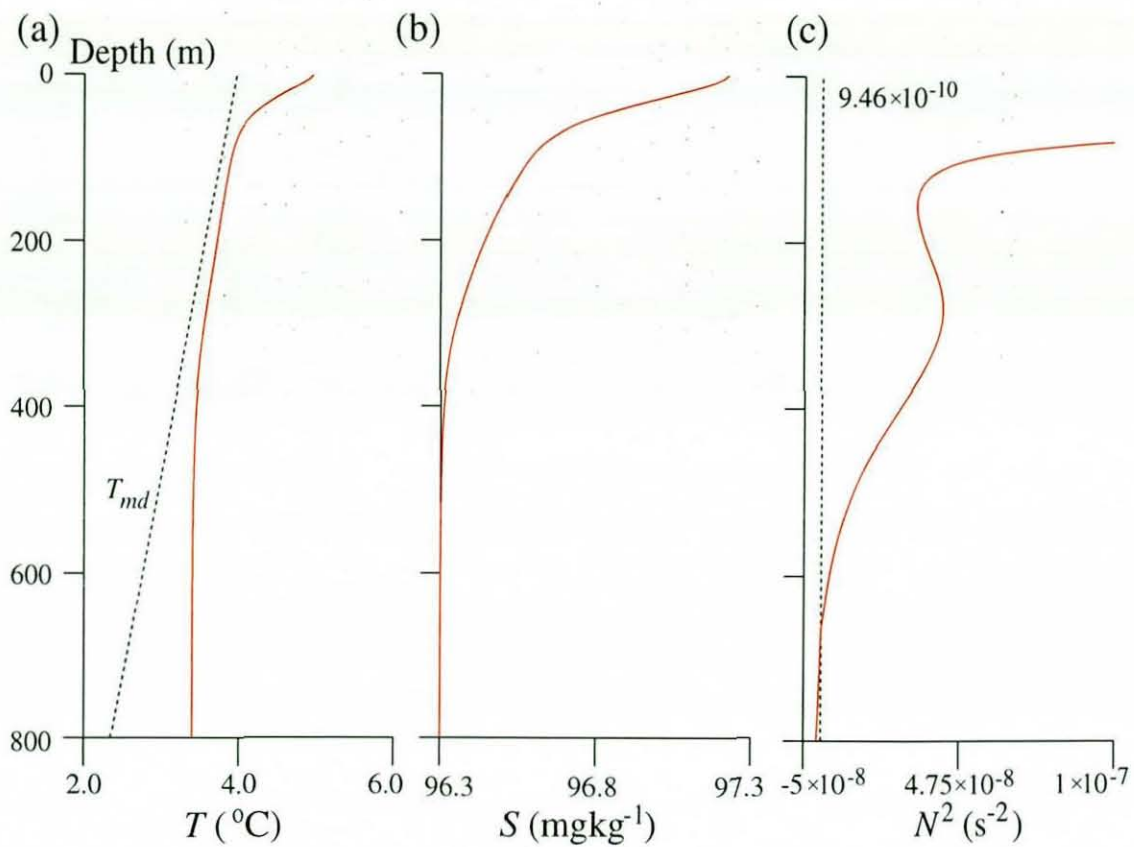


Figure 4.8: Properties of simulation *T11S1* with model 2 and 1 mgkg^{-1} salinity added to the inflow, in the centre of the lake after 20 days. (a) temperature profile, (b) salinity profile, (c) stability.

Chapter 5

Preliminary Results

To provide a basis for comparison of later deep-lake simulations, some preliminary results are presented here which are taken from simulations without a thermal bar. These results are used to assess the effects of the thermal bar on the dynamics of the river plume and the transport of riverine substances around a lake. Basic results from three control cases in which the dynamics are relatively well understood are described here.

5.1 Simulation *C*

Simulation *C* is intended to quantify the flow-field and transport which is due to the river velocity and initial conditions in the absence of any buoyancy effects. The river's temperature and salinity are therefore assumed to be equal to the lake, at $T_R = T_L = 3.4^\circ\text{C}$ and $S_R = S_L = 96.3 \text{ mgkg}^{-1}$. The absence of a density difference between river and lake therefore means that all flows are generated by the mass flux of $u_R = 0.005 \text{ ms}^{-1}$ at the inflow and outflow.

As there are no gradients of temperature or salinity in this simulation, the parameterisation of the vertical eddy viscosity is redundant here and the domain is neutrally stratified ($N^2 = 0$) throughout. A_v is therefore given a constant value, chosen from the range assigned to stable and unstable conditions in the other simulations. An intermediate value of $A_v = 0.01 \text{ m}^2\text{s}^{-1}$ is employed on the basis that neither a stable or unstable value has any physical justification. Numerical testing shows that in this simulation the exact value adopted from this range makes very little quantitative difference to the predicted motions on the time-scale of interest.

The simulation starts from the usual initial flow field, described in sections 2.2 and 2.3.2, with u_R fixed on the top 10 rows and zero velocity everywhere else. As the simulation proceeds, the flow along the surface is maintained by the mass fluxes at the top corners of the domain, with an extremely weak flow traversing the depths of the lake in the same direction (figure 5.1). As the simulation proceeds, vertical diffusion of momentum causes the horizontal flow to spread downwards and gradually weaken.

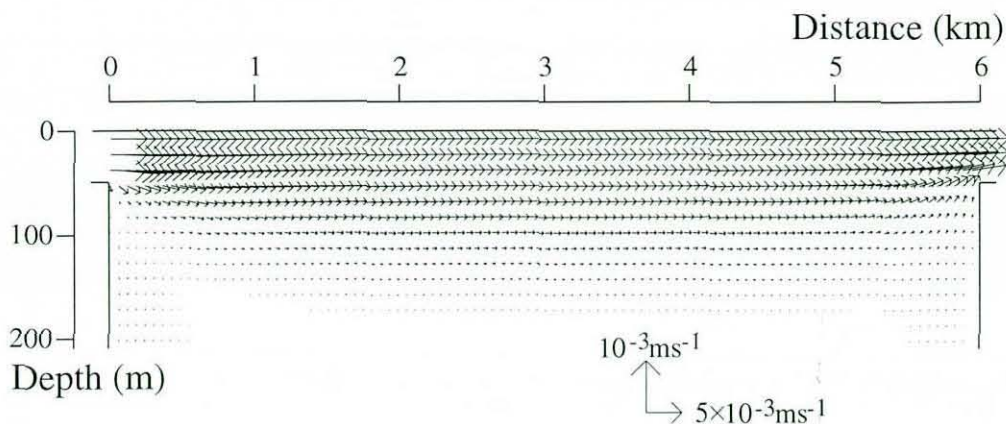


Figure 5.1: Velocity vectors for simulation C after 2 days (plot resolution is $\frac{1}{3}$ of model resolution).

Tracer distributions from this simulation are very important, as the study of deep vertical mixing caused by the thermal bar cannot be quantified without such a reference case. Concentrations given in figure 5.2 illustrate the difference in the riverine influence on vertical and horizontal mixing rates. This anisotropy is primarily caused by convection, since a river throughflow of this form is far more effective in mixing the tracer across the lake than it is in depositing materials vertically into the deeper regions. It may be noticed from this plot that vertical transport seems to be much larger than that accounted for by the vertical diffusion rates alone. This transport results from shear in the horizontal flows, which produces a small circulation beneath the river inflow in the early stages of the simulation.

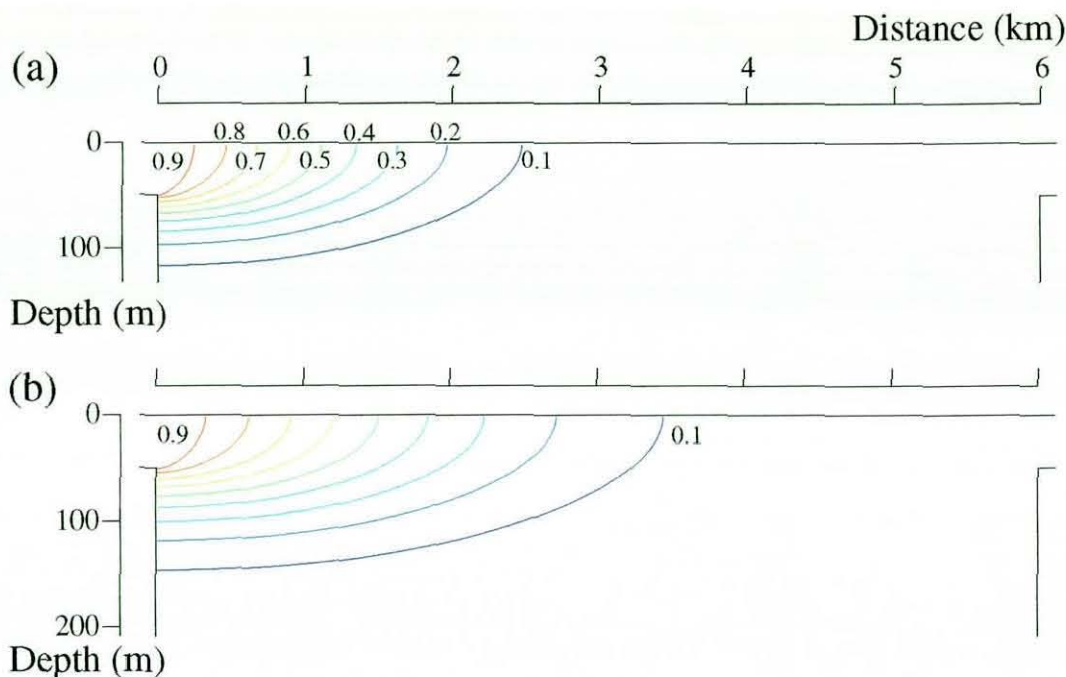


Figure 5.2: Contours of tracer concentration for simulation *C*: (a) after 2 days, (b) after 4 days.

5.2 Simulations *S1* and *S2*

A major part of this work is concerned with the effects of a salinity gradient over the river inflow, so simulations *S1* and *S2* are introduced in order to quantify the dynamical effect of adding a straightforward density increase to the river. These simulations also display the characteristics of a saline sinking density current for comparison to a thermobaricity-controlled case (see section 6.1.3). A simulation is identified as $S\sigma$ if it has σ mgkg^{-1} salinity added to the river and $T_R = T_L = 3.4^\circ\text{C}$, as detailed in appendix A.

Velocity vectors from simulation *S1* (figure 5.3(a)) show the anticipated flow field, with the river plume sinking to the bed of the lake immediately upon entry. This movement is caused by the density increase at the surface due to salinity, which induces a downwards buoyancy forcing which is strongest near the inflow region but extends right to the bottom of the lake.

A brief analysis of results from simulation *S2* also yields few surprises. Doubling the salinity difference between the lake and river virtually doubles the density anomaly and

a much stronger sinking flow is the result. Figures 5.3(b) and (c) show the difference in vertical sinking speed between the two cases; the deepest waters in the domain are quickly ventilated in both cases with saline waters from the river. The sinking current in these simulations initiates a lake-wide circulation which results in a return flow towards the inflow at the surface and a curtailment of the horizontal spreading of riverine substances. This is an important feature which is discussed with reference to other simulations in later chapters. It may be noticed from this plot that vertical transport seems to be much larger than that accounted for by the vertical diffusion rates alone. This transport results from shear in the horizontal flows, which produces a small circulation beneath the river inflow in the early stages of the simulation.

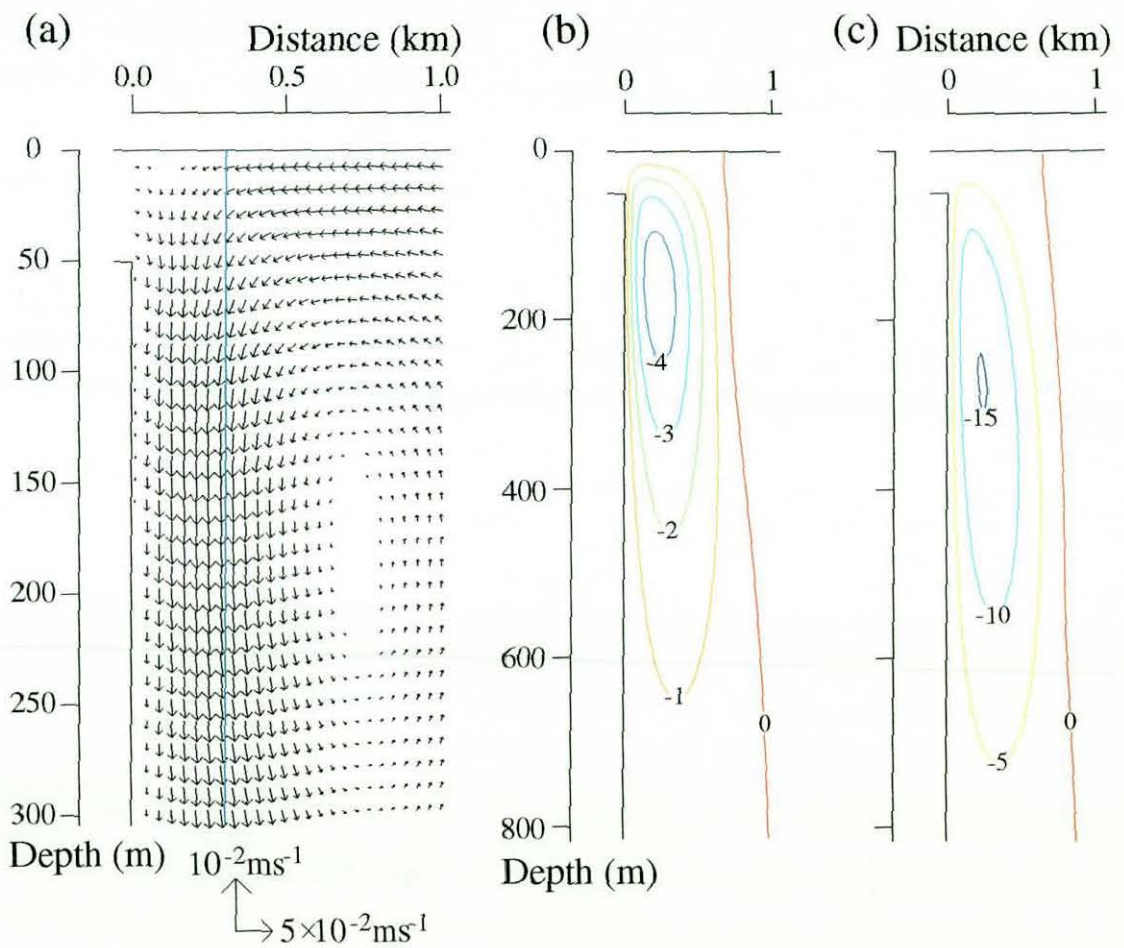


Figure 5.3: Characteristics of the saline simulations after 2 days: (a) $\frac{1}{2}$ -resolution *S1* velocity vectors and position of profile in figure 6.7, (b) *S1* vertical velocity contours (10^{-3}ms^{-1}), (c) *S2* vertical velocity contours (10^{-3}ms^{-1}).

Chapter 6

Results - Simulation of The Thermal Bar

This chapter presents a discussion of three deep-lake simulations with different initial and boundary conditions for temperature. As described in section 2.3.3, one-dimensional models of the river and lake are mixed in a two-dimensional section after three different periods of warming, which provides a comparison between thermal bar simulations with different temperature differences between river and lake. This approach is necessary because insufficient computer power makes a full spring warming model of river and lake interaction impossible on these relatively fine spatial scales. The effects of a riverine salinity influx are not studied until chapter 7, so the salinity transport equation is neglected for the time being.

Characteristics of the predicted flow-field are first described and justified individually, and then important similarities and differences are raised in a comparison section. The effect of different dynamics on the transport of riverine substances is then discussed with reference to the neutral tracer φ , before the chapter is completed with a sensitivity study of the river inflow rate and an examination of the effects of thermobaricity.

6.1 Flow Dynamics

6.1.1 Simulation $T9$

Simulation $T9$ has a river of surface temperature 5.3°C flowing into a lake with surface temperature 3.8°C , and is described first because it is arbitrarily chosen to be the reference thermal bar model from which all comparisons are drawn. After 2 days of simulation a plot of velocity vectors (figure 6.1) shows a clearly-defined thermal bar, in which the front of the line of $T = T_{md}$ is accompanied by converging horizontal flows and a descending plume of water due to the density maximum. This sinking region induces lake-wide circulation patterns which clearly transfer heat and riverine substances downwards into the domain. The stagnation point lags a little behind the surface outcropping of the $T = T_{md}$ contour, probably because of the inertia in the flow ahead of it (Farrow 1995a).

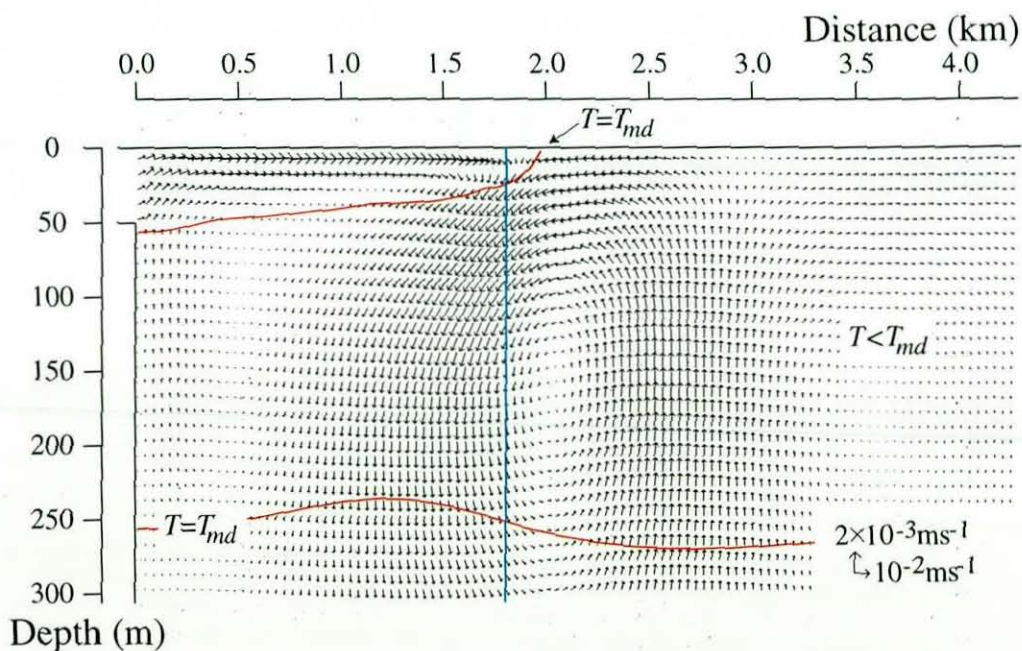


Figure 6.1: Velocity vectors and $T = T_{md}$ line for simulation $T9$ after 2 days (resolution $\frac{1}{2}$). The vertical line marks the position of the profiles in figures 6.3 and 6.7.

The river inflow produces a stably-stratified region (which is warmer than the T_{md}) on the inshore side of the thermal bar. Everywhere else in the domain the initial

thermal conditions from the one-dimensional modelling give an unstable situation above approximately 250 m and a marginally stable water column beneath this. The stable river inflow region contains a shallow horizontal current at the very surface due to the buoyancy of the warm inflow and the stability of the surroundings.

The horizontal current on the offshore side of the thermal bar has a much larger vertical extent. Examination of contours of $T - T_{md}$ (figure 6.2) shows that the thermal bar causes a mixed region beneath the stable surface intrusion which is warmer than the waters offshore of the surface T_{md} signature. This induces a horizontal density gradient extending down to almost 200 m depth which drives the flow offshore of the thermal bar. Surface currents in this region also experience a larger diffusion of momentum downwards due to the unstable conditions.

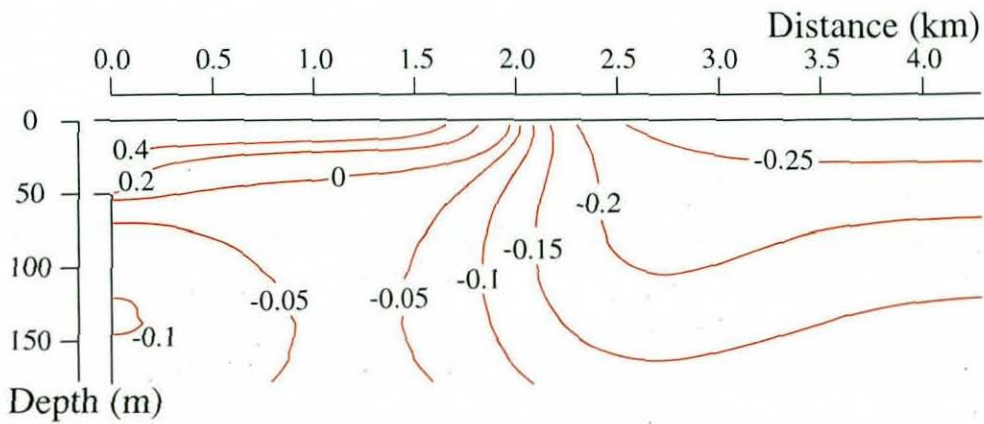


Figure 6.2: Contours of $T - T_{md}$ for simulation $T9$ after 2 days.

The maximum vertical acceleration at each depth in the nose of the stable intrusion occurs at the horizontal position of the T_{md} , and diffusion of momentum then forms the resulting downwelling into a cohesive plume. A characteristic trait of the results in this simulation is that the descending fluid is deflected back towards the inflow as it sinks. This finding is consistent with the numerical results of Malm (1995) and the field results of many other authors (Hubbard & Spain (1973), Carmack et al. (1979), etc.).

Close inspection of the thermal characteristics throughout the depths of the lake (figure 6.2) shows that the centre of sinking follows the locus of the densest water at each

particular depth, which leads us to conclude that earlier convection of heat downwards by the thermal bar is responsible for the deflection of the plume at these later stages of the thermal bar development. This is also visible in figure 6.1 as the local raising of the lower $T = T_{md}$ line.

Some characteristics of a typical thermal bar plume are displayed in figure 6.3, a vertical profile taken through the sinking region of figure 6.1. Plotting the thermal change in the buoyancy term from initial conditions,

$$\Delta B_T = -\frac{g}{\rho_0} (\rho(T, S_{in}, p_{in}) - \rho(T_{in}, S_{in}, p_{in})), \quad (6.1)$$

where the subscript 'in' denotes an initial value, gives a qualitative indication of the buoyancy forces acting upon the water column. The water accelerates downwards due to its increased density but begins to decelerate shortly after since water at the surface T_{md} is warmer than the T_{md} at depth due to the decrease in the T_{md} with increasing pressure. The decrease in magnitude of ΔB_T with depth is mainly due to the surface spreading of the warm-water intrusion. Raising the temperature actually decreases the density of water near 300 m depth (and therefore causes a positive profile of ΔB_T) because heating moves the water temperature further from the T_{md} in this region.

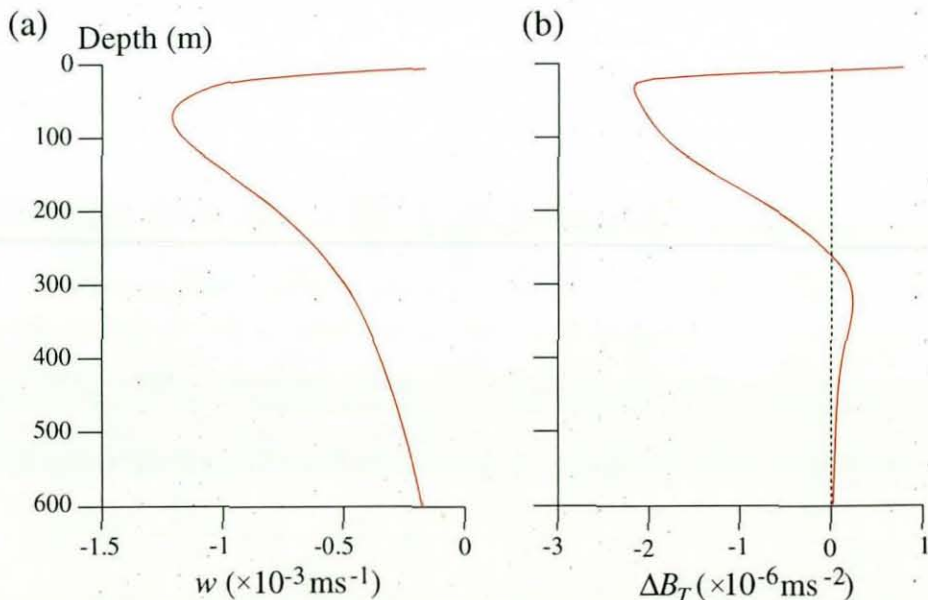


Figure 6.3: Profiles of simulation $T9$ after 2 days at the position marked in figure 6.1: (a) vertical velocity, (b) buoyancy forcing ΔB_T .

The development of the subsequent circulation is best described with reference to the

experimental results of Marmoush et al. (1984), who studied the thermal bar in a lock-exchange tank experiment. Marmoush et al. (1984) report that after an initial period of horizontal spreading, warm waters sinking within the thermal bar form a vertical front beneath the surface point of $T = T_{md}$. In the tank experiment, this distinct vertical boundary between cool waters offshore of the T_{md} and denser waters at (and inshore of) the T_{md} is then the site of a natural lock-exchange mechanism whereby the cabbeling waters move horizontally along the bottom boundary beneath the lighter offshore waters.

The analogous flows in this simulation (after 8 days) are shown in figure 6.4. The vertical front seen in figure 6.2 at about 2 km from the shore separates water bodies of different densities, and the ‘thermobaric barrier’ at about 300 m depth is effectively equivalent to the base of the Marmoush et al. (1984) tank. As the simulation proceeds the lock-exchange character of the flow in the uppermost 300 m becomes apparent as the denser water moves to the right at depths between 150 - 300 m and the lighter offshore water moves shoreward to compensate at the surface (figure 6.4).

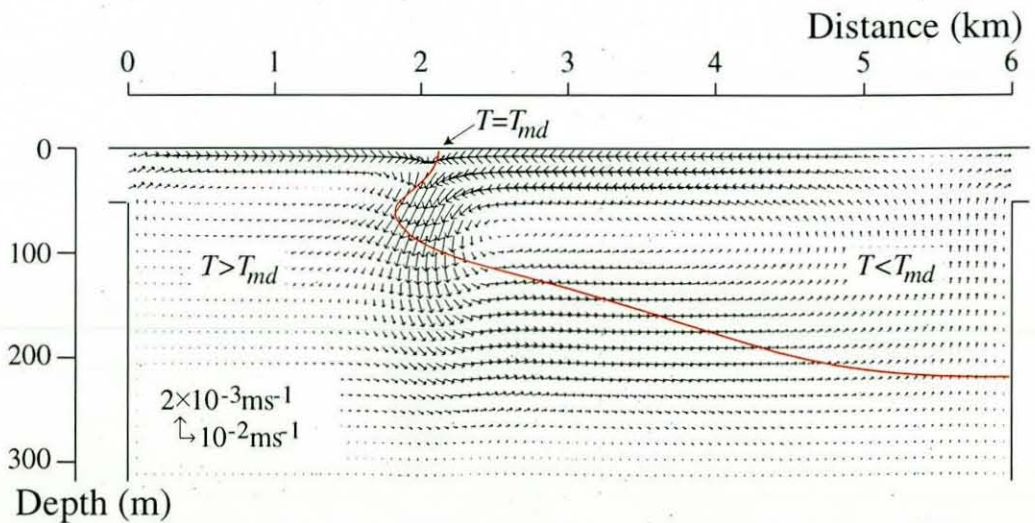


Figure 6.4: Velocity vectors and $T = T_{md}$ line for simulation $T9$ after 8 days (resolution $\frac{1}{3}$).

This analysis regards the $T9$ thermal bar as a two-stage phenomenon. The first stage features a rapidly-moving thermal bar with a warm river intrusion floating on the cooler lake and downwelling where cabbeling is active. The slower second stage

begins when the surface gravity current is balanced by the offshore return flow and the thermal bar can only proceed by gradual warming from the river. This takes place as the river progressively warms the entire epilimnion to above the T_{md} through a horizontal intrusion immediately above the thermobaric barrier.

This process continues until, after more than 30 days, the thermal bar finally reaches the opposite shoreline. The whole of the surface layer is then warmer than the T_{md} , and the travelling thermal bar ceases to exist. Our interest in the predicted motions wanes long before this time as the assumptions of no surface heating, no coriolis forcing, and no effect of outflow conditions are all invalid over long time scales, as discussed in section 2.3.4.

6.1.2 Simulation *T11*

Increasing the time of simulation of the one-dimensional models before mixing river and lake produces a drastic change in the flows associated with the thermal bar, emphasising the sensitivity of the thermal bar to particular density conditions. Two days of warming from the *T9* scenario increases the river surface temperature to approximately 5.7°C while the lake surface hardly changes at 3.9°C . However, the small change in lake temperature is more important as the associated density increase of the ambient lake water means that much less mixed river and lake water will be denser and involved in cabbelling. Velocity vectors in figure 6.5 show that the thermal bar propagates far more rapidly in this case, unrealistically traversing the 6 km-width of the domain in approximately 4 days.

The rapid movement of the thermal bar in this case is due to a strengthening in the surface current on the inshore side of the density maximum. Unlike case *T9* there is very little return flow on the offshore side of the thermal bar to balance this strong current. The return flow would usually counteract a rapid propagation by advecting cooler water towards the line of $T = T_{md}$ and thereby preventing the advance of the warmer waters and density maximum.

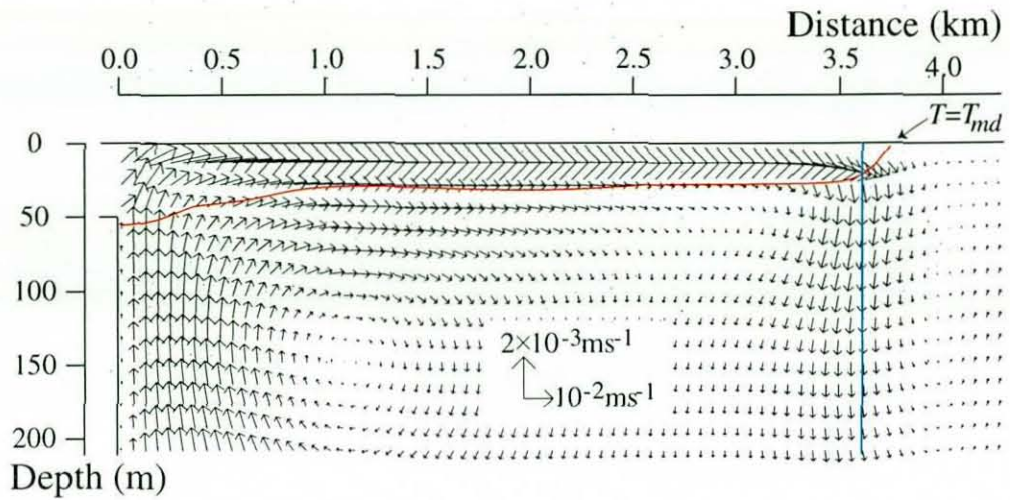


Figure 6.5: Velocity vectors and $T = T_{md}$ line for simulation $T11$ after 2 days (resolution $\frac{1}{3}$). The vertical line marks the position of the section shown in figure 6.7.

The river water, which is warmed far above the T_{md} , immediately rises to the surface upon entry to the lake. The large horizontal temperature gradient in the inflow region initiates a rapid surface current, but only in the thin layer which is above the T_{md} . The warmer river increases the buoyancy of this region to such an extent that the river inflow behaves like a surface gravity current rather than a cabbeling river plume.

Inspection of the velocity vectors does reveal a dense sinking plume at the nose of this gravity current but this sinking flow is weaker than the horizontal current which pushes it across the lake. The speed of propagation and the relative weakness of the sinking means that vertical advection of heat is vastly reduced in this case. The density of waters beneath the surface intrusion is therefore not increased as much as in case $T9$ (which is shown in figure 6.2). As a result, the density gradient between waters at depth in front of and behind the surface position of $T = T_{md}$ is small and the return flow in front of the thermal bar is significantly weaker.

6.1.3 Simulation $T7$

Mixing the river and lake after only 7 days of simulation produces the opposite scenario to $T11$, generating a thermal bar circulation from a relatively small temperature gradient at the inflow (surface river temperature 4.7°C against a lake surface temperature of

3.8°C). Unlike the previous cases, this thermal bar does not propagate away from the river mouth and the river simply sinks upon entry to the lake, as shown in figure 6.6(a). This simulation is thus included as an example of a riverine thermal bar which is not capable of travelling away from the source of cabbeling.

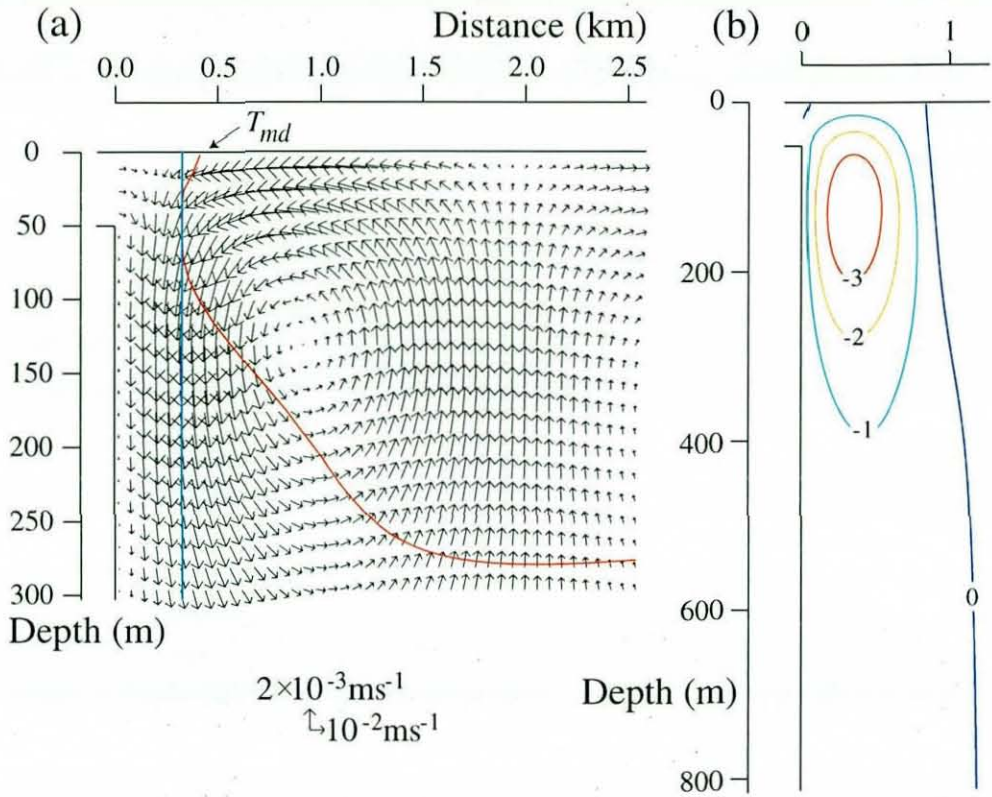


Figure 6.6: Characteristics of case $T7$ after 2 days of simulation: (a) Velocity vectors, $T = T_{md}$ line, and position of the section shown in figure 6.7 (resolution $\frac{1}{3}$, (b) isotachs of vertical velocity (10^{-3} ms^{-1}).

The thermal bar does not move away from the river mouth because the temperature difference between it and the river ($T_R - T_{md}$) is too small to generate the strong surface current seen in cases $T9$ and $T11$ on the inshore side of the thermal bar. The river temperature is close enough to the T_{md} for the majority of the inflow waters to become involved in cabbeling as soon as they enter the domain. This means that there is very little mixed water which is less dense than the ambient lake and therefore capable of forming a strong current to move the thermal bar.

As there is no significant surface gravity current to move the cabbeling away from the inflow, the sinking plume remains near the boundary and induces a large circulation cell in the remainder of the lake. This structure includes a return flow at the surface which impedes any possible propagation of the thermal bar, strengthening the descending flow near the river inflow. This feedback process prevents the thermal bar from moving until the whole lake is significantly warmer than the T_{md} and the inflow floats on the surface of a stable body of water.

Although the river plunges upon entry to the lake, the dynamics are not simply those of a straightforward boundary current. Comparison of vertical velocity isotachs for $T7$ with those for $S1$ (figures 5.3(b) and 6.6(b)) reveals that the descending fluid motion is damped far more rapidly in the thermally-controlled case. This is due to the fundamental difference between the virtually linear relationship between salinity and density and the non-monotonic relationship between temperature and density.

Flow characteristics of $T7$ and $S1$ are initially very similar; the river induces a density increase near the surface, producing a near-boundary sinking flow which decelerates with depth due to continuity, diffusion of momentum, and the decrease in the T_{md} . However, vertical advection of heat and salinity in these plumes affects the subsequent circulation in very different ways. Introducing the buoyancy change due to salinity,

$$\Delta B_S = -\frac{g}{\rho_0} (\rho(T_{in}, S, p_{in}) - \rho(T_{in}, S_{in}, p_{in})), \quad (6.2)$$

figure 6.7(b) shows that advection of salinity increases the downwards buoyancy force at depth, which strengthens the resulting flow, whereas advection of heat downwards moves the water column further from the T_{md} and produces an upwards buoyancy force which suppresses sinking at that depth. Figure 6.7 is discussed in greater detail in the following section.

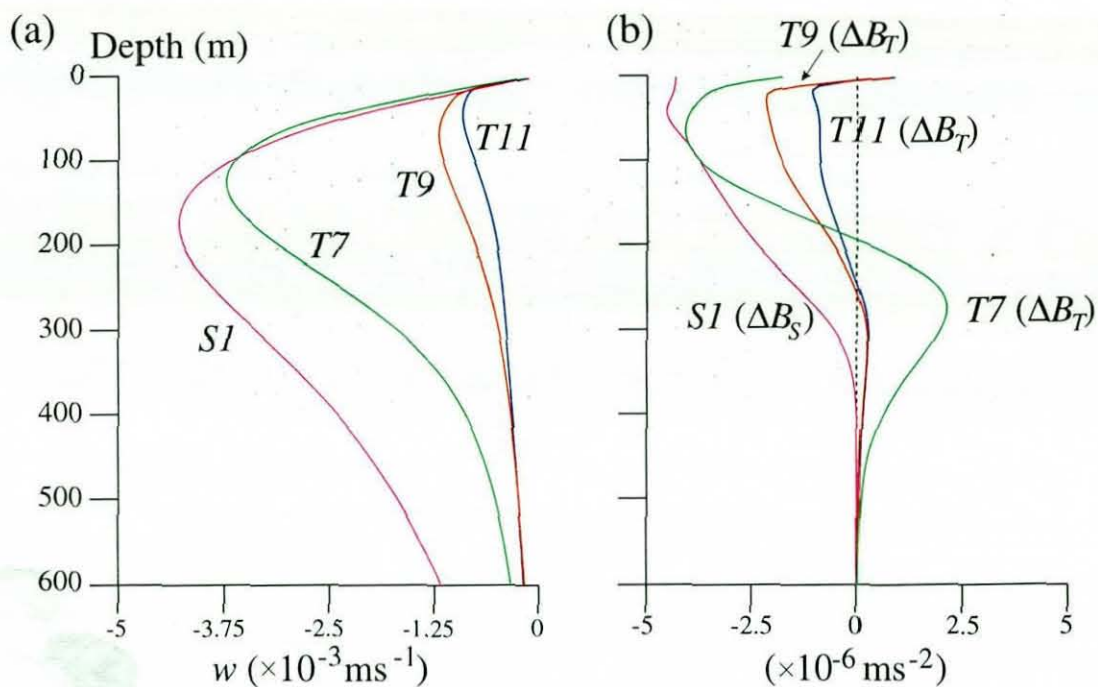


Figure 6.7: Properties of each simulation at the position of the main downwelling plume after 2 days: (a) vertical velocity, (b) appropriate change in buoyancy (ΔB_T or ΔB_S). The position of each of these sections is shown in figures 5.3(a), 6.1, 6.5, and 6.6(a).

6.1.4 Comparison

The three thermal bar scenarios presented above have several important similarities and differences. They all have a region of fluid which sinks due to compaction on mixing, but they have totally different overall circulation patterns as a result of the varying horizontal movement of this sinking region.

The cause of this variation in flow regime is the difference in horizontal density distribution between the three cases, which is shown at 10 m depth in figure 6.8. The most important feature of this plot is the imbalance in each case between density gradients on the inshore and offshore sides of the maximum. It is this imbalance which governs the horizontal position of the thermal bar, implying that the density characteristics distinguish between the three types of dynamics described previously.

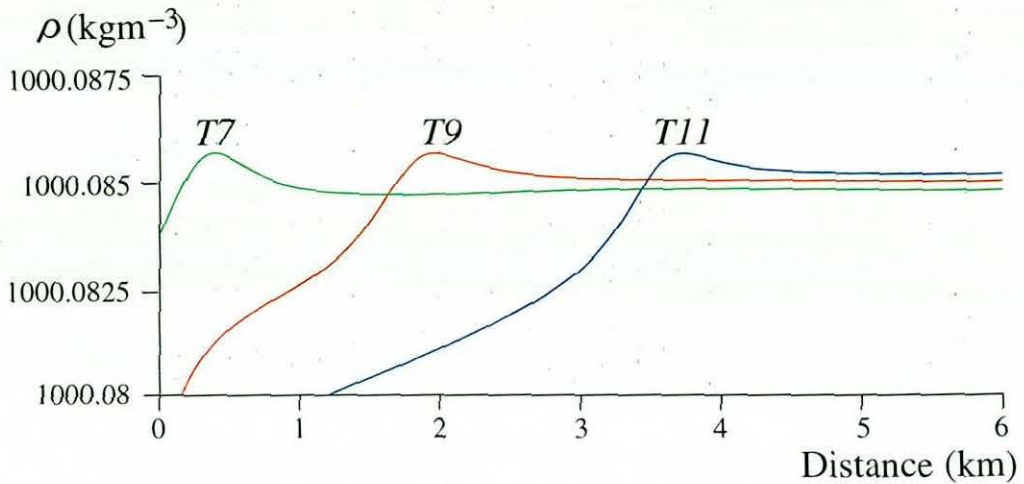


Figure 6.8: Density profiles for all non-saline cases at 10 m depth after 2 days of simulation.

Comparison of vertical sinking rates in the centre of each plume (figure 6.7(a)) shows that a slowly-moving thermal bar has a stronger downwelling than a rapidly-propagating one. This is because the vertical advection of heat in one position is more pronounced in a slowly-propagating thermal bar, and this transport results in a larger downwards buoyancy forcing (figure 6.7(b)), which causes the higher downwelling speeds.

6.2 Transport of River-Borne Materials

The converging surface flows and descending plume of the thermal bar are commonly viewed as a dynamical barrier to horizontal advection within a water body (Carmack et al. 1979, Kay et al. 1995). This barrier limits the amount of water available for dilution of any noxious substances carried in the river, which produces the need for special care when determining maximum effluent release concentrations (Hubbard & Spain 1973, Wetzel 1983, Moll et al. 1993).

Many authors also discuss how the thermal bar may advect Oxygen vertically to considerable depths (Carmack et al. 1979, Shimaraev et al. 1993), with the implication that pollutants could be similarly transported. Sinking generally increases the residence time of any particular substance in a lake because outflowing river waters are usually drawn from the surface (Carmack et al. 1979). In addition, transport of pollutants

to a significant depth could generate particular problems for Baikal's rare deep-water organisms (Haedrich 1996). The vertical currents generated by the thermal bar may also form a crucial mechanism in the annual plankton cycle of Baikal by re-suspending heavy diatoms which sink in the spring after an under-ice bloom in the winter (S.Semovski, personal communication).

In this section each of these claims are tested on the non-saline thermal bar by close scrutiny of transported concentrations of the tracer variable φ which represents a river influx of neutrally-buoyant material.

6.2.1 Horizontal Transport

The horizontal transport of riverine materials is mainly of interest at the surface of the lake, since most characteristics of the river water transfer at depth are governed by vertical movements. Propagation rates from different simulations are therefore compared by plotting the movement of the surface signature of the 10% concentration of tracer against time (figure 6.9).

10% is chosen as the representative proportion of riverine tracer for several reasons. Firstly, it follows the position of the thermal bar plume quite closely, as converging flows above the plume produce a gradient in tracer which usually contains this value. This means that information on the movement of the thermal bar as well as riverine substances may be gleaned from this plot. In addition, testing has shown that other tracer concentrations have very similar characteristics but on different time-scales, and 10% is therefore chosen because it is sufficiently representative of the differences between simulations but also minimises data storage requirements.

Although the flow in control case C is purely driven by fixed velocities, it is clear from figure 6.9 that the horizontal movement of riverine substances is governed by diffusion across most of the domain. This is obvious from the nonlinear increase in distance travelled with time; initially there is a large horizontal tracer gradient and the propagation (diffusion) is rapid, and later on the tracer spreading is slower because the gradients are weaker. Inspection of horizontal terms in the transport equation for tracer φ confirms this analysis, although convection does play a small role in producing this

tendency because horizontal advective flows also weaken as the simulation proceeds.

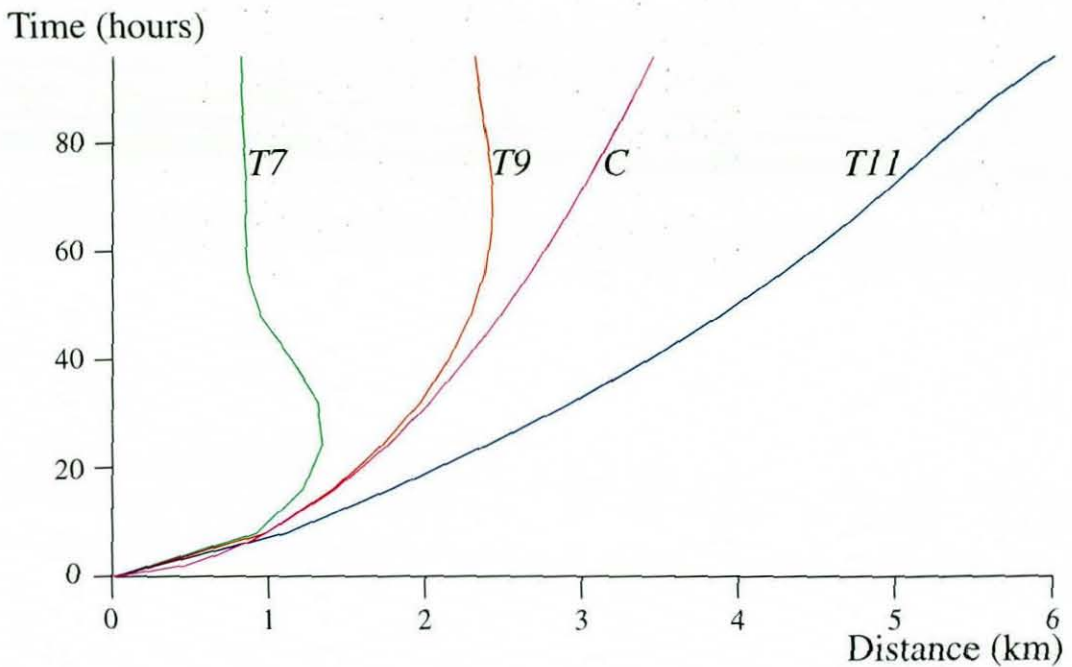


Figure 6.9: Horizontal movement of 10% riverine tracer value at surface in all simulations.

Since the 10% contour closely follows the position of the thermal bar, the differences in horizontal movement of tracer between the other cases pictured in figure 6.9 have already been discussed and justified. In case *T9* the movement of tracer is very similar to the control case for the first day of simulation, despite the huge difference in forces governing this propagation.

The explanation for this similarity lies in the transport properties at the nose of the river intrusion, which are studied by scrutiny of a horizontal profile of tracer convective and diffusive flux terms 25 m below the surface. The discussion behind the choice of horizontal diffusivity K_h in section 4.2 should be remembered when referring to a convection-diffusion comparison of this nature; a rather qualitative analysis is the best that can be expected due to the arbitrariness of the choice of K_h .

In case *C*, tracer propagates as a result of convection and diffusion away from the inflow in this region (figure 6.10(a)), whereas movement of tracer at this position in

simulation *T9* is produced from a conflict between advection of tracer-free water towards the inflow and the increased diffusion of tracer away from the inflow which results from the steep tracer gradient caused by convergence in the thermal bar zone (figure 6.10(b)). After one day the balance between convection and diffusion in case *T9* produces the same net transport as case *C*. However, after two days the growing convection from the offshore circulation begins to delay the thermal bar and horizontal propagation of tracer away from the river mouth in simulation *T9* is halted rather sharply, as described in section 6.1.1, before actually reversing for a short time.

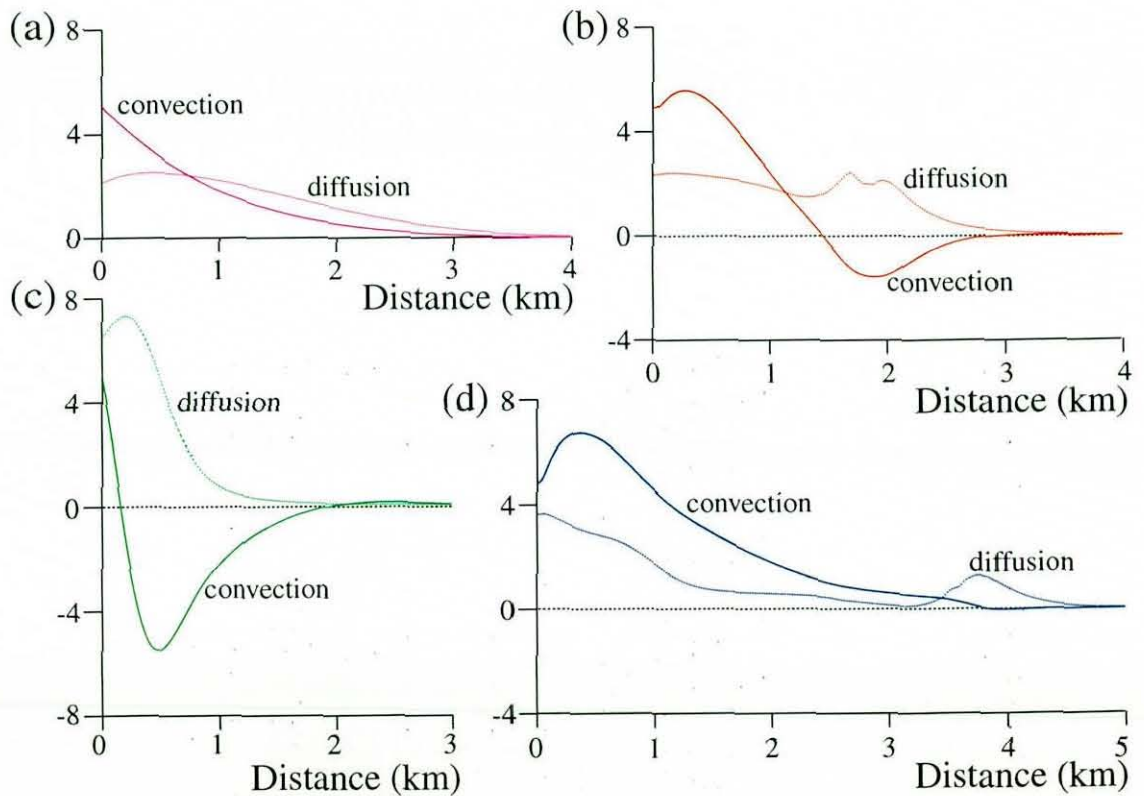


Figure 6.10: Horizontal convective and diffusive fluxes of tracer ($u\varphi$ and $-K_h \frac{\partial \varphi}{\partial x}$ respectively) in the different simulations after 2 days ($\times 10^{-3} \text{s}^{-1}$): (a) *C*, (b) *T7*, (c) *T9*, (d) *T11*.

Unsurprisingly the horizontal movement of tracer is impeded quite severely in case *T7*. As in the other cases the initial movement is fairly rapid due to convection from the fixed inflow velocity, but the effects of vertical sinking down the boundary soon become apparent as the recirculation begins. The movement of tracer away from the river is first

halted and then reversed by ever-stronger convection of tracer-free water towards the inflow which is forced by the sinking region. This reversal ceases only when convection towards the river mouth steepens the tracer gradient to such an extent that diffusion equals convection, forming a horizontal equilibrium which is almost present in figure 6.10(c).

The results for case *T11* show an enhanced rate of horizontal mixing by the thermal bar as a consequence of the rapid movement of the surface gravity current across the lake. It is also observed that the propagation curve is nearly linear in this case, which indicates that convection is the driving force behind this movement. Closer inspection of tracer transport terms (figure 6.10(d)) confirms that the horizontal convection of tracer dominates diffusion over most of the domain, although interestingly diffusion is strongest at the very nose of the river intrusion. It is therefore the strong convection of heat (which has a similar profile to that of tracer convection in figure 6.10(d)) which propagates the thermal bar rapidly across the domain.

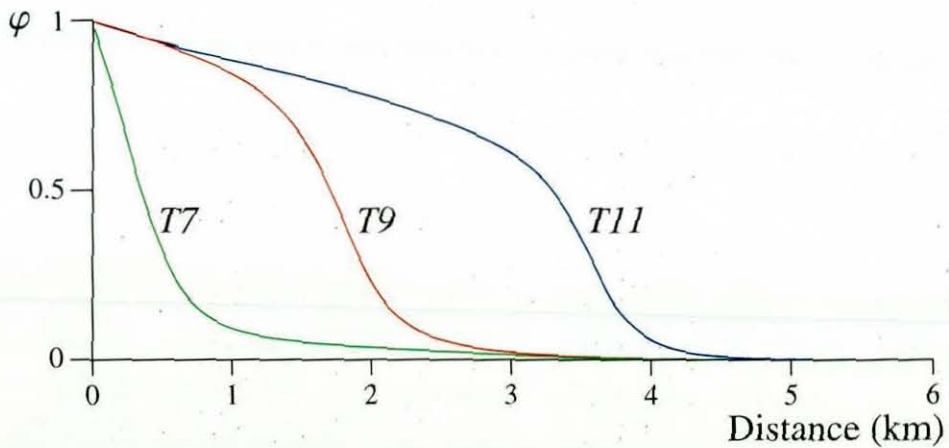


Figure 6.11: Horizontal distribution of riverine tracer for thermal bar simulations after 2 days.

The above results show that the thermal bar may increase or decrease the horizontal spreading of riverine substances from a lake-wide perspective, but locally the thermal bar always acts as a barrier to horizontal spreading due to its horizontal convergence and increased vertical mixing. Horizontal profiles of tracer (figure 6.11) confirm this analysis

by showing that in every simulation the tracer gradient is steepened in the region of the thermal bar.

6.2.2 Vertical Transport

Assessing the vertical transport by the thermal bar is the primary aim of this study, but unfortunately it is rather difficult to quantify the vertical movement of tracer substances in flow regimes of such a varying nature. To avoid this problem, plots of the sinking achieved by a particular tracer concentration are taken at the horizontal distance from the inflow which gives the deepest value. Extreme care must therefore be taken with this discussion because the given depths may be taken at a different horizontal position for each simulation and time increment. The smallest maximum depth which the tracer value will reach is 50 m, the depth of the inflow region.

Figure 6.12 shows the maximum depth achieved by a 1% concentration of tracer for each simulation as a function of time. As in section 6.2.1, the 1% value was chosen to minimise storage requirements after testing showed that the characteristics of figure 6.12 are preserved when using other reasonable reference values of φ . This choice is also suitable because a 1% concentration of any riverine substance is a significant amount for the purposes of pollution and oxygenation studies.

In general terms this picture shows that the thermal bar is rather ineffective at mixing high concentrations of riverine matter to the bottom of any lake which is deeper than about 350 m. This agrees with thermal bar maximum-depth estimations based upon the decrease of the T_{md} with depth (Carmack & Weiss 1991). This maximum mixing depth is not unique to the tracer concentration of 1%; a closer analysis shows that vertical convection plays a secondary role to diffusion beneath 400 m and values of tracer are lower than 0.01% there while the thermal bar operates. In contrast to this result, it can be seen that saline gravity currents renew waters at the very bottom of the domain after a continuous downwards mixing near the mouth of the river. Case *T9P* is a *T9* simulation which has all thermobaric effects removed, and is fully discussed in section 6.4; for the time being it is sufficient to note that the plume immediately transports riverine matter to the lake bed in this case. The plot clearly shows that it is the pressure effects upon the thermal control of density which impedes mixing in the

thermal bar cases.

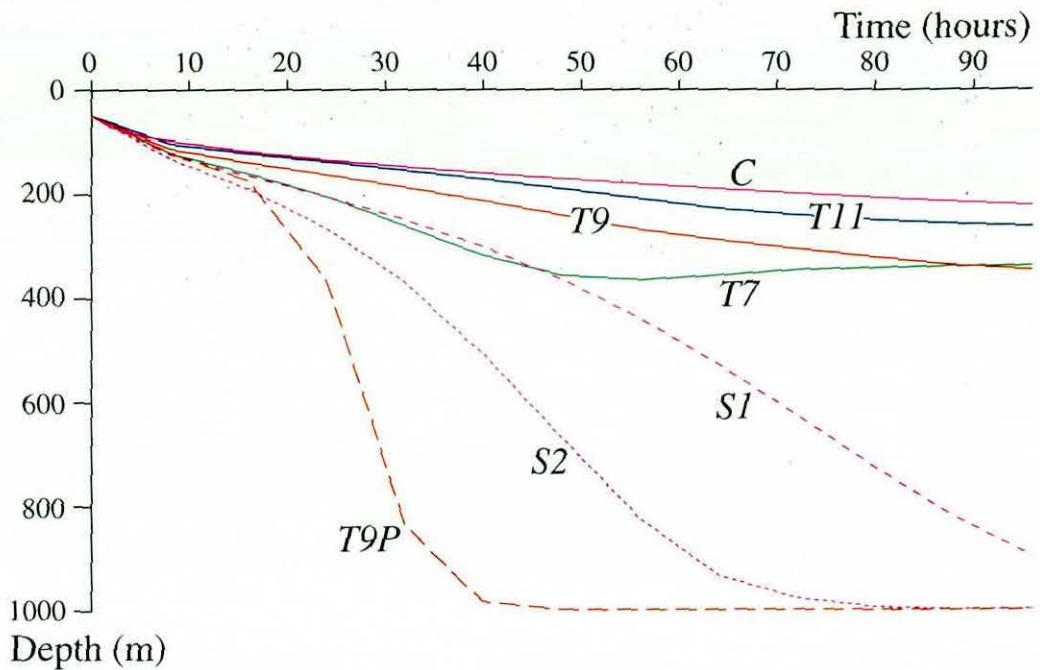


Figure 6.12: Maximum depth of 1% riverine tracer concentration for all simulations.

The least vigorous vertical transport is given by the control case *C* which has no variation in density. Due to the lack of any buoyancy forcing, the vertical velocity in this case is produced solely as a response to the horizontal motion at the inflow and outflow boundaries, and is very weak accordingly. The vertical transport of tracer is thus solely governed by diffusion at the intermediate value of vertical eddy viscosity which is arbitrarily assigned to this simulation.

Case *T11* barely provides any increase on control simulation *C*, giving the least vertical transport of all of the cases involving density-induced momentum. This happens because the thermal bar traverses the lake so quickly that there is not enough downwelling in one position for descending flows to produce a significant downwards transport of tracer.

Simulation *T9* shows an increase over case *T11* in the vertical movement of tracer. This is partly due to the larger vertical velocity in this case (figure 6.7(a)), but is

primarily a result of the slower horizontal propagation of the thermal bar. Since the thermal bar renews water in one place for longer, the maximum depth of the 1% tracer concentration in the domain is deeper than that of simulation *T11* even though the total mixing averaged over the domain is initially similar. It is emphasised that this case, which is considered to be the reference thermal bar simulation, does not produce enough mixing to carry tracer concentrations of 1% or larger beneath 350 m.

A comparison of tracer plots for simulations *T7* and *S1* invokes the discussion of section 6.1.3. Initially the tracer transport profiles for these two scenarios are extremely similar, and the vertical transport due to cabbeling in case *T7* actually exceeds the transport of case *S1* for the second day of simulation. However, while transport in the saline case continues as before after this time, the descending flows of the *T7* thermal bar cease to transport matter any deeper. In fact the downwards movement of tracer is reversed after 2 days of simulation because the water column near the inflow becomes warmer than the T_{md} throughout. Advection of warm waters downwards then produces an upwards buoyancy force due to the decrease in the T_{md} (figure 6.7(b)), which forces the water to stop sinking and move horizontally away from the boundary. This movement causes a small upwards convection of tracer-free water near the boundary, which is just powerful enough to account for the raising of the deepest 1% tracer concentration.

6.3 Effects of Inflow Velocity u_R

Since the velocity of the throughflowing river is arbitrarily chosen in this work, this section contains results and a brief discussion of an inflow-velocity sensitivity study based on a comparison of case *T9* with simulations *T9U0* and *T9U1*, which are identical to *T9* apart from their inflow velocity, which is $u_R = 0$ and 0.01 ms^{-1} respectively.

When compared to figure 6.1, velocity vectors in figure 6.13 show that the speed of propagation of the thermal bar is significantly altered by changes to the inflow velocity, even at these low values. It can be observed that the river's discharge pushes the thermal bar across the lake by strongly influencing the inshore currents at the very surface. The inflow rate also controls the circulation beneath this surface flow, as *T9U1* contains a clockwise-rotating current which accompanies a strong upwelling beneath the river

inflow, while *T9U0* has no such upwelling motions and displays a weak circulation only within the stable river intrusion.

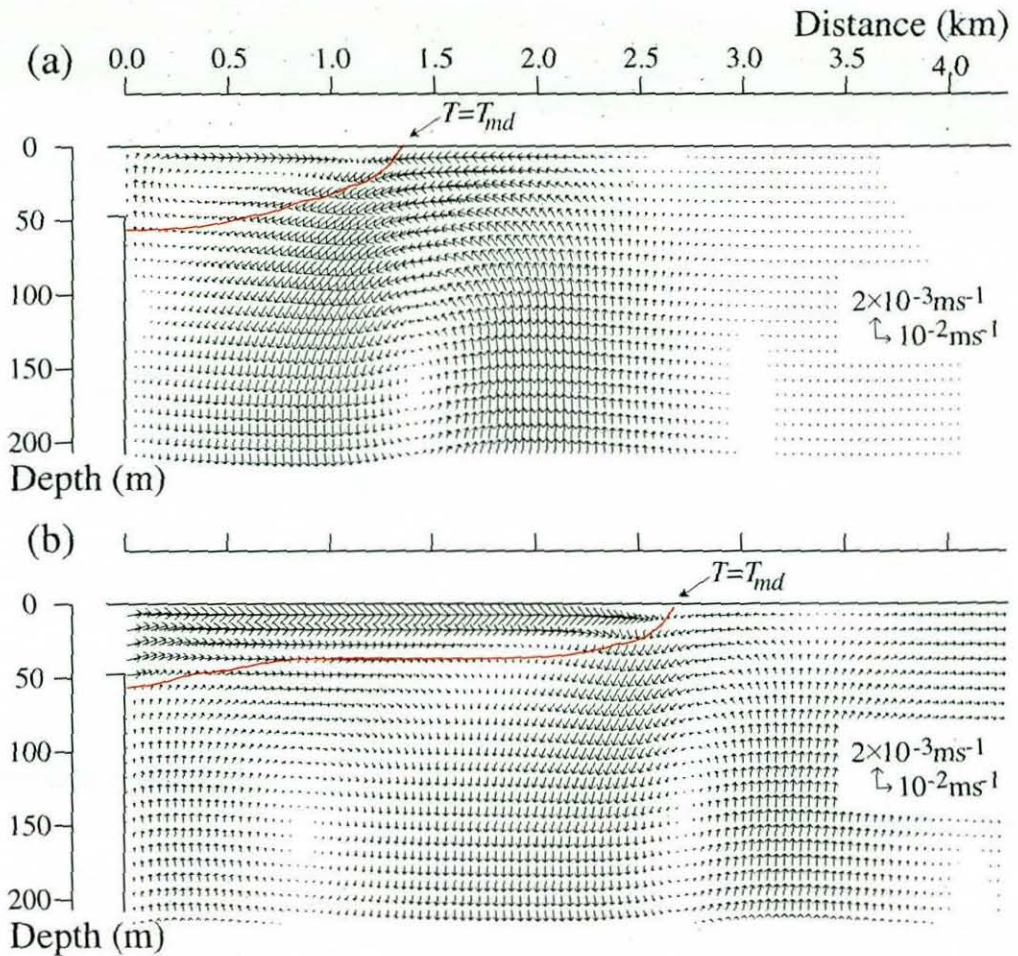


Figure 6.13: Velocity vectors and $T = T_{md}$ line after 2 days for simulations with various u_R (resolution $\frac{1}{2}$): (a) *T9U0*, (b) *T9U1*.

Despite these differences, this study shows that, like increasing A_h , the qualitative effects of increasing u_R on the actual form of the thermal bar and flows around the lake are relatively small. The fluid motions plotted in figure 6.13 show all of the major *T9* characteristics discussed in section 6.1.1, such as the inshore surface current, deflected sinking plume, and unbalanced vertical extent of horizontal currents on either side of the thermal bar. Most importantly, the vertical motions generated by the river inflow are of a very similar magnitude in all three cases. This happens because raising the inflow velocity does not significantly alter the horizontal density gradient (containing the T_{md}) at the very nose of the river intrusion, which is responsible for the vertical

motions of the thermal bar and therefore the circulations in the lake. Instead, the river merely transports this region of horizontal density variation across the lake.

Numerical testing shows that it is possible to produce more dramatic changes in the flow regime by increasing the rate of flow through the domain further. However, while the tested u_R values may be low for a shallow river outlet, it is important to remember that the river inflow to this model is 50 m deep and velocities should not be much larger than those tested here, as discussed in section 2.3.2. In any case, the object of this study is to examine flows driven by buoyancy effects rather than kinematic forcing.

6.4 Effects of Thermobaricity

An important advance of this study over most previous work is the inclusion of pressure terms in the equation of state, which resolves the decrease in the T_{md} with depth. The effect of pressure variation on the thermal expansion coefficient is called thermobaricity and is an important consideration when studying vertical advection in lakes as deep as Baikal. Thermobaricity is generally neglected in lacustrine modelling because the pressure variation in the vast majority of lakes is negligible due to their shallowness relative to Baikal. Results from this section and chapter 8 show that this assumption is broadly valid for lakes of up to 200 m depth.

As thermobaricity is so important to thermal bar dynamics in a deep lake, it is included in all simulations and a simplification of the model is therefore required in order to gauge its effects. For comparative purposes a modified version of simulation *T9* was performed in which the pressure variation throughout the depth of Baikal was ignored in density calculations, so that $p = 0$ was fixed in the equation of state (2.8) and eddy-viscosity formulation (i.e. α and N^2). The resulting simulation, *T9P*, is crucial to the study because it justifies some of the buoyancy arguments made in the thermobaricity-resolving cases and allows this modelling work to illustrate the situations under which thermobaricity is vitally important.

Results in this simulation are considered after only one day of simulation to ease a comparison with other cases; after two days the circulation is so strong that buoyancy

changes and vertical velocities are unrecognisable in the context of the previous results. After this time, the non-thermobaric cabbeling is responsible for a significant downwelling near the inflow region, as shown in figure 6.14(a). This sinking region extends to the very bed of the lake and attains vertical velocities which are an order of magnitude larger than those of case *T9* after half of the simulation time, as shown by a comparison of figures 6.7(a) and 6.14(b). This strong vertical movement impedes the propagation of the thermal bar in the same fashion as that of case *T7*; the extra sinking velocity relative to the horizontal temperature gradient causes a larger shoreward return flow at the surface (via continuity) and the movement of the $T = T_{md}$ line is halted.

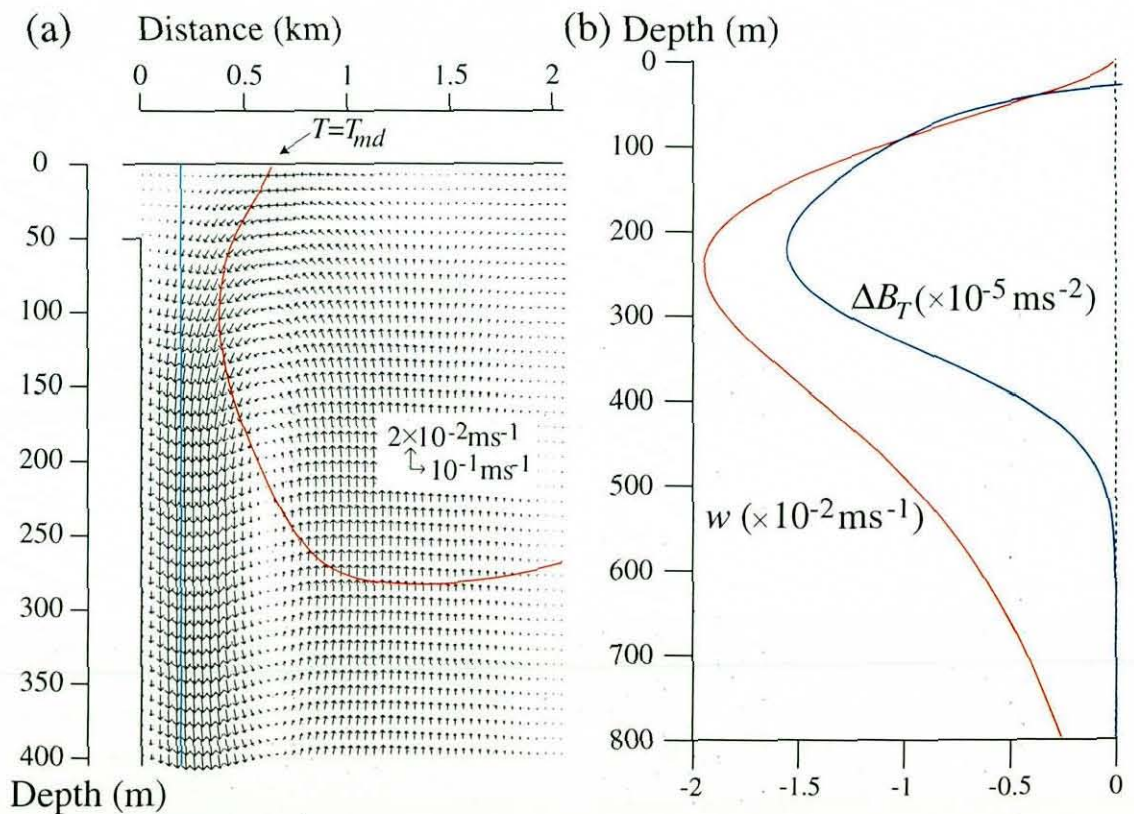


Figure 6.14: Characteristics of case *T9P* after 1 day of simulation: (a) Velocity vectors and $T = T_{md}$ line (resolution $\frac{1}{2}$), (b) vertical velocity and change in buoyancy ΔB_T at the position marked in (a).

The extra sinking induced in this case is clearly a result of the depth-uniformity of the equation of state, and figure 6.14(b) reveals how the lack of pressure dependence affects the buoyancy forcing. Clearly a depth-constant T_{md} ensures that the downwards

advection of heat always produces a density increase and downwards buoyancy forcing, inducing a strong descending current throughout the depth of the lake.

Plotting the vertical transport in *T9P* against some other cases (figure 6.12) highlights the importance of thermobaric effects in Lake Baikal. While vertical transport is severely impeded in case *T9*, the boundary current of *T9P* plunges river water to the bed of the lake even more quickly than the higher-salinity control case *S2*. As well as illustrating the theory of Carmack & Weiss (1991), this result confirms the uniqueness of Baikal's deep ventilation mechanisms, since there can be no other temperate lake in which thermobaricity is so important.

Chapter 7

Results - Effects of Salinity

Introducing a riverine influx of salinity to the simulation of the thermal bar is the primary advance of this deep-lake study over previous modelling work. This chapter details the effects of a difference in salinity between river and lake upon the thermal bar results described earlier.

Average salinity values for Lake Baikal and the Selenga River are given at 96.3 mgkg^{-1} and 126.8 mgkg^{-1} by Falkner et al. (1991) and Votintsev (1993) respectively. Unfortunately, the use of this exact Selenga value is not appropriate here as it is taken from a measuring station immediately above the Selenga delta, and is therefore a concentration from a relatively shallow river several kilometres upstream of the 50m-deep inflow region used in these simulations. The salinity of the river inflow used in this work is much closer to the ambient lake value as it is assumed that the river water undergoes considerable mixing in the delta before entering the model domain.

As described in section 2.3.2, these salinity studies were performed by adding concentrations of 1, 2, 5, and 10 mgkg^{-1} to the river salinity and keeping the lake value constant at 96.3 mgkg^{-1} . These small differences in salinity are sufficient to radically alter the flows predicted in each simulation, and in the majority of cases described here the thermal bar is transformed into a boundary current similar to that of case T7.

The effects on density of the ranges of temperature and salinity employed here are illustrated in figure 7.1, where isopycnals are plotted for pressure levels of 0 and 50 bar. This plot is provided as a reference for the discussion in this chapter, which often cites the complex interplay of temperature, salinity, and pressure effects upon density

as justification for the predicted motions.

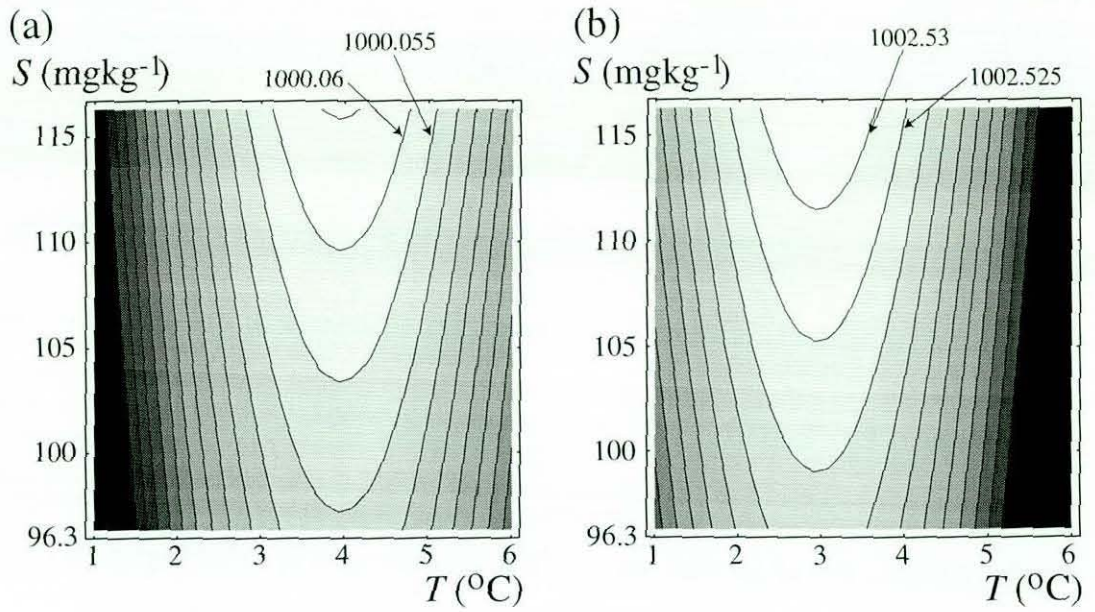


Figure 7.1: Isopycnals at two pressure levels over the ranges of temperature and salinity relevant to this study: (a) atmospheric pressure, (b) 50 bar.

7.1 Simulation *T9*

Since the three thermal cases have four saline variants each, the saline *T7* and *T11* sets are not described in full here in the interests of brevity. Instead, a full description and analysis of each saline *T9* case is given and results of the other cases are related to these findings as appropriate.

7.1.1 Case *T9S1*

A representative impression of the effect of riverine salinity on the thermal bar may be gained by comparing velocity vectors after 2 days from case *T9* with those from *T9S1* (figures 6.1 and 7.2(b) respectively). It is clear from these plots that the saline component of the river-lake density difference impedes the horizontal propagation of the thermal bar and causes a localised circulation at the river mouth. However, figure 7.2(b)

also shows that this salinity-enhanced vertical flow is sharply suppressed beneath about 350 m in depth.

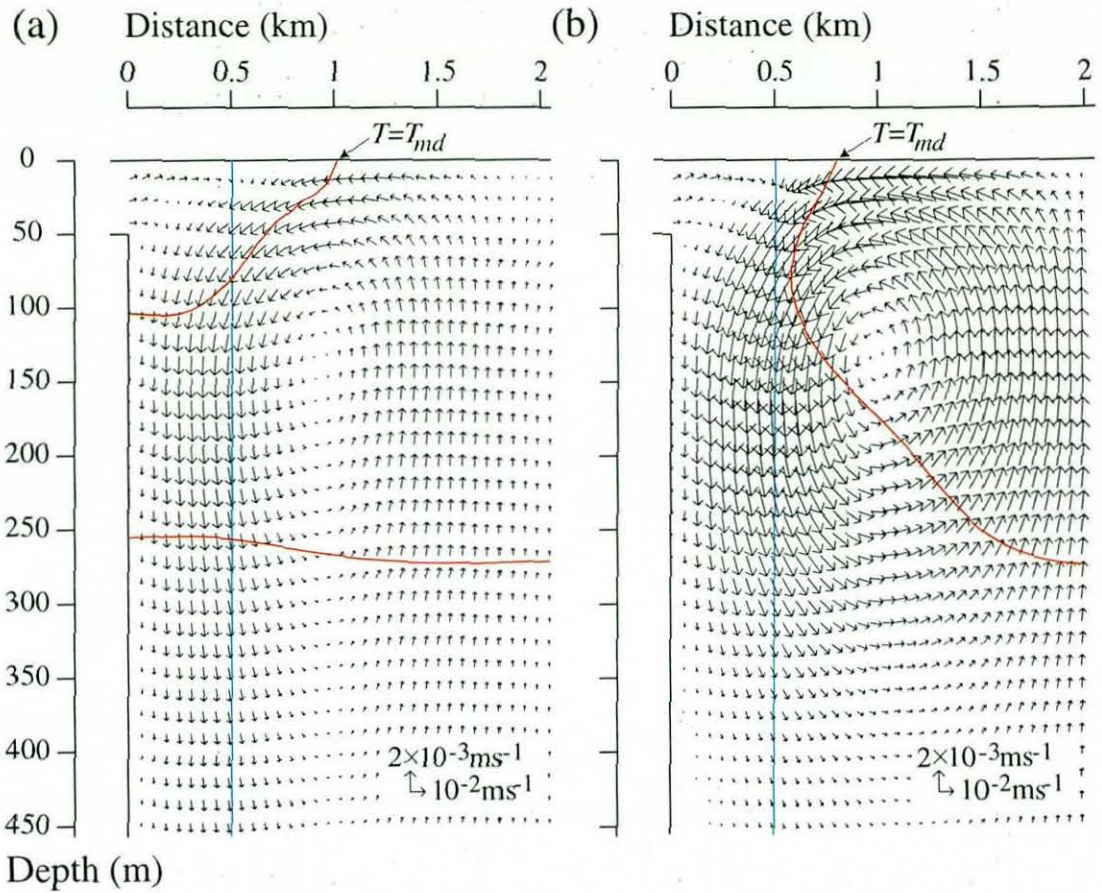


Figure 7.2: Velocity vectors for case $T9S1$ (resolution $\frac{1}{3}$): (a) after 1 day, (b) after 2 days.

A study of earlier vectors (figure 7.2(a)) shows that the downwelling at the boundary starts as soon as the simulation is initiated because mineralisation and cabbeling ensures that the mixture of river and lake water is denser than the ambient lake. The surface T_{md} position is offset slightly from the river mouth by the warm waters inshore of the density maximum, but beneath this the sinking takes place immediately adjacent to the boundary. At this time the river plume descends relatively slowly but the depth attained by the sinking is much greater than later in the simulation (compare figures 7.2(a) and (b)).

Later vector plots reveal that the near-boundary sinking gets stronger and shallower

with time, so that after 4 days the descending flow is much stronger but does not sink past 250 m (not shown). The river water moves horizontally away from the boundary at this depth and a circulation cell is formed in the top section of the domain, with very little vertical movement below this.

As before, the flow patterns described above can be explained by consideration of the buoyancy forcing and continuity effects. The progression of the total change in buoyancy plotted in figures 7.3(a) and (b), where

$$\Delta B = -\frac{g}{\rho_0} (\rho(T, S, P_{in}) - \rho(T_{in}, S_{in}, P_{in})), \quad (7.1)$$

shows that the magnitude of the density change from initial conditions increases as time proceeds. The near-river increase in density due to salinity (which generates the ΔB_S profile) is seen to be more extensive at depth after 2 days due to the movement of salinity downwards. This acts against the increase in positive buoyancy change at depth which results from the downwards advection of warm waters (ΔB_T). Overall, however, the total density change ΔB reflects the ΔB_T profile more than the ΔB_S profile and thermal effects are therefore held to dominate salinity in determining ΔB . ΔB seems to become more polarised with time, as the large positive and negative buoyancy forcings

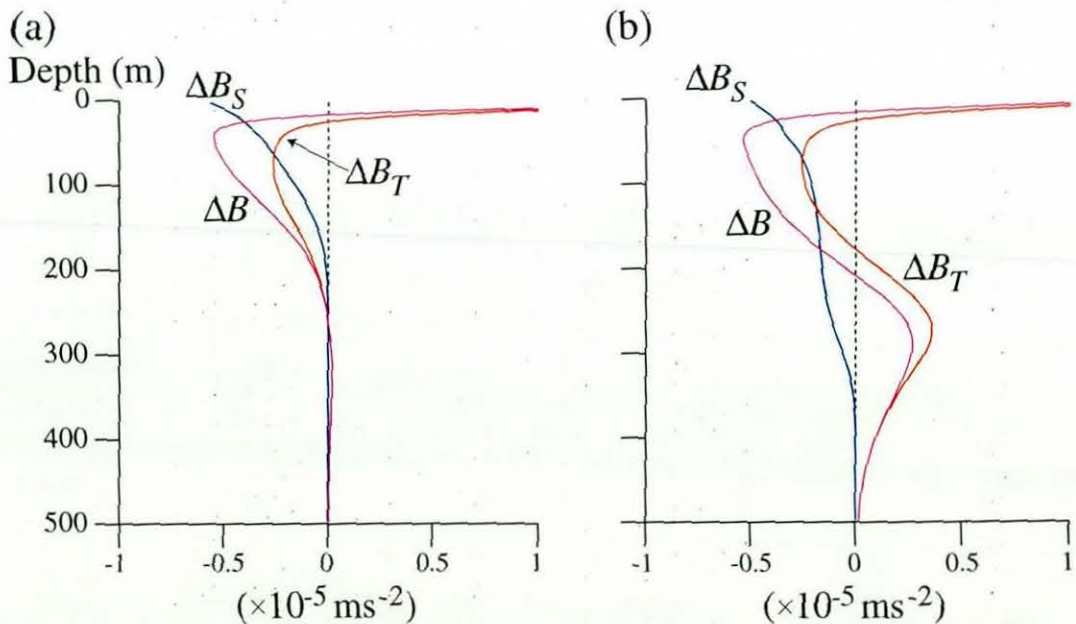


Figure 7.3: Buoyancy characteristics ΔB_T , ΔB_S and ΔB for simulation *T9S1*: (a) after 1 day, 500 m from left shore, (b) after 2 days, 500 m from left shore.

from the different sources grow over a small vertical extent.

This component analysis indicates that after 24 hours the flows are governed by near-surface density characteristics, resulting in a weak flow extending to a relatively great depth, but after 2 days buoyancy forcings down to 400 m depth are important due to the vertical advection of density-altering substances. On longer timescales the thermal dominance of buoyancy change at 300 - 400 m depth grows to such an extent that water cannot sink past this region, and descending waters are therefore deflected out into the lake.

These deflected waters travel horizontally away from the plume, heedless of the downwards curvature of the $T - T_{md}$ contours, under similar forcings to the deflected plume of the $T9$ case after 8 days, which is described in section 6.1.1. This water does not sink due to the presence of the thermobaric barrier and rises instead to form the rapid circulation offshore of the T_{md} which feeds the near-boundary sinking region.

7.1.2 Case $T9S2$

Increasing the input of riverine salinity in case $T9S2$ produces qualitatively similar dynamics, but with a considerably stronger downwelling (figure 7.4). An important difference is that the small horizontal propagation seen in case $T9S1$ is suppressed much more quickly and after 2 days the surface cabbeling takes place immediately adjacent to the river mouth. This plot also shows that the stronger forcing and faster flows of this case produce a narrower boundary current than previously, allowing the growth of a deeper circulation offshore of the main plume. A good example of this lower sinking plume is shown in figure 7.4 at 300 m - 400 m depth and 1.5 km from the river mouth.

These new features can also be related to changes in buoyancy forcing from initial conditions. Comparing figures 7.3(b) and 7.5 it can be seen that salinity effects characterised by ΔB_S exert a significant influence over the total buoyancy change ΔB in case $T9S2$. The maximum absolute value of ΔB_S is larger than in case $T9S1$ and this quantity attains a consistently large negative value over a considerable vertical distance as a result of increased downwards advection of salinity in one fixed position. This means that the total change in buoyancy forcing ΔB is directed downwards with a

larger magnitude and over a greater depth than previously.

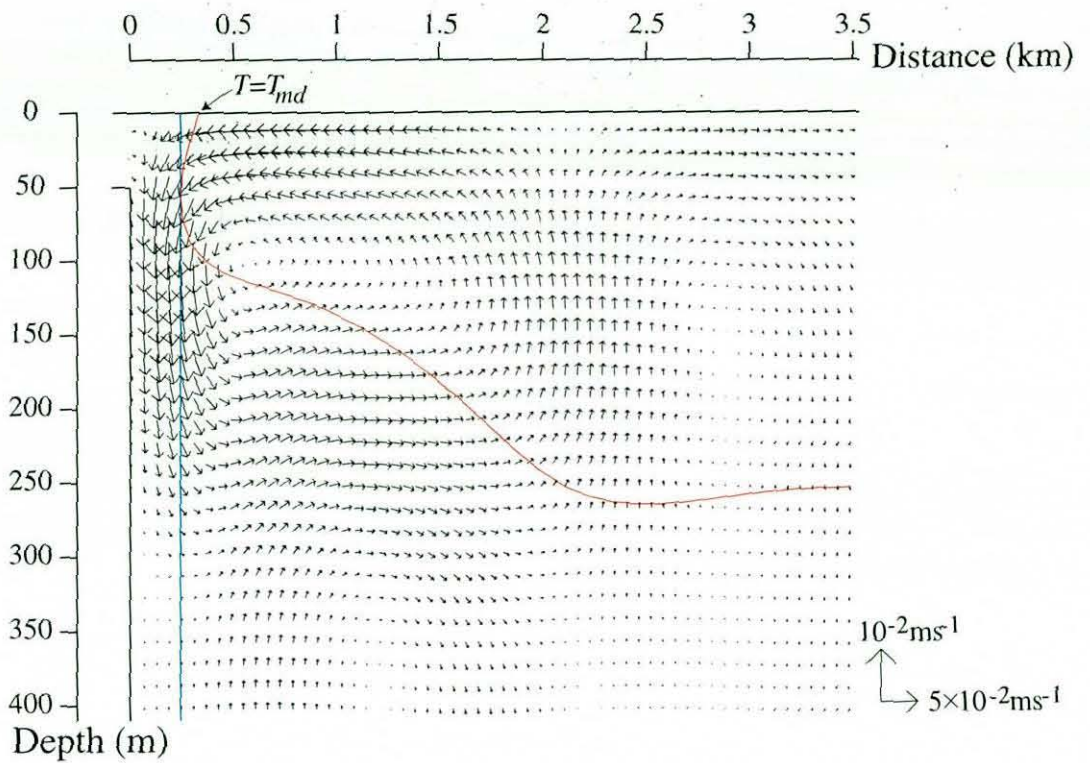


Figure 7.4: Velocity vectors for case *T9S2* after 2 days (resolution $\frac{1}{3}$).

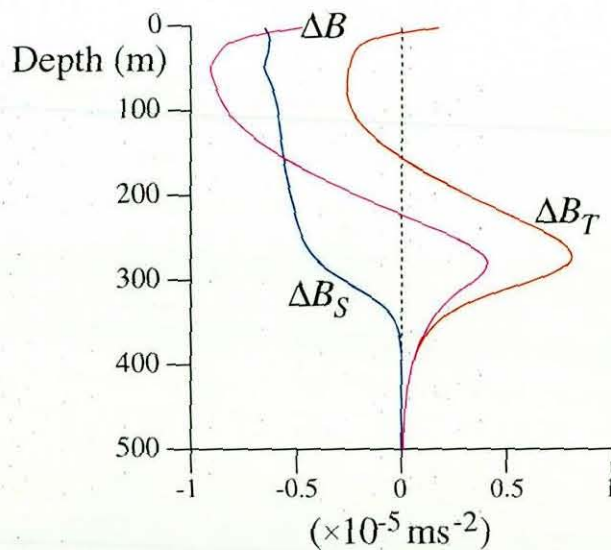


Figure 7.5: Buoyancy characteristics ΔB_T , ΔB_S and ΔB for simulation *T9S2* after 2 days, 250 m from left shore.

It is tempting to postulate that this rapid downwelling caused by extra salinity would partially overcome the thermally-induced positive buoyancy change at depth and ventilate much deeper waters than in case *T9S1*. However, a comparison of figures 7.2(b) and 7.4 shows that waters do not sink much further, a surprising result which can be explained by consideration of ΔB_T in figure 7.5. It can be seen that the increased vertical advection of case *T9S2* transports more heat downwards than case *T9S1*, which increases the positive values of buoyancy change at depth and therefore brings the downwelling to a halt.

The secondary plume in case *T9S2* results from the increased levels of salinity in the flows emanating from the base of the descending boundary current. The control of the flow horizontally away from the boundary is described in section 6.1.1 as a lock-exchange mechanism whereby a dense intrusion spreads along the thermobaric barrier. In contrast to *T9*, the *T9S2* version of this current transports increased salinity to this region, causing the water to breach the thermobaric barrier when it has travelled far enough from the region of strong resistance caused by the downwards heat transfer near the boundary.

7.1.3 Cases *T9S5* and *T9S10*

Adding larger salinities to the inflow generates results which extrapolate the trends established by cases *T9S1* and *T9S2*. Velocity plots show that in each case the cabbelling generates a boundary plume which sinks to a particular depth and is then halted, with waters propagating away from the boundary at the base of the plume (not shown). The depth at which this plume stops sinking will hereafter be referred to as the 'equilibrium depth' because it arises from a balance of buoyancy effects. A secondary plume is also observed in both cases, and closer examination reveals that this flow is stronger in case *T9S10*. This provides more circumstantial evidence to support the proposition that salinity is the governing factor in this phenomenon.

Profiles of buoyancy forcing change ΔB taken down the centre of each sinking boundary current are remarkably similar to each other in tendency (figure 7.6(a) and (b)). In both cases the ΔB profile has the general characteristics of ΔB_T but is modified by a ΔB_S -induced shift towards negative change (i.e. downwards forcing) which is almost

uniform with depth. Figure 7.6(b) shows that buoyancy change in case *T9S10* is utterly dominated by ΔB_S above 200 m depth.

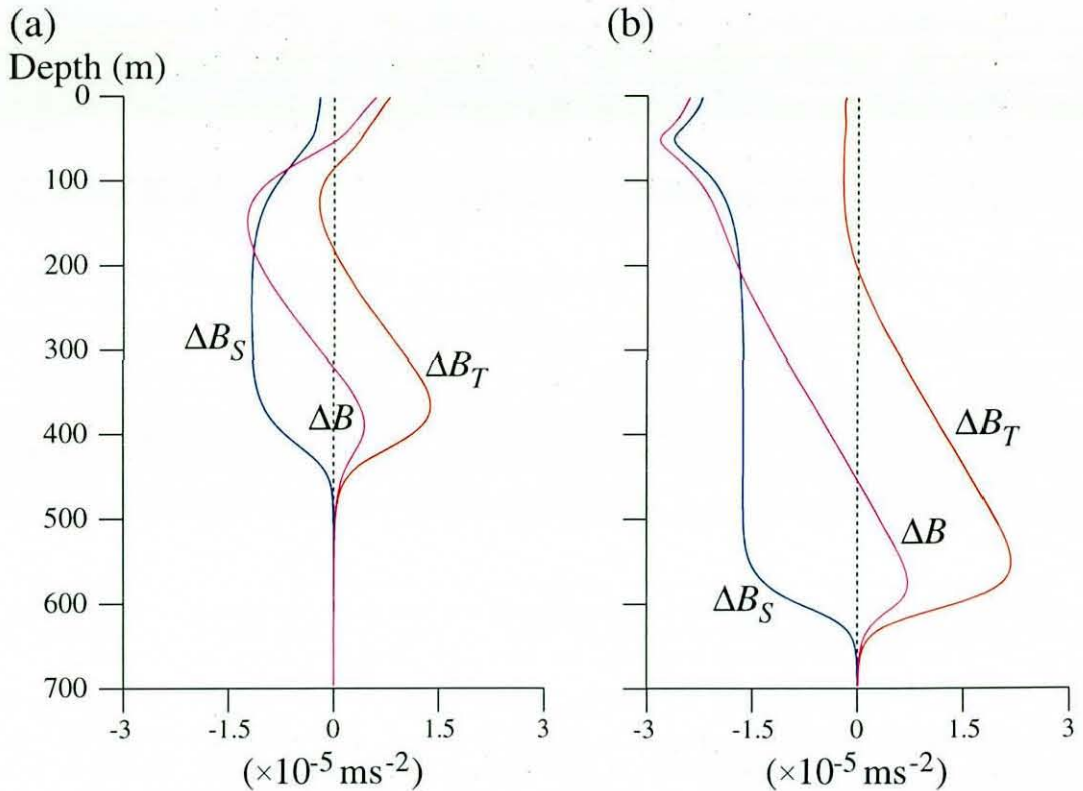


Figure 7.6: Buoyancy characteristics $\Delta B_T, \Delta B_S$, and ΔB after 2 days: (a) case *T9S5*, 400 m from left shore, (b) case *T9S10*, 150 m from left shore.

It is clear that the addition of salinity to these plumes increases the plume density relative to the lake, and thus modifies the overall thermal control of the sinking. Plumes with a higher salinity sink further because a larger difference between plume temperature and the local T_{md} is required to balance the haline density increase and set the plume's equilibrium depth.

7.1.4 Comparison

The delaying effect of riverine salinity on the horizontal propagation of the thermal bar is a direct consequence of its influence on the delicate balance of density gradients on either side of the maximum. Figure 7.7 shows near-surface horizontal density profiles

after 2 days for the $T9$ cases of various riverine salinity. A clear observation from this figure is that the density maximum attains a higher value in saline cases than otherwise. This is fairly obvious, since salinity always increases density, but is very important in understanding the mechanisms behind the overall flow pattern. As the density of the plume is further from the ambient lake density than in non-saline cases, the plume will sink more rapidly into the lake water and the flow towards the thermal bar on the offshore side (i.e. between lake and thermal bar) will be stronger due to the steeper density gradient.

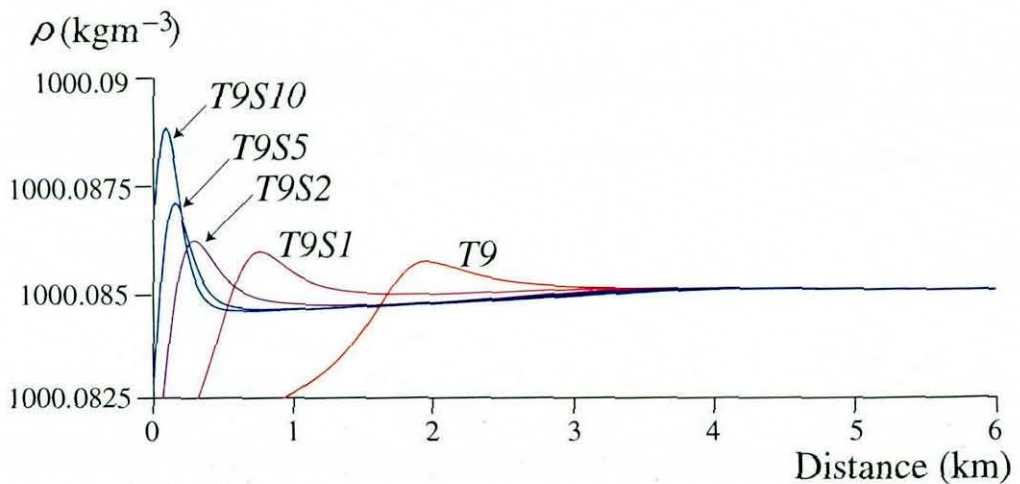


Figure 7.7: Density profiles at 10 m depth for all $T9$ simulations after 2 days.

The increase in the offshore density gradient is particularly important because the riverine salinity also lessens the density difference between the maximum and the river by increasing the river's density more than the density maximum (figure 7.7). As a result the dominant flow switches from inshore of the density maximum in case $T9$ to offshore in case $T9S5$, with drastic consequences for the propagation of the thermal bar. Continuity-driven return surface flow from the stronger sinking also plays a part in curtailing the forward movement of the saline thermal bar.

Figure 7.7 also shows that $T9$ cases with river salinity differences of 10 mgkg^{-1} and above have a river inflow which is denser than the lake before any mixing has taken place. This plume would never propagate away from the river inflow but is of interest to this study because thermobaric control of the equilibrium depth takes place as before.

7.1.5 Transport Properties

The effect of salinity on transport is studied, as before, by consideration of position vs. time charts of a concentration of river tracer φ . The plot of horizontal tracer propagation (figure 7.8(a)) is relatively uninteresting; clearly the horizontal movement of the thermal bar is impeded by salinity, an effect which is intensified as more salinity is added to the inflow.

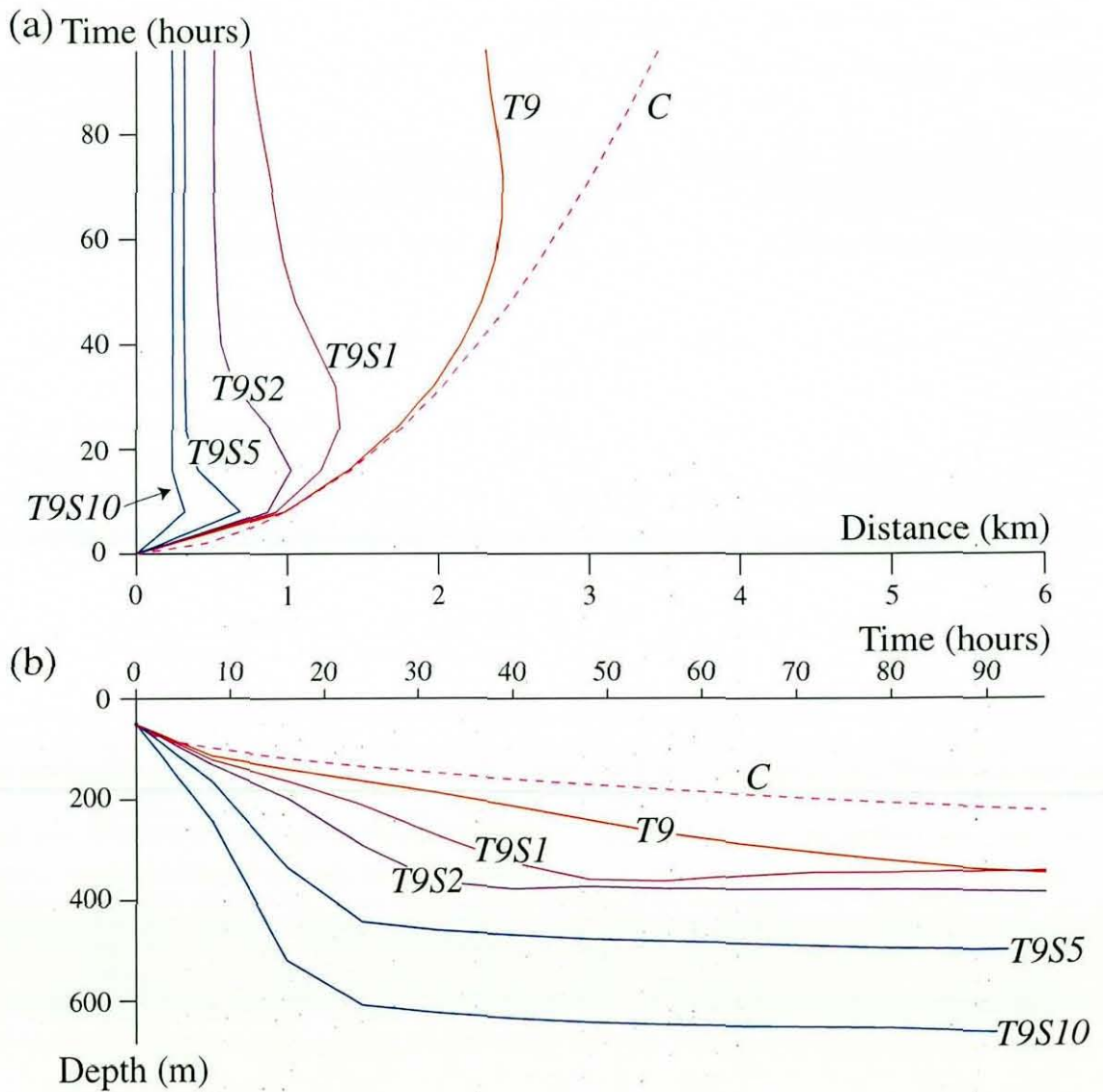


Figure 7.8: Transport properties of $T9$ simulations with various riverine salinity: (a) horizontal movement of 10% tracer value at surface, (b) maximum depth of 1% riverine tracer concentration.

In all saline cases, the thermal bar initially propagates away from the river before the buoyancy-driven circulation from the boundary flow initiates a significant return current. By advecting cool tracer-free water towards the river this return flow forces a retrograding in the movement of the tracer and thermal bar. Therefore the more salinity is added to the river, the more the horizontal propagation of tracer is suppressed.

Saline effects on vertical transport are a little more interesting. Figure 7.8(b) shows that adding 1 mgkg^{-1} salinity to a river initially increases the mixing of riverine substances into the lake, but surprisingly after 4 days the net penetration is the same as case *T9*, with a maximum 1% tracer concentration depth of just 350 m. The tracer sinks more rapidly, but then rises slightly as the positive buoyancy changes at this depth force the sunken fluid to resettle.

The effect of adding extra salinity in case *T9S2* is equally surprising. Although a marked increase in tracer sinking rate is noted, the maximum depth of net tracer transport is rather similar to case *T9S1*. Indeed, after 2 days the maximum depth of 1% river water is only 10 m deeper in case *T9S2* than in case *T9S1*. Moreover, after 4 days the effect of doubling the salinity difference between river and lake (at these values, which are admittedly small) is to increase the maximum transport depth by a mere 40 m.

Once more, cases *T9S5* and *T9S10* follow the trend laid down by the simulations with a lower river salinity. Adding salinity initially quickens the rate of downwards vertical transport but an equilibrium is then formed which prevents any further sinking. The time taken for the formation of this vertical balance decreases with increasing salinity, since stronger downwards flows rapidly move warm waters into a position where they are far from the T_{md} , generating the positive buoyancy change required to balance the saline density increase and set the equilibrium depth.

7.2 Simulation *T11*

Streamline plots for the four saline variants of case *T11* show that there are two distinct flow regimes found at different salinity levels (figure 7.9). Higher-salinity cases *T11S5* and *T11S10* produce the familiar dynamics of a sinking boundary current and thermobaric barrier, while cases *T11S1* and *T11S2* feature an entirely new phenomenon: the travelling saline thermal bar.

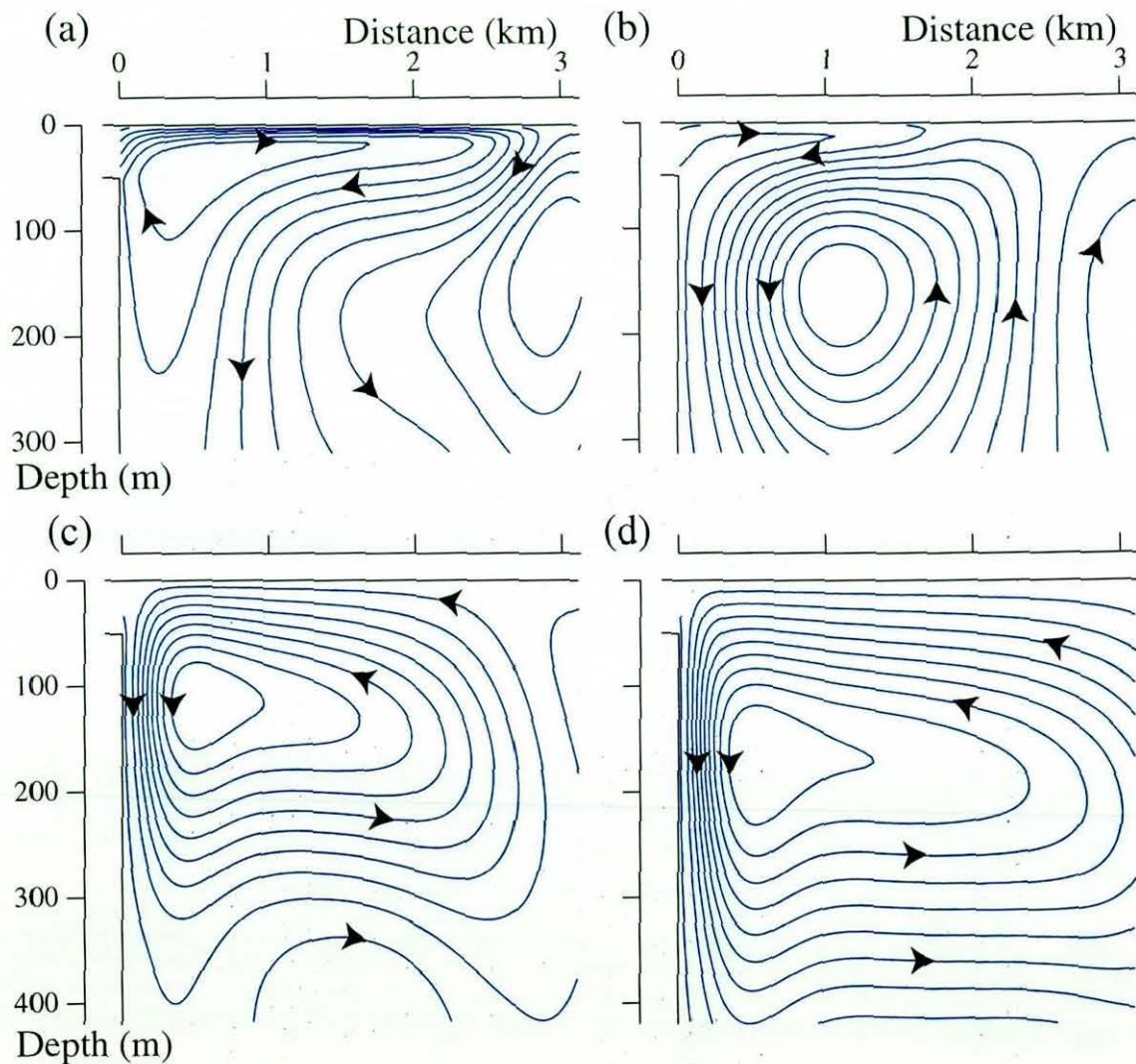


Figure 7.9: Streamlines for each saline *T11* case after 2 days: (a) *T11S1*, (b) *T11S2*, (c) *T11S5*, (d) *T11S10*.

The driving force behind the movement of this travelling thermal bar is the large temperature anomaly between river and lake which is the defining characteristic of case

T11. Streamlines in figure 7.9(a) show that the gravity current near the surface behaves similarly to that of the non-saline case (compare to figure 6.5), but beneath the surface flow conditions are very different. Since *T11S2* has similar dynamics to *T11S1*, its description is neglected here in favour of a fuller explanation of *T11S1* flows.

When the surface point of $T = T_{md}$ moves away from the river in case *T11*, the sinking region beneath the maximum in density moves with it, as shown in figure 6.5. This happens because all buoyancy forces in the domain are dominated by the relatively large temperature gradients near the surface of the lake. In case *T11S1*, early advection by the thermal bar in the vicinity of the river mouth alters the density characteristics at depth considerably by transporting salinity downwards, initiating a plume at depth which persists even when the surface gravity current moves the near-surface cabbeling away from the river inflow. This plume, which attains the maximum density at depths greater than 100 m, then draws thermal bar waters horizontally back into it, eventually warming a column of water through the T_{md} and establishing stable stratification.

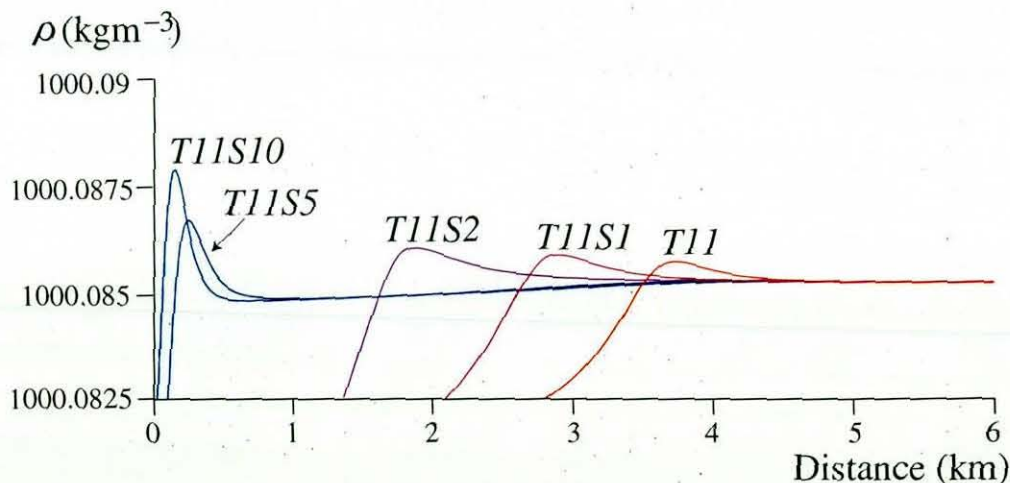


Figure 7.10: Density profiles for all *T11* cases after 2 days at 10 m depth

In contrast to the travelling thermal bar in the above discussion, the flows generated in cases *T11S5* and *T11S10* are remarkably similar to the boundary currents of their saline *T9* counterparts, even as far as the close correlation between the depths achieved by each sinking plume. The explanation of this distinction between the two flow regimes lies in the balance of thermal and haline effects, which can be inferred from the horizontal

density profiles from each case (figure 7.10).

This figure shows that the density maxima for the two higher-salinity cases are in similar positions to the corresponding members of the *T9* series, whereas the lower-salinity thermal bars have progressed much further in the *T11* scenario (compare to figure 7.7). This is clearly due to the massive density gradient on the inshore side of the thermal bar in case *T11*, the impact of which is only nullified by salinity inputs of 5 and 10 mgkg^{-1} .

The horizontal propagation of tracer under the *T11* thermal regime with various saline forcings is quite straightforward and is only briefly discussed here. The rapid movement of the thermal bar case *T11* (figure 6.11) is damped quite sharply by the effects of salinity in cases *T11S1* and *T11S2*, and in the two higher-salinity cases propagation of the thermal bar is totally halted.

Vertical transport characteristics also reflect the differences between the two distinct flow types found here. Lower salinity cases produce small increases in vertical transport over *T11* but these are limited by the travelling nature of the thermal bar in addition to the usual buoyancy effects. Higher salinities produce deeper plumes with similar effects to those noted in the *T9* series, albeit with a slightly shallower maximum depth as a result of the warmer inflow.

7.3 Simulation *T7*

The dynamics of the saline *T7* simulations are the simplest of all, due to the fact that the *T7* thermal bar is a boundary sinking current even before the addition of any riverine salinity. Figure 7.11 shows that the depth of sinking is slightly deeper than that of *T9* simulations, which is expected because the cooler inflow of *T7* cases has to sink further to provide the same compensating upwards buoyancy as *T9*.

Density plots show why the dynamics of all *T7* simulations are so similar, and only differ in the speed of flows in the circulation; the density maxima are all in the same place but are of varying magnitudes. All cases are sinking gravity currents because the

density gradient inshore of the thermal bar is not sufficient to overpower the offshore density gradient and move the thermal bar. In the extreme case *T7S10* it can be seen that the effects of salinity are so strong compared to thermal effects that the density monotonically decreases away from the river inflow.

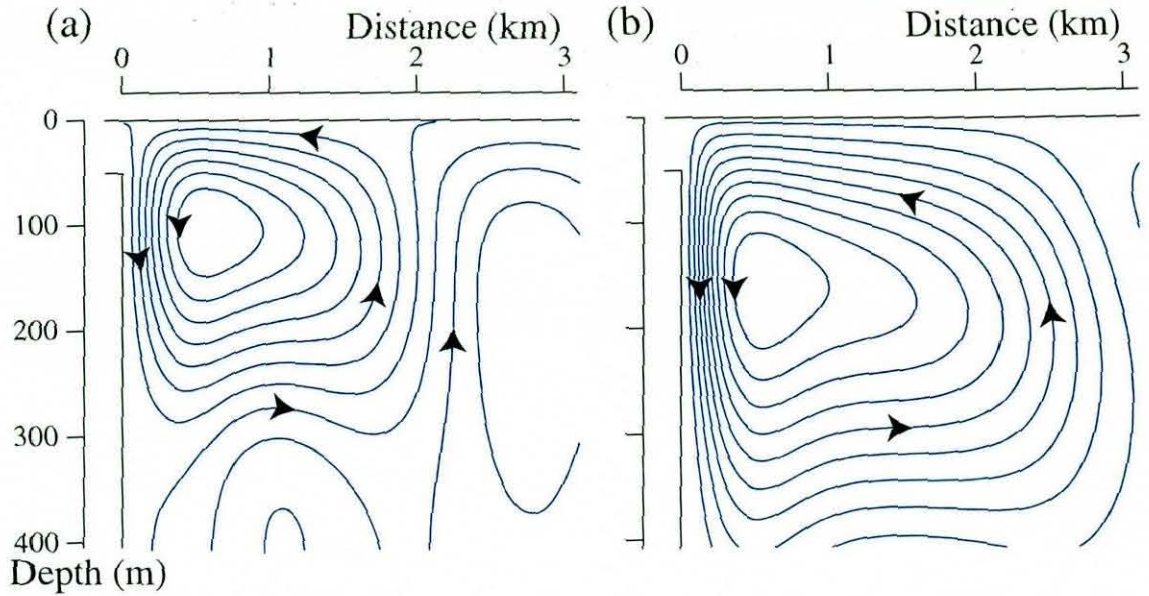


Figure 7.11: Streamlines for each saline *T7* case after 2 days: (a) *T7S1*, (b) *T7S5*.

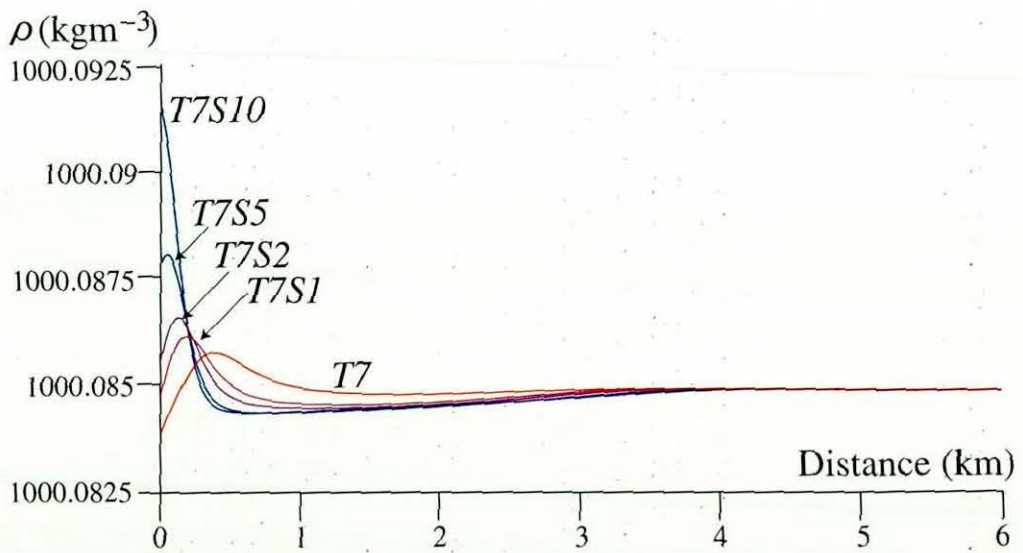


Figure 7.12: Density profiles for all *T7* cases after 2 days at 10 m depth.

Horizontal tracer transport is predictably trivial in that plots which are a more extreme version of figure 7.8(a) are obtained. Vertical transport is also surprisingly close to results from the *T9* scenario, with a slight increase in the maximum depth of downwelling as mentioned above. Neither plot is sufficiently original to merit inclusion in this study.

Chapter 8

Results - Small Lake Dynamics

While the deep lake model in the previous study of the riverine thermal bar allows interesting conclusions to be drawn about the maximum plume sinking depth and thermobaric effects, its large domain and relatively fine resolution requires some drastic assumptions to avoid excessive demands on computational power. In contrast, this chapter details the results of a more sophisticated riverine thermal bar simulation in a smaller lake section, nominally representative of the South Thompson River inflow to Kamloops Lake in British Columbia. In this way it is possible to test and extend the validity of results in chapters 5 - 7 with the resources available to this study.

The main advantage of studying the thermal bar in a smaller domain is the longer simulation time scales which are possible, enabling a model of the spring riverine thermal bar in Kamloops Lake throughout the majority of its lifespan. This longer simulation timespan is sufficient for a study of the interaction of the riverine thermal bar dynamics with the spring plankton bloom, and results extending the work of BK to the riverine case are presented in the next chapter.

Running each simulation for a longer period of time brings into question several assumptions made in the previous study of Lake Baikal, so the code is modified to cope with the removal of these simplifications, as fully described in section 2.1. Adopting the latitude and angle relative to north of the centreline of Kamloops Lake, coriolis forcing is now included in the momentum equations. In addition, surface heating of the river and lake will become important to the calculation of temperature gradients controlling the thermal bar, so a heat flux of $Q_s = 170 \text{ Wm}^{-2}$ is applied to the lake surface throughout

the simulation, while the river inflow is warmed by 0.2°C for every day of simulation (Carmack 1979). Another benefit derived from the consideration of a shallower domain is the increase in lake width which is possible. The lake in this study is taken to be 10 km wide accordingly, and the domain is also given a sloping river delta as the results are viewed as more of a realistic case study than the abstraction of the previous chapters.

Dynamical results of the reference shallow-lake simulation K are presented first, and then the consequences of a range of alterations to the model are studied. Effects of salinity and thermobaricity are also discussed, and the overall transport of riverine substances is illustrated to provide a complete background for the plankton population studies in chapters 9 and 10. Finally, the consequences of this work are discussed with reference to the deep-lake findings of earlier chapters. Throughout this chapter all velocity vector plots are shown at the actual grid resolution.

8.1 Background Flow-Field

As detailed in section 2.4.2, the temperature of the river inflow rises above the T_{md} after three days of simulation time and the onset of cabbeling takes place. The progression of streamline plots in figure 8.1 shows the characteristics of the resulting thermal bar throughout the 24-day span of the simulation.

This time-series of flow characteristics shows that the nature of the thermal bar is critically dependent upon the position of the T_{md} relative to the river mouth. In the early stages of the simulation there are steep localised temperature gradients near the inflow, generating a strong plume which sinks down the boundary (figure 8.1(a)). Conversely, the widely-spaced horizontal temperature gradients present in the later stages of the model generate a weak sinking region which is represented by vertical streamlines spread over several kilometres beneath a horizontal surface flow directed away from the river mouth (figures 8.1(b) and (c)). Studies presented in section 8.2.2 indicate that the development of coriolis forces may also be partly responsible for the width of this sinking region, through a weak downwards forcing inshore of the surface T_{md} .

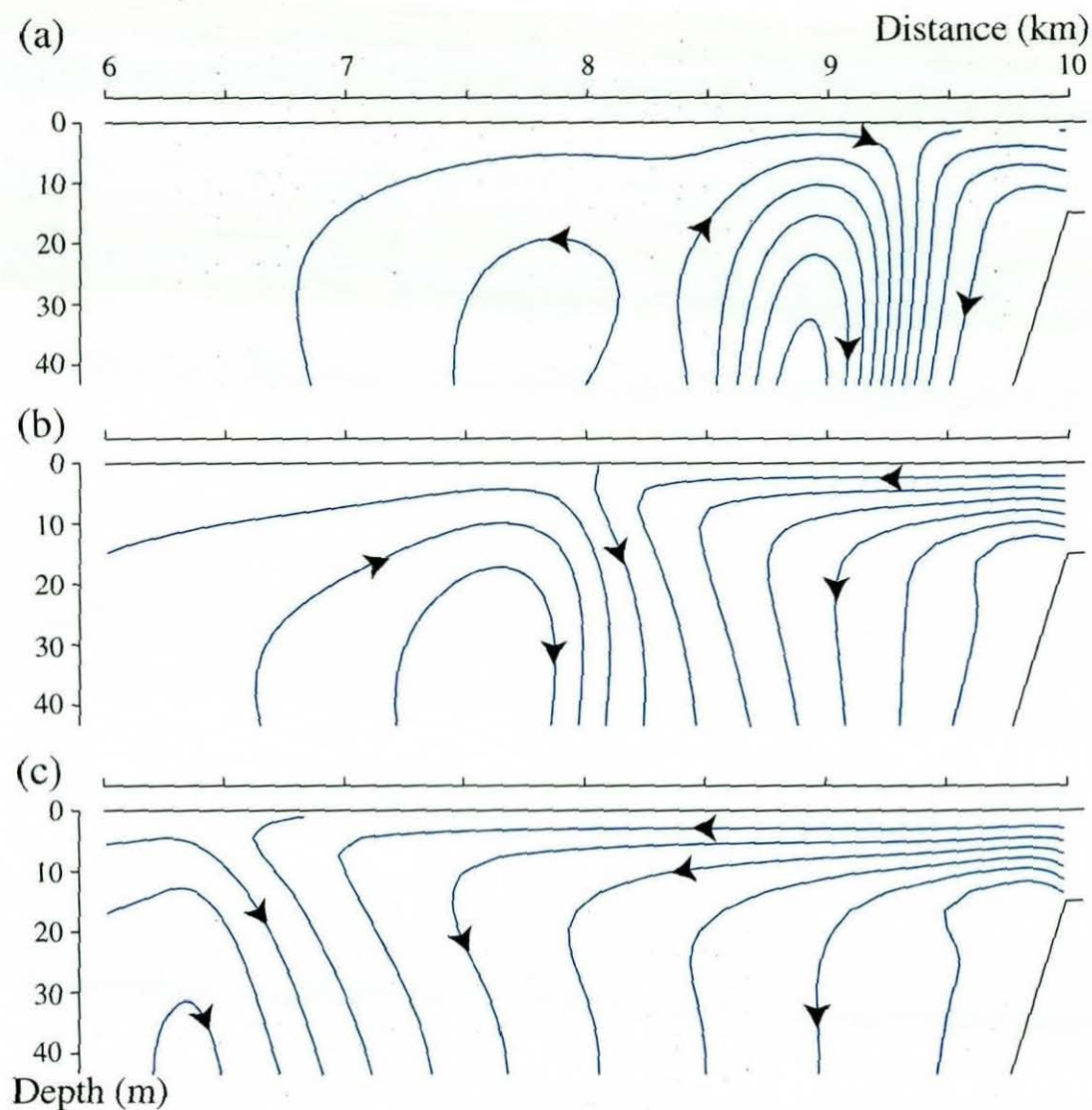


Figure 8.1: Progression of streamlines in simulation *K*: (a) 8 days, (b) 16 days, (c) 24 days.

Following the tradition of earlier thermal bar analyses, the above description of the evolution of this flow regime is related to plots of the near-surface density profile, shown in figure 8.2, which illustrate the temperature-based arguments above. Initially the density variation is confined to a very narrow area, but after 20 days the region of water containing the horizontal density gradient inshore of the T_{md} is nearly 3 km wide.

It can be seen that the river's density falls rapidly as the simulation proceeds, while the lake's density increases towards the maximum due to the slow warming imposed on the surface. Thus the density profile around the thermal bar evolves from an evenly-

balanced peak after 8 days to a steep one-sided density gradient after 20 days. Results of the simulation are thought to lose accuracy after 24 days as the effects of the arbitrary outflow condition become important once the thermal bar approaches the half-way point of the lake (see section 2.4.3).

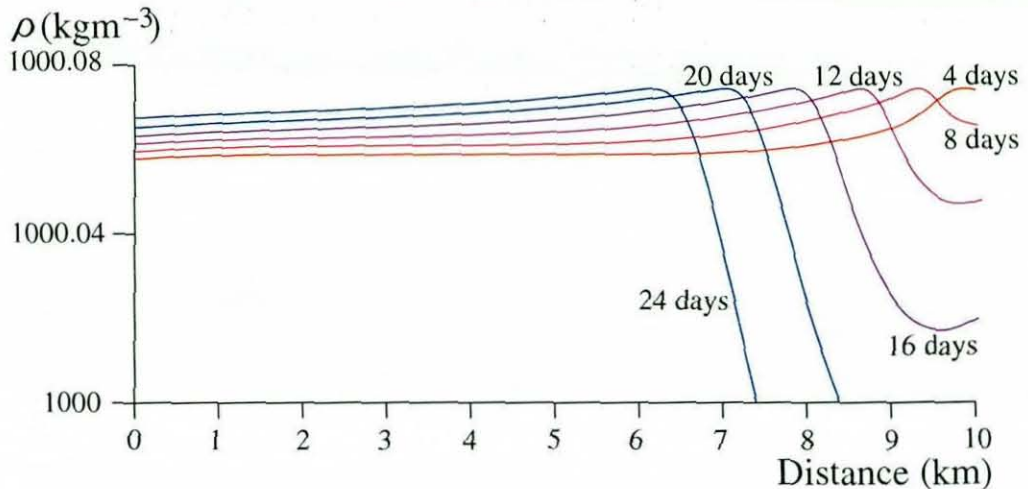


Figure 8.2: Horizontal density distribution at 5 m depth throughout simulation *K*.

This progression allows us to clarify the discussion by loosely defining three stages of thermal bar development, each roughly corresponding to a particular thermal case in the previous deep-lake chapters. These three stages are defined as follows:

Sinking Boundary Plume (days 3 - 8): density gradient is larger offshore of the thermal bar (density maximum) than inshore.

Travelling Thermal Bar (days 9 - 16): the offshore density gradient is smaller than the inshore gradient but is still large enough for a slowly-moving double-cell circulation to be present.

Surface Gravity Current (days 16 - 24): the inshore density gradient is so much larger than the offshore gradient that a strong horizontal surface current is generated. Cabbelling and sinking is present at the nose of this surface intrusion but is weakened considerably.

Each case is discussed individually in the following sections.

8.1.1 Sinking Boundary Plume

Flow patterns after 6 days are representative of dynamics of a thermal bar plume which flows down the near-river boundary (figure 8.3). Since mixed river and lake water is always denser than the ambient lake during this stage (see figure 8.2), the river plume immediately sinks on entry to the lake in a similar fashion to case $T7$. River water is quickly advected down the slope to the bed of this shallow lake and a powerful circulation cell is induced nearby. The steep density gradient offshore of the T_{md} causes strong flows towards the river near the surface which delay the propagation of the thermal bar.

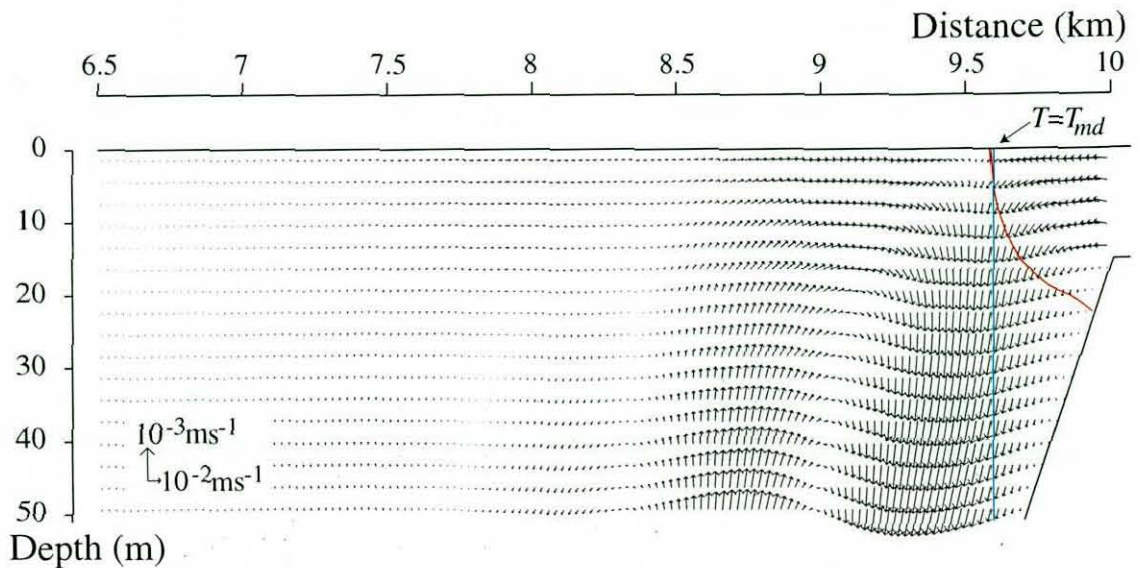


Figure 8.3: Velocity vectors and $T = T_{md}$ line for case K after 6 days of simulation. The vertical line marks the position of the profile in figure 8.6.

8.1.2 Travelling Thermal Bar

As the inflow temperature continues to rise, the density gradient inshore of the thermal bar grows and starts to move the thermal bar plume away from the boundary, forcing the sinking to take place over a broader region. Surface heating also weakens the density gradient offshore of the thermal bar, so that the delaying return flow at the surface slackens considerably. The situation after 12 days of simulation time is a good illustration of the travelling thermal bar stage, with a substantial stable region inshore of the

T_{md} and a slightly weakened downwelling spread over a wide area (compare figures 8.3 and 8.4(a)). Dense descending waters are formed at the position of the $T = T_{md}$ line throughout the depth of the lake, including the waters beneath those shown in figure 8.4(a).

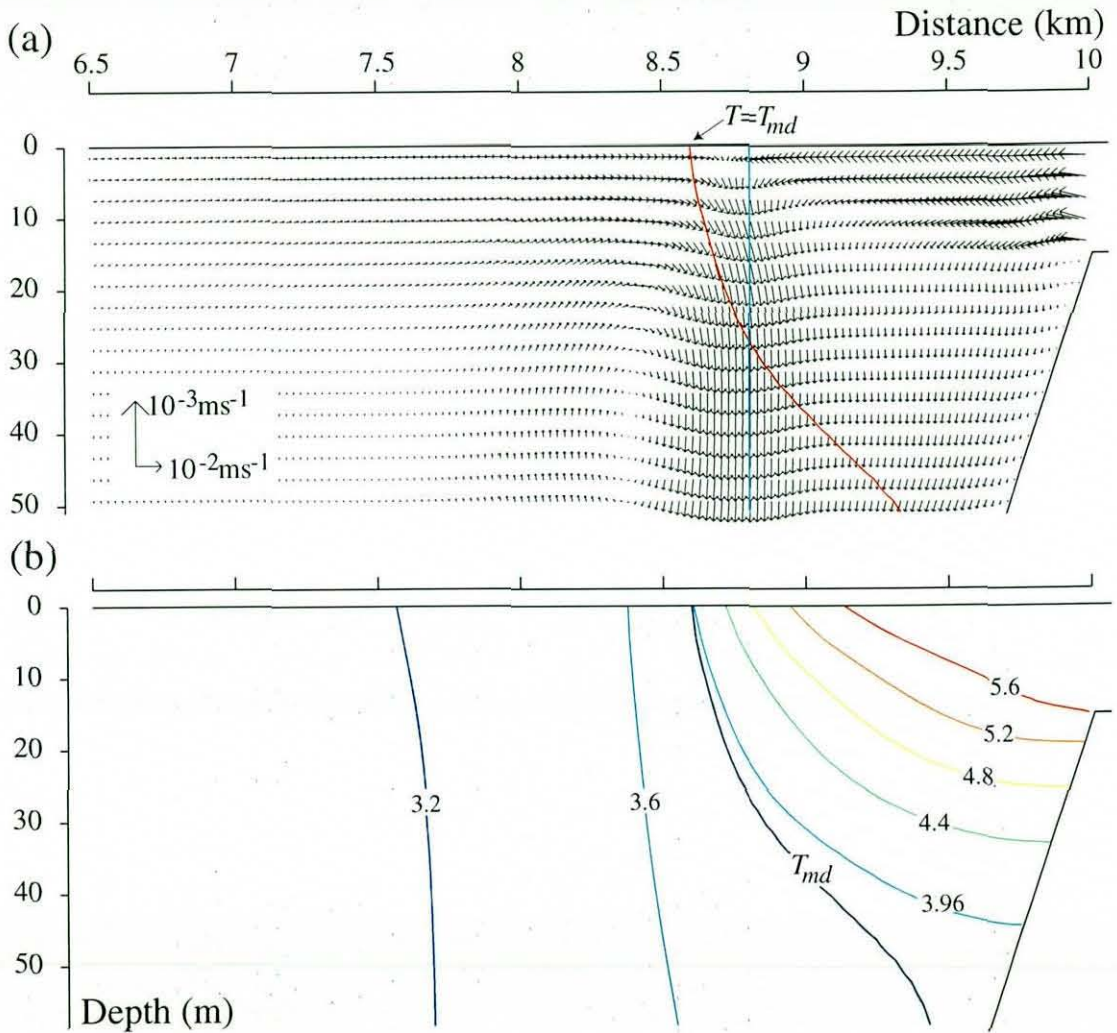


Figure 8.4: Properties of simulation K after 12 days: (a) velocity vectors and $T = T_{md}$ line (the vertical line marks the position of the profile in figure 8.6), (b) isotherms and $T = T_{md}$ line.

In contradiction to the deep-lake results, coriolis forcing ensures that there is no circulation inshore of the riverine thermal bar during this stage, a feature which is discussed in great detail in section 8.2.2 below. This result agrees with the conceptual model and observational data of the riverine thermal bar in Kamloops Lake (Hamblin

& Carmack 1978, Carmack 1979). The localised upwelling and 'arrested thermocline' inshore of the thermal bar reported by Carmack (1979) do not take place until later in the spring, so that unfortunately the temporal and spatial scales of these phenomena are too small for the present study.

Isotherms in figure 8.4(b) reveal that even in this relatively shallow lake the flow is slightly affected by the decrease in the T_{md} with depth. As the $T = T_{md}$ contour differs from the 3.96°C isotherm (the T_{md} at $p = 0$ and $S = 100 \text{ mgkg}^{-1}$) significantly at depth the decrease in the T_{md} clearly affects the buoyancy forcing in this simulation. This observation is pursued further in a full study of the effects of thermobaricity presented in section 8.3.

8.1.3 Surface Gravity Current

Velocities after only 20 days are selected to illustrate the behaviour of a cabbelling plume at the nose of a gravity current on the surface of the lake, although this flow regime actually continues until the thermal bar nearly reaches the outflow region. Vectors in figure 8.5 show that the former situation of downwards flow between the boundary and $T = T_{md}$ line persists until this time, but the most important feature of the circulation is the rapid surface current on the inshore side of the thermal bar. This horizontal current is two orders of magnitude larger than the downwelling (at $O(10^{-2}) \text{ ms}^{-1}$ and $O(10^{-4}) \text{ ms}^{-1}$ respectively), and is responsible for moving the T_{md} line swiftly across the lake.

By this time the thermal bar is almost 3 km from the river mouth, and horizontal temperature gradients are weakened to such an extent that the buoyancy forces, which attempt to compensate density differences by acting in proportion to their magnitude, are much weaker. This slackening of forces results in a much slower downwelling. A progression of vertical velocity profiles from a section which is taken as close as possible to the centre of each thermal bar plume shows this weakening clearly (figure 8.6). It seems that after 20 days the lake's circulation has switched from diverting most of the river through the depths of the lake to mixing inflow water throughout the region behind the thermal bar. This is an intermediate stage in the typical spring succession, since the disappearance of the thermal bar marks the onset of summer stratification and the short-circuiting of river water across the surface of the lake (Carmack 1979).

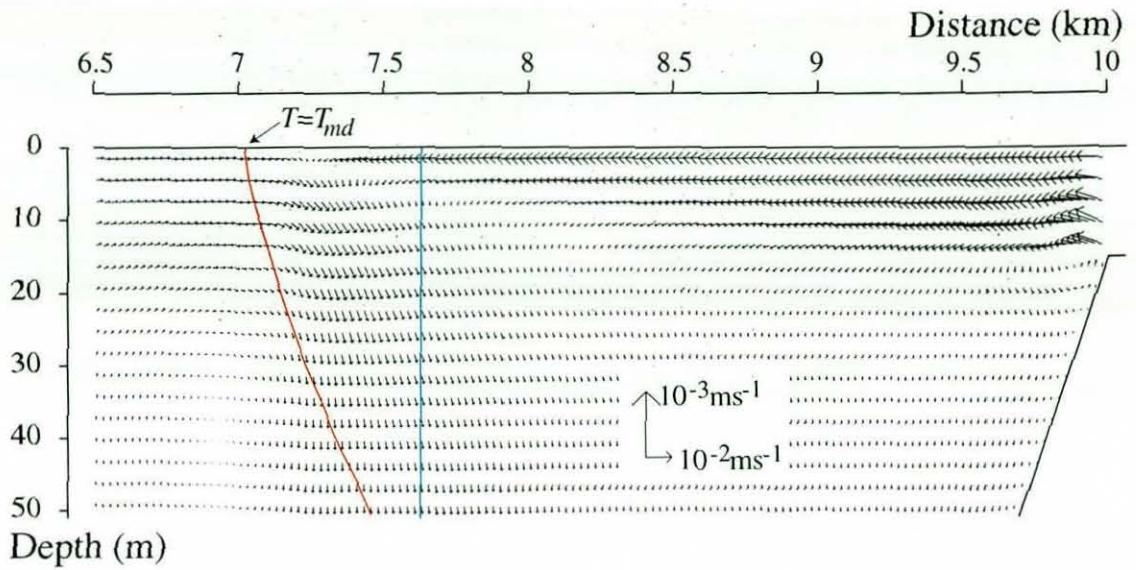


Figure 8.5: Velocity vectors and $T = T_{md}$ line for case K after 20 days of simulation. The vertical line marks the position of the profile in figure 8.6

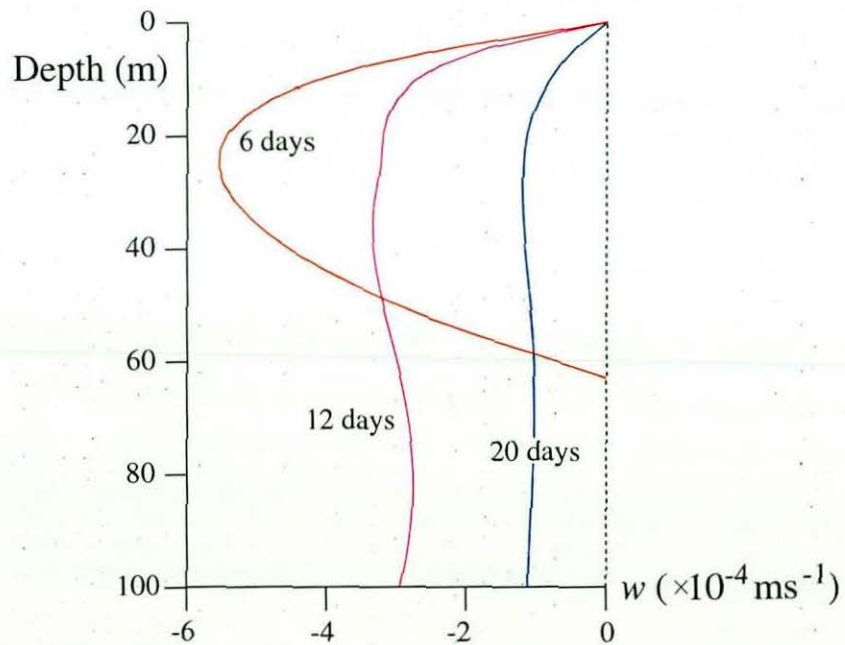


Figure 8.6: Vertical velocity in thermal bar plumes for case K after various simulation times. The position of each profile is marked in figures 8.3, 8.4(a) and 8.5.

8.2 Effects of Model Improvements

If the earlier discussion of Lake Baikal is to be compared in any way to the results of this long-term simulation, it is important to assess the contribution of factors which are not included in the former model but which are required in the latter for accuracy. To this end the effects of insolation, rotation, and bathymetry are discussed in this section.

8.2.1 Surface Heat Flux

An important development of the basic riverine thermal bar model is the introduction of an increasing lake temperature via the surface heat flux Q_s . Importantly, introducing surface heating at a realistic value for Kamloops Lake should not shift our attention away from the riverine thermal bar, since the thermal structure of this lake is dominated by riverine fluxes (Carmack et al. 1986). While the results of the model reflect this riverine dominance (see, for example, the isotherms in figure 8.4(b)), surface heating still has a significant influence on the thermal bar phenomenon.

Figure 8.2 clearly shows the increasing lake density offshore of the thermal bar which results from a temperature increase in this region. As the inshore density decreases throughout the simulation, the surface heat flux therefore quickens the development of uneven density gradients on either side of the thermal bar and hastens the progression through the three flow stages discussed above. This effect is intensified by the thermal bar's role as a vertical boundary between stable and unstable regions. The stable area on the inshore side of the T_{md} warms more rapidly under the same heat flux due to a decreased vertical thermal diffusivity, thus widening even further the anomaly between density gradients on either side of the maximum. The effect of surface heating of the inshore region is evident from the temperature maxima of figure 8.7(a), which are slightly warmer than the river inflow in the later stages of the simulation. These predicted thermal profiles are strongly reminiscent of near-shore measurements in Lake Ontario by Gbah & Murthy (1998).

Figure 8.7(b) shows temperature profiles from a test case, KH , in which the model is similar to case K but with the surface heat flux removed. Comparing the profiles illustrates the effect of surface heating on the temperature distribution around the T_{md} .

These plots also show that the thermal bar propagates more quickly when under the influence of a surface heat flux, because the additional heat input to the lake (which has a more profound effect on the stable region inshore of the density maximum) increases the amount of water warmed to above the T_{md} in a given time. In addition, heating of the unstable waters in the open lake reduces the density gradient offshore of the T_{md} and thus weakens the return flows responsible for delaying the horizontal spreading of warm river waters.

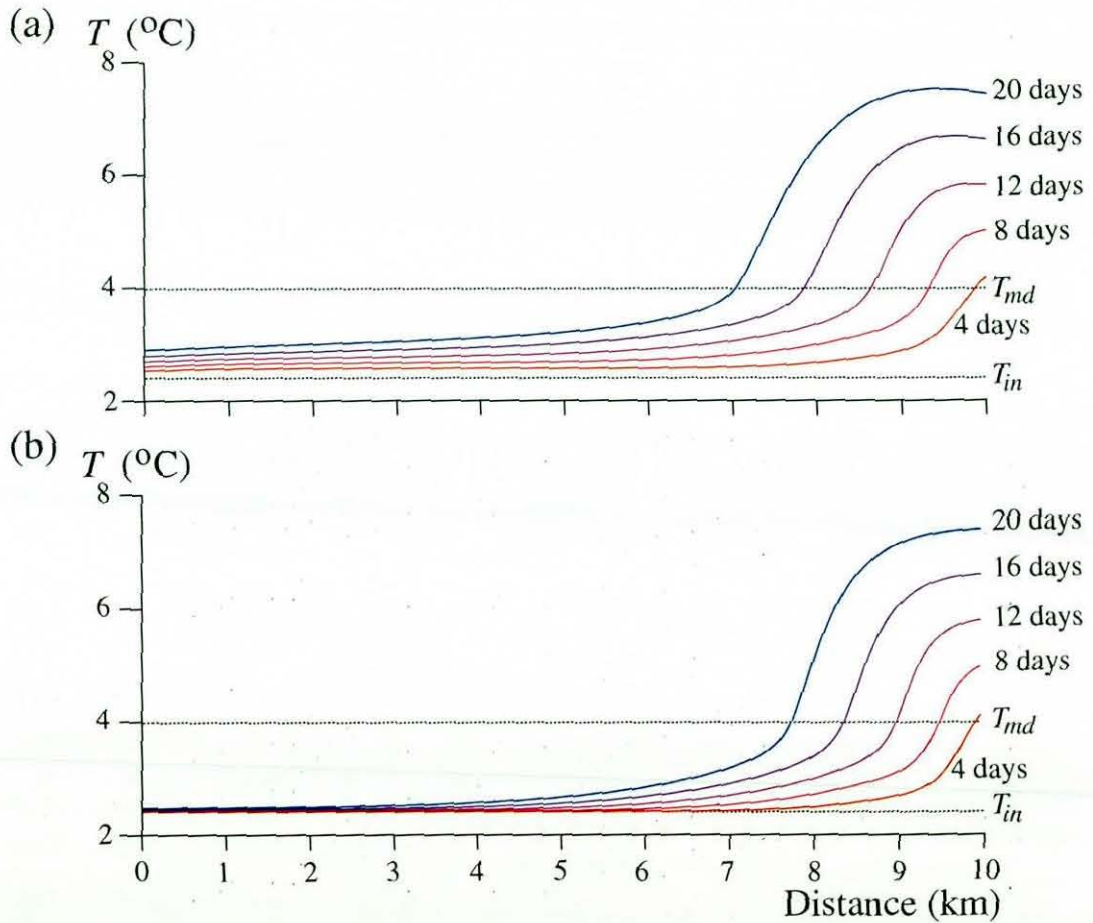


Figure 8.7: Temperature profiles 5 m from the surface throughout each simulation: (a) case K , (b) case KH .

8.2.2 Coriolis Forces

In order to examine the effects of coriolis force on the dynamics of simulation K , an extra simulation is introduced, KC , in which coriolis forces are neglected. By explaining the

differences between cases K and KC with reference to the coriolis forces in simulation K it is then possible to scrutinise the effects of the Earth's rotation on the riverine thermal bar.

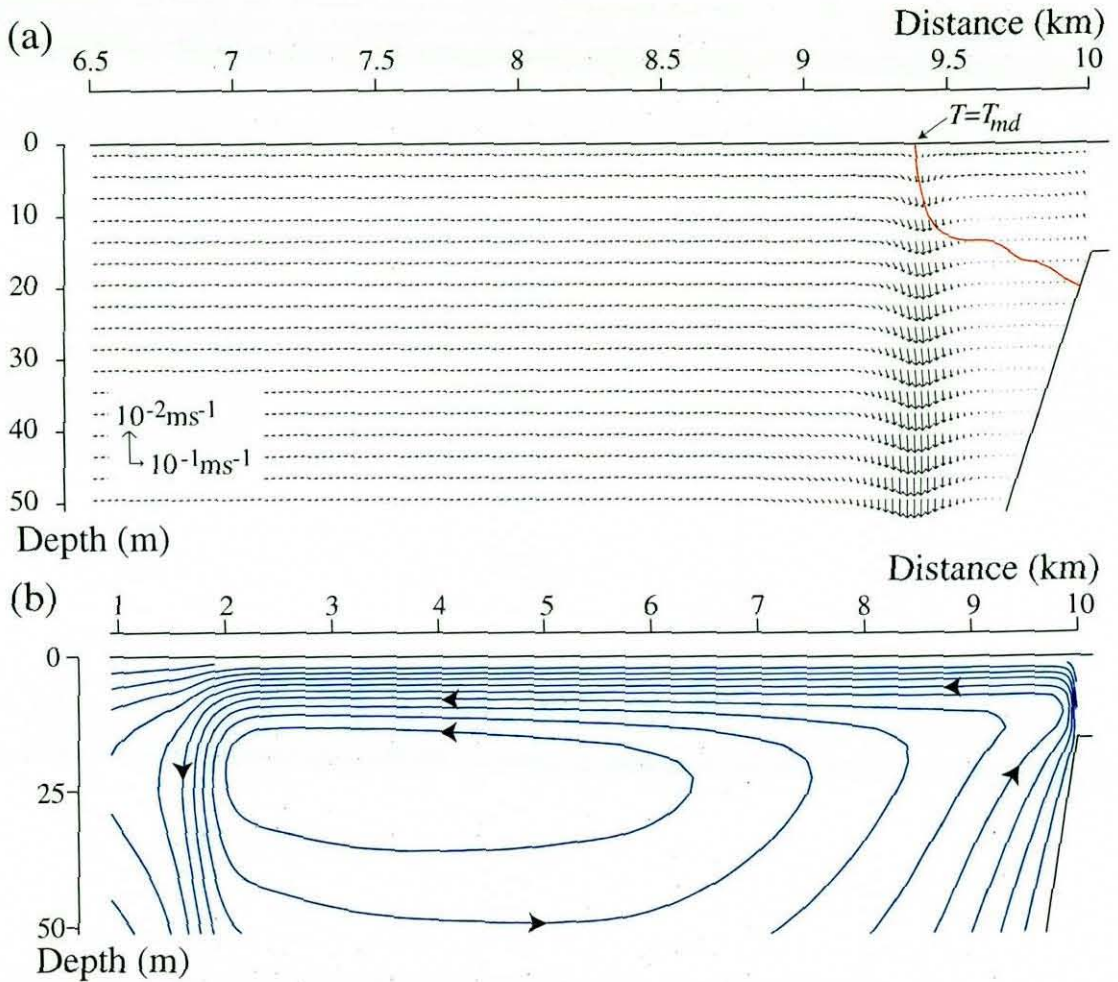


Figure 8.8: Dynamics of case KC after two simulation times: (a) velocity vectors and $T = T_{md}$ line after 6 days, (b) streamlines after 24 days.

Figure 8.8 shows the dynamical behaviour of case KC at two stages of the simulation, revealing that the sinking velocities are an order of magnitude larger than those of case K , and have reached unrealistic levels on the basis of observations discussed in section 1.3. It is also clear from a comparison of these plots with figure 8.1 that the propagation rate of the thermal bar is initially slightly increased and then massively reduced by coriolis forces, and that the presence of a circulation (i.e. upwards motion) on the

inshore side of the thermal bar plume is suppressed by coriolis forcing. With reference to the formulation of components of the coriolis force (as detailed in chapter 2), each of these observations is dealt with separately below.

An increase in velocity in the coordinate directions contained in the two-dimensional section could be expected with the neglect of coriolis, because the thermal buoyancy forcing remains the same while transfer of momentum to the velocity component normal to the section is removed. In figure 8.9(a) the coriolis forcing in the normal direction is plotted for case *K*, which gives a good indication of how the familiar two-dimensional riverine thermal bar drives flow in the alongshore direction.

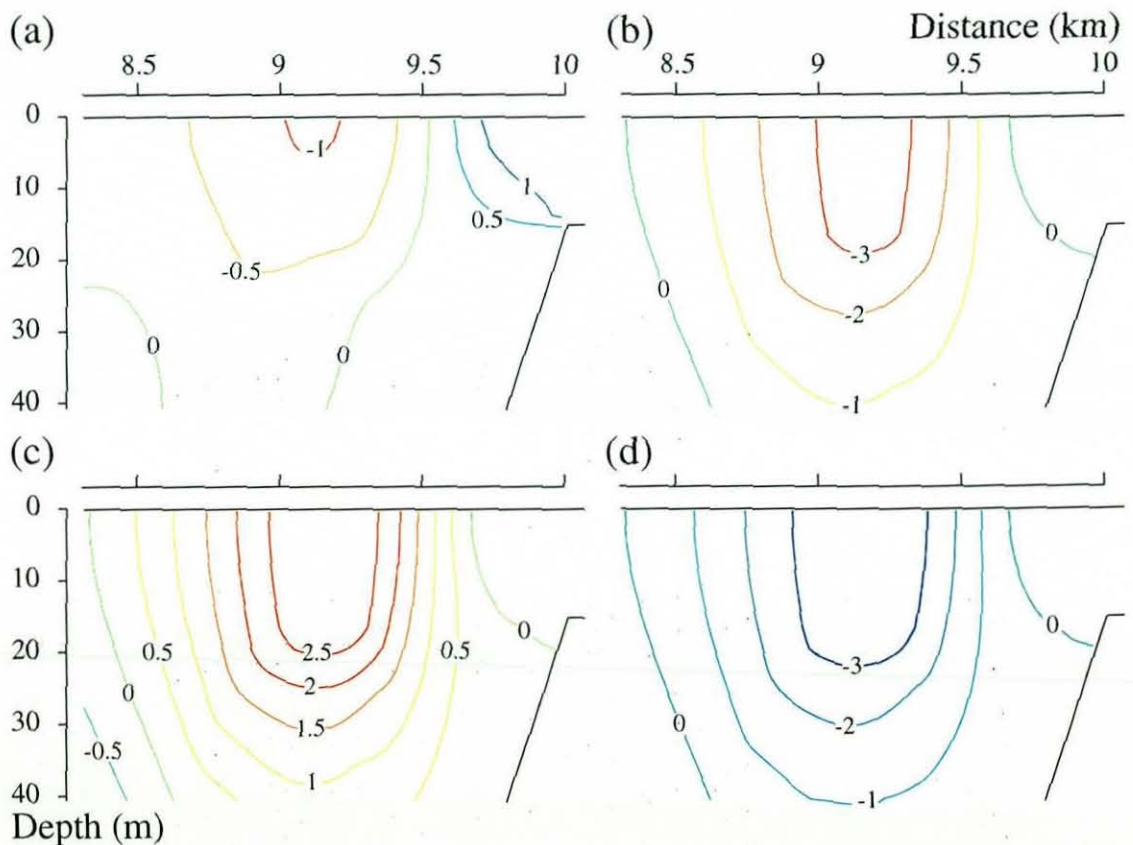


Figure 8.9: Characteristics of the coriolis forcing in case *K* after 6 days of simulation: (a) component normal to section ($\times 10^{-6} \text{ ms}^{-2}$), (b) velocity normal to section ($\times 10^{-2} \text{ ms}^{-1}$), (c) vertical component ($\times 10^{-6} \text{ ms}^{-2}$), (d) horizontal component ($\times 10^{-6} \text{ ms}^{-2}$).

The figure shows that the converging flows near the surface T_{md} cause a reversal

in this forcing near the position of the thermal bar, with flows accelerated 'out of the page' (in the negative y -direction) offshore of the thermal bar and 'into the page' inshore of the thermal bar. The resulting v -velocities, shown in figure 8.9(b), show a similar pattern, implying that these forces are persistent, but with an increased dominance of the offshore velocity in the negative y -direction.

Plots of the other coriolis terms from simulation K after 6 days show that in the area of interest, the vertical component is acting upwards (figure 8.9(c)) and the transverse component (in the x -direction) is acting away from the shore (figure 8.9(d)). A close examination of the formulation of these coriolis components (equations (2.2) - (2.4)) reveals that both of these effects are consistent with a strong velocity directed in the negative y -direction. Therefore, the coriolis-derived generation of velocities normal to the section in response to the buoyancy forcings of the thermal bar initially causes the sinking velocity to decrease and the horizontal propagation rate to increase. Neglecting coriolis therefore causes the observed strengthening of descending flows and a slackening of the horizontal propagation rate in the early stages of simulation KC .

A striking feature of simulation KC is that it has a circulation cell inshore of the thermal bar while K has a uniformly sinking region between the inflow and the thermal bar plume throughout the simulation. Vertical velocity in the non-coriolis simulation responds solely to horizontal variations in buoyancy forcing and has very localised flows accordingly, while vertical velocity in simulation K is influenced by all of the other velocity components in its neighbourhood via coriolis forcing. Once the thermal bar has moved away from the inflow, the near-shore region is allowed to rise in simulation KC as it feels no downwards buoyancy forcing, whereas it experiences a downwards forcing in simulation K as an ultimate result of the momentum transfer of the velocity component perpendicular to the section.

In figure 8.10, an examination of the coriolis forces after 12 days explains this process. Horizontal flow inshore of the thermal bar causes a coriolis forcing in the positive y -direction (figure 8.10(a)), which generates a corresponding flow (figure 8.10(b)). This result is in agreement with many experimental and theoretical studies of Kamloops Lake, where a deflection to the right is often observed in the spring river plume (St.John et al.

1976, Hamblin & Carmack 1978). This effect on the horizontal flow leads to a negative vertical coriolis forcing over most of the near-river region (figure 8.10(c)), causing a weak downwelling inshore of the thermal bar.

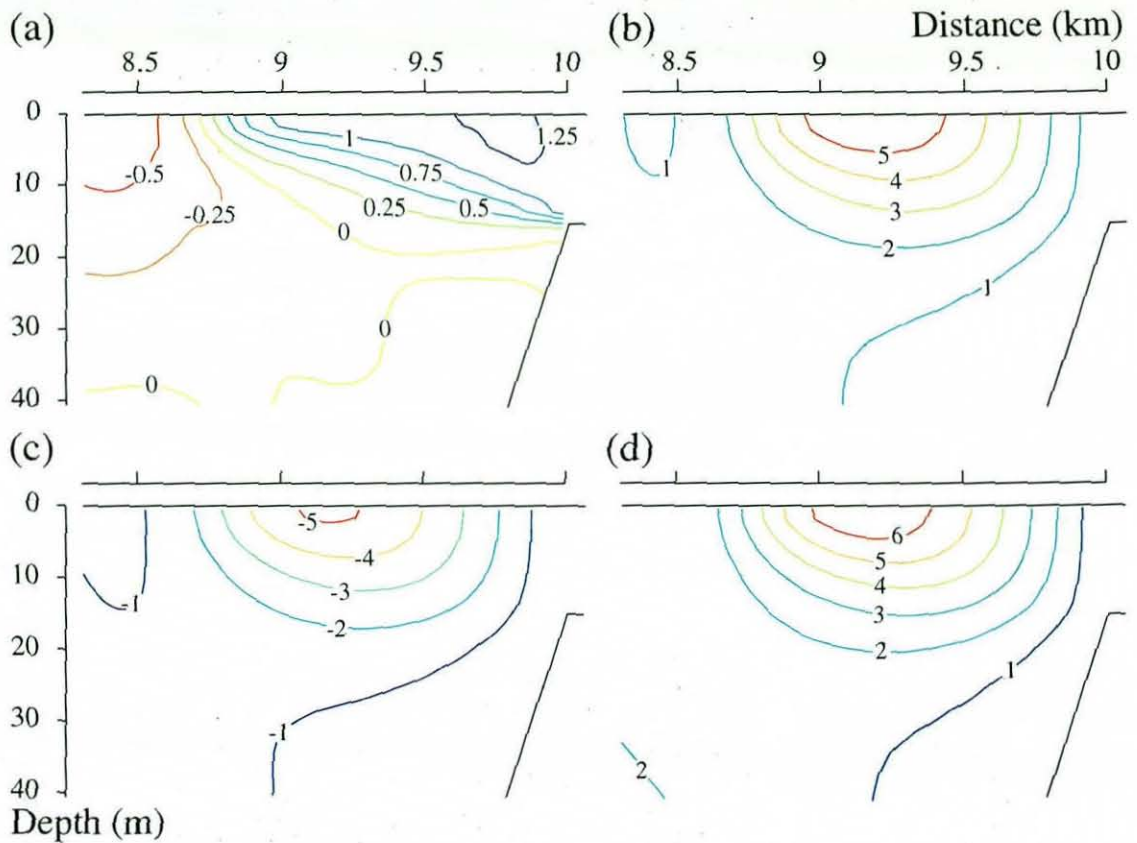


Figure 8.10: Characteristics of the coriolis forcing in case *K* after 12 days of simulation: (a) component normal to section ($\times 10^{-6} \text{ ms}^{-2}$), (b) velocity normal to section ($\times 10^{-2} \text{ ms}^{-1}$), (c) vertical component ($\times 10^{-6} \text{ ms}^{-2}$), (d) horizontal component ($\times 10^{-6} \text{ ms}^{-2}$).

Interestingly, flow in the positive y -direction (into the page) causes a coriolis forcing in the positive x -direction, i.e. towards the shore (figure 8.10(d)). This explains why the horizontal propagation of the non-coriolis case *KC* eventually overtakes that of case *K*. Initially the coriolis forces act to increase the horizontal spreading of warm river water (figure 8.9(d)) and the propagation of the thermal bar is encouraged, but later the coriolis forces suppress the horizontal movement by acting towards the river (figure 8.10(d)) and the non-coriolis plume of case *KC* propagates more quickly.

8.2.3 Realistic Bathymetry

The intention of this section is to test the effects of a sloping river delta on the results generated by the riverine thermal bar model. This analysis is performed by comparing case *K* with a similar model, *KB*, which is identical apart from the section bathymetry, which is taken to be a 10 km \times 150 m rectangular box.

Velocity vectors from simulation *KB* after 12 days (figure 8.11) show remarkably similar results to vectors from simulation *K* after the same time period (figure 8.4(a)). In fact, the top 20 m of each domain are virtually identical to each other, although the sloping domain marginally increases the horizontal propagation of the thermal bar.

There is, however, a significant difference between the dynamics of the thermal bar plumes at depth, and the difference in curvature of the $T = T_{md}$ contours provides a useful clue as to why this is. Unlike case *K*, the water sinking beneath the warm river intrusion in case *KB* is not channeled into the thermal bar plume by a sloping boundary. This channeling has the obvious important consequence of directly strengthening the plume in simulation *K*, but also accounts for the difference in downwards transport of heat which is responsible for the variation in curvature between the two $T = T_{md}$ contours.

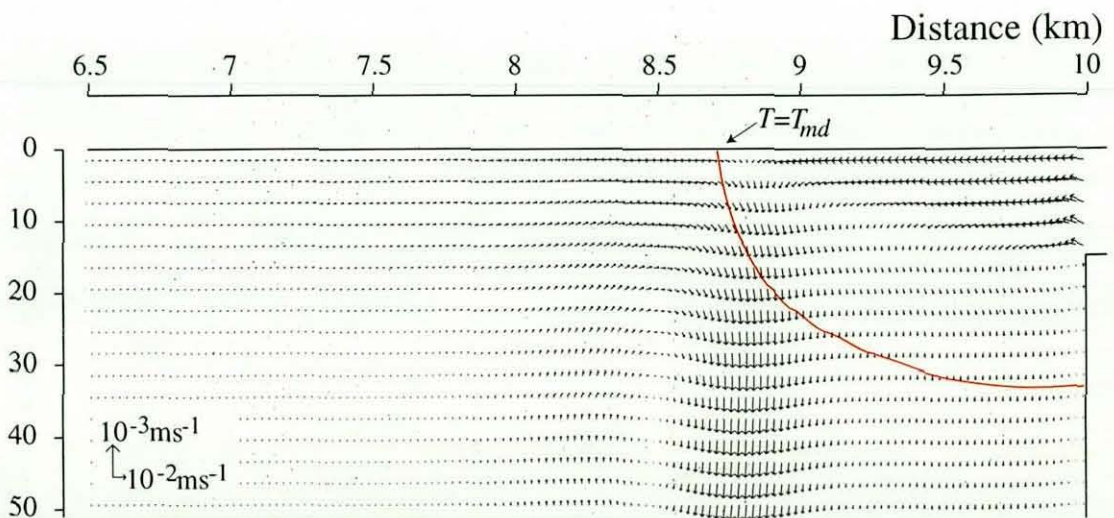


Figure 8.11: Velocity vectors for case *KB* after 12 days of simulation.

8.3 Effects of Thermobaricity

In chapters 6 and 7 it is shown that thermobaricity has a vitally important influence on the vertical movement of waters in the thermal bar plume of a deep lake. In shallower lakes such as Kamloops, thermobaricity is usually neglected as the vertical variation of the thermal expansion coefficient is assumed negligible due to the small magnitude of the T_{md} variation between the lake surface and bed. However, thermobaricity is fully resolved in this study and it is thus important to examine its effect, both to justify its inclusion and for comparison of these results with the deep lake studies.

Comparing velocity vectors from the reference simulation K with those from a new simulation, KP , which has no thermobaricity (figures 8.4(a) and 8.12 respectively), immediately reveals the strong influence of thermobaricity on the vertical position of the $T = T_{md}$ line. Whereas the $T = T_{md}$ contour in simulation K is shifted towards cooler water at depths between 40-80 m as a result of the decrease in the T_{md} with depth, in simulation KP it follows the 3.96°C isotherm.

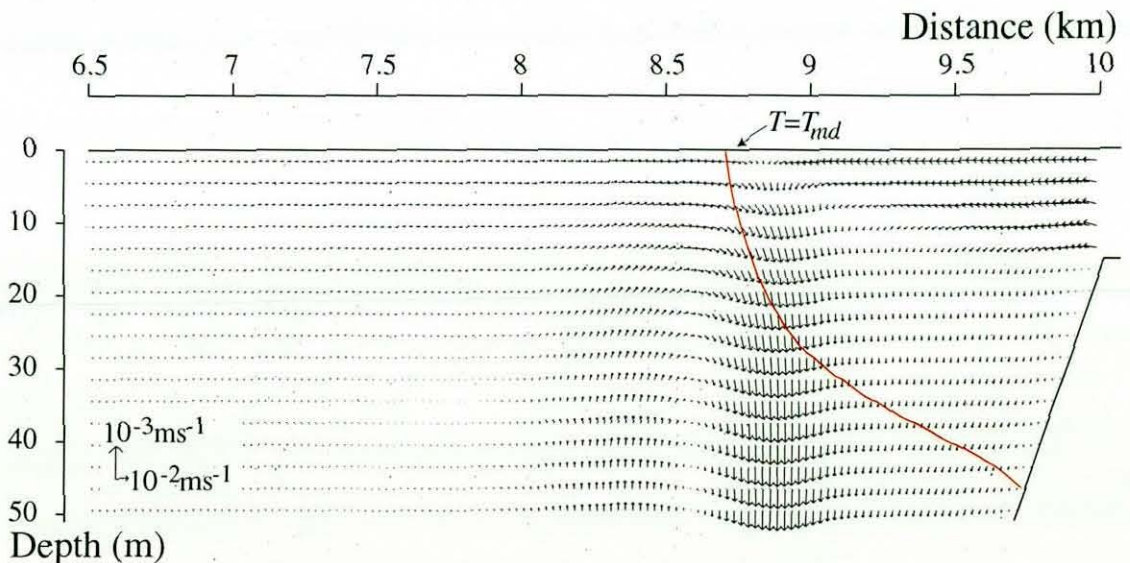


Figure 8.12: Velocity vectors for case KP after 12 days of simulation.

Close examination of the velocity vectors shows that sinking motions are slightly stronger in case KP , despite the fact that the simulation K plume sinks down the $T = T_{md}$ line for longer due to its thermobaricity-induced curvature. This is explained

by consideration of the buoyancy change ΔB , which reveals that the negative change in buoyancy is larger in case *KP* and does not decrease with depth (not shown). Although the direct effects of this small difference in ΔB are small, the extra advection of heat down the sloping boundary it causes throughout the early stages of simulation *KP* produces larger horizontal temperature gradients at depth which culminate in stronger descending flows.

This discussion proves that thermobaricity has an effect in shallower lakes, but that it is probably negligible in most modelling of lakes with a comparable depth to Kamloops when vertical mixing is not the main object of the study. Slight differences in vertical motion are observed but these are only important over relatively long time periods, and it is concluded that thermobaricity need only be included in relatively detailed shallow lake models which are seeking quantitative results. Thermobaricity is not neglected here as the model is designed for the study of vertical motions, and analogies are drawn between Kamloops and Lake Baikal, in which thermobaricity is much more important.

8.4 Effects of Salinity

Salinity data from Kamloops Lake is relatively difficult to find, even in comparison with Lake Baikal, but it is clear from the small discussion of conductivity data by St. John et al. (1976) that the salinity of Kamloops Lake and the South Thompson River have a significant annual variability, peaking in late winter and troughing in the early-summer freshet period. In summer, the river salinity can actually sink below that of Kamloops Lake, but during the period which is modelled here the salinities appear to be relatively homogeneous in Kamloops Lake and slightly higher in the South Thompson River.

The salinities added to the river in this study are considerably larger than those added to the Selenga River in previous chapters. This is necessary for the examination of saline effects because the wider range of temperatures involved in the longer time-period of this study means that salinity is less important in the calculation of buoyancy forcing. Saline cases described in this section range from *KS5*, with a reasonable 5 mgkg^{-1} salinity added to the river, to case *KS50*, which has an unrealistically large 50 mgkg^{-1} (50%) increase applied to the river salinity.

The necessity of introducing larger riverine salinities is highlighted by the large thermally-induced variation in density seen in the horizontal profiles of figure 8.13. It is obvious that even with relatively large riverine salinities (up to 20 mgkg^{-1}), the change in density due to haline effects is a fraction of the total spatial variation due to thermal conditions. However, with a large enough riverine mineral loading the density profiles show similar trends to results from chapter 7, with an increase in the maximum density and offshore density difference and a reduced density difference inshore of the thermal bar.

These observations of thermal dominance over haline effects are borne out by the velocity vector plots from the saline simulations. Contrary to expectations, figure 8.14 shows that the downwelling is very resistant to saline influence, and that a 50 mgkg^{-1} increase in riverine salinity is necessary to force a qualitative change in the flow field. The most obvious effect of the introduction of salinity gradients is the slight decrease in horizontal propagation of the $T = T_{md}$ line near the surface (figure 8.14). This straightens the $T = T_{md}$ contour throughout the depth of the lake, which increases the plume velocity because the water is accelerated by the thermally-derived buoyancy forces for longer as it sinks. Sinking within the thermal bar plume therefore becomes slightly stronger and is concentrated into a narrower region.

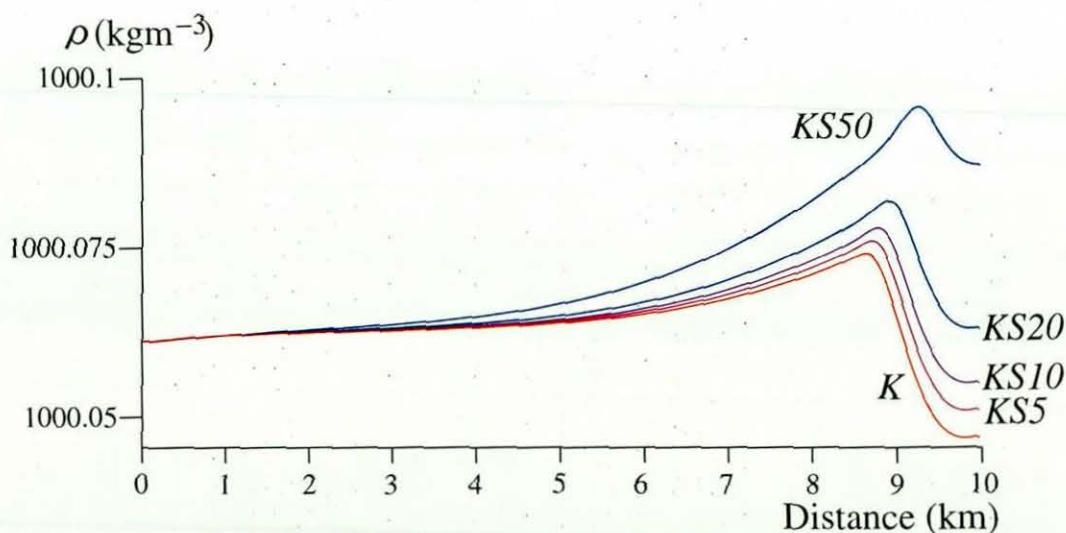


Figure 8.13: Density profiles for all saline variants of case *K* after 12 days at 5m depth.

Plots of ΔB , ΔB_T and ΔB_S clearly state that thermal buoyancy change dominates haline effects in all simulations apart from the most saline, *KS50*, which also has the only really significant change in flow regime (not shown). It therefore takes a riverine salinity increase which is unrealistically large (according to St. John et al. (1976)) to seriously influence the dynamics of the spring thermal bar in Kamloops Lake, and salinity is assumed to be negligible in this shallow-lake model.

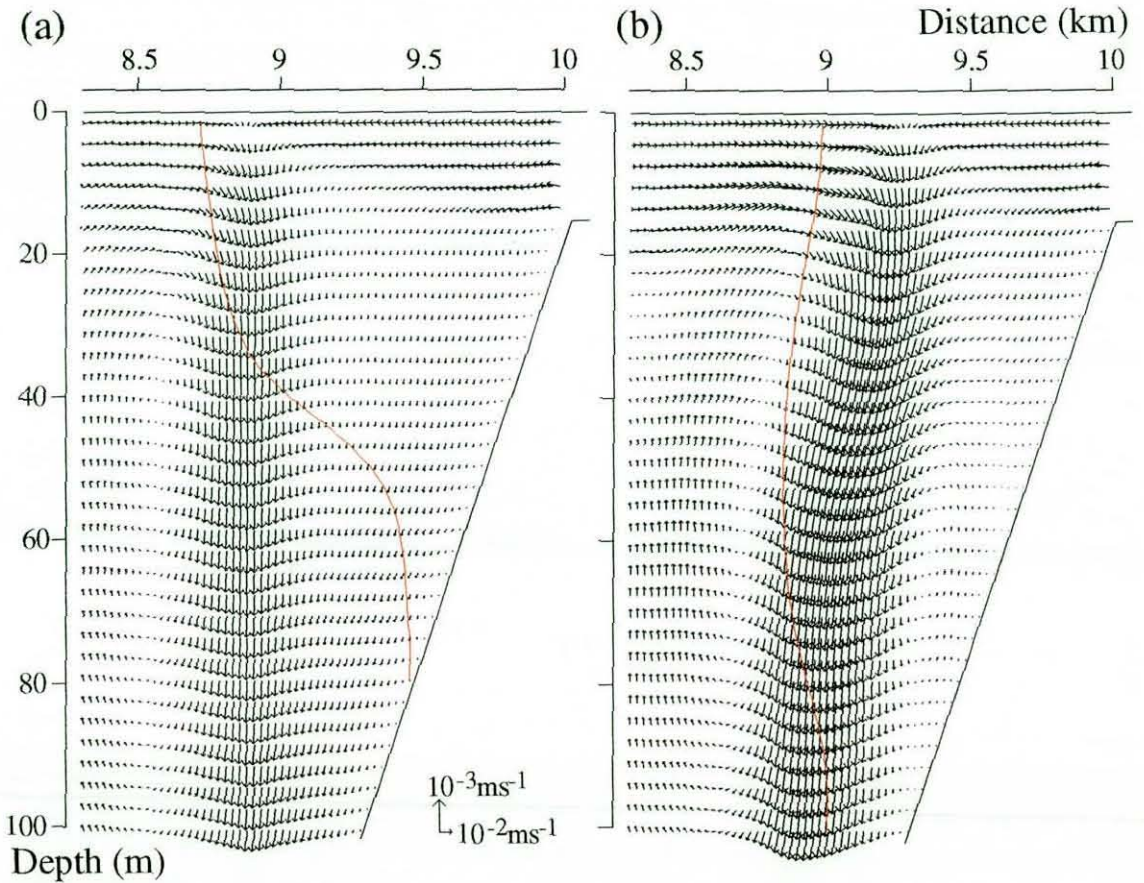


Figure 8.14: Velocity vectors and $T = T_{md}$ contour for saline variants of K after 12 days: (a) case *KS10*, (b) case *KS50*.

It should be emphasised here that large salinities have not been considered in great detail in this study as the dynamics of primary interest are those dominated by buoyancy forcings dependant on local temperature variations relative to the T_{md} . In any case, Kamloops Lake is a relatively fresh lake which is known to be almost completely dominated by the large temperature gradients found in Spring (Carmack 1979). However, salinity distributions may also be extremely important in determining lake flows,

as shown in the study of Lake Baikal, and should not be dismissed on the basis of this study of Kamloops Lake.

8.5 Transport of Riverine Substances

In this section the various choices made in the formulation of simulation *K* are assessed in terms of the resulting transport of riverine substances. The movement of river-borne matter is worthy of study in its own right as an indicator of pollution, oxygenation, etc. but in this section the analysis is also regarded as a preliminary result for the plankton studies of chapter 9.

The plankton study is an attempt to quantify the effects of the riverine thermal bar on the spring phytoplankton growth in Kamloops Lake. A study of the riverine tracer distribution is therefore required in order to quantify the effects of plankton boundary conditions and thus decide whether the plankton model is predicting effects caused by the inflowing river, the dynamics of the thermal bar, or biological factors controlling plankton interaction.

8.5.1 Chosen Simulation

Tracer characteristics in the chosen simulation *K* follow a straightforward progression which characterises the flow-field throughout the model run (figure 8.15). The riverine tracer initially sinks down the boundary but then spreads horizontally across the lake in reflection of the change in flows within the thermal bar, which is described in section 8.1. The contours of tracer concentration switch accordingly from a vertical structure with transport predominantly downwards, to a horizontal formation in which high concentrations of the tracer-rich river water float on the surface of the lake.

The vertical transport which takes place early in the simulation (figure 8.15(a)) means that river-borne matter will not initially travel far in the euphotic zone before sinking, heralding an initial period of low influence of riverine conditions on plankton growth. However, after 20 days of simulation there is an extensive near-surface region which contains 90% river water (figure 8.15(b)), indicating that the plankton productivity in this area will eventually be heavily influenced by the riverine boundary conditions.

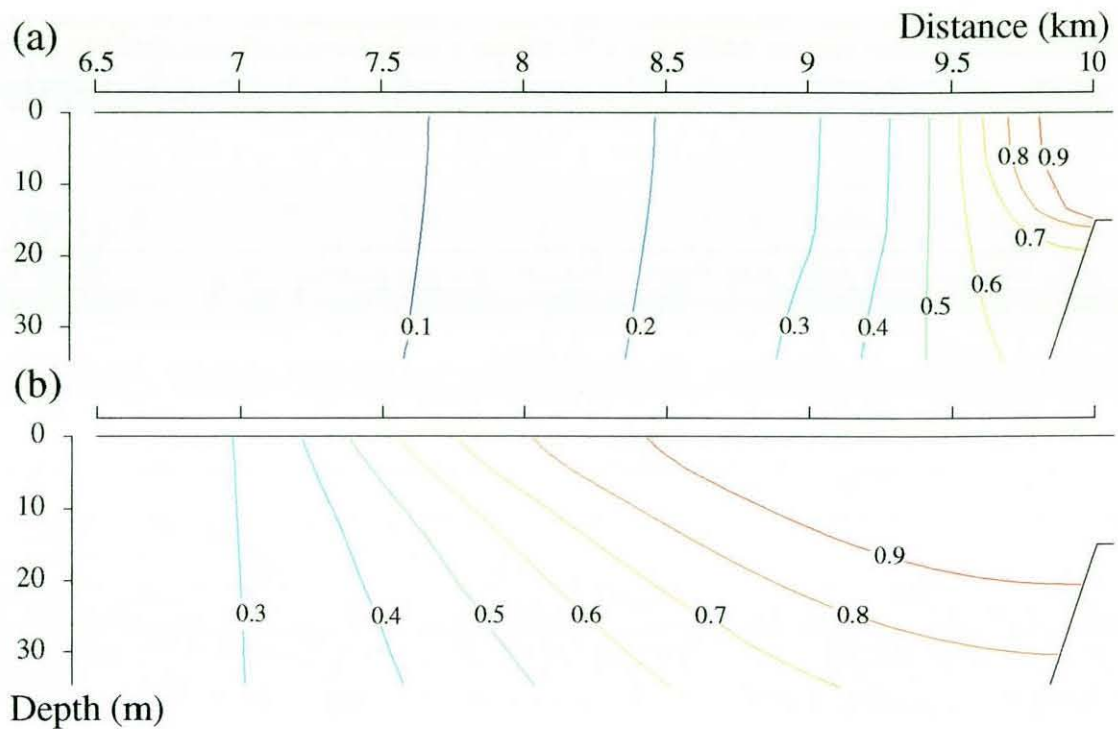


Figure 8.15: Contours of tracer concentration in simulation *K*: (a) 6 days, (b) 20 days.

8.5.2 Comparison With Test Cases

Plotting the horizontal movement of the surface T_{md} signature, figure 8.16 shows a reasonable similarity in the rate of horizontal propagation of the thermal bar between most of the different cases. Unsurprisingly the neglect of thermobaricity in this shallower lake has very little effect on the horizontal movement of the thermal bar, but unexpectedly this plot shows that the influence of bathymetry is also rather small. After 30 days of mixing the position of the riverine thermal bar in a rectangular lake is within 300 m of the position of the same phenomenon in a sloping river delta, which highlights the riverine dominance of thermal effects in these simulations. The progression plot also confirms that the surface heat flux has a significant role in increasing the horizontal propagation of the thermal bar by warming more water through the T_{md} .

By far the most important feature of this horizontal progression plot is the qualitative change in thermal bar behaviour which may be induced by the addition or neglect of coriolis forces. This result illustrates the findings of section 8.2.2, where a direction

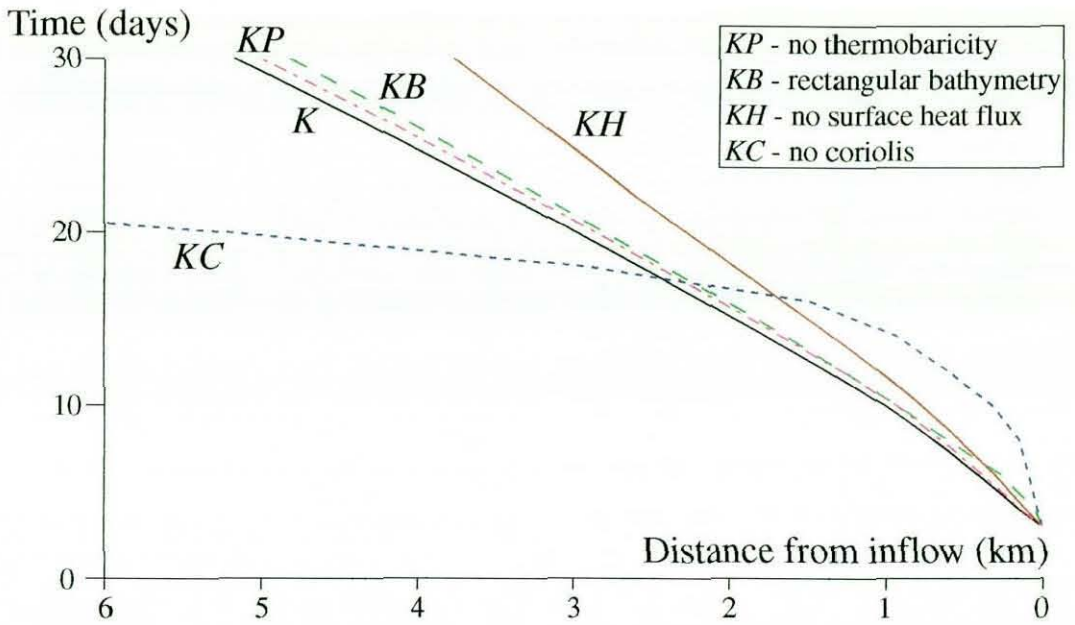


Figure 8.16: Horizontal propagation of the surface T_{md} in all test cases.

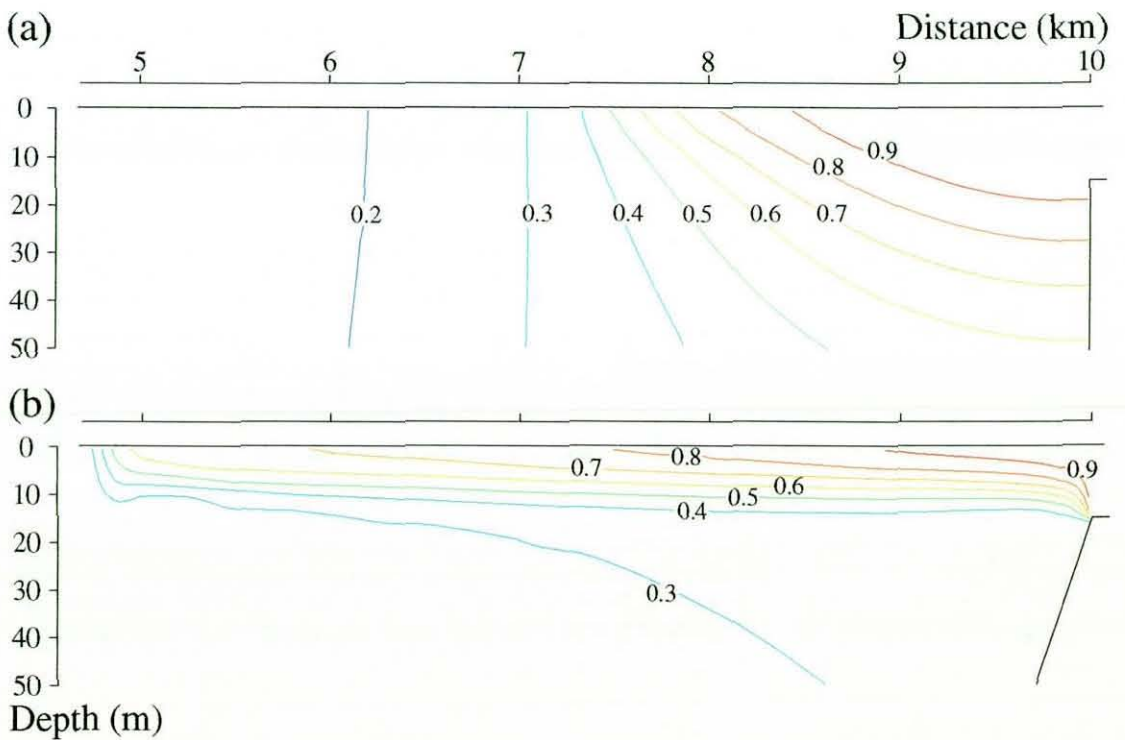


Figure 8.17: Contours of tracer concentration after 20 days of simulation: (a) KB , (b) KC .

reversal of the dominant velocity component normal to the section reverses the coriolis

force acting in the x -direction. This component is found to accelerate the movement of the thermal bar initially but impede it later on, producing the near-linear propagation curve of simulation K out of the constantly accelerating profile of simulation KC .

The vertical tracer transport of selected trial simulations is examined through contours of riverine tracer, plotted in figure 8.17, which are then compared to figure 8.15(b). Contours of tracer from cases KP and KH are not shown as they differ very little from those of case K , with the vertical transport slightly increased in both cases.

The results of figure 8.17(a) show that the rectangular-box domain has an extremely similar distribution of tracer to case K after 20 days because the extra downwards advection predicted in this case has little effect upon the tracer contours. Unsurprisingly, figure 8.17(b) also shows that the neglect of coriolis force causes the most significant changes to the transfer of riverine tracer, with qualitative changes in the character of the tracer distribution. The stronger return flows which initially delay the thermal bar clearly produce a significant vertical mixing of river water into the lake, which accounts for the riverine tracer content of over 20% everywhere in the domain after 20 days (although not clear from figure 8.15(b), tracer concentrations decrease to less than 5% away from the river after 20 days in simulation K). Later on the strong horizontal flows of the coriolis-free simulation effectively mix the riverine tracer across the surface of the lake in the thin, stable surface layer shown in figure 8.8(b).

8.6 Consequences for Deep-Lake study

The results of model testing presented in this chapter show that the thermal bar dynamics are quite sensitive to several characteristics of the model, notably coriolis forcing. The aim of this section is to justify, with hindsight, the choices made in the deep-lake thermal bar modelling work of previous chapters. Reasoning must be given for the choices made for each of the model features tested above apart from thermobaricity, which has already been proven to be crucial in the Lake Baikal study.

If the results of saline thermal bar simulations in a deep lake are to be accepted, it must be explained why the thermal bar dynamics are so insensitive to the same levels of

salinity in this Kamloops Lake study. The reason for this is the difference in magnitude and variation of the thermal conditions in the vicinity of the thermal bar. In the deep-lake simulations the propagation of the thermal bar is governed by an extremely delicate balance between temperature differences of (at most) 0.2°C offshore of the thermal bar and 2°C inshore of it. In contrast, the offshore thermal difference after 4 days in the Kamloops Lake model is 1.5°C and the inshore difference is 1.8°C after 12 days.

This explains why the propagation rate generally decreases with time in the deep lake simulations and increases in the Kamloops Lake model; inshore gradients slacken to match those offshore as the thermal bar propagates in the former case whereas surface heating and continually rising river temperatures increases the dominance of inshore density gradients in the latter case.

However, this difference in the balance of density differences also means that the propagation rate of the thermal bar in the deep-lake thermal scenario is more vulnerable to the effects of salinity. Tiny increases in salinity (e.g. 5 mgkg^{-1}) will only alter the water's density by a fraction (see figures 7.7 and 8.13) but in the deep-lake case this change will add to the density gradient offshore of the thermal bar and decrease the density gradient inshore, upsetting the original balance of forces and thus halting the thermal bar's propagation. In Kamloops Lake, the density gradient offshore of the thermal bar is so large already (due to a much lower initial lake temperature) that this increase has virtually no effect upon the dynamics. The same can be said for the temperature gradients inshore of the thermal bar, as they soon grow so large that the haline effects are inconsequential. At the only time when the thermal gradients are small enough to be affected by salinity, in the early stages of simulation *K*, the thermal bar is already a sinking boundary plume.

The salinity increase is therefore less important in Kamloops Lake because of its different thermal regime, which in no way detracts from the results of the deep-lake simulation. This finding implies that after the period of validity of the Baikal simulations the Selenga River would warm up and the (saline) thermal bar would propagate out into the lake, but the predicted flows and increased vertical penetration of our modelled thermal bars would still take place. In any case there is no way that the deep lake models

could be improved without better data coverage and more substantial computing power.

Comparing models with and without a realistic surface heat flux provided surprising results about the importance of surface heating in modelling a lake whose circulation is supposedly controlled by river-lake density anomalies. As described earlier, the main effect of surface heating is to increase horizontal propagation of the thermal bar by warming more water to above the T_{md} and altering the balance of density gradients about the thermal bar. However, it is proposed that the deep-lake studies lose little from the neglect of this factor because the timespan of the deep simulations is so short that there is little time for surface heating to make a significant difference (see figures 8.7(a) and (b)).

The most significant difference between the two thermal bar simulations is the inclusion and neglect of coriolis forces. As a result of the introduction of a velocity component normal to the section, coriolis is found to have a profound effect on the dynamics of the thermal bar in Kamloops Lake, which prompts a justification of the validity of the coriolis-free work of the previous chapters.

The main reason for neglecting coriolis forcings in the deep lake is the timespan of each simulation, since the results of figure 8.16 show that the effects of coriolis force vary according to the length of the model run. The coriolis force takes 10 days to establish a velocity in the y -direction which then proceeds to modify the thermal bar dynamics, producing an intermediate stage of coriolis spin-up which would be prevalent for all of the simulation in each short model of the deep lake. Coriolis forcing is therefore not appropriate in the deep-lake studies as it would be in a state of adjustment from the initial conditions for the whole simulation.

It is also important to bear in mind the possible consequences of adding coriolis forces to the deep-lake study. Coriolis forcing would interact with buoyancy forces in every facet of the simulation, modifying the effects of river temperature, thermobaricity, and salinity. Since these effects would mask the underlying buoyancy-driven flows which are the main object of study in the deep lake, a study of coriolis on the deep lake section is not pursued in this work.

The introduction of a sloping bathymetry has surprisingly little effect on the flow regime of the thermal bar, producing a small increase in horizontal propagation rate and a slight decrease in the maximum sinking depth. This implies that the dynamics of a river-dominated thermal bar are relatively indifferent to topography, which gives us some confidence that the conclusions from the deep-lake work would not be seriously affected by the introduction of a realistic Selenga delta bathymetry.

The results of all of the test simulations detailed above indicate that the extent of vertical mixing in the deep lake section would be increased by coriolis forces and decreased by surface heating and a realistic bathymetry, so that there would be some balance of these effects in a model resolving all features. Horizontal propagation of the thermal bar would be increased by all of the factors tested, since the coriolis force would act away from the river mouth on the short timescale of the deep lake studies.

The conclusion of this chapter must be that deep-lake studies of the riverine thermal bar are not yet complete and that modellers with access to greater computational resources could extend the work of the previous chapters significantly. However, no major reason is found to reject the basic findings of chapters 5 - 7, which are an important first step towards a deep-lake model which is as detailed as the Kamloops Lake model of this section.

Chapter 9

Results - Plankton Modelling

It is well-known that the flow patterns associated with the thermal bar can have an important influence on the plankton ecosystem of a temperate lake (Moll et al. 1993, Likhoshway et al. 1996, Parfenova et al. 2000), so this chapter is dedicated to analysis of results from a simple plankton model which is coupled to the Kamloops Lake dynamics described in the previous chapter.

In a study which is fully described in chapter 1, Botte & Kay (2000) (hereafter referred to as BK) qualitatively reproduced the Likhoshway et al. (1996) observations of plankton distributions around a spring thermal bar in Lake Baikal using the simple *N-P-Z* formulation of Franks et al. (1986). On the much shallower Kamloops Lake section, this chapter represents an extension of that work to the case of a riverine thermal bar.

For comparative purposes, the plankton model is unchanged from that of BK in this chapter. Apart from the differences in thermal regime and resulting dynamics between the two studies, the only difference is the effect of the river inflow boundary conditions on the ecosystem model.

The chapter proceeds with a full discussion of model results and examines in detail the influence of several characteristics of the riverine thermal bar on the ecosystem model. It is particularly important to quantify the effects of riverine boundary conditions, so a sensitivity study is performed with various states assigned to the river ecosystem which flows into the lake. Results are discussed from cases with a variety of riverine nutrient levels, qualitatively representing the natural variation in discharge and nutrient loading which takes place in the South Thompson River in spring (St. John et

al. 1976).

This study concludes that the simplified Franks et al. (1986) model produces some slightly spurious predictions of the ecosystem state, although it is impossible to rule these predictions out with the current sparsity of available data. In chapter 10 a more sophisticated plankton model is adopted which contradicts some of the most suspicious results of the Franks et al. (1986) model. Comparison between models is feasible because all plankton model components are expressed in common units of mmol N m^{-3} . These plots therefore represent the distribution of the available Nitrogen contained in a particular model component at a certain time.

9.1 Temporal Evolution of Plankton Population

The basic simulation of this chapter involves the model of Franks et al. (1986) under riverine boundary conditions of $N_R\text{-}P_R\text{-}Z_R = 4\text{-}1\text{-}1 \text{ mmol N m}^{-3}$ (as described in section 2.5.1), and is therefore referred to as simulation *F*. The discussion of plankton behaviour is centred on three stages of the simulation, each roughly analogous to one of the phases of thermal bar dynamics described in sections 8.1.1 - 8.1.3. However, in this chapter the three chosen times are evenly spaced in order to give an impression of the temporal evolution of plankton in the vicinity of a riverine thermal bar.

9.1.1 8 days of simulation

After 8 days of simulation the thermal bar is positioned about 600 m from the river inflow, so that the majority of the sinking takes place down the boundary (figure 8.1(a)). The phytoplankton shows significant growth near the surface and in the vicinity of the thermal bar (figure 9.1(a)), but the zooplankton hardly reacts at all with the other components of the plankton model and seems to be totally dominated by the riverine boundary conditions (figure 9.1(b)).

Closer inspection of the contours of phytoplankton biomass reveals that the centre of the bloom is actually at the position of the T_{md} , slightly offshore of the stagnation point above the descending plume of the thermal bar. A later analysis in section 9.2 shows that this is a consequence of the fixed riverine plankton boundary conditions, and

has nothing to do with nutrient concentrations; since P_R is set to 1 mmol N m^{-3} the phytoplankton concentration decreases sharply towards this level in the region inshore of the thermal bar.

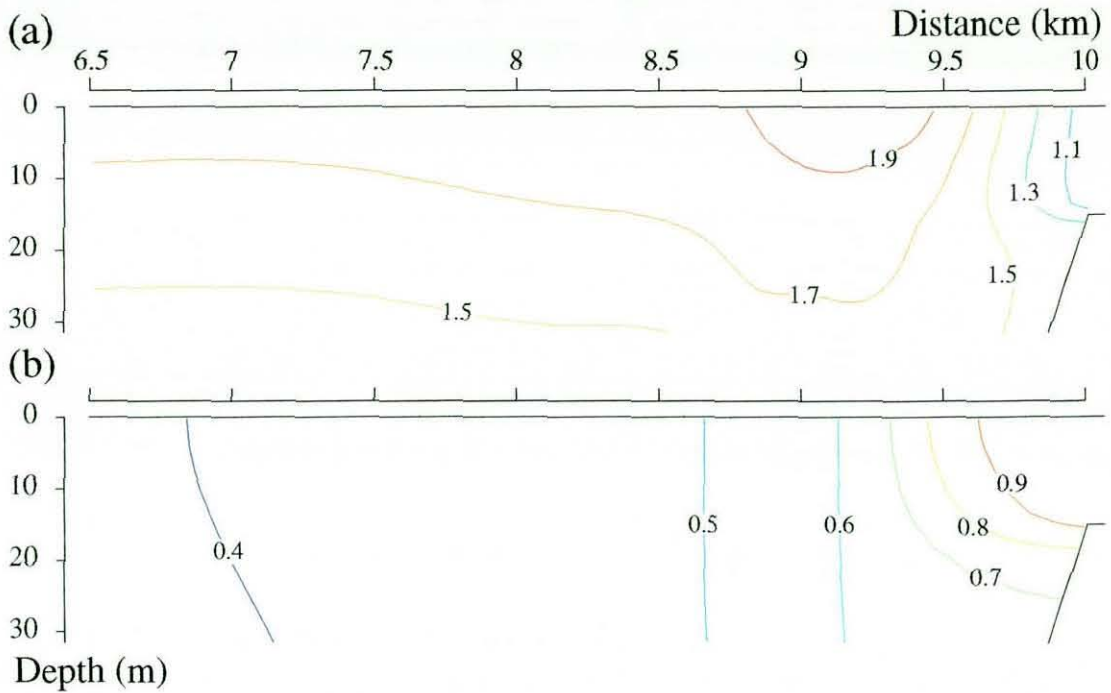


Figure 9.1: Characteristics of simulation F after 8 days: (a) phytoplankton concentration (mmol N m^{-3}), (b) zooplankton concentration (mmol N m^{-3}).

Also in figure 9.1(b) we can observe the effects of vertical convection on the plankton distribution, as sinking within the thermal bar plume is strong enough to increase phytoplankton concentrations near the boundary at depth. A deeper plot than figure 9.1(a) would also show that the upwelling offshore of the thermal bar is sufficiently strong to decrease phytoplankton concentrations in parts of the open lake by advecting low-biomass waters upwards.

Although noticeably increased, phytoplankton concentrations at the thermal bar are still too low to support any significant growth in zooplankton at this stage. In fact the zooplankton contours show a similar distribution to those of the neutral tracer φ which are shown in figure 8.15, implying that zooplankton source terms are negligible in the

vast majority of the domain.

9.1.2 16 days of simulation

After 16 days of simulation the thermal bar has progressed much further from the inflow (figure 8.1(b)), with important consequences for the organisms living in the near-shore region of figure 9.2. The phytoplankton growth at the position of the thermal bar has reached bloom levels (figure 9.2(a)), and zooplankton concentrations also now reach a shallow maximum at the thermal bar, although these quantities could not yet be described as a bloom (figure 9.2(b)).

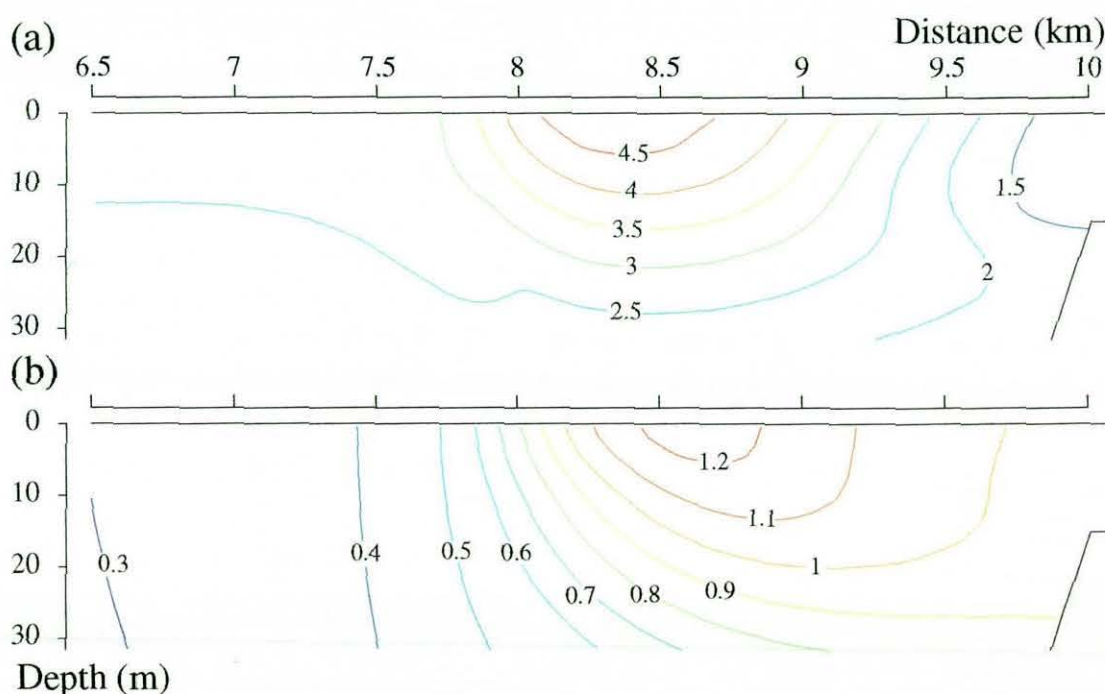


Figure 9.2: Characteristics of simulation F after 16 days: (a) phytoplankton concentration (mmol N m^{-3}), (b) zooplankton concentration (mmol N m^{-3}).

Comparing the position of the thermal bar with the phytoplankton bloom, it is found that the highest concentrations of phytoplankton are now inshore of the T_{md} . An exact explanation for this is given in section 9.2.2, but essentially the thermal bar has moved to such a distance from the river inflow that the low-phytoplankton boundary conditions

are ineffective against the improved productivity which results from the stable, nutrient-rich conditions inshore of the T_{md} .

The large horizontal gradient in phytoplankton concentration inshore of the bloom near the thermal bar reflects the continued influence of the riverine boundary conditions throughout the near-shore region. As water is descending over all of the 2.5 km closest to the river, phytoplankton concentrations at depth in this region reflect the state of plankton growth in the surface layer above. As a result of advection down the boundary, the riverine conditions are instrumental in decreasing the phytoplankton concentration at depth over a large proportion of the domain beneath the pictured region.

The phytoplankton bloom is now large enough to support mass zooplankton grazing, and the carnivorous population develops accordingly. As discussed in section 9.2.3, however, there is plenty of evidence to show that riverine boundary conditions outweigh the discrepancy between mortality and grazing in determining the distribution of zooplankton at this stage. The most convincing evidence of this is that the contours of zooplankton concentration follow the tendency of neutral tracer concentrations (figure 8.15) more closely than contours of phytoplankton, implying that transport of riverine zooplankton is more important than the net growth of zooplankton through grazing.

9.1.3 24 days of simulation

The thermal bar is well into the 'surface gravity current' stage of its development after 24 days of simulation, with a warm river inflow floating on the stably-stratified waters inshore of the T_{md} (figure 8.1(c)). The phytoplankton are now concentrated into two distinct blooms which are of a similar magnitude to the previous stage, one at the exact position of the thermal bar and the other mid-way between the thermal bar and the river inflow (figure 9.3(a)). The cause of this unusual distribution is later shown to be nutrient limitation, which impedes growth in the nutrient minimum at the very centre of the previous single bloom, but allows phytoplankton to grow unrestricted in the higher nutrient levels on either side.

Figure 9.3(b) shows that the main zooplankton growth takes place between the two phytoplankton blooms, indicating that zooplankton may promote the formation of a

double bloom by consuming phytoplankton in the central region of limited nutrient availability. A combination of nutrient limitation and zooplankton grazing therefore restricts the phytoplankton bloom in between the T_{md} and the stable region located 1.5 km from the river inflow.

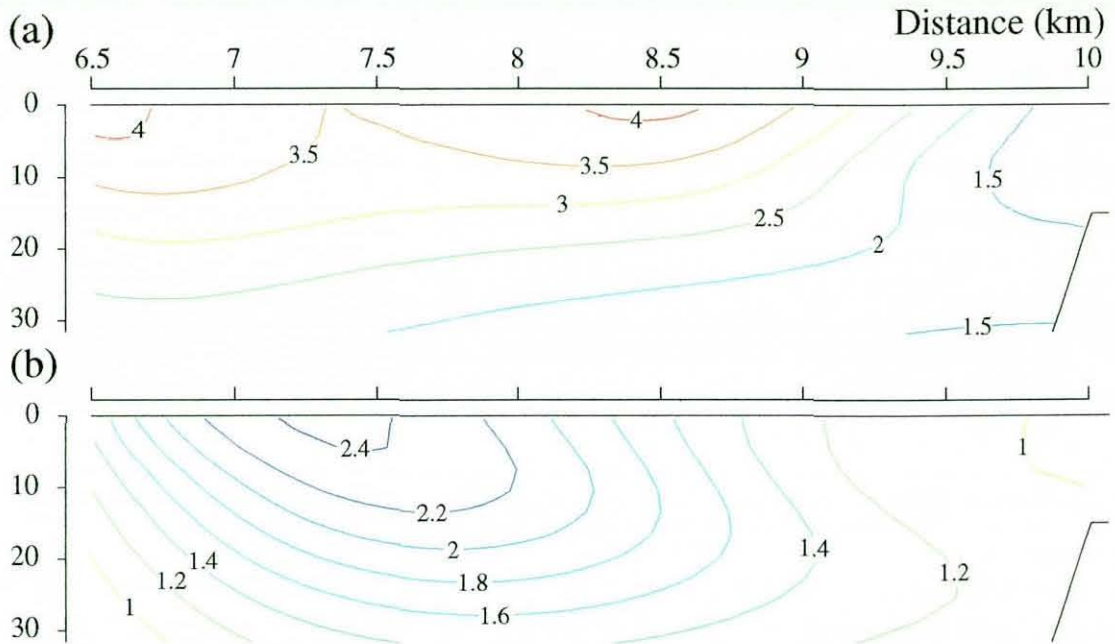


Figure 9.3: Characteristics of simulation F after 24 days: (a) phytoplankton concentration (mmol N m^{-3}), (b) zooplankton concentration (mmol N m^{-3}).

In both phytoplankton and zooplankton plots it is clear that, by this stage of the simulation, the interaction of source terms in the plankton model is much more influential than the effects of riverine boundary conditions. However, a small influence of the boundary conditions is felt in the depths of the lake as the down-slope convection of lower values of plankton is clearly still operating (not shown).

9.2 Closer Examination of Plankton Growth

This section is dedicated to explaining the prediction of these plankton blooms by the simple N - P - Z model employed here. Figure 9.4 shows the state of the model components at various simulation times along a horizontal profile taken 5 m beneath the surface of

the lake.

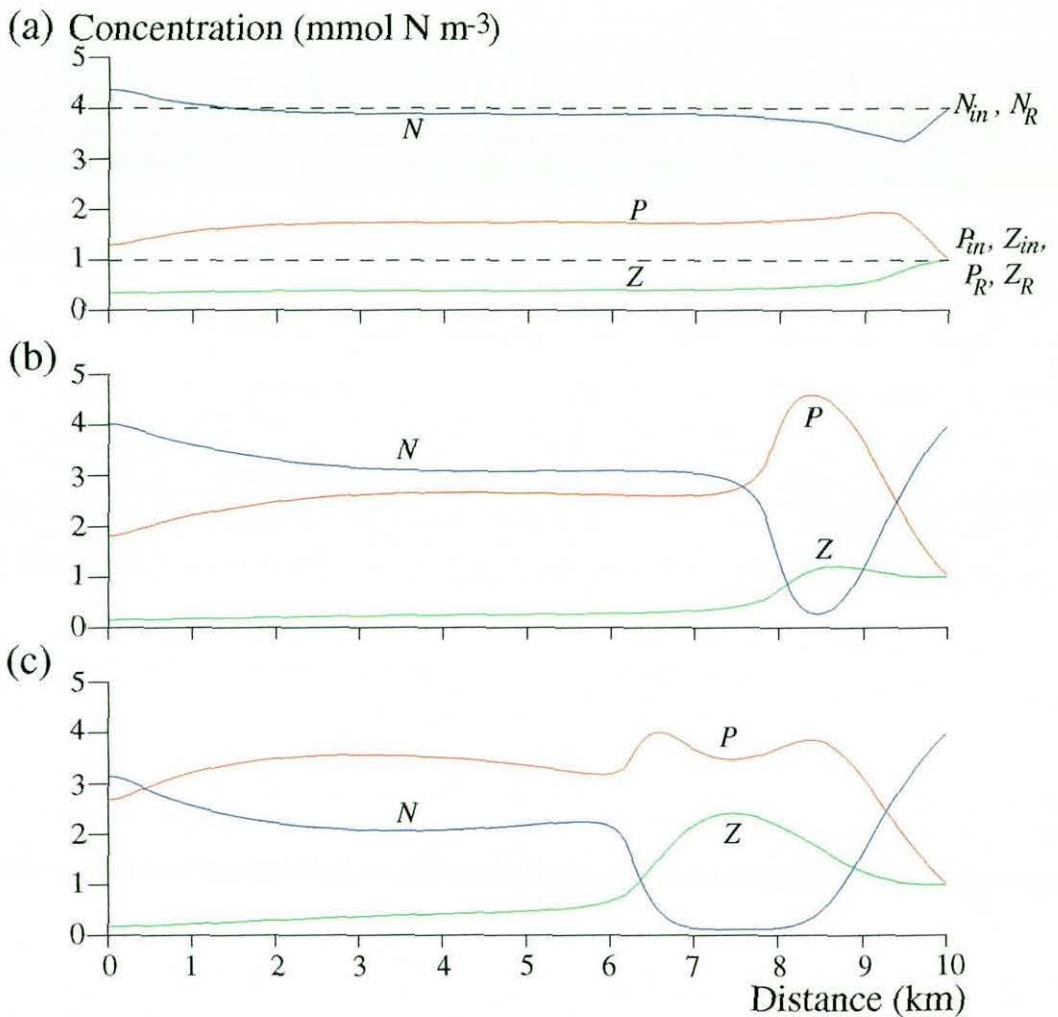


Figure 9.4: Horizontal N - P - Z profiles at 5 m depth throughout the simulation: (a) 8 days, (b) 16 days, (c) 24 days.

After 8 days of simulation the ecosystem model is only just beginning to evolve and shows little evidence of interaction with the dynamics of the thermal bar. The phytoplankton have grown in a spatially uniform manner, albeit with a shallow maximum at the thermal bar, and have taken up more Nitrogen than is depleted from the nutrient pool, indicating that zooplankton mortality and the river inflow are maintaining available nutrient levels.

After 16 days of simulation the spring phytoplankton bloom at the thermal bar is revealed by a doubling in phytoplankton concentrations at the position of the surface

T_{md} . The nutrient pool has been greatly reduced by this bloom, and is now at a level which will limit any further production in this location. The magnitude of the small local maximum in the zooplankton concentrations is revealed to be mainly due to the fixed value of Z_R at this stage.

Phytoplankton growth is still nutrient-limited after 24 days, and as the thermal bar propagates it leaves a large region in its wake which contains virtually no available nutrients. With increasing predation from the zooplankton and growth limited by the lack of nutrients, the phytoplankton bloom at the thermal bar recedes to such an extent that remaining undulations in the phytoplankton distribution are relatively small throughout the whole surface layer. In conjunction with the pressures of zooplankton grazing, the lack of nutrients in the centre of the phytoplankton bloom causes a localised decrease in photosynthetic production which leads to a trough in the bloom and thus the formation of the two separate phytoplankton concentration maxima seen in figure 9.3.

9.2.1 Effects of Stability

An important point demonstrated by the work of BK is that the productivity of a plankton ecosystem is fundamentally dependent upon the effects of stability in the water column, which can delay the diffusion of phytoplankton away from the euphotic zone near the lake surface. Since this simple plankton model resolves the dependence of productivity on phytoplankton biomass and light availability, and the vertical eddy-viscosity is a function of stability, it is appropriate to study this effect in the setting of the riverine thermal bar.

BK adopt a stable initial temperature profile which has a band of high-stability water between depths of approximately 100 - 130 m. As the simulation proceeds, the surface heat flux forms an area of instability which is confined to the waters above this stable layer, growing slowly deeper with time until the open lake has an almost uniform vertical temperature profile. In this way BK are able to compare the effects on plankton of unstable waters overlying stable waters offshore of the thermal bar against the usual scenario of stable waters overlying unstable waters inshore of the thermal bar.

In contrast to this, the adoption of a uniform initial temperature in this study means

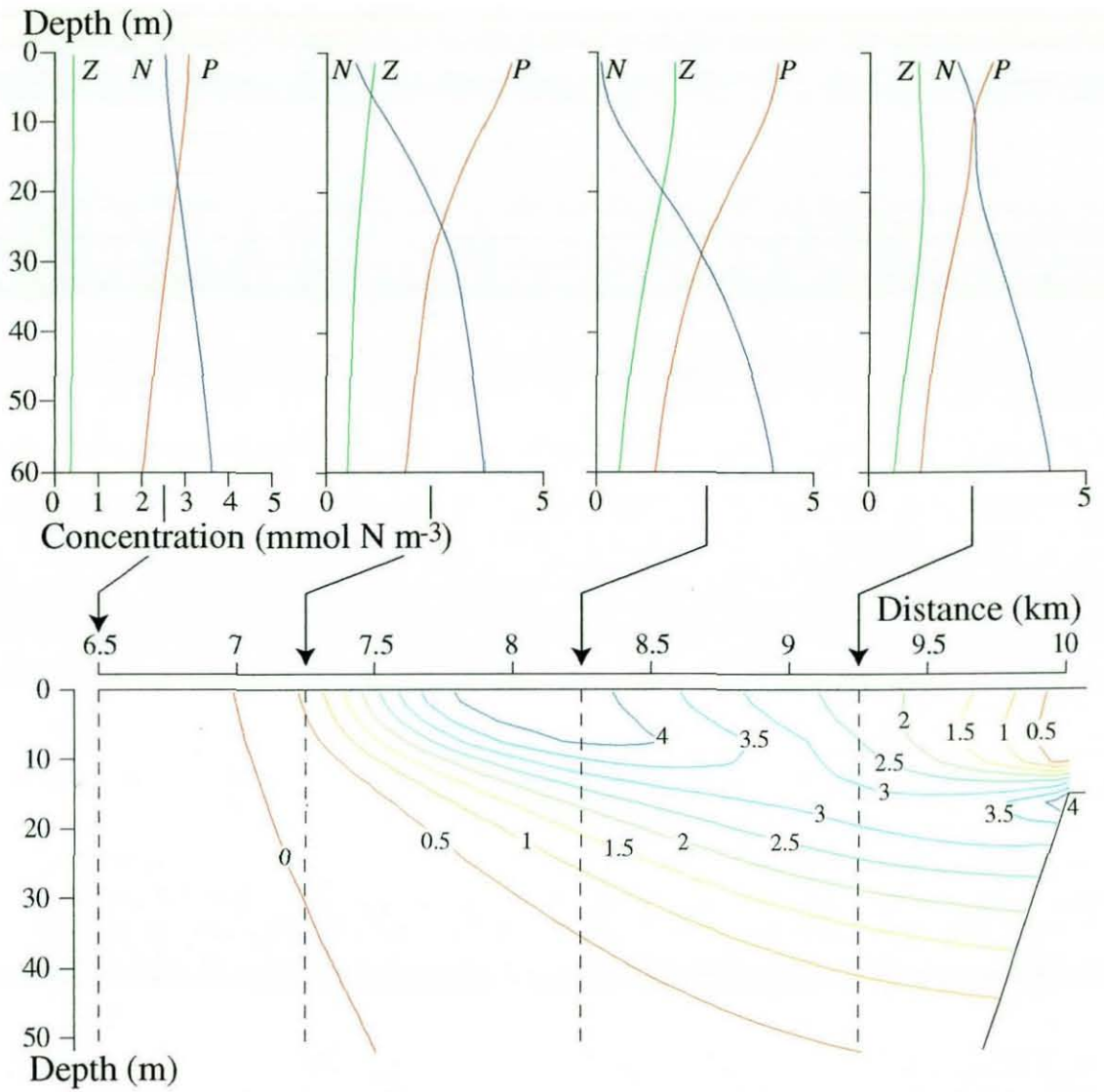


Figure 9.5: Contours of stability $N^2(\times 10^{-5}\text{s}^{-1})$ and profiles of N - P - Z at various positions in case F after 20 days. Results are studied after this time to enable a comparison with the results of BK.

that only the stable/unstable interface inshore of the thermal bar may be studied as the offshore water is already unstable throughout the depth of the lake. In addition, the stability profile of the region inshore of the T_{md} has a rather different structure in the case of the riverine thermal bar. In BK stability increases monotonically towards the surface due to the exponential decay of the surface heat source with depth, but in the riverine thermal bar model contours of N^2 after 20 days of simulation (in figure 9.5) show that there is a sub-surface stability maximum near the river due to the localised thermocline generated at the base of the river influx, which has a vertically-uniform

temperature.

Figure 9.5 shows that stability is a crucial factor in the plankton blooms which are observed on longer timescales. After 20 days the stable region of the lake is of a considerable size due to the propagation of the thermal bar, and contours of stability show that there is a localised stability maximum at a distance of about 2 km from the river inflow. This surface maximum in the value of N^2 occurs at the position where the sloping thermocline between river plume and lake water intersects the surface.

Comparing vertical N - P - Z profiles from positions inshore of, at, and offshore of the thermal bar reinforces the observation that water column stability is critically important in determining the productivity of a plankton ecosystem in the vicinity of a riverine thermal bar. Plankton development offshore of the thermal bar (6.5 km from the origin) is clearly limited by diffusion of the photosynthesising phytoplankton downwards, whereas growth at the stability maximum inshore of the T_{md} (8.25 km from the origin) continues until the water is almost completely devoid of nutrients. This is shown to be due to the high stability of the water column by the close relationship between the N - P - Z profile and the vertical variation of N^2 .

Further proof of the dominance of stability is given by the fact that plankton growth is more prolific in the stable regions inshore of the T_{md} than it is at the stagnation point above the thermal bar plume (7.25 km from the origin). Despite the converging horizontal transport at the surface T_{md} and the influence of low-plankton riverine boundary conditions on the inshore region, the lesser stability in the vicinity of the T_{md} leads to lower growth rates than inshore.

It is also interesting to note the effects of the subsurface stability maximum on the N - P - Z profiles. By comparing N - P - Z profiles from positions with and without a subsurface stability maximum (9.25 and 8.25 km from the origin respectively), it can be clearly seen that productivity is significantly reduced above the stability maximum in the former profile due to the decrease in N^2 . These inflexions in the N - P - Z profiles cannot be due to the riverine plankton conditions because reductions in the plankton concentrations would then be greatest at the lake surface where the mixed water has

the highest riverine content (as shown in figure 8.15(b)).

The criticism remains that these different profiles, taken at various distances from the river, are simply a result of the time-varying condition of the lake into which the riverine plankton components are introduced. Since the lakeward flows dominate it is possible that variations in these profiles are solely due to differences in the flow-field after various times, rather than being produced by in-situ stability variations. However, examination of similar plots after different time periods confirms that the physical mechanisms noted above are persistently linked with the biological phenomena attributed to them.

9.2.2 Phytoplankton Blooms

A more detailed analysis of the causal factors of the phytoplankton blooms may be gained by separating the various terms of the phytoplankton transport equation so that convection and diffusion terms may be compared to the biological interaction terms contained in \mathbb{S}_P (equation (2.20)). The range of values attained by each term over a horizontal profile traversing the entire lake at 5 m depth is given in table 9.1, and some of the most influential quantities are then plotted in figure 9.6. In this analysis a negative value implies that the mechanism in question decreases the in-situ concentration of phytoplankton.

Term in P transport equation	Minimum	Maximum
Primary production	1×10^{-5}	5×10^{-5}
Grazing	-2×10^{-5}	-1×10^{-6}
Mortality	-5×10^{-6}	-1×10^{-6}
Vertical diffusion	-1×10^{-4}	1×10^{-6}
Horizontal diffusion	-3×10^{-5}	8×10^{-5}
Vertical convection	-1×10^{-6}	7×10^{-6}
Horizontal convection	-3×10^{-5}	5×10^{-6}

Table 9.1: Range of values of each term in the P transport equation along a near-surface horizontal profile during the first 24 days of simulation F . All values are $\text{mmol N m}^{-3} \text{ s}^{-1}$

Vertical convection of phytoplankton and phytoplankton mortality are disregarded in the following discussion as they are an order of magnitude smaller than the leading terms. Horizontal diffusion is found to achieve its large values simply by transporting phytoplankton across the large gradients present at the thermal bar plume from the productive areas inshore of the T_{md} to the open lake. In addition, values of horizontal convection attained in the converging flows near the thermal bar are insignificant in comparison to those near the river inflow, which are recorded in table 9.1. Therefore only photosynthetic production, zooplankton grazing, and vertical diffusion of phytoplankton are considered in the detailed discussion which follows.

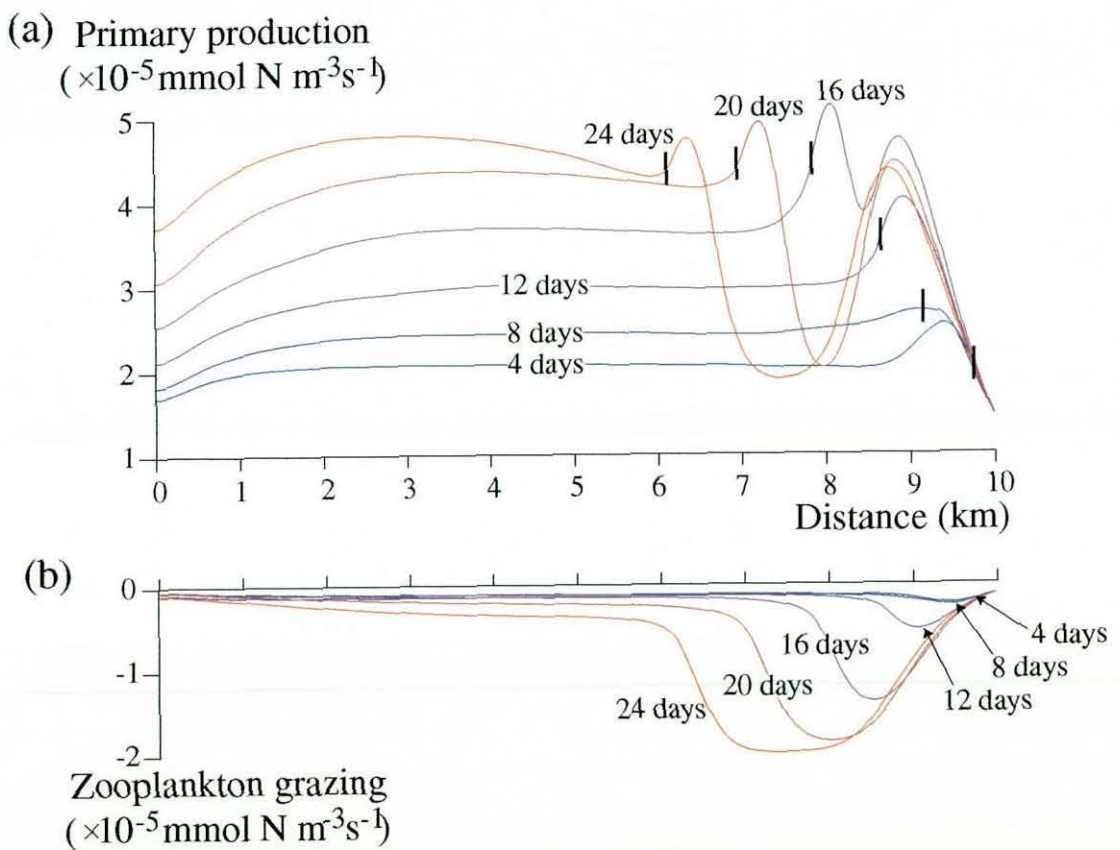


Figure 9.6: Source terms in the phytoplankton transport equation at 5 m depth throughout simulation F : (a) photosynthetic production and position of the T_{md} (|), (b) total zooplankton grazing.

A horizontal profile of the vertical diffusion term is not included in figure 9.6 in the interests of brevity, but the magnitude of vertical diffusion terms listed in table 9.1 reveals it to be of particular importance to this study. A close examination of the

vertical diffusion term shows that it is generally of the order of 10^{-5} ms^{-1} , but is locally increased to $O(10^{-4}) \text{ ms}^{-1}$ in the vicinity of the $T = T_{md}$ line. A more detailed analysis shows that this is primarily due to the inflexion in the vertical phytoplankton profile which is generated by the transition between stable and unstable conditions (see section 9.2.1), but is also attributed to the change in K_v between the unstable waters offshore of the T_{md} and the stable inshore region.

Figure 9.6(a) shows that the primary production has a consistently important influence on phytoplankton concentration over the whole lake. Growth of phytoplankton develops steadily at the position of the thermal bar until 16 days have elapsed, when nutrient limitation at the very centre of the bloom causes a localised reduction in growth which eventually produces the 'double-bloom' phytoplankton distribution.

It is very difficult to quantify the role of zooplankton grazing in the development of this structure, but a close examination of the Michaelis-Menten factor in the photosynthesis formulation (equation 2.23) confirms that nutrient limitation must be responsible for actually initiating the depression in the centre of the original phytoplankton bloom. Nevertheless, zooplankton grazing significantly depletes phytoplankton concentrations in the region between the two blooms throughout the later stages of the simulation (figure 9.6(b)).

Observing the position of the primary production maximum in comparison to the T_{md} in figure 9.6(a) allows us to conclude the earlier discussion of the temporal variation of the position of the phytoplankton bloom with respect to the thermal bar. After 8 days the maximum phytoplankton concentration is found at the position of the T_{md} due to the sharp decline near the river which results from the inflow boundary conditions, but after 16 days the blooms are situated inshore of the T_{md} because the thermal bar is far enough from the river for the benefits of the stable stratification inshore to become apparent.

9.2.3 Zooplankton Bloom

A similar analysis of the zooplankton bloom in simulation F reveals that comments relating to all convection and diffusion terms of the phytoplankton transport equation hold for zooplankton, as indicated by table 9.2, leaving only the two components of S_Z to be discussed (equation 2.21). While mortality solely depends upon zooplankton concentrations, grazing is a function of both zooplankton and phytoplankton concentrations, and profiles of each term in figure 9.7 show that the sharply increasing phytoplankton concentrations soon lead to an imbalance and net zooplankton growth.

(a) Assimilated zooplankton grazing
($\times 10^{-5} \text{mmol N m}^{-3} \text{s}^{-1}$)

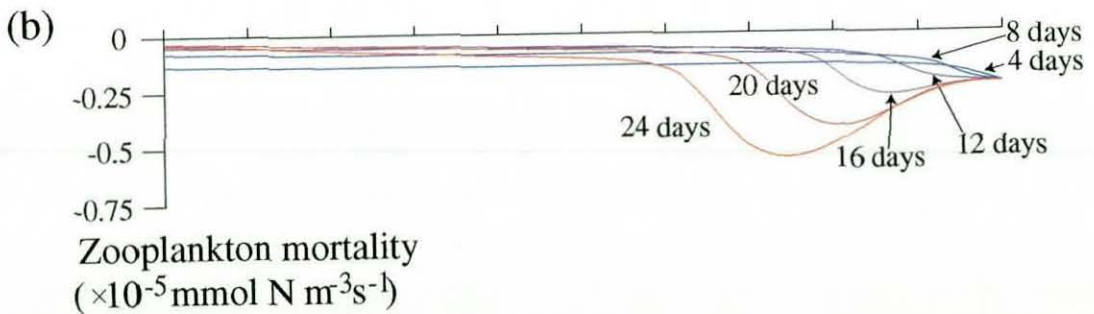
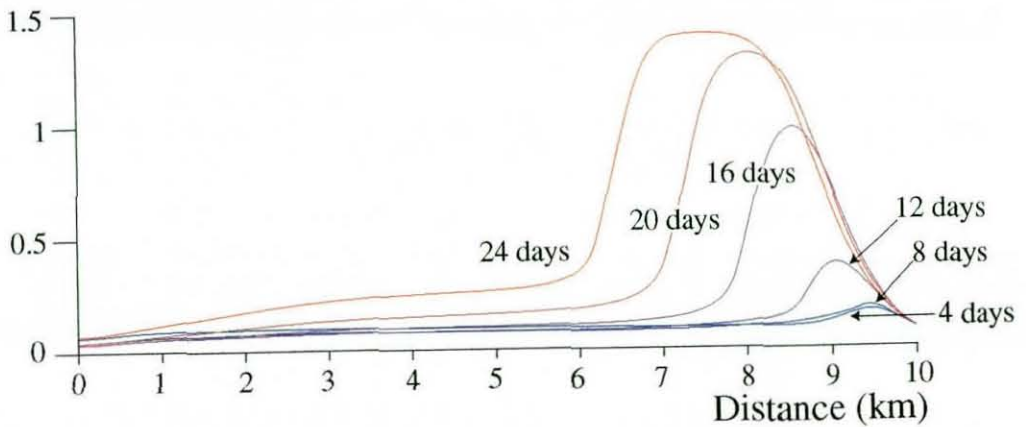


Figure 9.7: Source terms in the zooplankton transport equation at 5 m depth throughout simulation F : (a) assimilated zooplankton grazing, (b) zooplankton mortality.

Term in Z transport equation	Minimum	Maximum
Assimilated grazing	3×10^{-7}	2×10^{-5}
Mortality	-6×10^{-6}	-5×10^{-7}
Vertical diffusion	-2×10^{-5}	1×10^{-6}
Horizontal diffusion	-7×10^{-6}	2×10^{-5}
Vertical convection	-1×10^{-7}	2×10^{-6}
Horizontal convection	-8×10^{-6}	5×10^{-6}

Table 9.2: Range of values of each term in the Z transport equation along a near-surface horizontal profile during the first 24 days of simulation F . All units are $\text{mmol N m}^{-3} \text{ s}^{-1}$.

Assimilated grazing and mortality are roughly equal for the first 8 days of the simulation, causing tracer-like zooplankton concentrations (see section 9.1.1), but after 12 days the zooplankton start to show signs of a net increase in biomass. However, it is not until 20 days of grazing have passed that zooplankton populations start to significantly exceed riverine concentrations and begin to bloom in their own right.

9.3 Variation of Riverine Boundary Conditions

This section is concerned with the results of alternative simulations in which the state of the inflowing river ecosystem is varied. In the case of the plankton components P_R and Z_R this work is done solely as a sensitivity study of the lake ecosystem to the arbitrarily-assigned river plankton levels, but the simulations with a varying N_R also have a physical justification in that the South Thompson River shows a significant variability in available Nitrogen on both spring-warming and interannual timescales (St. John et al. 1976).

9.3.1 Nutrients

As the observed nutrient limitation of phytoplankton growth could be significantly delayed by the nutrient-rich inflow, it could easily be assumed that altering the value of inflow nutrients N_R will have a drastic effect on the resulting plankton growth. This hypothesis is tested by the introduction of simulations $F30$ and $FM30$, which have N_R increased by 30% and decreased by 30% respectively (see appendix A).

Results of these simulations reveal that changing N_R has little effect upon the predicted concentrations of either phytoplankton or zooplankton after 8 days (not shown). Close scrutiny of the Michaelis-Menten nutrient-limitation factor in equation (2.23) reveals that productivity changes of up to 30% could theoretically occur as a result of this nutrient variation, but this fails to happen in practice. This is because the significantly altered nutrient levels are confined to a very narrow region near to the river inflow, partly due to the flow regime of the thermal bar, and plankton growth is suppressed in this area as a result of the fixed values of P_R and Z_R .

After 16 days the influence of the N_R variation has spread away from the near-river region and induced significant changes in the growth rates of phytoplankton (figure 9.8(a)). Interestingly, it is only at the position of the bloom that large differences in phytoplankton concentration are noted, because this is the only place where nutrient levels seriously limit growth in simulation F and phytoplankton variation between simulations is not suppressed by the fixed value of P_R . Zooplankton populations are still relatively unaffected as these differences in phytoplankton concentration produce only slight changes in the grazing rates.

Figure 9.8(b) shows the results of varying inflow nutrients after 24 days, when the effects of N_R variation have finally filtered through the food web and significantly altered concentrations of zooplankton. By this stage the differences in nutrient levels between each case are generally less than the differences in phytoplankton and zooplankton concentration at the location of their respective blooms. This is because the phytoplankton take up all nutrients available to them during the simulation, transferring the river's variation in Nitrogen content from the nutrients to the plankton levels of the model.

These simulations confirm that nutrient limitation of photosynthesis is very important in the later stages of case F and show that most qualitative features of the ecosystem model are independent of reasonable variations in the river nutrient level. These results imply that a difference in the spring riverine nutrient loading to a lake will not become apparent in plankton levels for a considerable time, but could eventually have noticeable consequences for the near-shore flora and fauna. This delay must be at least partly due to the riverine thermal bar, as varying nutrient concentrations from the river are not

allowed to mix away from the low riverine levels of plankton for some time. These results also suggest that a lake of this sort could act as a 'nutrient regulator', transferring inflow nutrient fluctuations to plankton biomass and thus suppressing the variation in the nutrient itself.

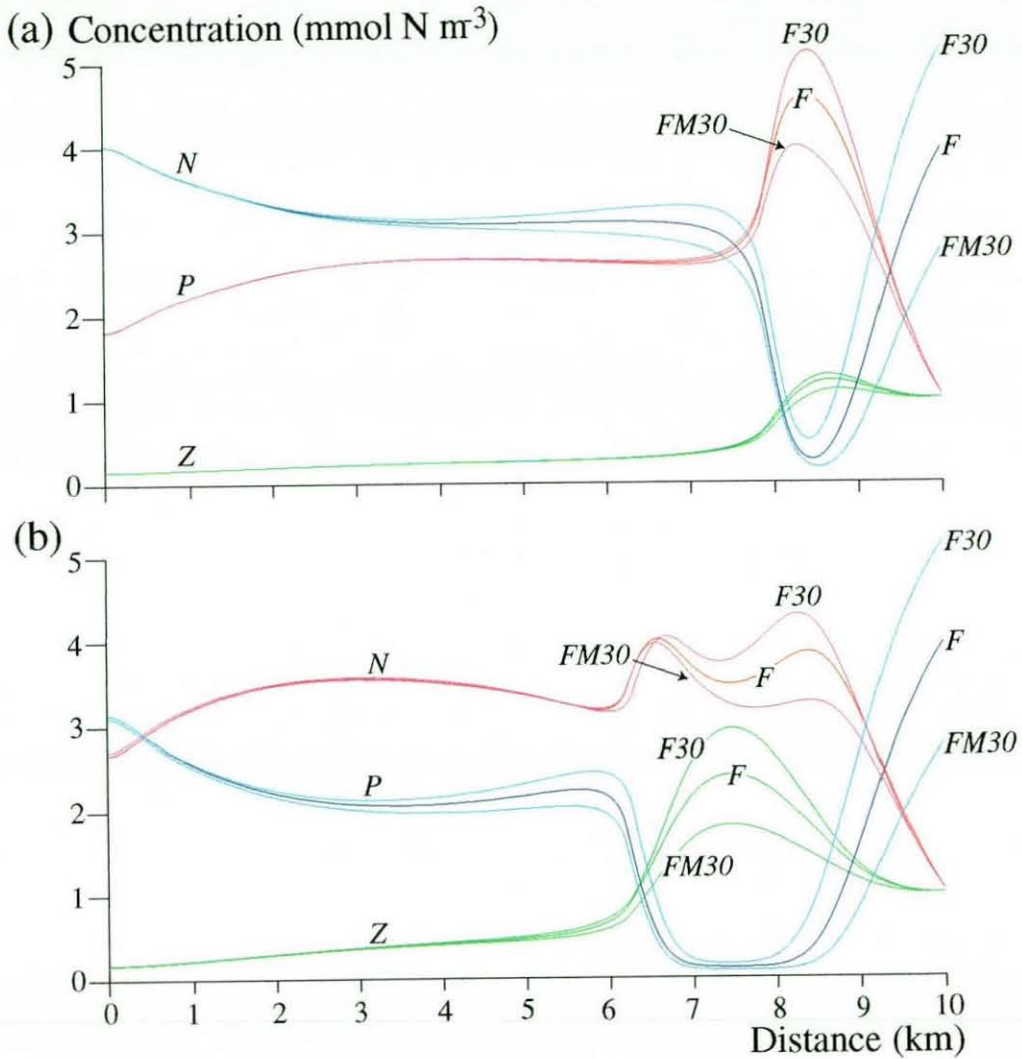


Figure 9.8: Comparison of N - P - Z characteristics for F simulations with various values of N_R : (a) 16 days, (b) 24 days.

9.3.2 Phytoplankton

Fixing a P_R value of 1 mmol N m^{-3} could have a disproportionate effect upon the qualitative behaviour of the ecosystem model by promoting excessive growth at the start of the simulation or suppressing phytoplankton development later on. As there is little plankton data for the South Thompson River, a crude idea of the effects of the P_R

level is obtained from simulation *FPM50*, which has a reduced P_R value of $0.5 \text{ mmol N m}^{-3}$.

Decreasing the phytoplankton influx P_R has a noticeable effect on the Franks et al. (1986) model much more quickly than varying N_R . Although zooplankton concentrations are hardly affected after 8 days, the lower P_R level apparently depletes the phytoplankton concentration at the most important time, reducing the thermal bar bloom when it is near the river inflow in the early stages of the simulation. This is evident from the disappearance of the localised phytoplankton maximum at the thermal bar which is seen in simulation *F* at this time.

The reduced magnitude of the phytoplankton bloom after 16 days which arises from this situation has a marked effect on zooplankton concentrations, removing the zooplankton maximum seen in figure 9.4(b). Due to the suppression of primary production, nutrient levels are also higher and do not limit photosynthesis at this stage.

Zooplankton levels are eventually affected the most by decreasing P_R , as shown in figure 9.9, because the phytoplankton population manages to attain similar bloom values to case *F*, albeit at a position which is slightly further away from the riverine boundary conditions. The zooplankton bloom takes place much later and is therefore less substantial and a little further to the shoreward side of the main phytoplankton bloom, which follows the thermal bar's propagation. This leads to a less symmetrical 'double bloom' in the phytoplankton, allowing slightly higher maximum phytoplankton concentrations after 24 days than simulation *F*.

Although the value of P_R is clearly very important for fixing the exact size and position of the respective plankton blooms, greatly reducing its value does not suppress either bloom or prevent nutrient limitation from creating a local minimum in the earlier phytoplankton bloom. It is therefore shown that the qualitative behaviour of this ecosystem model does not directly result from the arbitrarily-chosen value of P_R .

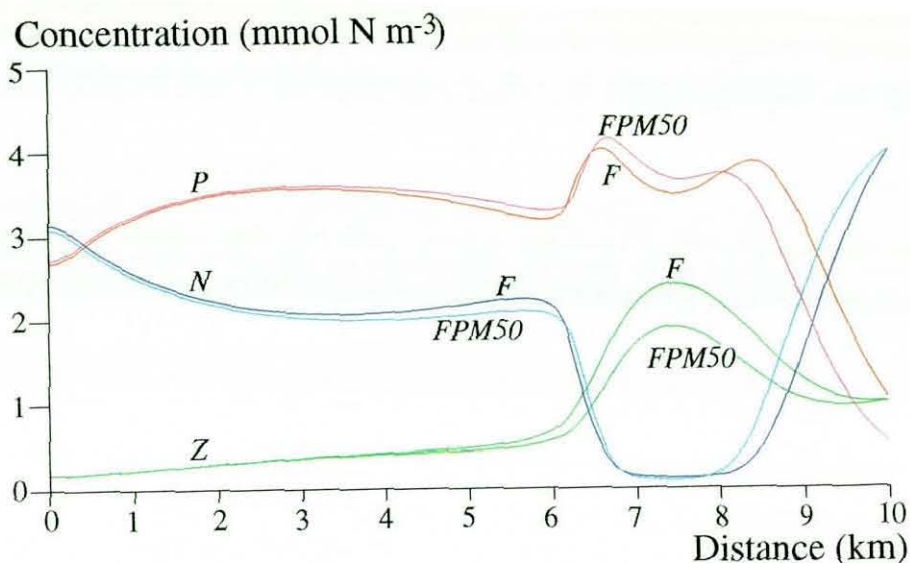


Figure 9.9: Comparison of *N-P-Z* characteristics for simulations *F* and *FPM50* after 24 days.

9.3.3 Zooplankton

With the zooplankton blooming in their own right after 24 days and playing an ancillary role in the development of the double phytoplankton bloom, the potential exists for the arbitrarily-fixed Z_R value of 1 mmol N m^{-3} to have a controlling influence on the qualitative behaviour of the whole ecosystem model. Since the fixed zooplankton mortality rate ensures that concentrations in the lake immediately recede from this value during the simulation, the influence of the Z_R value is tested here by a discussion of results from simulation *FZM50*, which has a reduced Z_R value of $0.5 \text{ mmol N m}^{-3}$.

In contrast to the model's behaviour when nutrients and phytoplankton are varied, the alteration of Z_R has a rapid effect on the state of every component of the *N-P-Z* model. This happens because, in *non-limited* feeding situations, grazing or photosynthesis rates are affected more quickly by changes to the 'feeder' concentration than by changes to the 'food'. Reducing Z_R immediately allows more phytoplankton growth by decreasing the grazing rate, and available nutrient levels are reduced accordingly in the near-shore region.

Although fairly significant, the net effect of these changes after 24 days is restricted

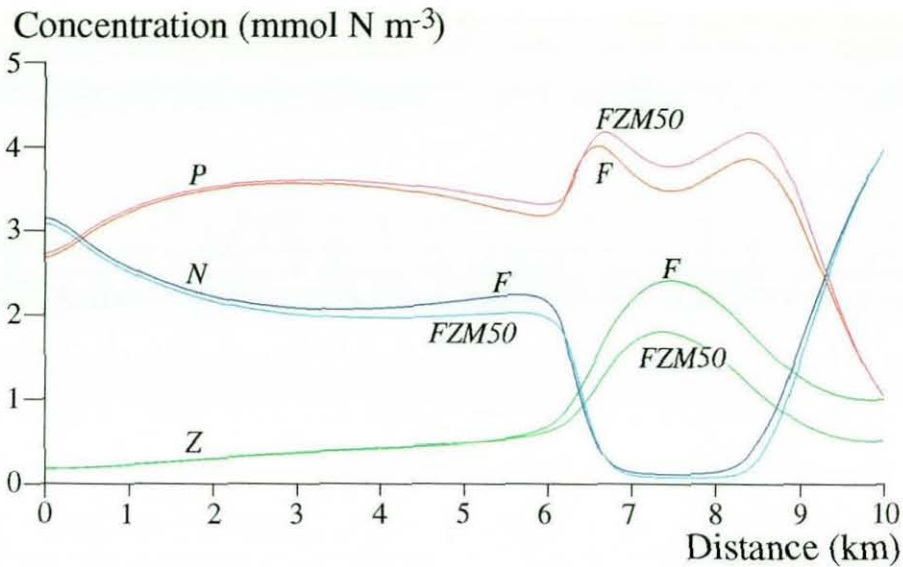


Figure 9.10: Comparison of *N-P-Z* characteristics for simulations *F* and *FZM50* after 24 days.

to the absolute values of plankton concentrations rather than their spatial tendency (figure 9.10), which is not unduly worrying given that the lack of data means that the model is only capable of giving qualitative results anyway. Importantly, the change in lake zooplankton concentrations is no larger than the change applied to Z_R , confirming that variations in riverine conditions are not magnified in any part of the lake ecosystem.

9.4 Discussion and Comparison with BK

In contrast to the 'bloom and bust' character of the phytoplankton predicted by this model, St. John et al. (1976) found that phytoplankton populations in Kamloops Lake continue to develop steadily throughout spring and into late summer. Although the results detailed here could be completely accurate and are a correct solution of the Franks et al. (1986) model, the prediction of this double phytoplankton bloom after only 24 days is viewed as suspicious because it lies in contradiction to these (admittedly sparse) observations and other available data on the distribution of plankton around a spring thermal bar or similar convergence zone. In reality, the absence of any detailed plankton data from Kamloops Lake on the spatial and temporal scales required for this study makes it impossible to quantitatively validate results, and so this discussion regards only the qualitative predictions of this plankton model.

Using an identical version of the Franks et al. (1986) model, BK produced a reasonable preliminary fit to the data of Likhoshway et al. (1996), so it is the purpose of this section to justify why these results differ from those of BK and are not considered to be as satisfactory. Comparing contours of phytoplankton and zooplankton concentration after 16 days (figure 9.2) with those from BK after 20 days (figure 12 of BK), it is obvious to the reader that the rate of phytoplankton growth is strongly promoted in the riverine simulation. This considerable photosynthesis rate is responsible for the quick succession of simulation F , which is why plots of primary production in BK (their figure 16) show the double phytoplankton bloom only just beginning to appear after 40 days of simulation.

Comparing the photosynthesis terms of \mathbb{S}_P throughout the work of BK and simulation F (figure 16 of BK and figure 9.6(a) respectively), it can be seen that phytoplankton growth rates are similar after 10 days, but that simulation F has a maximum productivity which is 50% higher than BK after 20 days. Furthermore, N - P - Z profiles after 20 days of simulation (figure 9.5 and figure 10 of BK) show that the two ecosystems are in a very similar state in the unstable waters offshore of the T_{md} , but that the riverine scenario promotes the growth of plankton both inshore of and at the thermal bar.

These observations can now be used to explain the differing plankton growth rates between BK and this work. As all model parameters are the same in each study, there are only two broad potential causes: the lake's thermal regime and the influence of the riverine boundary conditions. The work on the effects of stability and boundary conditions presented in sections 9.2.1 and 9.3 provides the necessary background for this discussion, and indicates that it is the stability-led differences in vertical diffusivity which leads to the differences in growth rate rather than increased nutrient supply from the river.

This conclusion is reached because simulations with N_R , P_R , and Z_R reduced by 30%, 50%, and 50% respectively still have zooplankton bloom levels of at least double the BK magnitude after 24 days. In addition, vertical N - P - Z variations are shown to be strongly correlated with N^2 profiles, and stability values are generally several orders of magnitude higher in simulation F than in BK. In simulation F , the growth of plankton

at the stability maximum inshore of the thermal bar exceeds that at the T_{md} , despite the suppressive effect of the riverine boundary conditions for plankton, and actually exceeds the magnitude of the BK bloom at the location of the thermal bar. Tests have shown that the high growth rate is independent of P_R and Z_R values, and these features cannot be due to the continued riverine nutrient input because growth is not Nitrogen-limited at this stage in the BK case. Therefore this extra growth must be due to the stronger static stability imparted by the rapidly-warming river inflow.

It is reasonable to assume that a strong enough river inflow could cause enough turbulence in the near-shore region to offset these effects of stability on the plankton growth. As the neglect of shear effects in the vertical eddy viscosity is fully justified in chapter 4, the consequences of this effect are ignored here, as they are beyond the resolution of the present model. Considerable improvements to the turbulence model could form the basis of an extension of this study, and are probably necessary to properly describe the effects of river-generated turbulence and their influence on plankton populations.

It is concluded that the phytoplankton growth in this model is probably excessive, even though the available data on plankton about a riverine thermal bar is not of a fine enough scale to refute the existence of the predicted 'double' phytoplankton bloom after only 24 days of spring warming. In adopting the Franks et al. (1986) model, BK argued that its growth rates were not ideally suited to temperate lake plankton modelling in spring due to the lack of any temperature dependence (see section 2.5.1). When the absence of self-shading and the immediate return of detritus to the available nutrient pool are also considered, it is clear that the most controversial simplifications of this model all tend to produce higher productivity than would otherwise be the case.

The lower stability of BK allowed plankton growth values to remain reasonable in their work, but in the case of the riverine thermal bar a model incorporating a more realistic photosynthetic production is probably required. The extent to which this model oversimplification can be rectified realistically and at reasonable computational expense is explored in the next chapter by discussion of the results of the *N-P-Z-D* ecosystem model of Parker (1991), which is coupled to these Kamloops Lake dynamics.

Chapter 10

Results - Improved Plankton

Modelling

It is shown in this chapter that doubts over the validity of the results in chapter 9 are probably well-justified. By studying the development of a more sophisticated plankton model on the same flow-field and thermal regime, it is possible to test the influence of some of the more controversial simplifications of the Franks et al. (1986) model.

As detailed thoroughly in chapter 2, the plankton model of Parker (1991) contains a detritus component and is fully dependent upon temperature, with every biological interaction multiplied by a thermal variation factor q . Results of the Franks et al. model presented in chapter 9 lead to a particular interest in the effects of improvements to the photosynthesis formulation, catered for in the Parker model with the inclusion of the diurnal light fluctuation, self-shading, and optimum light intensity for phytoplankton.

This chapter proceeds with a discussion of results from simulation P , the predictions of the basic Parker model on Kamloops Lake under riverine boundary conditions of $N_R-P_R-Z_R-D_R = 4-1-1-1 \text{ mmol N m}^{-3}$. A closer inspection of each of the source terms in the Parker model is then presented, and the relative importance of each is discussed.

In order to provide a thorough basis for the comparison of the two models at the end of this chapter, the effects of simplifying the Parker model are studied in detail. A particularly important finding is that by removing the detritus component and ignoring temperature dependence and self-shading, it is possible for the Parker model to qual-

itatively reproduce the suspicious 'double-bloom' results of the previous chapter. This suggests that the oversimplification of the Franks et al. model could be responsible for the potentially excessive phytoplankton growth seen in simulation *F* and illustrates that the qualitative *N-P-Z* behaviour is independent of model parameter choices.

10.1 Temporal Evolution of Plankton Population

10.1.1 8 days of simulation

After only 8 days of simulation it is obvious from phytoplankton concentrations that simulation *P* will produce a totally different ecosystem to simulation *F*. Phytoplankton growth is obviously less prolific in the Parker model because concentrations are much lower after this time than in simulation *F* (compare figures 10.1(a) and 9.1(a)). The growth which has taken place is restricted to the near-river region and seems to be dominated by the inflow boundary conditions, with riverine phytoplankton values being transported vertically in a similar manner to the tracer concentrations in figure 8.15.

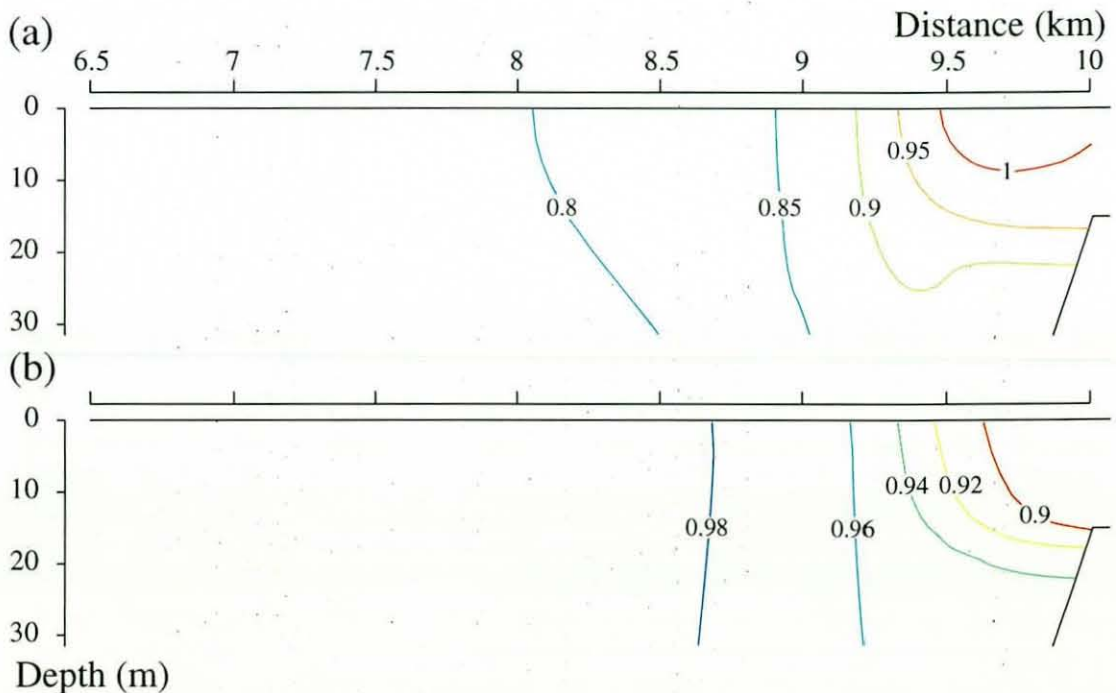


Figure 10.1: Characteristics of simulation *P* after 8 days: (a) phytoplankton concentration (mmol N m^{-3}), (b) zooplankton concentration (mmol N m^{-3}).

However, this distribution is actually supported by photosynthesis, as the temperature dependence prompts growth in the warm river region rather than at the T_{md} .

Zooplankton behave in a qualitatively similar way in simulations P and F , but the actual zooplankton concentrations in the lake after 8 days are much lower in simulation F . In simulation P , the halved zooplankton mortality overcomes the generally lower assimilated grazing rate and allows far more zooplankton to survive the initial stages of ecosystem development. In fact the mortality is reduced to such an extent that zooplankton concentrations are virtually uniform at this stage of the simulation.

10.1.2 16 days of simulation

Results follow a similar pattern after 16 days of simulation. The phytoplankton bloom which emerges has a much smaller magnitude than that of simulation F (compare figures 9.2(a) and 10.2(a)), and is localised closer to the river at the stability maximum inshore of the surface T_{md} which is described in section 9.2.1. As shown in later analyses,

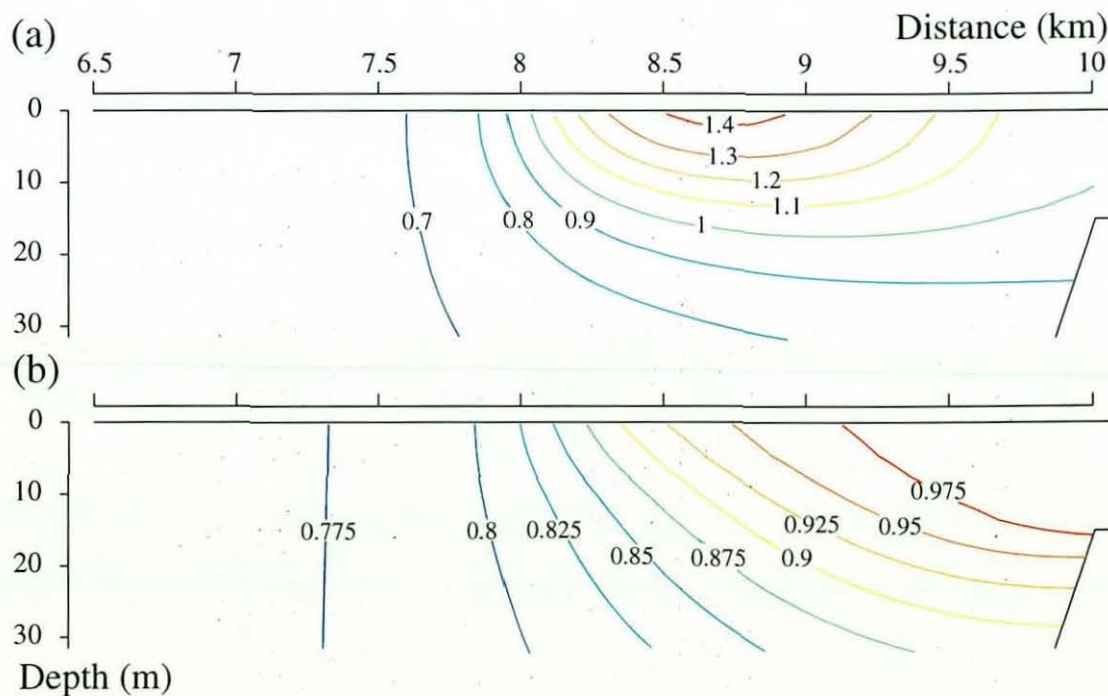


Figure 10.2: Characteristics of simulation P after 16 days: (a) phytoplankton concentration (mmol N m^{-3}), (b) zooplankton concentration (mmol N m^{-3}).

this arises from the skewing of growth towards the warm river by the temperature dependence.

Zooplankton characteristics are very slowly-varying, and after 16 days there is still little sign of any growth which is independent of the riverine boundary conditions. The qualitative similarities between contours of zooplankton and tracer at this time indicates once again that zooplankton mortality and grazing have nearly identical distributions (if not absolute values) within the lake.

10.1.3 24 days of simulation

After 24 days the predictions of phytoplankton concentration in models P and F are qualitatively different. While simulation F now has a fully-developed double phytoplankton bloom, simulation P still shows a single bloom, far inshore of the T_{md} , with maximum phytoplankton concentrations at a value of half of that attained by simulation F after only 16 days. Values at depth are also much lower, due to the convection of

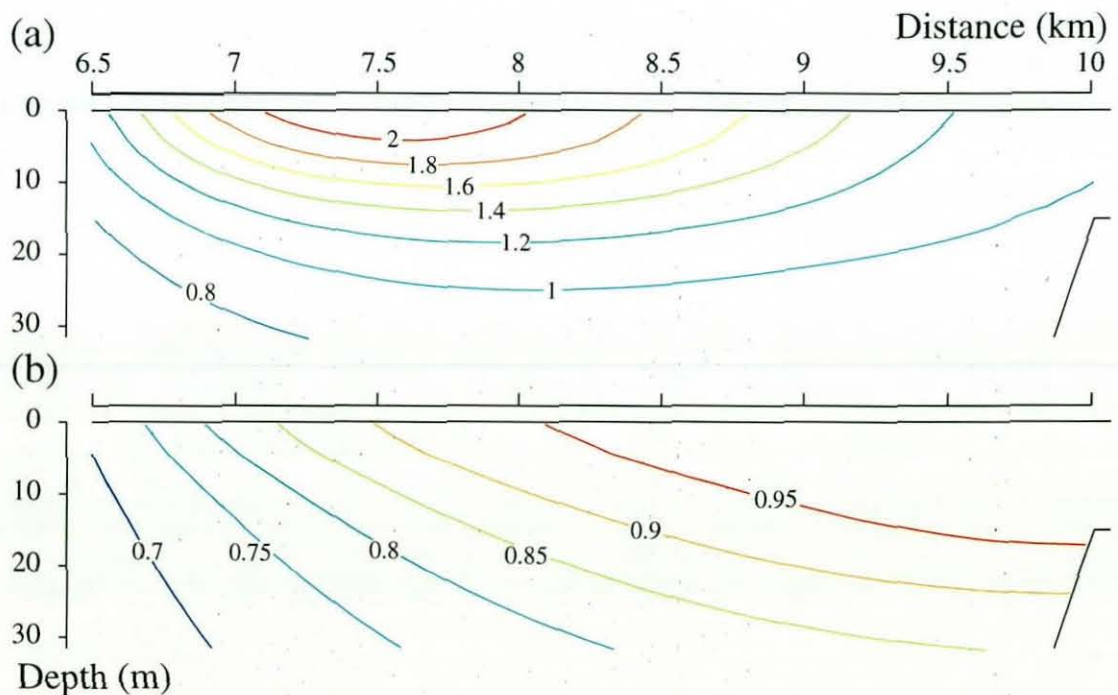


Figure 10.3: Characteristics of simulation P after 24 days: (a) phytoplankton concentration (mmol N m^{-3}), (b) zooplankton concentration (mmol N m^{-3}).

reduced phytoplankton concentrations downwards, and the largest concentrations are no longer carried downwards by the thermal bar because the bloom is so much further inshore of the main downwelling motions.

As with the earlier stages of simulation *P*, zooplankton distributions are still dominated by riverine effects after 24 days of open-lake grazing. In total contrast to the zooplankton bloom of simulation *F* (figure 9.3(b)), zooplankton concentrations experience a shallow gradient of decrease away from the river plume region to offshore of the T_{md} and the depths of the lake.

10.2 Closer Examination of Plankton Growth

A horizontal profile of all four components of the plankton model gives a very economical view of the status of the entire ecosystem and permits a discussion of the nutrient and detritus components of the model (figure 10.4). The plot shows how slowly the Parker model develops, with the main biological interactions being the gradual blooming of phytoplankton inshore of the T_{md} and the death of both plankton types increasing detritus concentrations away from the river inflow. This plot also highlights the limitations of the zooplankton, which do not seem to display any net growth through grazing during simulation *P*.

Comparing these profiles with the equivalent for simulation *F* (figure 9.4) emphasises the massive difference in the rates of interaction between the components of each model. The most important change in simulation *P* is the decreased photosynthesis rate, and these plots show that after only 8 days there is a significant difference in phytoplankton concentrations everywhere in the domain. It is especially interesting to note that simulation *P* restricts the majority of phytoplankton growth to the near-river areas, while a fair amount of photosynthesis takes place offshore of the T_{md} in simulation *F*.

As a result of the stunted phytoplankton growth in the open lake, nutrient levels stay constant there throughout simulation *P* despite the delay in returning planktonic detritus to the nutrient pool. This result is contrary to the observations of simulation *F*, where nutrients are rapidly depleted everywhere under the pressure of mass phyto-

plankton growth. Of all components it is the detritus which gains the most Nitrogen when averaged over the whole open lake, because plankton mortality and unassimilated zooplankton grazing exceed the detritus to nutrient conversion rate. The large detritus availability means that the conversion rate will be relatively high, so the nutrients should continue to grow with time in the open lake. These observations are explained in the following sections by a closer analysis of the source and transport terms in the governing equations.

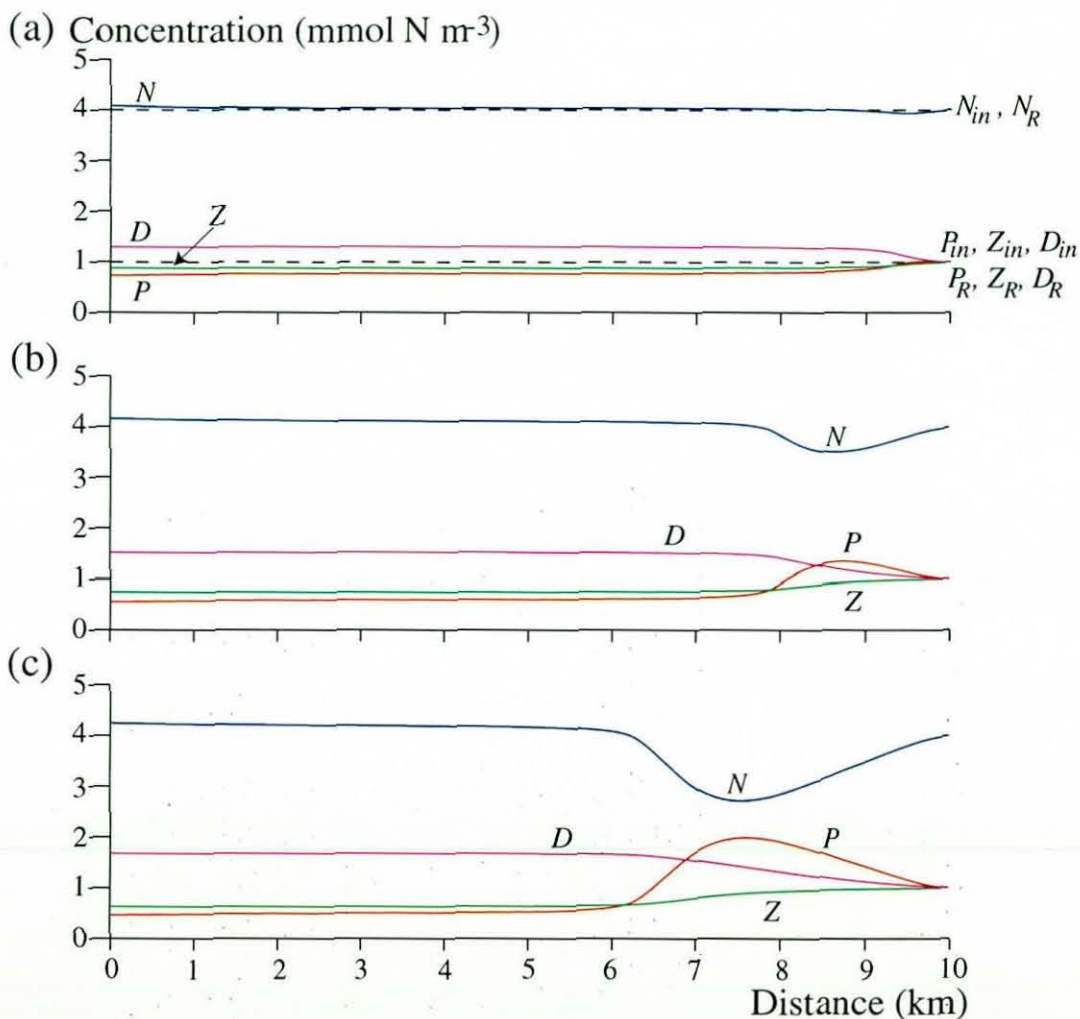


Figure 10.4: Horizontal *N-P-Z-D* profiles at 5 m depth throughout simulation *P*: (a) 8 days, (b) 16 days, (c) 24 days.

10.2.1 Phytoplankton

The single phytoplankton bloom predicted by the Parker model is explained here by examining each term of the governing advection-diffusion equation (table 10.1). As in

simulation F , vertical convection and phytoplankton mortality terms may be ignored immediately due to their small magnitude. Also as before the distribution of horizontal convective and diffusive processes is not of particular interest as they simply denote transport at the river inflow and across the thermal bar respectively.

As in simulation F it can be seen that vertical diffusion and photosynthesis (at the average light intensity) are the leading-order terms, but unlike simulation F the latter significantly outweighs the former almost everywhere in this model. This happens because, despite having a similar distribution, vertical diffusion of phytoplankton is lower due to a reduction in the curvature of the vertical phytoplankton profile which is caused by the lower phytoplankton growth, especially offshore of the T_{md} . Overall the vertical diffusion of phytoplankton is reduced by a larger quantity in simulation P than the primary production, and therefore production is now largest.

Term in P transport equation	Minimum	Maximum
Primary production (average)	4×10^{-6}	2×10^{-5}
Grazing	-2×10^{-6}	-2×10^{-7}
Mortality	-4×10^{-9}	0
Vertical diffusion	-2×10^{-5}	0
Horizontal diffusion	-5×10^{-6}	1×10^{-5}
Vertical convection	-1×10^{-7}	2×10^{-6}
Horizontal convection	-5×10^{-6}	2×10^{-6}
Thermal variation factor	0.3	0.6

Table 10.1: Range of values of each term in the P transport equation along a near-surface horizontal profile during the first 24 days of simulation P . All units are $\text{mmol N m}^{-3} \text{s}^{-1}$

By comparing figures 10.5(a) and 9.6(a) it can be seen that the horizontal distribution of primary production is fundamentally altered by temperature dependence even before the effects of nutrient limitation become apparent in simulation F . Table 10.1 shows that q changes by a factor of 2 over the domain, and figure 10.5(b) shows that this variation favours biological interaction near the warm river inflow. This results in the situation

pictured in figure 10.5(a), where the photosynthesis is always greater near the river than in the open lake offshore of the T_{md} , a result which contrasts with simulation F , where photosynthesis reaches a minimum near the river inflow due to the fixed value of P_R (figure 9.6(a)).

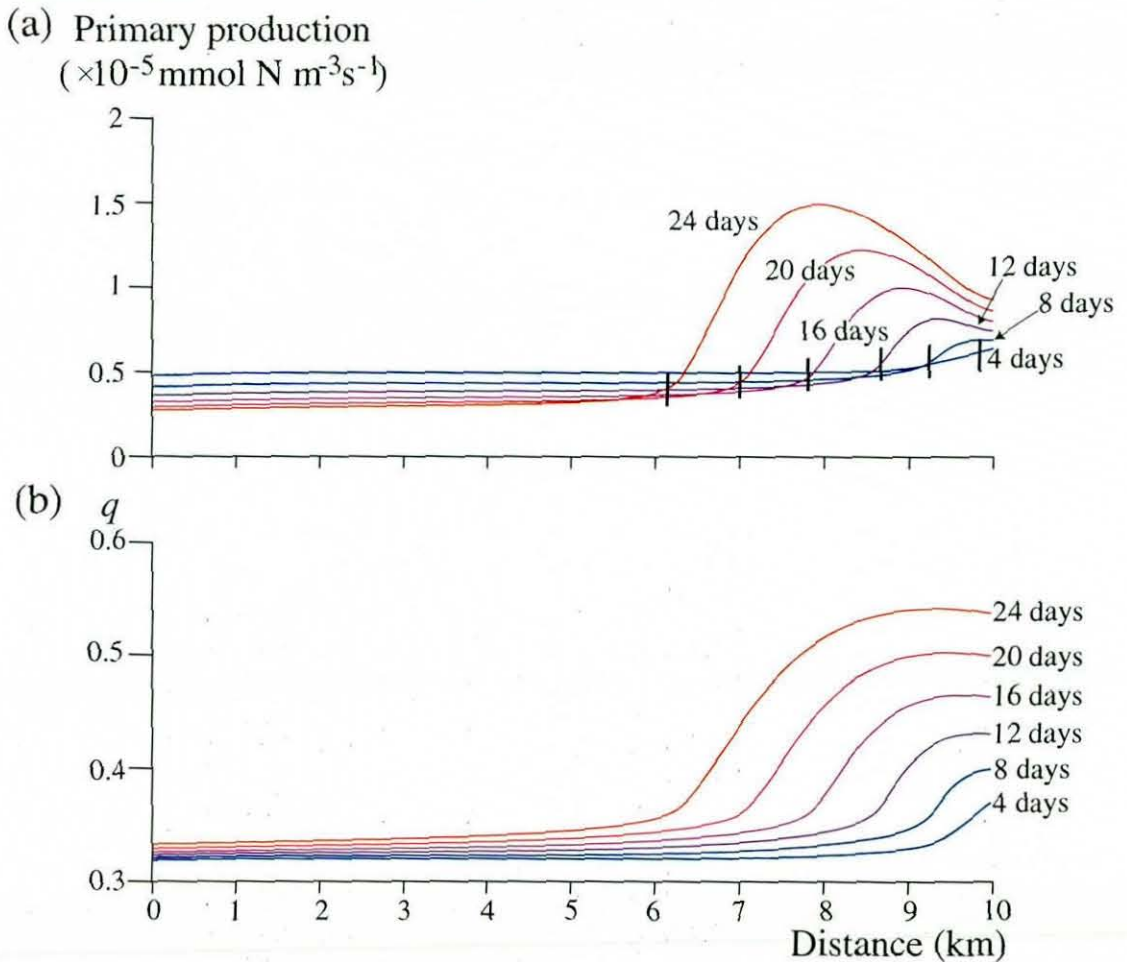


Figure 10.5: Source terms for phytoplankton throughout the simulation: (a) photosynthetic production (taken at the average value of light intensity) and position of the T_{md} (|), (b) thermal variation factor q .

By stressing the importance of q , it can be argued that the temperature dependence of the Parker model is responsible for both the lack of phytoplankton growth offshore of the T_{md} (which is noted in the discussion of figure 10.4) and the lagging of the phytoplankton bloom further behind the T_{md} than in simulation F , which was noticed

throughout section 10.1. Temperature dependence is also seen to influence zooplankton grazing in simulation *P*, but the effects of this particular phenomenon are minimal because overall grazing rates are found to be a much lower proportion of photosynthesis than in simulation *F*.

10.2.2 Zooplankton

Examining the magnitude of terms in the zooplankton equation (table 10.2) reveals the dominance of transport processes over the biological production and destruction of zooplankton. This supports the observations that zooplankton concentrations are dominated by the riverine boundary conditions throughout simulation *P*, as it implies that the transport of riverine values around the domain will obscure any zooplankton grazing or mortality which may take place.

Term in <i>Z</i> transport equation	Minimum	Maximum
Assimilated grazing	5×10^{-8}	7×10^{-7}
Mortality	-7×10^{-7}	-2×10^{-7}
Vertical diffusion	-2×10^{-6}	0
Horizontal diffusion	-8×10^{-7}	2×10^{-6}
Vertical convection	-1×10^{-8}	2×10^{-7}
Horizontal convection	-4×10^{-7}	1×10^{-6}

Table 10.2: Range of values of each term in the *Z* transport equation along a near-surface horizontal profile during the first 24 days of simulation *P*. All units are $\text{mmol N m}^{-3} \text{s}^{-1}$.

In addition, plotting the assimilated grazing and mortality rates for zooplankton in figure 10.6, we can see that mortality overturns most of the zooplankton growth throughout the simulation. This is partly due to temperature dependence, which will ensure that all biological interactions tend to attain their most significant values in the same area of the domain. It can be concluded from this study that zooplankton behave as a virtually neutral tracer in simulation *P*.

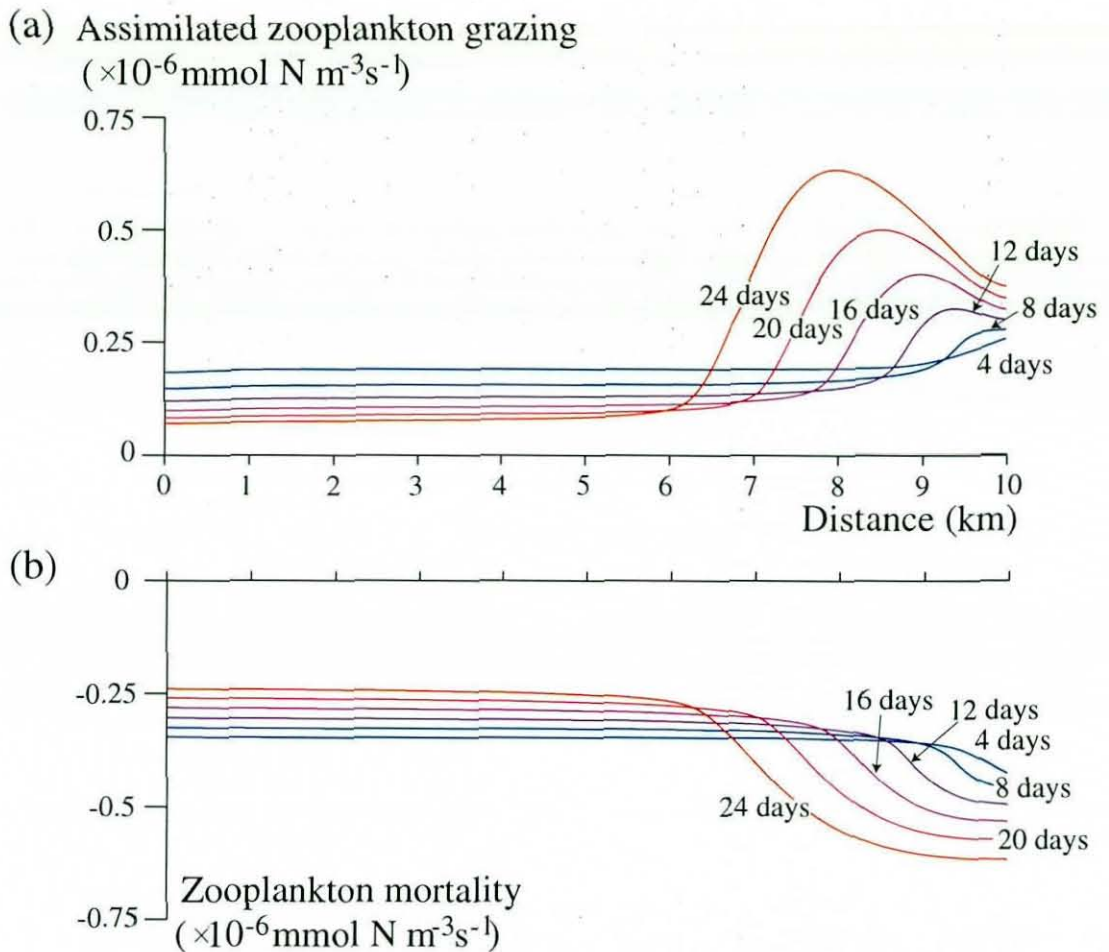


Figure 10.6: Source terms for zooplankton throughout the simulation: (a) assimilated zooplankton grazing, (b) zooplankton mortality.

10.3 Effect of New Features in Model

The qualitative differences in the plankton predictions of each model lead to the question of why these simple models would give such vastly different answers in the same dynamical and thermal regime. The intention of this section is to gradually strip away the sophisticated features of the Parker model until the basic functionality of the Franks et al. model is recovered. This is done in order to assess the contribution of each individual improvement of the Parker formulation over Franks et al. so the neglect of each component is discussed individually before all relevant components are removed in section 10.3.4.

Comparing the formulation of the two plankton models it is easy to deduce that there are five major differences: the detritus component, temperature dependence, the zooplankton grazing formulation, the phytoplankton mortality formulation, and the inclusion of self-shading. Since the phytoplankton mortality and zooplankton grazing terms are found to be relatively unimportant in this test (table 10.2), we proceed by discussion of three Parker model simulations which each have one of the other factors removed.

In the following sections, the simulations with and without detritus, self-shading, or temperature dependence (the formulations of which are all fully described in section 2.5) are referred to as simulations *PD*, *PS*, and *PT* respectively. In addition, a simulation without any of these components will be referred to as *PTSD* here.

10.3.1 Detritus Removed

It can be seen from the results of simulation *PD* after 24 days in figure 10.7 that removing the detritus component of simulation *P* actually has very little effect on the plankton ecosystem. Nutrient levels are increased by the same amount that detritus gained previously, as all plankton waste products are now returned directly to the nutrient pool. In turn this allows a very slightly larger bloom of phytoplankton due to a minor reduction in nutrient limitation. However, this does not prompt a noticeable increase in zooplankton because the assimilated grazing rates are so small (see table 10.2), so that overall the effects of including the detritus component do not seem particularly important. This result is in full agreement with the findings of Edwards (2001), who showed that the inclusion of detritus only affects a model's behaviour significantly when zooplankton are allowed to graze it.

10.3.2 Self-Shading Removed

The removal of phytoplankton self-shading has a rather more profound effect on the whole ecosystem (figure 10.8). The obvious consequence of this step is an increase in photosynthesis, and comparing the *N-P-Z-D* profiles in figures 10.4(c) and 10.8 shows that this leads to a doubling in phytoplankton growth over the first 24 days of simulation.

Phytoplankton levels are mainly increased at the bloom inshore of the thermal bar, where the large quantities of biomass would normally produce significant shading, but a detailed comparison reveals that a small increase is also present throughout the rest of the lake.

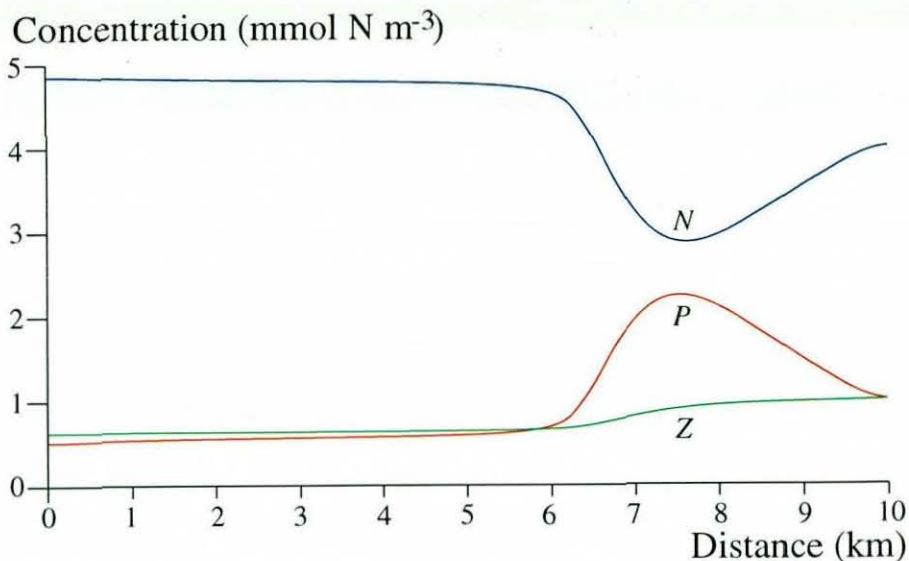


Figure 10.7: *N-P-Z* profile from simulation *PD* after 24 days.

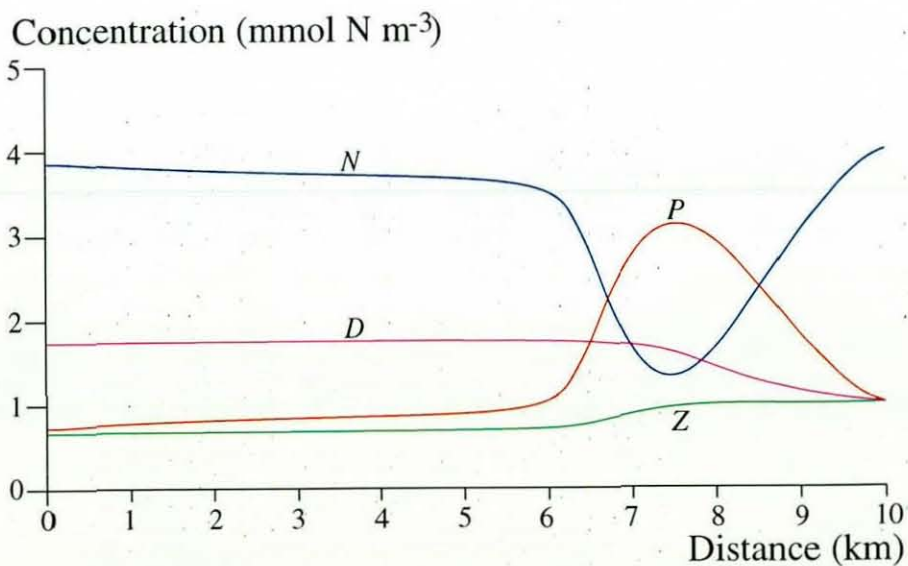


Figure 10.8: *N-P-Z-D* profile from simulation *PS* after 24 days.

This increased primary production leads to a greater nutrient depletion, so that

further photosynthesis is limited inshore of the T_{md} . The zooplankton and detritus components are surprisingly unaffected by the removal of self-shading, however, with only small increases in each component due to increased grazing and phytoplankton mortality respectively.

10.3.3 Temperature Dependence Removed

Ignoring the temperature dependence of the Parker model has a far more profound effect on the ecosystem predictions than either of the two previous changes. As this simulation was performed by fixing q to be constant at a value corresponding to the Franks model, the effects of this step are to remove the preferential interaction rates in the warm river inflow and to generally increase the rate of all biological interactions.

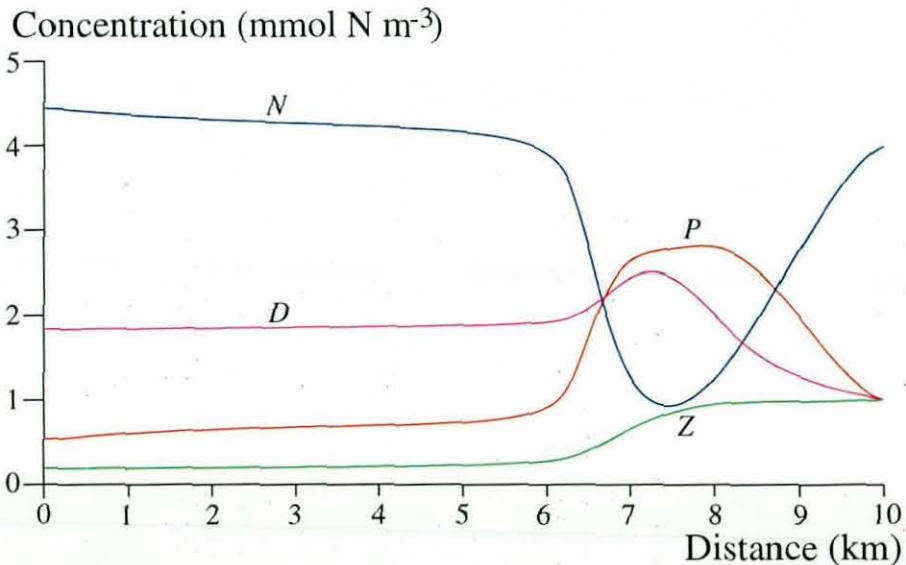


Figure 10.9: *N-P-Z-D* profile from simulation *PT* after 24 days.

Figure 10.9 shows that the effect of standardising q is to increase the phytoplankton production and promote photosynthesis over a much wider area, including offshore of the T_{md} . This extra growth may not seem obvious from a comparison of figures 10.4(c) and 10.9, but must happen because the detritus component is so vastly increased. This implies that phytoplankton growth is constantly increased here, but the similarly-increased mortality rates (particularly offshore of the T_{md}) transfer the plankton biomass to detritus.

Increased photosynthesis leads to a greater nutrient depletion, causing the 'flatter' phytoplankton bloom seen in figure 10.9, which could be the precursor to a double bloom caused by nutrient limitation. Zooplankton grazing rates are not sufficiently increased by the removal of temperature dependence to cause a bloom inshore of the thermal bar, and the increased mortality makes zooplankton depletion in the open lake even more prevalent.

10.3.4 All Three Components Removed

The results of simulation *PTSD* are crucial to this study, since it is postulated in the rest of this chapter that the three removed components contain the most important quantities separating the Franks et al. model from the Parker model. None of the variant simulations above seem to be much closer to simulation *F* than simulation *P*, but the progression of simulation *PTSD* which is plotted in figure 10.10 shows results which are remarkably similar to those of figure 9.4. Considering the differences in formulation and parameter values which are still present between simulations *F* and *PTSD*, it is very interesting that this simplified version of simulation *P* is able to qualitatively reproduce the results of chapter 9.

By comparing figures 9.4 and 10.10 we can assess exactly how different the two simulations are. After 16 days it is obvious that the photosynthesis rate is still slightly lower in simulation *PTSD*, a difference which becomes more substantial with time. This is a consequence of the higher nutrient half-saturation constant, k_s , in the Parker model, which leads to nutrient limitation of photosynthesis at much higher nutrient concentrations than in simulation *F*. Also from these plots it is obvious that the zooplankton mortality rate is much larger in simulation *F*.

After 24 days of simulation, case *F* has the fully-developed double bloom described previously but despite having a similar distribution of all three ecosystem components, simulation *PTSD* only shows a small inflexion in the centre of the phytoplankton bloom. This is mainly due to the difference in k_s value, as nutrient limitation in simulation *PTSD* causes a much gentler process than the sudden drop in photosynthetic production rates which takes place in the centre of the phytoplankton bloom of simulation *F*. It should also be noted that the zooplankton grazing rate is much lower in simulation *PTSD*,

which explains the low predictions of zooplankton concentration in all of the Parker model variants.

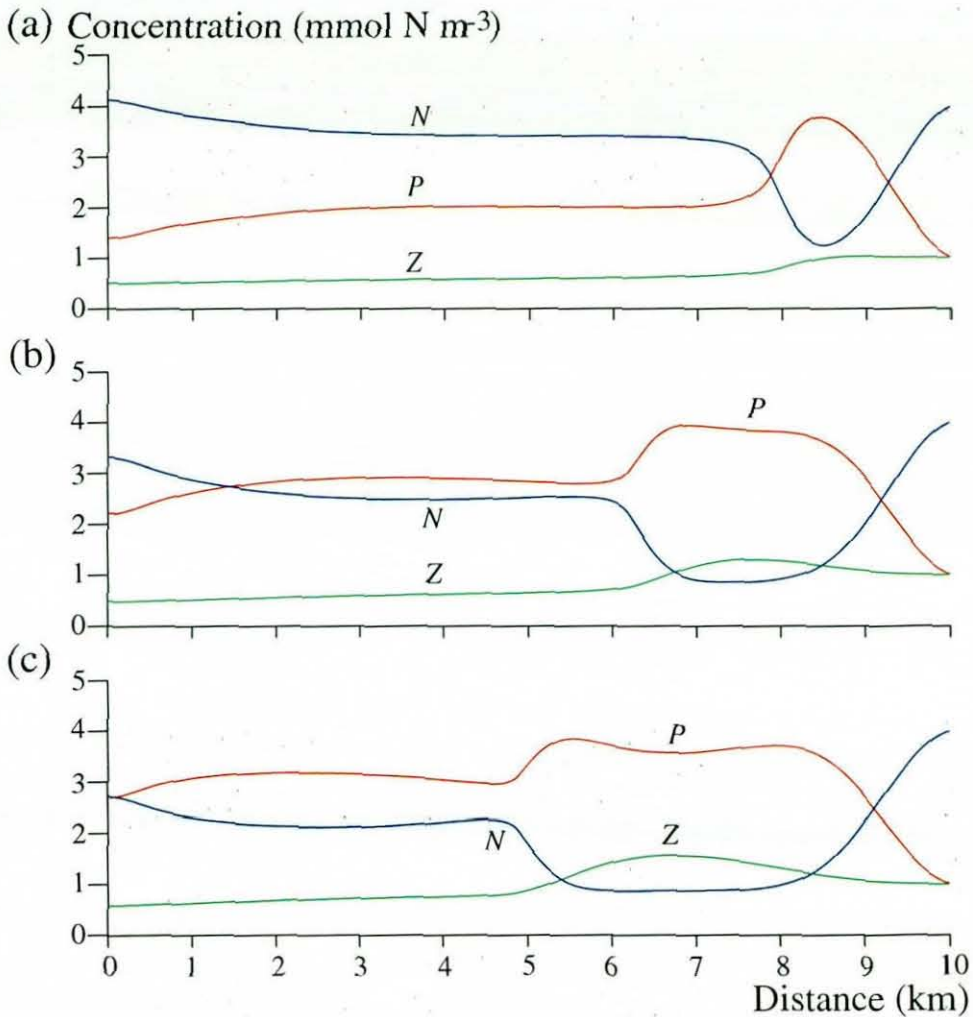


Figure 10.10: Horizontal *N-P-Z* profiles throughout simulation *PTSD*: (a) 16 days, (b) 24 days, (c) 30 days.

After 30 days, simulation *PTSD* has qualitatively reproduced all of the predictions of simulation *F*. Nutrients are not reduced to such a drastic level, and as a result the double bloom is much wider as the smoother impedance of photosynthesis allows a more gradual, and therefore less localised, bloom development. Zooplankton levels are also much lower, so the effect of zooplankton grazing on the double bloom formation is lessened. It is therefore proposed that with alteration of the nutrient-limitation factor and zooplankton growth and mortality rates it would certainly be possible to quantitatively reproduce simulation *F* from the basis of the Parker model.

10.4 Discussion and Comparison With Franks et al.

Before fully comparing the results of the Parker model with those of the Franks et al. model, it is vitally important to note that, in the absence of any high-resolution data on the spring phytoplankton bloom in Kamloops Lake, it is impossible to conclusively say which of the two models produces the most reasonable approximation to real plankton populations. This is why the 'double bloom' predictions of Franks et al. are never definitively held to be wrong; although it has been shown that they are not found in a more sophisticated model, there is no certain way of knowing whether this complex model is a more appropriate formulation for Kamloops Lake in the spring. However, it is noted here that the Parker model predicts photosynthesis rates which generally agree with a steady productivity over several months, as observed in Kamloops Lake by St. John et al. (1976).

As the available data are so sparse, the strength and motivation of this work primarily comes from the desire to test and extend the results of BK to a riverine thermal bar in a shallow lake, initially producing a purely qualitative comparison between the 'classical' thermal bars of their work and the riverine thermal bars of this study. After the results were found to differ in chapter 9, this chapter is intended to study the sensitivity of those early results to greater levels of sophistication in the basic model formulation.

Although there is no proof, it is thought that growth is probably excessive in simulation *F* since the Franks et al. model is conditioned to the marine pelagic ecosystem in summer and there are no reports of a 'double bloom' in phytoplankton in temperate lakes in spring. By experimentation with a more complex model (which admittedly is also conditioned for summer marine waters) it is shown in this chapter that the double bloom results may only be reproduced by ignoring three of the most significant facets of the new model.

Interestingly, it is found that these results may only be achieved by neglecting all three of these differences at the same time. The removal of temperature dependence and self-shading simultaneously allows a large increase in photosynthesis and a shift of phytoplankton growth away from the river inflow (not shown), and the removal of the detritus component in simulation *PTSD* then ensures that nutrient limitation acts in

exactly the manner required for the prediction of a double bloom. This supports the contention that the double bloom is probably due to the excessive phytoplankton growth which results from oversimplification of the Franks et al. model, since it takes a particular combination of three clearly unphysical assumptions to produce this phenomenon.

The main achievements of this chapter are therefore the elucidation of the effects of detritus, self-shading, and temperature dependence on simple plankton formulations. Each of these factors can clearly produce qualitative differences in the predictions of a plankton model, so they should be included whenever an application includes sufficient data for parameter-fitting. Of course a great deal of useful information can be gained from a very simple plankton model, as shown by BK, but this study concludes that the applicability of these results should be viewed with extreme caution.

Chapter 11

Conclusions and Suggested Further Work

Chapters 5 - 10 of this thesis present the results of three different studies of the riverine thermal bar which have implications for several areas of limnology. The validity of these results, however, relies upon the assumptions made in the formulation of the original model. Due to limitations in observational data and available computer power, these assumptions are rather restrictive, so that most results are considered to be a qualitative first step towards a full understanding of this previously-unmodelled phenomenon.

The intention of this chapter is to summarise the results and consequences of each set of simulations and, more importantly, suggest ways in which this rather basic research could be extended in future. In particular, it is argued how the project could proceed given greater computational resources, but work on the riverine thermal bar is also limited by a serious lack of field observations. In order to provide accurate initial and boundary conditions for these suggested model improvements, new field studies of the riverine thermal bar must be made, particularly in Lake Baikal.

11.1 Numerical Procedure

A significant impediment to progress on this work, to which a large proportion of this thesis is dedicated, is the cumbersome nature of the solution procedure. A highly-accurate solution of the elliptic pressure correction equation is required in order to enforce continuity and thereby avoid spurious flows, as discussed in section 3.3. This

necessitates the use of a direct matrix solver which places heavy demands on memory, limiting the number of grid points, and consumes a large proportion of the total solution time.

With hindsight, a far more economical solution procedure could be implemented by adopting a streamfunction/vorticity formulation of the governing equations. A streamfunction could be defined for the two-dimensional flow, with values fixed on the boundary, so that the vorticity equation becomes a Poisson equation with a known right-hand side for the time derivative. The advantage of this approach is that mass is always conserved exactly, so an acceptable solution to the flow field could be achieved by solving the elliptic vorticity equation to a much lower accuracy than that required for the pressure-correction equation.

11.2 Lake Baikal

The study of Lake Baikal is undertaken on a deep, rectangular section which is nominally representative of the Selenga River delta. Different thermal scenarios are modelled at three stages of the spring development of a thermal bar, elucidating a range of possible dynamics available to this single phenomenon. A river which is only slightly warmer than the T_{md} is found to produce a cabbelling plume which sinks down the nearshore boundary, while warmer rivers will create a buoyant gravity current inshore of the thermal bar which moves the cabbelling away from the river inflow by overpowering return flows on the bar's offshore side. Increasing the salinity of the inflow tends to convert the flow regime from the latter situation towards the former, with the density increase due to salinity generally suppressing the horizontal propagation of the thermal bar and increasing the downwelling rate and maximum plume penetration depth.

This study explicitly illustrates the buoyancy forces involved in thermobaric control of a thermal bar's sinking plume for the first time. In the absence of salinity differences, the depth at which thermobaric control operates is where the initial temperature profile crosses the $T = T_{md}$ profile. If very cold waters were present at all depths, there would be no thermobaric control (Kay 2001); however in lake Baikal there is a winter mid-depth temperature maximum of 3.4 - 3.6°C (Shimaraev & Granin 1991), implying the

thermobaric control at depths of 200 - 300 m which is observed in the non-saline cases of this model.

As detailed in chapter 7, a saline thermal bar's increased mineralisation counteracts the thermobaric deceleration by raising the plume's density relative to that of the ambient lake water. This increases the maximum plume penetration depth, because the water has to sink further for the thermobaric buoyancy forcing to become large enough to halt the downwelling.

The evaluation of saline effects on a riverine thermal bar is probably the most significant advance of this work. The curtailment of horizontal propagation of the thermal bar which is associated with a riverine salinity increase could severely inhibit the dispersion of riverine pollutants and nutrients in a temperate lake, while the increased vertical mixing could substantially increase the residence times of these undesirable substances (Killworth & Carmack 1979). A riverine loading of pollutants which is safe when dispersed throughout the lake could be concentrated to a harmful level when localised by flow patterns within specific regions, and it is therefore important to consider the possible effects of salinity when determining acceptable levels of pollution in a deep temperate lake.

Of most importance to Baikal is the deepened vertical advection which results from a salinity increase suppressing the thermally-induced resistance to sinking. The model predicts that the thermal bar plume could certainly be involved in deep mixing of Lake Baikal if combined with an increased riverine salinity of the magnitudes studied here.

The crucial point is that salinity cannot be ignored in any temperate lake during spring and autumn overturn, when temperatures are close to the T_{md} . Neglect of the buoyancy forcings arising from salinity variation in Baikal has been shown here to be flawed, at least when considering regions in the vicinity of a river delta. There is clearly an important range of conditions under which the complex interplay between thermal and haline effects must be included in modelling efforts.

Although this study yields new results on the riverine thermal bar in a deep lake and

is an important base for future work, the model employed is barely satisfactory in this particular case due to the limited domain size and simulation timespan which is caused by restrictions on computational power. The first and most important improvement which could be made to this model on a more powerful machine is to run longer simulations, preferably of the entire spring warming, so that a variable inflow temperature could be employed. A longer simulation time would also allow the inclusion of coriolis forces and a surface heat flux, removing the main potential criticisms of the existing model. Introducing a wind stress on this more realistic riverine thermal bar could provide an interesting and important robustness study by quantifying the wind-sensitivity of the motions predicted in the original model.

After many basic results have been achieved on a rectangular domain by varying river discharge and temperature and the surface heat flux and wind stress, the next model development phase would be an improvement of the section bathymetry. A selected Selenga delta cross-section would be more realistic, but a truly accurate prediction of the flow in this area of Lake Baikal can only be made with a three-dimensional model. Supercomputing time would almost certainly be required for this intensive simulation, but its use would be thoroughly justified by the considerable increase in realism that a third active dimension would bring.

In order to properly quantify the effects of turbulent mixing of the river and lake, future high-resolution studies should attempt to include more sophisticated turbulence closure schemes than the algebraic model applied here. Shear in horizontal flows will increase vertical mixing inshore of the thermal bar, so that the results presented here may be altered as the vertical diffusivity is based solely upon stability. As a related study, a Large-Eddy Simulation could be employed under carefully controlled conditions to examine the reported inducement of the thermobaric instability by a thermal bar (Shimaraev et al. 1993) and the effect of salinity on this potential mechanism for deep-water renewal.

As mentioned in section 1.1, most studies of the thermal bar concentrate upon the spring warming period. It would be a fitting counterpart to the work in this thesis if a similar model were applied to the autumn riverine thermal bar. A detailed numerical

comparison of the properties of both classical and riverine, spring and autumn thermal bars could then complete our knowledge of the thermal bar in all its guises. The ultimate aim of this study would therefore be to perform a three-dimensional model of the Selenga inflow and its influence on mixing in Lake Baikal throughout the entire annual temperature cycle, including both spring and autumn thermal bars.

11.3 Kamloops Lake Dynamical Work

The dynamical study of Kamloops Lake presented in chapter 8 is basically successful as it qualitatively reproduces the measured temperature fields of Carmack et al. (1979). In particular, the riverine thermal bar's transition from sinking boundary plume to surface gravity current is reproduced so that three distinct stages of thermal bar development may be defined. These three stages are found to correspond quite closely to the dynamics of the three thermal cases selected in the Lake Baikal study. The thermal bar's circulation is found to weaken as it propagates across the lake due to the slackening of horizontal density gradients away from the inflow.

This verified simulation is then tested for sensitivity to various model factors in order to gain insight into their overall importance. The study shows that a surface heat flux unsurprisingly increases the propagation rate of the thermal bar slightly by warming more water through the T_{md} in a given time. Unexpectedly, switching to a rectangular bathymetry has little effect upon the horizontal propagation of the thermal bar, but does seem to weaken downwelling flows in this model. Thermobaricity is also rather ineffectual in this shallow lake, despite significantly influencing the positioning of maximally dense water in the mid-depths (see section 8.3).

Removing coriolis forces from the model, however, changes the resulting dynamics drastically. Coriolis forces are found to regulate the horizontal movement of the thermal bar and suppress its downwelling, transferring momentum to the strong longshore flow predicted by previous authors (Huang 1972). However, it should be noted that in reality this flow would soon be deflected by the sides of the inflow region. Indeed, the narrow fjord-like bathymetry of Kamloops Lake clearly contravenes the assumption of no variation in the longshore direction upon which the model formulation is based (see

section 2.1). Despite this caveat, simulations *K* and *KQ* show that with the inclusion of coriolis forces the flow field within the modelled section produces a temperature distribution which is closer to that observed by Carmack (1979).

In contrast, the Selenga River inflow to Lake Baikal is located in a region which provides a reasonable basis for the neglect of variations in the longshore direction. However, coriolis forces are not adopted in the deep-lake model because the effects of rotation are subject to a misleading period of spin-up which persists for longer than the entire timespan of these simulations, as discussed in section 8.6.

Another surprising result from these simulations is that it takes an extremely large increase in riverine salinity to noticeably affect the thermal bar circulation. This happens because the spatial temperature variation (which follows observed values) is so great during most of the simulation that thermal effects dominate buoyancy, unlike the delicately-balanced temperature gradients in the Selenga delta model, which is rather more susceptible to saline effects.

Many of the later improvements recommended for the deep-lake model in section 11.2 would also be sensible model development steps when applied to this study. Since simulation *K* has been validated against measurements, a full study of the effects of other inflow and surface heating rates, river delta slopes, and wind forcings in the style of Malm (1995) could use this base simulation to build a body of theory on the dynamics of the riverine thermal bar.

The changes proposed above tend to bias the model towards a general description of the riverine thermal bar, but the study could also produce an accurate model of the particular flow conditions of Kamloops Lake. The three-dimensional bathymetry of the whole lake could probably be adopted at reasonable computational cost due to its relatively small proportions. The wide range of information on the lake's annual circulation cycle and river plume dynamics present in the literature means that, under a variable surface heat flux and river temperature, the entire annual range of flow conditions in Kamloops Lake could be predicted.

11.4 Kamloops Lake Biological Work

The plankton studies in this thesis were originally conceived as an extension of the work of BK (in modelling plankton populations in the presence of a classical thermal bar) to the riverine case. To this end, the Franks et al. (1986) model is first fully studied in the context of the riverine thermal bar and then the simple results from this simulation are compared to those of the Parker (1991) ecosystem model, which is considerably more sophisticated.

The Franks et al. (1986) model predicts a swiftly-developing phytoplankton bloom at the position of the thermal bar. This bloom soon suffers depletion in its centre due to nutrient limitation and zooplankton feeding, so that by the end of the simulation there are two distinct blooms, one centred upon the position of the thermal bar and one halfway between the bar and the river mouth. The zooplankton also grow relatively quickly and have produced a small local population maximum by the end of the simulation.

Analysis of this 'double bloom' in phytoplankton populations reveals that one bloom is supported by the convergence of the thermal bar, while the inshore bloom is at the position of a stability maximum caused by the mixed interface of river and lake water. Further investigations show that the double bloom is also present in simulations in which the riverine boundary conditions have been drastically altered. The extra stability of the riverine thermal bar is therefore responsible for generating the second inshore bloom and producing a generally higher growth rate than is present in BK. As this double bloom distribution has never been observed in the field, these results raise suspicions about the applicability of the Franks et al. (1986) model.

The Parker (1991) model has lower growth rates from the very beginning, with the phytoplankton only producing a shallow, single bloom at the end of the simulation. Zooplankton growth rates are also comparatively tiny and the zooplankton distribution is generally that of a neutral tracer.

The Parker (1991) model's behaviour is compared to the suspicious results of the Franks et al. (1986) model by removing the extra features which separate the two formu-

lations. Removing the detrital component has surprisingly little effect on the ecosystem dynamics, but neglecting self-shading or temperature dependence has a massive effect upon the phytoplankton productivity. By removing all three together it is possible to produce a double bloom similar to that of the Franks et al. (1986) model, which shows that this feature is caused by a qualitative oversimplification of the model. The use of this formulation to predict lake plankton in spring is therefore brought into question.

In the absence of the detailed data required to justify more complex ecosystem models it is difficult to propose a reasonable extension of these numerical studies. The discussion of river and lake plankton trends in section 1.6 shows that the riverine thermal bar may have a wide range of interesting effects upon plankton populations, but without accurate river and lake measurements of each biological component, nutrients, and turbidity, it is difficult to produce any useful results which are specific to Kamloops Lake.

Given a more sophisticated turbulence model, there is some scope for development of an abstract model of the ecological implications of the riverine thermal bar, based on a range of different boundary and initial conditions on the river and lake. Improvement of the turbulence modelling would be absolutely vital to this study, as the eddy diffusivities have been shown to control the plankton productivity and the possibility exists that the present model is over-predicting growth due to the lack of shear effects in the vertical eddy diffusivity.

Two basic phenomena which are not resolved in the Parker (1991) model are plankton sinking and the shading of plankton by riverine turbidity. As mentioned by BK, sinking could possibly be represented by applying a fixed rate proportional to the vertical turbulent diffusivity, as plankton re-suspension is a consequence of convective motions associated with instability (Kelley 1997). Turbidity could be represented by the tracer variable, introducing an extra shading term into the exponent of equations (2.23) and (2.30). A specifically riverine plankton model could also be developed in order to provide boundary conditions for a coupled river and lake solution, but river plankton are currently far too poorly understood to begin this development.

Throughout this thesis I have tried to emphasise that all results are considered to be

a qualitatively correct first modelling attempt, and could be vastly improved by future researchers in possession of a powerful computer. I sincerely hope that this work will promote the continued study of the riverine thermal bar, perhaps to such an extent that field workers might undertake the highly detailed and wide-ranging field studies of the riverine thermal bar which are required to support further numerical models.

Appendix A

Simulation Details

Preliminary Models:

Identifier	S_R (mgkg ⁻¹)
<i>C</i>	96.3
<i>S1</i>	97.3
<i>S2</i>	98.3

Table A.1: Characteristics of the deep-lake control simulations in this work.

All have $T_R = T_L = 3.4^\circ\text{C}$ and $S_L = 96.3 \text{ mgkg}^{-1}$.

Lake Baikal Dynamical Models:

Identifier	Time (days)	S_R (mgkg ⁻¹)	Features
<i>T7</i>	7	96.3	
<i>T7S1</i>	7	97.3	
<i>T7S2</i>	7	98.3	
<i>T7S5</i>	7	101.3	
<i>T7S10</i>	7	106.3	
<i>T9</i>	9	96.3	
<i>T9S1</i>	9	97.3	
<i>T9S2</i>	9	98.3	
<i>T9S5</i>	9	101.3	
<i>T9S10</i>	9	106.3	
<i>T9P</i>	9	96.3	Thermobaricity neglected
<i>T9D</i>	9	96.3	Domain width 10 km
<i>T9UP</i>	9	96.3	QUICK differencing neglected
<i>T9U0</i>	9	96.3	$u_R = 0$
<i>T9U1</i>	9	96.3	$u_R = 0.01 \text{ ms}^{-1}$
<i>T9A2.5</i>	9	96.3	$A_h = 2.5 \text{ m}^2\text{s}^{-1}$
<i>T9A7.5</i>	9	96.3	$A_h = 7.5 \text{ m}^2\text{s}^{-1}$
<i>T11</i>	11	96.3	
<i>T11S1</i>	11	97.3	
<i>T11S2</i>	11	98.3	
<i>T11S5</i>	11	101.3	
<i>T11S10</i>	11	106.3	

Table A.2: Characteristics of the deep-lake simulations in this work, including simulation time of the one-dimensional preconditioning models, inflow salinity level and details of special features.

Kamloops Lake Dynamical Models:

Identifier	Features
<i>K</i>	Basic Kamloops simulation
<i>KD</i>	Domain width 20 km
<i>KQ</i>	QUICK differencing included
<i>KH</i>	No surface heat flux
<i>KB</i>	Rectangular-box bathymetry
<i>KP</i>	Thermobaricity neglected
<i>KC</i>	Coriolis neglected
<i>KS5</i>	$S_R = 105 \text{ mgkg}^{-1}$
<i>KS10</i>	$S_R = 110 \text{ mgkg}^{-1}$
<i>KS20</i>	$S_R = 120 \text{ mgkg}^{-1}$
<i>KS50</i>	$S_R = 150 \text{ mgkg}^{-1}$

Table A.3: Characteristics of the dynamical Kamloops Lake simulations in this work.

Franks et al. Ecosystem Models:

Identifier	Features
<i>F</i>	Basic Franks simulation
<i>F30</i>	$N_R = 5.2 \text{ mmol N m}^{-3}$
<i>FM30</i>	$N_R = 2.8 \text{ mmol N m}^{-3}$
<i>FPM50</i>	$P_R = 0.5 \text{ mmol N m}^{-3}$
<i>FZM50</i>	$Z_R = 0.5 \text{ mmol N m}^{-3}$

Table A.4: Characteristics of the plankton simulations employing the model of Franks et al. (1986).

Parker Ecosystem Models:

Identifier	Features
<i>P</i>	Basic Parker simulation
<i>PS</i>	No self-shading
<i>PT</i>	No temperature dependance
<i>PD</i>	No detritus component
<i>PTSD</i>	All of the above

Table A.5: Characteristics of the plankton simulations employing the model of Parker (1991).

Nomenclature

Roman script:

a_i, a_{nb}, a_X	coefficients representing neighbouring node influence
\hat{A}	coefficient matrix
A_h, A_v	horizontal and vertical eddy viscosities
B	solid boundary
B_o, B_{oI}, B_{oO}	open boundary, inflow boundary, outflow boundary
c_p	specific heat at constant pressure
C_i	concentration of the i th component of a plankton model
C_o	detritus to nutrient conversion rate
d	general depth
\bar{d}	cut-off depth for vertical eddy viscosity
D	detritus
F	height of free surface above lake bed
F	external forcing vector
g	acceleration due to gravity
G	phytoplankton primary production rate
h_x, h_z	horizontal and vertical grid spacing
H	pressure variation function in the equation of state
i, j	grid indices in x and z directions
I	zooplankton grazing rate
\hat{I}	unit tensor
k	turbulent kinetic energy
k_s	phytoplankton nutrient uptake half-saturation coefficient
K, K_h, K_v	eddy diffusion coefficients for scalar variables
L	length of domain
L_s, L_d	light intensity at surface and depth d
m_P, m_Z	phytoplankton and zooplankton mortality rates

M	maximum phytoplankton death rate
n (n_x, n_z)	number of cells (in horizontal and vertical directions)
n_l	phytoplankton mortality rate N dependance coefficient
n_o	coordinate direction normal to a given boundary
N	nutrients
N^2	stability (square of Brunt-Väisälä frequency)
N_{min}	cut-off value of stability
$N(\alpha, \beta)$	normal distribution with mean α and variance β
p	pressure
p'	pressure correction
P	phytoplankton
Pe	cell Peclet number
$\hat{P}, \hat{Q}, \hat{L}, \hat{U}$	matrices used in the solution procedure
q	plankton interaction thermal dependance factor
Q_s	surface heat flux
Q_j, S_j	general result of forward-elimination step in TDMA
r, s	constants in vertical eddy viscosity parameterisation
R_m	maximum zooplankton ingestion rate
Ri (Ri_C)	Richardson number (critical value of)
$Res(\mathbf{x})$	residual of solution \mathbf{x}
\mathbf{s}	vector of source terms
s_c	light saturation coefficient
s_j	j th-level source term in one-dimensional model
S	salinity
S_e	east-face source term minus pressure gradient
S_s	self-shading coefficient
$S_{C_i}, S_X, S_\Phi, S_{P'}$	source term associated with subscript
t	time
T	temperature
T_{md}	temperature of maximum density
\mathbf{u} (u_i)	velocity vector (i th component of)
u, v, w	velocity components

V_m	maximum phytoplankton growth rate
V_Φ	control volume of integration
\mathbf{x}, \mathbf{y}	general system solution
x, y, z, x_i	model coordinates
Z	zooplankton

Greek script:

α	thermal expansion coefficient
β	coefficient of haline contraction
$\gamma, \gamma_N, \gamma_D$	unassimilated fractions of zooplankton grazing
Γ	adiabatic temperature gradient
δ	angle of section relative to north
δ_{ij}	Kronecker delta
Δt	time step
ΔB	buoyancy change from initial conditions
$\Delta B_S, \Delta B_T$	buoyancy change due to salinity, temperature
ε	dissipation rate of k
η	light attenuation coefficient
Λ	Ivlev constant for zooplankton grazing
μ, μ^V, μ^R	general, molecular and turbulent eddy viscosity
ν_b	background vertical eddy viscosity
ν_0	vertical eddy viscosity for unstable conditions
ν_{ref}	reference molecular viscosity
ρ	density
ρ_c	maximum density at $p = S = 0$
ρ_0	general density at $p = 0$
σ, τ	salinity difference and preconditioning time for Baikal studies
$\hat{\tau} [\hat{\tau}^V] (\tau_{ij})$	viscous shear stress tensor [averaged] (component of)
$\hat{\tau}^R (\tau_{ij}^R)$	Reynolds stress tensor (component of)
v	percentage change in riverine plankton model component
ϕ	latitude of section
φ	riverine tracer
Φ	general scalar variable

Φ	vector of node values of Φ
Ω	Earth's angular velocity vector
$\Omega_x, \Omega_y, \Omega_z$	components of Earth's angular velocity vector

subscripts:

e, w, n, s	value at cell face
E, W, N, S	value at neighbouring node
f	value at general cell face
i, j	general indexed value
in	initial lake value
L	lake value
nb	value at general neighbouring node
R	river value (boundary condition)
U, C, D	value at upstream, central, and downstream nodes
X	value at node of interest

superscripts:

$n, n + 1$	time step of value
*	guessed value
'	correction value / fluctuation from mean
—	mean value

Bibliography

- Akopian, M., Garnier, J. & Pourriot, R. (1999), 'A large reservoir as a source of zooplankton for the river: structure of the populations and influence of fish predation', *J. Plankton Res.* **21**(2), 285–297.
- Archer, D. (1995), 'Upper ocean physics as relevant to ecosystem dynamics: a tutorial', *Ecological Applications* **5**, 724–739.
- Avinsky, V. A., Kapustina, L., Letanskaja, G. & Protopopova, E. (1999), Plankton communities of Lake Ladoga under thermal bar conditions, *in* 'Proc. 3rd Int. Lake Ladoga Symposium', University of Joensuu, Publications of Karelian Institute No. 129, pp. 21–26.
- Barrett, R., Berry, M., Chan, T. F., Demmel, J., Donato, J. M., Dongarra, J., Eijkhout, V., Pozo, R., Romine, C. & der Vorst, H. V. (1994), *Templates for the Solution of Linear Systems: Building Blocks for Iterative Methods*, SIAM, Philadelphia, PA.
- Bennett, J. R. (1971), Thermally driven lake currents during the spring and fall transition periods, *in* 'Proc. 14th Conf. Great Lakes Res.', Intl. Assoc. Great Lakes Res., pp. 535–544.
- Blackman, R. G. & Tukey, J. W. (1959), *The Measurement of Power Spectra From the Point of View of Communications Engineering*, Dover Publications, New York.
- Bolgrien, D. W. & Brooks, A. S. (1992), 'Analysis of thermal features of Lake Michigan from AVHRR satellite images', *J. Great Lakes Res.* **18**(2), 259–266.
- Bolgrien, D. W., Granin, N. G. & Levin, L. (1995), 'Surface temperature dynamics of Lake Baikal observed from AVHRR images', *Photogrammetric Engineering and Remote Sensing* **61**(2), 211–216.

- Bondarenko, N. A., Guselnikova, N. E., Logacheva, N. F. & Tomazkina, G. V. (1996), 'Spatial distribution of phytoplankton in Lake Baikal, spring 1991', *Freshwater Biol.* **35**, 517–523.
- Botte, V. (1999), A Robust and Accurate Navier-Stokes Algorithm For Three-Dimensional Applications Adopting Arbitrary Modelling of the Reynolds Stresses, PhD thesis, Dept. of Turbomachinery and Engineering Mechanics, Cranfield Univ., U.K.
- Botte, V. & Kay, A. (2000), 'A numerical study of plankton population dynamics in a deep lake during the passage of the Spring thermal bar', *J. Mar. Sys.* **26**, 367–386.
- Botte, V. & Kay, A. (2001), 'A model of the wind-driven circulation in Lake Baikal', *Submitted to Dynamics of Atmospheres and Oceans*.
- Botte, V., Tourlidakis, A. & Elder, R. L. (1996), Influence of convection scheme on the solution of the pressure correction equation using GMRES with short restart, in F. Benkhaldoun & R. Vilsmeier, eds, 'Finite Volumes for Complex Applications', Hermès, Paris, pp. 417–424.
- Boussinesq, J. (1877), 'Théorie de l'écoulement tourbillant', *Memoires Presentes par Divers Savants Sciences Mathematique et Physiques, Academie des sciences, Paris*.
- Boussinesq, J. (1903), *Théorie Analytique de la chaleur*, Vol. 2, Gauthier-Villars, Paris.
- Brooks, I. & Lick, W. (1972), 'Lake currents associated with the thermal bar', *J. Geophys. Res.* **77**(30), 6000–6013.
- Budd, J., Kerfoot, W. C., Pilant, A. & Jipping, L. M. (1999), 'The Kweenaw Current and ice rafting: use of satellite imagery to investigate copper-rich particle dispersal', *J. Great Lakes Res.* **25**(4), 642–662.
- Callender, E. & Granina, L. (1997), 'Geochemical mass balance of major elements in Lake Baikal', *Limnol. Oceanogr.* **42**, 148–155.
- Carmack, E. C. (1979), 'Combined influence of inflow and lake temperatures on spring circulation in a riverine lake', *J. Phys. Oceanogr.* **9**, 422–434.

- Carmack, E. C. & Gray, C. B. J. (1982), 'Patterns of circulation and nutrient supply in a medium residence-time reservoir: Kootenay Lake, British Columbia', *Can. Water Resour.* **7**, 51-70.
- Carmack, E. C. & Weiss, R. F. (1991), Convection in Lake Baikal: an example of thermobaric instability, in P. C. Chu & J. C. Garcard, eds, 'Deep Convection and Deep Water Formation in the Oceans', Elsevier Oceanography Series, 57, pp. 215-228.
- Carmack, E. C., Gray, C. B. J., Pharo, C. H. & Daley, R. J. (1979), 'Importance of lake-river interaction on seasonal patterns in the general circulation of Kamloops Lake, British Columbia', *Limnol. Oceanogr.* **24**(4), 634-644.
- Carmack, E. C., Wiegand, R. C., Daley, R. J., Gray, C. B. J., Jasper, S. & Pharo, C. H. (1986), 'Mechanisms influencing the circulation and distribution of water mass in a medium residence time lake', *Limnol. Oceanogr.* **31**(2), 249-265.
- Chen, C. T. A. & Millero, F. J. (1977), 'Effect of salt content on the temperature of maximum density and on static stability in Lake Ontario', *Limnol. Oceanogr.* **22**(1), 158-159.
- Chen, C. T. A. & Millero, F. J. (1986), 'Precise thermodynamic properties for natural waters covering only the limnological range', *Limnol. Oceanogr.* **31**(3), 657-662.
- Cheng, R. T., Powell, T. M. & Dillon, T. M. (1976), 'Numerical models of wind driven circulation in lakes', *Appl. Math. Modell.* **1**, 141-159.
- Csanady, G. T. (1971), 'On the equilibrium shape of the thermocline in the shore zone', *J. Phys. Oceanogr.* **1**(2), 263-270.
- Dokulil, M. T. (1994), 'Environmental control of phytoplankton productivity in turbulent turbid systems', *Hydrobiologia* **289**, 65-72.
- Edlund, M. B., Stoermer, E. F. & Pilskaln, C. H. (1995), 'Siliceous microfossil succession in the recent history of two basins in Lake Baikal, Siberia', *J. Paleolimnology* **14**(2), 165-184.
- Edwards, A. M. (2001), 'Adding detritus to a nutrient-phytoplankton-zooplankton model: a dynamical-systems approach', *J. Plankton Res.* **23**(4), 389-413.

- Eklund, H. (1963), 'Fresh water: temperature of maximum density calculated from compressibility', *Science* **142**, 1457-1458.
- Elliott, G. H. (1970), A laboratory and mathematical study of the 'thermal bar', PhD thesis, Inst. of Oceanogr., Univ. of British Columbia, Vancouver, B.C., Canada.
- Elliott, G. H. (1971), A mathematical study of the thermal bar, in 'Proc. 14th Conf. Great Lakes Res.', Int. Assoc. Great Lakes Res., pp. 545-554.
- Elliott, G. H. & Elliott, J. A. (1969), Small-scale model of the 'thermal bar', in 'Proc. 12th Conf. Great Lakes Res.', Int. Assoc. Great Lakes Res., pp. 553-557.
- Elliott, G. H. & Elliott, J. A. (1970), Laboratory studies on the thermal bar, in 'Proc. 13th Conf. Great Lakes Res.', Int. Assoc. Great Lakes Res., pp. 413-418.
- Falkner, K. K., Church, M., Measures, C. I., LeBaron, G., Thouron, D., Jeandel, C., Stourdal, M. C., Gill, G. A., Mortlock, R., Froelich, P. & Chan, L.-H. (1997), 'Major and trace element chemistry of Lake Baikal, its tributaries, and surrounding hot springs', *Limnol. Oceanogr.* **42**(2), 329-345.
- Falkner, K. K., Measures, C. I., Herbelin, S. E., Edmond, J. M. & Weiss, R. F. (1991), 'The major and minor element geochemistry of Lake Baikal', *Limnol. Oceanogr.* **36**(3), 413-423.
- Farmer, D. M. & Carmack, E. C. (1981), 'Wind mixing and restratification in a lake near the temperature of maximum density', *J. Phys. Oceanogr.* **11**, 1516-1533.
- Farrow, D. E. (1995a), 'An asymptotic model for the hydrodynamics of the thermal bar', *J. Fluid Mech.* **289**, 129-140.
- Farrow, D. E. (1995b), 'A numerical model of the hydrodynamics of the thermal bar', *J. Fluid Mech.* **303**, 279-295.
- Fasham, M. J. R., Ducklow, H. W. & McKelvie, S. M. (1990), 'A nitrogen-based model of plankton dynamics in the oceanic mixed layer', *J. Mar. Res.* **48**, 591-639.
- Forel, F. A. (1880), 'La congélation des lacs Suisses et savoyards pendant l'hiver 1879-1880. 11 - Lac Léman', *L'Écho des Alpes* **3**, 149-161.

- Foster, T. D. (1972), 'An analysis of the cabbeling instability in sea water', *J. Phys. Oceanogr.* **2**, 294-301.
- Franke, U., Hutter, K. & Johnk, K. (1999), 'A physical-biological coupled model for algal dynamics in lakes', *Bull. Math. Biol.* **61**(2), 239-272.
- Franks, P. J. S., Wroblewski, J. S. & Flieri, G. R. (1986), 'Behaviour of a simple plankton model with food-level acclimation by herbivores', *Mar. Biol.* **91**, 121-129.
- Gaskell, P. H. & Lau, A. K. C. (1988), 'Curvature-compensated convective transport: SMART, a new boundedness-preserving transport algorithm', *Int. J. Num. Methods in Fluids* **8**, 617-641.
- Gbah, M. B. & Murthy, R. C. (1998), 'Characteristics of turbulent cross and along-shore momentum exchanges during a thermal bar episode in Lake Ontario', *Nordic Hydrology* **29**(1), 57-72.
- Gbah, M. B., Jacobs, S. J., Meadows, G. A. & Bratkovitch, A. (1998), 'A model of the thermal bar circulation in a long basin', *J. Geophys. Res.* **103**(C6), 12807-12821.
- Gill, A. E. (1982), *Atmosphere-Ocean Dynamics*, Vol. 30 of *International Geophysics Series*, Academic Press, New York.
- Goldman, C. R., Elser, J. J., Richards, R. C., Reuter, J. E., Priscu, J. C. & Levin, A. L. (1996), 'Thermal stratification, nutrient dynamics, and phytoplankton productivity during the onset of spring phytoplankton growth in Lake Baikal, Russia', *Hydrobiologia* **331**, 9-24.
- Grachev, M. A. (1991), 'Slow renewal of deep waters', *Nature* **349**, 654-655.
- Gray, C. B. J. & Tuominen, T. M., eds (1999), *Health of the Fraser River Aquatic Ecosystem: A Synthesis of Research Conducted Under the Fraser River Action Plan*, Environment Canada, Vancouver, B.C., Canada. 2 Volumes. DOE FRAP 1998-11.
- Gronskaya, T. P. & Littova, T. E. (1991), Brief characteristics of the water budget of Lake Baikal from 1962 through 1988, in 'Monitoring of the Lake Baikal environment', Gidrometeoizdat, Leningrad, pp. 153-158 (in Russian).

- Haedrich, R. L. (1996), 'Deep-water fishes: evolution and adaptation in the Earth's largest living spaces', *J. Fish Biol.* **49**, 40-53.
- Hamblin, P. F. (1971), An investigation of horizontal diffusion in Lake Ontario, in 'Proc. 14th Conf. Great Lakes Res.', Int. Assoc. Great Lakes Res., pp. 570-577.
- Hamblin, P. F. & Carmack, E. C. (1978), 'River-induced currents in a fjord lake', *J. Geophys. Res.* **83**, 885-899.
- Henderson-Sellers, B. (1984), *Engineering Limnology*, Monographs and Surveys in Water Resources Engineering; 8, Pitman.
- Hirsch, C. (1988), *Numerical Computation of Internal and External Fluid Flows Vol. 1 - Fundamentals of Numerical Discretization*, Numerical Methods in Engineering, John Wiley and Sons, New York.
- Hohmann, R., Kipfer, R., Peeters, F., Piepke, G., Imboden, D. M. & Shimaraev, M. N. (1997), 'Processes of deep-water renewal in Lake Baikal', *Limnol. Oceanogr.* **42**(5), 841-855.
- Holland, P. R., Kay, A. & Botte, V. (2000), The riverine thermal bar, in 'Proc. 5th Workshop on Physical Processes in Natural Waters', Limnological Institute SB RAS, Preprint No. 4, pp. 369-374.
- Holland, P. R., Kay, A. & Botte, V. (2001), 'A numerical study of the dynamics of the riverine thermal bar in a deep lake', *Environmental Fluid Mechanics* **1**, 311-332.
- Holland, P. R., Kay, A. & Botte, V. (2002), 'A numerical study of the ecological implications of the riverine thermal bar circulation', *In preparation*.
- Howard, L. N. (1961), 'Note on a paper of John W. Miles', *J. Fluid Mech.* **10**, 509-512.
- Huang, J. C. K. (1969), The thermal current structure in Lake Michigan, a theoretical and observational model study, Special report no. 43, Great Lakes Res. Div., Univ. of Mich., Ann Arbor.
- Huang, J. C. K. (1971), 'The thermal current in Lake Michigan', *J. Phys. Oceanogr.* **1**(2), 105-122.
- Huang, J. C. K. (1972), 'The thermal bar', *Geophys. Fluid Dyn.* **3**(1), 1-25.

- Hubbard, D. W. & Spain, J. D. (1973), The structure of the early Spring thermal bar in Lake Superior, in 'Proc. 16th Conf. Great Lakes Res.', Int. Assoc. Great Lakes Res., pp. 735-742.
- ILEC (n.d.), World Lakes Database - International Lakes Environment Committee, Database of unpublished questionnaires, personal communications and government internal reports. Collected at <http://www.ilec.or.jp/>.
- Imboden, D. M. & Wüest, A. (1995), Mixing mechanisms in lakes, in A. Lerman, D. Imboden & J. Gat, eds, 'Physics and Chemistry of Lakes', Springer-Verlag, pp. 83-138.
- Inaba, I. & Fukuda, T. (1986), 'Natural convection in an inclined square cavity in regions of density inversion of water', *J. Fluid Mech.* **142**, 363-381.
- Ivey, G. N. & Hamblin, P. F. (1989), 'Convection near the temperature of maximum density for high Rayleigh number, low aspect ratio, rectangular cavities', *Trans. of the ASME* **111**, 100-105.
- Jasper, S., Carmack, E. C., Daley, R. J., Gray, C. B. J., Pharo, C. H. & Wiegand, R. C. (1983), 'Primary productivity in a large, temperate lake with river interflow: Kootenay Lake, British Columbia', *Can. J. Fish. Aquat. Sci.* **40**, 319-327.
- Jones, H. & Marshall, J. (1993), 'Convection with rotation in a neutral ocean: a study of open-ocean deep convection', *J. Phys. Oceanogr.* **23**, 1009-1039.
- Karabanov, E. B., Prokopenko, A. A., Williams, D. F. & Khursevich, G. K. (2000), 'A new record of Holocene climate change from the bottom sediments of Lake Baikal', *Palaeogeography Palaeoclimatology Palaeoecology* **156**(3-4), 211-224.
- Kay, A. (2001), 'Thermobaric flow', *Dynamics of Atmospheres and Oceans* **34**(2-4), 263-289.
- Kay, A., Kuiken, H. K. & Merkin, J. H. (1995), 'Boundary-layer analysis of the thermal bar', *J. Fluid Mech.* **303**, 253-278.
- Kelley, D. E. (1997), 'Convection in ice-covered lakes: effects upon algal suspension', *J. Plankton Res.* **19**(12), 1859-1880.
- Killworth, P. D. & Carmack, E. C. (1979), 'A filling-box model of river-dominated lakes', *Limnol. Oceanogr.* **24**(2), 201-217.

- Killworth, P. D., Carmack, E. C., Weiss, R. F. & Matear, R. (1996), 'Modelling deep-water renewal in Lake Baikal', *Limnol. Oceanogr.* **41**(7), 1521-1538.
- Kipfer, R., Hofer, M., Peeters, F., Imboden, D. M. & Domysheva, V. M. (2000), 'Vertical turbulent diffusion and upwelling in Lake Baikal estimated by inverse modeling of transient tracers', *J. Geophys. Res.* **105**(C2), 3451-3464.
- Kozhova, O. M. & Izmet'seva, L. R. (1998), *Lake Baikal - Evolution and Biodiversity*, Biology of Inland Waters, Backhuys, Leiden, The Netherlands.
- Kreiman, K. D. (1989), 'Thermal bar based on laboratory experiments', *Oceanology* **29**, 695-697.
- Landahl, M. T. & Mollo-Christenson, E. (1986), *Turbulence and Random Processes in Fluid Mechanics*, Cambridge University Press, Cambridge.
- Lankford, K. E. & Bejan, A. (1986), 'Natural convection in a vertical enclosure filled with water near 4°C', *ASME J. Heat Trans.* **108**, 755-763.
- Lean, D. R. S., Abbott, A. A. & Pick, F. R. (1987), 'Phosphorous deficiency of Lake Ontario plankton', *Can. J. Fish. Aquat. Sci.* **44**, 2069-2076.
- Leonard, B. P. (1979), 'A stable and accurate convective modelling procedure based on quadratic upstream interpolation', *Comput. Methods Appl. Mech. Eng.* **19**, 59-98.
- Leonard, B. P. & Drummond, J. E. (1995), 'Why you should not use 'Hybrid', 'Power-Law' or related exponential schemes for convective modelling - there are much better alternatives', *Int. J. Numer. Methods in Fluids* **20**, 421-442.
- Leonard, B. P. & Mokhtari, S. (1990), 'Beyond first-order upwinding: the ULTRA-SHARP alternative for non-oscillatory steady-state simulation of convection', *Int. J. Numer. Methods Eng.* **30**, 729-766.
- Likhoshway, Y. V., Kuzmina, A. Y., Potyemkina, T. G., Potyemkin, V. L. & Shimaraev, M. N. (1996), 'The distribution of diatoms near a thermal bar in Lake Baikal', *J. Great Lakes Res.* **22**, 5-14.
- Liu, J. W. (1985), 'Modification of the minimum degree algorithm by multiple elimination', *ACM Transactions of Math. Software* **11**, 141-153.

- Liu, J. W. (1992), 'The multifrontal method for sparse matrix solution: theory and practice', *SIAM Review* **34**, 82-109.
- MacKay, A. W., Flower, R. J., Kuzmina, A. E., Granina, L. Z., Rose, N. L., Appleby, P. G., Boyle, J. F. & Battarbee, R. W. (1998), 'Diatom secession trends in recent sediments from Lake Baikal and their relation to atmospheric pollution and to climate change', *Phil. Trans. Roy. Soc. Lond. B* **353**(1371), 1011-1055.
- Malm, J. (1995), 'Spring circulation associated with the thermal bar in large temperate lakes', *Nordic Hydrology* **26**, 331-358.
- Marmoush, Y. R., Smith, A. A. & Hamblin, P. F. (1984), 'Pilot experiments on the thermal bar in lock-exchange flow', *ASCE J. Energy Eng.* **110**(3), 215-227.
- Mayzaud, P. & Poulet, S. A. (1978), 'The importance of the time factor in the response of zooplankton to varying concentrations of naturally occurring particulate matter', *Limnol. Oceanogr.* **23**, 1144-1154.
- Mellor, G. L. (1973), 'Analytic prediction of the properties of stratified planetary surface layers', *J. Atmos. Sci.* **30**, 1061-1069.
- Mellor, G. L. & Durbin, P. A. (1975), 'The structure and dynamics of the ocean surface mixed layer', *J. Phys. Oceanogr.* **5**, 718-728.
- Michalsky, J. & Lemmin, U. (1995), 'Dynamics of vertical mixing in the hypolimnion of a deep lake: Lake Geneva', *Limnol. Oceanogr.* **40**, 809-816.
- Miles, J. W. (1961), 'On the stability of heterogeneous shear flows', *J. Fluid Mech.* **10**, 496-508.
- Moll, R. A. & Brahe, M. (1986), 'Seasonal and spatial distribution of bacteria, Chlorophyll and nutrients in nearshore Lake Michigan', *J. Great Lakes Res.* **12**(1), 52-62.
- Moll, R. A., Bratkovitch, A., Chang, W. Y. B. & Pu, P. (1993), 'Physical, chemical, and biological conditions associated with the early stages of the Lake Michigan vernal thermal front', *Estuaries* **16**(1), 92-103.
- Moll, R. A., Davis, C. O. & Schelske, C. L. (1980), 'Phytoplankton productivity and standing crop in the vicinity of the Lake Huron - Saginaw Bay front', *J. Great Lakes Res.* **6**(3), 232-246.

- Mortimer, C. H. (1974), 'Lake hydrodynamics', *Mitteilungen Int. Ver. Limnol.* **20**, 124–197.
- Naumenko, M. A. (1994), 'Some aspects of the thermal regime of large lakes: Lake Ladoga and Lake Onega', *Water Poll. Res. J. Can.* **29**(2-3), 423–439.
- Oppe, T. C., Joubert, W. D. & Kincaid, D. R. (1988), *NSPCG User's Guide*, Center for Numerical Analysis, The University of Texas at Austin.
- Pacanowsky, R. C. & Philander, S. G. (1981), 'Parameterisation of vertical mixing in numerical models of tropical oceans', *J. Phys. Oceanogr.* **11**, 1443–1451.
- Paffenhöfer, G. A. & Knowles, S. C. (1979), 'Ecological implications of fecal pellet size, production and consumption of copepods', *J. Mar. Res.* **37**, 35–49.
- Parfenova, V. V., Shimaraev, M. N., Kostornova, T. Y., Domysheva, V. M., Levin, L. A., Dryukker, V. V., Zhdanov, A. A., Gnatovskii, R. Y., Tsekhanovskii, V. V. & Logacheva, N. F. (2000), 'On the vertical distribution of microorganisms in Lake Baikal during spring deep-water renewal', *Microbiology* **69**, 357–363.
- Parker, R. A. (1986), 'Simulating the development of Chlorophyll maxima in the Celtic Sea', *Ecol. Modelling* **33**, 1–11.
- Parker, R. A. (1991), 'Eddy diffusion of phytoplankton and nutrients: estimating coefficients from simulated and observed vertical distributions', *J. Plankton Res.* **13**, 815–830.
- Parsons, T. R., Brasseur, R. J. L. & Fulton, J. D. (1967), 'Some observations on the dependance of zooplankton grazing on the cell size and concentration of phytoplankton blooms', *J. Oceanogr. Soc. Jap.* **23**, 10–17.
- Patankar, S. V. (1980), *Numerical Heat Transfer and Fluid Flow*, Computational Methods in Mechanics and Thermal Sciences, Hemisphere, New York.
- Patankar, S. V. & Spalding, D. B. (1972), 'A calculation procedure for heat, mass, and momentum transfer in three-dimensional parabolic flows', *Int. J. Heat and Mass Transfer* **15**, 1787–1806.

- Popova, E. E., Fasham, M. J. R., Osipov, A. V. & Ryabchenko, V. A. (1997), 'Chaotic behaviour of an ocean ecosystem model under seasonal external forcing', *J. Plankton Res.* **19**, 1495-1515.
- Quay, P. D., Broecker, W. S., Hesslein, R. H. & Schindler, D. W. (1980), 'Vertical diffusion rates determined by tritium tracer experiments in the thermocline and hypolimnion of two lakes', *Limnol. Oceanogr.* **25**, 201-218.
- Ravens, T. M., Kocsis, O., Wüest, A. & Granin, N. (2000), 'Small-scale turbulence and vertical mixing in Lake Baikal', *Limnol. Oceanogr.* **45**(1), 159-173.
- Reynolds, C. S. (1994), 'The long and the short and the stalled: on the attributes of phytoplankton selected by physical mixing in lakes and rivers', *Hydrobiologia* **289**, 9-21.
- Reynolds, C. S., Descy, J.-P. & Padisák, J. (1994), 'Are phytoplankton dynamics in rivers so different from those in shallow lakes?', *Hydrobiologia* **289**, 1-7.
- Rodgers, G. K. (1965), The thermal bar in the Laurentian Great Lakes, in 'Proc. 8th Conf. Great Lakes Res.', Univ. Michigan, Great Lakes Res. Div., Publ. 15, pp. 369-374.
- Ruban, G. I. (1997), 'Species structure, contemporary distribution and status of the Siberian sturgeon, *Acipenser baerii*', *Env. Biol. Fishes* **48**, 221-230.
- Saad, Y. & Schoults, M. H. (1986), 'GMRES: a generalised minimal residual algorithm for solving non-symmetric linear systems', *SIAM J. Sci. Statist. Comput.* **7**(3), 856-869.
- Scavia, D. & Bennett, J. R. (1980), 'Spring transition period in Lake Ontario - a numerical study of the causes of the large biological and chemical gradients', *Can. J. Fish. Aquat. Sci.* **37**, 823-833.
- Scavia, D. & Fahnenstiel, G. L. (1987), 'Dynamics of Lake Michigan phytoplankton: mechanisms controlling epilimnetic communities', *J. Great Lakes Res.* **13**(2), 103-120.
- Shimaraev, M. N. & Granin, N. G. (1991), 'Temperature stratification and the mechanism of convection in Lake Baikal', *Dokl. Akad. Nauk.* **321**, 381-385.

- Shimaraev, M. N., Granin, N. G. & Zhdanov, A. A. (1993), 'Deep ventilation of Lake Baikal due to spring thermal bars', *Limnol. Oceanogr.* **38**(5), 1068-1072.
- Shimaraev, M. N., Verbolov, V. I., Granin, N. G. & Sherstyankin, P. P. (1994), *Physical Limnology of Lake Baikal: A Review*, Print No. 2, Baikal International Center for Ecological Research, Irkutsk - Okayama.
- Smith, I. R. (1975), *Turbulence in Lakes and Rivers*, Scientific Publication 29, Freshwater Biological Association, UK.
- Soballe, D. M. & Kimmel, B. L. (1987), 'A large-scale comparison of factors influencing phytoplankton abundance in rivers, lakes, and impoundments', *Ecology* **68**(6), 1943-1954.
- Steele, J. H. (1965), 'Notes on some theoretical problems in production ecology', *Mem. Ist. Ital. Idrobiol., Dott Marco de Marchi* **18**(Suppl.), 383-398.
- St. John, B. E., Carmack, E. C., Daley, R. J., Gray, C. B. J. & Pharo, C. H. (1976), *The Limnology of Kamloops Lake, British Columbia*, Inland Waters Directorate, Vancouver, B.C., Canada.
- Thomas, L. H. (1949), Elliptic problems in linear difference equations over a network, Technical report, Watson Scientific Computing Lab., Columbia University, New York.
- Tikhomirov, A. I. (1963), 'The thermal bar of Lake Ladoga', *Izv. Akad. Nauk SSSR Ser. Geogr.* **95**, 134-142. [Transl. Amer. Geophys. Univ., Soviet Hydrology Selected Papers No. 2].
- Truscott, J. E. & Brindley, J. (1994), 'Stability and excitability in a general class of plankton population models', *Phil. Trans. R. Soc. Lond. A* **347**, 703-718.
- Tsvetova, E. A. (1995), Convective currents associated with the thermal bar of Lake Baikal, in A. S. Alekseev & N. S. Bakhvalov, eds, 'Advanced Mathematics: Computations and Applications', Novosibirsk Computer Centre, pp. 386-393.
- Tsvetova, E. A. (1999), 'Mathematical modelling of Lake Baikal hydrodynamics', *Hydrobiologia* **407**, 37-43.

- Ullman, D., Brown, J., Cornillon, P. & Mavor, T. (1998), 'Surface temperature fronts in the Great Lakes', *J. Great Lakes Res.* **24**(4), 753-775.
- Votintsev, K. K. (1993), 'On the natural conditions of Lake Baikal in connection with the development of its water quality standard', *Water Resources* **20**(5), 595-604.
- Votintsev, K. K., Glazunov, I. V. & Tolmacheva, A. P. (1965), Hydrochemistry of the rivers of the basin of Lake Baikal, in G. I. Galazii, ed., 'Limnological Institute Studies, Vol.8', Izdatel'stvo, Nauka.
- Walker, S. J. & Watts, R. G. (1995), 'A three-dimensional numerical model of deep ventilation in temperate lakes', *J. Geophys. Res.* **100**(C11), 22,711-22,731.
- Ward, F. J. (1964), *Limnology of Kamloops Lake*, Bulletin XVI, International Pacific Salmon Fisheries Commission, New Westminster, BC, Canada.
- Weiss, R. F., Carmack, E. C. & Koropalov, V. M. (1991), 'Deep-water renewal and biological production in Lake Baikal', *Nature* **349**, 665-669.
- Welander, P. (1968), 'Theoretical forms for the vertical exchange coefficients in a stratified fluid with applications to lakes and seas.', *Acta R.Soc. Sci. Litt. Gothob. Geophys.* **1**, 1-26.
- Welker, M. & Welz, N. (1999), 'Plankton dynamics in a river-lake system - on continuity and discontinuity', *Hydrobiologia* **408/409**, 233-239.
- Wetzel, R. G. (1983), *Limnology*, Second edition, Saunders College Publishing, Philadelphia.
- Wiegand, R. C. & Carmack, E. C. (1981), 'Some types of temperature inversion encountered in a freshwater lake with short residence time', *Limnol. Oceanogr.* **26**(3), 565-571.
- Wilcox, D. C. (1993), *Turbulence Modelling for CFD*, DCW Industries Inc., California.
- Witte, E. (1902), 'Zur theorie der stromkabelungen', *Gaea(Cologne)* pp. 484-487.
- Wroblewski, J. S. & Richman, J. G. (1987), 'The non-linear response of plankton to wind mixing events - implications for survival of larval northern anchovy', *J. Plankton Res.* **9**, 103-123.

Zilitinkevich, S. S., Kreiman, K. D. & Terzhevik, A. Y. (1992), 'The thermal bar', *J. Fluid Mech.* **236**, 22-47.

